Title

Continuous Profiling of Magnetotelluric Fields

Author

Verdín, C T

Publication Date

1991-05-01

LBL-31334

Lawrence Berkeley Laboratory
UNIVERSITY OF CALIFORNIA

EARTH SCIENCES DIVISION

Continuous Profiling of Magnetotelluric Fields

C.T. Verdín
(Ph.D. Thesis)

May 1991

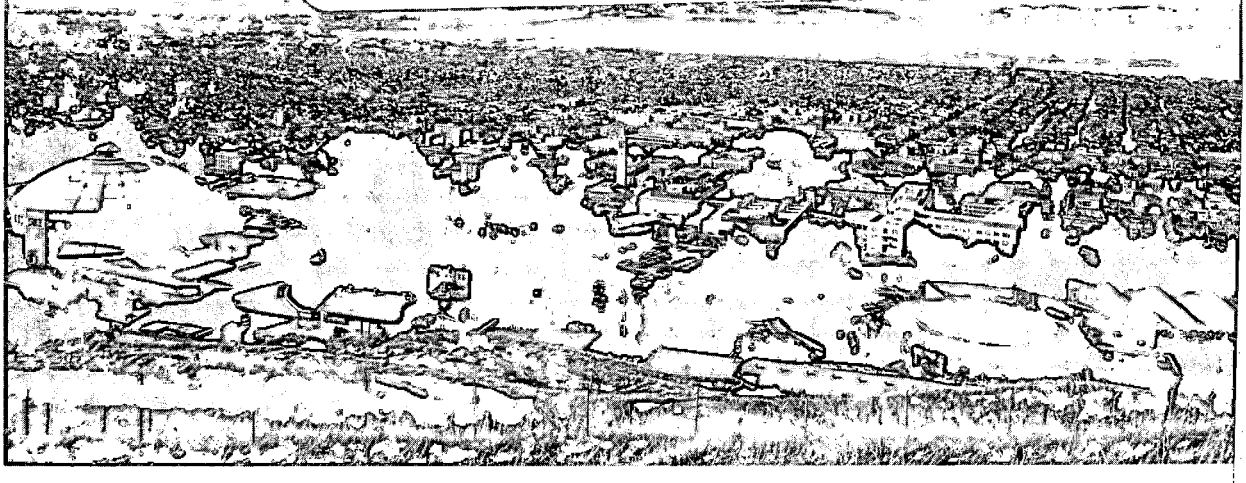

Prepared for the U.S. Department of Energy under Contract Number DE-AC03-76SF00098

DISCLAIMER

LBL-31334

Continuous Profiling of Magnetotelluric Fields

Carlos Torres-Verdín

(Ph.D. Thesis)

Engineering Geoscience
University of California

and

Earth Sciences Division
Lawrence Berkeley Laboratory
University of California
Berkeley, California 94720

May 1991

This work was supported in part by the Director, Office of Energy Research, Office of Basic Energy Sciences, Engineering and Geosciences Division, of the U.S. Department of Energy under Contract No. DE-AC03-76SF00098.

Continuous Profiling of Magnetotelluric Fields

by

Carlos Torres-Verdín

Abstract

The magnetotelluric (MT) method of mapping ground electrical conductivity is traditionally based on measurements of the surface impedance at widely spaced stations to infer models of the subsurface through a suitable pseudo 1-D inverse or with linearized least-squares inversion for 2- or 3-D geoelectric media. It is well known that small near-surface inhomogeneities can produce spatial discontinuities in the measured electric fields over a wide frequency range and may consequently bias the impedance on a very local scale. Inadequate station spacing effectively aliases the electric field measurements and results in distortions that cannot be removed in subsequent processing or modelling. In order to fully exploit the benefits of magnetotellurics in complex geological environments, closely spaced measurements must be used routinely. This thesis entertains an analysis of MT data taken along continuous profiles and is a first step that will allow more encompassing 2-D sampling techniques to become viable in the years to come.

The developments presented here are to a large extent motivated by the physical insight gained from low-contrast solutions to the forward MT problem. These solutions describe the relationship between a perturbation in the electrical conductivity of the subsurface and the ensuing perturbation of the MT response as the output of a linear system. Albeit strictly accurate in a limited subset of practical exploration problems, the linearized solutions allow one to pursue a model independent study of the response characteristics of MT data. In fact, these solutions yield simple expressions for 1-, 2-, and 3-D resistivity models which are here examined in progressive sequence.

Over 1-D media, study of the vertical resolution characteristics of MT data is pursued with a logarithmic parameterization of both frequency and depth which transforms the linear system equation into a simple convolutional formula. Standard Fourier analysis is then used to establish that the largest vertical wavenumber of the subsurface resistivity distribution that in practice can be recovered from noisy data is approximately 3.5 cycles/decade, which in turn implies that at most 7 or 8 frequency samples/decade are all that is needed to infer vertical variations of resistivity within the resolving power of magnetotellurics. Further, to evaluate the validity of the 1-D linear system equations, inversion experiments are performed over resistivity profiles wherein the low-contrast assumption is not acceptable. These experiments yield consistent checks when resistivity

contrasts are lower than 1:10 and therefore indicate that albeit of limited practical use, the linearized solutions do embody the physics of magnetotellurics.

The 1-D linear system concepts are extended to the study of 2-D MT data, electric and magnetic, in order to understand what properties of the subsurface resistivity distribution are borne by each field component. A major thrust of this section is the estimation of lateral resolution bounds with which features in the subsurface can be inferred from noisy data. It is found that, below the Nyquist wavenumber dictated by the sampling distance, the largest wavenumber that can be recovered with 1% noise in the data is approximately the inverse of the Bostick depth of penetration. Also, a 2-D inversion procedure is introduced in the wavenumber domain which consists of a sequence of 1-D pseudo inverses performed for each wavenumber harmonic. Numerical experiments with this new method of inversion confirm that TM electric field data possess superior lateral resolution to TE electric field data, and that the former may be subject to instability and hence poor vertical resolution because of static effects. However, it is found that a natural way to stabilize the inversion of TM electric field data is to prewhiten them prior to inversion. When prewhitening is enforced in the inversion of TM data, the wavenumber-domain inversion produces acceptable results when the resistivity contrasts are below 1:10 approximately.

The linearized 3-D equations describe the surface electric response as the additive interplay of static and induction components. The induction component is sensitive to the increase of depth of penetration with a decrease in frequency, whereas the static component is not, and this causes the electric amplitude response to be biased by shallow geoelectric features. Wavenumber-domain solutions for MT fields over 3-D media suggest that the static component may be separated from the induction component by way of spatial filtering of the surface electric field. Application of this processing step to field data requires that electric dipoles be deployed end-to-end continuously along a profile of measurements. Such is the basis of Electromagnetic Array Profiling (EMAP), a subject discussed in a second part of this thesis. A data-adaptive spatial filtering procedure is developed for the suppression of frequency-dependent static effects which consists of lateral and frequency adjustment of the cutoff wavenumber properties of the TM prewhitening filter elicited with the 2-D linearized inverse. Adaptive spatial filtering is tested on 2-D subsurface resistivity models which include static effects and exhibit strong nonlinear response characteristics. A simple 1-D Bostick pseudoinverse applied to the spatially filtered data yields relatively accurate resistivity cross-sections in negligible CPU times. The feasibility of EMAP is demonstrated by three field examples which reveal with unprecedented clarity the errors that would have been generated had the interpretation been performed with single-station data. Also, the level of lateral detail achieved with the use of spatial filtering is consistent with the vertical and lateral resolution bounds imposed by the underlying diffusion equation.

Even though a single profile of tangential electric field measurements often leads to reliable cross-sections of 3-D geoelectric media, the studies presented here indicate that measurements of orthogonal electric and vertical magnetic fields are needed to recognize lateral induction effects in the measured tangential electric field data. For instance, over 2-D ground, an EMAP line laid out at an angle with respect to strike can yield estimates of the TE and TM impedances provided that the field acquisition includes some measurements of the orthogonal electric field. However, the acquisition of orthogonal electric field data should be made in a way that does not incur on spatial aliasing problems and that permits one to suppress static effects. Procedures that can be used to infer induction and dimensionality parameters of the subsurface with the aid of spatial filtering are illustrated with a field example wherein electric field data gathered along intersecting lines is first filtered and then rotated to produce tensor impedances unbiased by static effects.

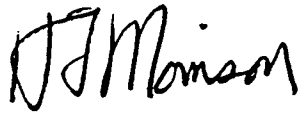

Va
para todas las personas
que con sus sortilegios mundos
contribuyeron a hacer de mi
experiencia doctoral
una aventura del
espíritu

Acknowledgements

I would like to express my gratitude to my supervising professor, Frank Morrison, whose academic support and constructive criticism were never a substitute for camaraderie, but rather a natural extension. He has always been enthusiastic and adroit at finding alleys to support my research in magnetotellurics. Francis Bostick has been an unending source of inspiration; without his creative influence and friendship much of this work would have never been possible. I am also grateful to the other two members of my dissertation committee, Alex Becker, and Ken Mei, whose teaching and encouragement have been enduring. Alex went out of his way to have a first draft of this thesis devoid of glaring mistakes.

Ki Ha Lee's thought-provoking comments and suggestions were crucial in understanding many loose ends during the course of my research. Philip Wannamaker generously shared his experience and numerical simulation codes, and Louise Pellerin provided me with valuable insights to three-dimensional modelling. Many of the long days and nights either at school or in the field were times to befriend my peers and engage with them in laborious digressions often with no end. In those times we learned the intricate worlds of each other's research amidst sincere interest, ecstasy, frustration, joy and what not. Among them, I would like to mention Ali Tura, Guimin Liu, Qiang Zhou, Ed Nichols, Maryla Deszcz-Pan, Cliff Schenkel, Seunghee Lee, Mike Wilt, Ted Asch, David Alumbaugh, and Dimitri Bevc.

Not to be held secondary to those whose names appear above, I would like to thank the encouragement, motivation and peerless affection of my wife, Laurel Treviño Murphy, who in good and bad times of her own doctorate seldom ceased to be *une source d'imagination, et un chamin à la découverte.* A special note of gratitude goes to my parents, brothers and sisters, for their continued understanding and help despite the distance and prolonged absences.

Financial support came in various ways. First, I am obliged to both the Mexican Institute for Petroleum (IMP), and the National Council of Science and Technology (CONACYT) of México, who bestowed on me fellowship and tuition support at different stages of the Ph.D. A grant-in-aid by Mintech Geosciences, USA, helped conduct a great deal of the numerical simulation work recounted here. The Geothermal Energy Resource and Development (GERD) of Tokyo, Japan, generously shared some of their field

experiences in various preliminary feasibility studies for the continuous measurement of magnetotelluric fields. The Surprise Valley field experiment was funded through a cooperative grant by Trans-Pacific Geothermal Co., and Lawrence Berkeley Laboratory. For this survey, equipment was made available by Electromagnetic Instruments, Inc. Last but not least, thanks are extended to the New Energy and Industrial Technology Development Organization (NEDO) of Japan for permission to use the Sengan EMAP data in some of the studies presented here, and to the geophysical exploration companies Marc-Rand and Advanced Energy Technology for organizing the data into a usable form.

This work was partially supported by the Director, Office of Energy Research, Office of Basic Energy Sciences, Engineering and Geosciences Division, of the U.S. Department of Energy under contract no. DE-AC03-76SF00098.

Table of Contents

CHAPTER I

INTRODUCTION

1.1 Magnetotellurics

Magnetotellurics is a geophysical technique that utilizes measurements of natural electric and magnetic fluctuations, typically in the frequency band from 0.001 to 20,000 Hz, to infer electrical properties of the subsurface. At frequencies below approximately 1 Hz, these fluctuations originate from interactions between streams of solar plasma and the outer envelopes of the ionosphere and magnetosphere. Above 1 Hz, useful electromagnetic (EM) energy is provided by electric thunderstorm activity taking place mainly about the equator and reaching other latitudes as propagation modes inside the earth-ionosphere cavity. There are two advantages in using these natural EM fluctuations for the sounding of the earth: their large energy levels (not yet artificially produced by man) and their wide frequency range. Both high energy levels and wide frequency range combine to allow, in principle, the probing of the subsurface anywhere from a few meters down to hundreds of kilometers.

The fundamentals of magnetotellurics followed from independent scientific endeavors in the Soviet Union by A. Tikhonov (1950) and in France by L. Cagniard (1953), both in the context of layered earth models. Practical considerations make it feasible for magnetotellurics to assume a source of EM excitation in the form of plane waves impinging normally upon the surface of the earth. Tikhonov and Cagniard's early work showed that lowering the sounding frequency provides a selective deepening of the zone of response within the earth. This result is consistent with the skin depth effect that best describes the diffusion of EM waves in conductive media.

Magnetotelluric (MT) soundings have been used in the past for the exploration of geothermal (Goldstein, 1988) and hydrocarbon (Orange, 1989) reservoirs. Other no less important applications of magnetotellurics include scientific studies aimed at defining the electrical properties of the earth's lower crust and mantle (Wannamaker at al., 1989), and in earthquake monitoring and prediction studies (Honkura et al., 1976, and Honkura, 1978). A high-frequency, artificial-source version of magnetotellurics referred to as the Controlled-Source Audio-Magnetotelluric (CSAMT) method (Goldstein and Strangway,

1975), purports to use the same interpretation principles used in magnetotellurics, with the difference that a measurable amount of current is artificially injected into the ground to increase signal levels at high frequencies. The CSAMT method has been used with moderate success in the exploration of mineral deposits (Zonge et al., 1986) and geothermal reservoirs (Goldstein, 1988).

In the hydrocarbon industry, magnetotellurics has played an auxiliary exploration role in geological situations difficult, if not impossible, to approach with the seismic method (Orange, 1989.) Examples of these situations are sedimentary basins underlying a thick surface volcanic stratum and regions in which abrupt topographic relief make seismic methods impractical. In geothermal exploration, magnetotellurics finds itself in natural advantage over the seismic methods because the bulk electrical contrasts that exist in a geothermal reservoir are much larger than those of an elastic nature (Goldstein, 1988). High-frequency (from 1 to 20,000 Hz) applications of magnetotellurics are suited for the exploration of massive mineral deposits (Morrison et al., 1990).

As the exploration for energy and mineral resources is directed toward more inaccessible and geologically complex regions in which conventional seismic techniques are expected to have little success, a more prominent role is anticipated for magnetotellurics. Also, growing interest in magnetotellurics can be expected because of its almost null environmental impact and relative ease of implementation in areas of difficult access. Nevertheless, even under favorable circumstances, because magnetotellurics obeys the physics of a diffusive EM process, its resolving power cannot compete with the wave-equation attributes of the seismic method. Hence, in reconciliation with its limited resolution, it is important that the MT response be sampled adequately both in frequency and spatially. Only when this is done can interpretation procedures be used to optimally extract the characteristics of the subsurface resistivity distribution within the resolution bounds imposed by the underlying diffusion equation. Meeting the required sampling conditions has led to a great deal of instrumentation and theoretical work by the MT community, and this work has advanced the technique to a fairly mature state of development.

1.2 Interpretation of MT data and the static effect

The relative simplicity with which MT data can be interpreted over one-dimensional (1-D) environments quickly disappears in the presence of lateral variations of subsurface

resistivity. Ways in which this data complexity can be dealt with have been the central subject of a myriad academic and practical MT studies (e.g. Vozoff, Ed., 1986.)

Results embodied in Cagniard's (1953) MT exposition suggest that, over a non-layered earth, lateral variations of the measured MT fields at high frequencies should reflect the lateral variations of near-surface resistivity, whereas lateral variations of the fields at lower frequencies should reflect the lateral variations in subsurface resistivity deeper in the earth. Put in Cagniard's own words:

> "... Consequently, one can lay out the survey of a large sedimentary basin by performing at the start a small number of MT-soundings far removed from one another, but with a great depth of investigation. In the second step, one will intercalate stations closer together, and at these he will perform MT-soundings with a more moderate depth of penetration. Finally, the continuity between the stations will be assured either by soundings with a relatively small depth of investigation, or, once in a while, by simple, quick determinations of the apparent resistivity summarily evaluated through a very simplified analysis of the magneto-telluric data... "

Unfortunately, the situation is not nearly so simple: field and theoretical MT studies (see, for instance, Swift, 1967, Word et al., 1969, Berdichevsky and Dmitriev, 1976, and Berdichevsky et al., 1980) have shown that in geoelectric environments other than 1-D, the low-frequency electric amplitude response from the subsurface can be dominated by the response from the shallowest resistivity anomalies. Since the electric response from the subsurface is the most prominent MT response (see section 1.3), this low-frequency sensitivity to near-surface geoelectric features (including abrupt topographic relief) is highly undesirable, and, because of its DC nature and partly in analogy with a similar problem faced by seismic exploration, it is usually referred to as the **static effect** by MT practitioners. The static effect arises at frequencies where the skin depth is larger than the size of the near-surface geoelectric features in the vicinity of the measurement point. Under these circumstances, the near-surface features exhibit electrostatic behavior, as though responding to a uniform DC electric field excitation, and their DC response is usually larger in magnitude than that of deeper subsurface structure responding inductively at the same frequency.

Below the frequency where the DC distortion comes into play, the electric static effect can be described as the product of a real constant times the otherwise undistorted electric field (Berdichevsky and Dmitriev, 1976). Because of this, the phase of the frequency-domain complex ratio total electric field to primary magnetic field often suffers no appreciable static distortion. This important property has suggested the possibility of

avoiding the static effect altogether by inverting the lateral variations of impedance phase alone into subsurface resistivity estimates. However, previous studies in this area (Weidelt, 1972, Boehl et al., 1977) show that, for instance, the interpretation of 1-D subsurface resistivity variations solely from phase data is unique provided that an amplitude response level is known beforehand. With the presence of electric static effects, the desired amplitude level is uncertain. To further complicate matters, shallow 3-D geoelectric features may sometimes cause DC current channeling effects capable of deflecting the secondary electric field vector and hence produce a non-inductive distortion in impedance phase (Bahr, 1987, and Groom and Bailey, 1989).

In the presence of static distortion, one may resort, in favorable situations, to auxiliary methods of interpretation to recover an undistorted amplitude level in the electrical response from the subsurface. One such situation occurs when both resistivity and depth to a spatially continuous feature in the geoelectric model are known from external information (Jones, 1988.) Other times, controlled-source EM methods can be used whenever the geometrical complexity of the surface resistivity does not introduce interpretation problems whose solution requires dense spatial sampling of the secondary magnetic fields (Andrieux and Wightman, 1984, Sternberg et al., 1988, and Pellerin and Hohmann, 1990.) Situations in which the electric static effect arises below some particular value of frequency rather than as a constant shift in logarithmic amplitude throughout the whole measured frequency range, are much more difficult to handle with auxiliary correction procedures than with MT data themselves. There exists another technique that even though offering only partial remedy to the static effect, sheds valuable insight to the physics of DC current channeling. This technique exploits the characteristics of the electric field sensor.

In magnetotellurics, electric field sensors, or dipoles, consist of conductive wires laid on the ground with end points in contact with the earth such that, in response to electric currents flowing in the ground, a potential difference develops between the two electrodes. The measured potential difference, V, is in general expressed by the line integral

$$\int_{\Gamma} \mathbf{E} \cdot d\boldsymbol{\ell} \,, \tag{1.1}$$

for which the path of integration, Γ, extends along the conductive wires, the vector $\mathbf{E}$ is the electric field in the earth along the wire path, and $d\boldsymbol{\ell}$ is the differential curve element tangential to Γ. The acquisition process described by equation (1.1) intrinsically averages,

i.e., low-pass filters the surface electric fields, thereby providing a measure of suppression to the contribution from the static effect local to the point of measurement.

To illustrate this situation, consider the two-dimensional (2-D) geoelectric model whose cross section is shown in Figure 1-1, with x- and y-axes oriented in directions perpendicular and parallel to strike, respectively. The model consists of a confined, 0.5 Ω•m, outcropping rectangular block embedded in a two-layer earth in which the upper layer has a thickness of 4 km and a resistivity of 20 Ω•m, and the lower layer is a 1 Ω•m half-space. Figure 1-2 shows the apparent resistivity and impedance phase curves simulated at an observation point located in the middle of the outcropping conductor for both, TE (electric field parallel to strike) and TM (electric field perpendicular to strike) polarization modes. The synthesized frequency range is from 0.001 to 1,000 Hz, with calculations performed at 10 frequencies per decade and evenly spaced in logarithmic fashion. For the computation of the TM curves shown in Figure 1-2, numerical integration was used to replicate the electric response of a finite-length electric dipole normal to strike and centered about the observation point. The dipole lengths considered are 100, 500 and 1,000 m. Also, for comparison, a 1-D response curve is plotted in Figure 1.2 for a medium in which the outcropping conductor has infinite lateral extent. Notice that lengthening the dipole in the strike direction does not have any consequence on the TE impedances because the electric field is constant in that direction; thus, the exercise described herein concerns only the TM impedances.

At the highest frequency, both TE and 1-D apparent resistivity curves in Figure 1-2 asymptote to the resistivity of the surface conductor (0.5 Ω•m), whereas at the lowest frequency the same curves asymptote to the resistivity of the deep layer (1 Ω•m). This behavior is consistent with the inverse relation between sounding frequency and depth of penetration described by Cagniard (1953) in his seminal publication. However, in the same figure, the TM 100-m apparent resistivity curve underestimates the resistivity of the conductive basement at the lowest frequency. A similar situation is not observed in the TE and TM impedance phase curves. The amplitude difference between both TE and TM apparent resistivity curves at the lowest frequencies in Figure 1-2 is a clear example of static shift, which in this case is conditioned by the DC response of the outcropping conductor. As the dipole length increases, the low-frequency split between the two curves decreases (in fact, at 1,000 m the split has practically disappeared.) At the high frequencies, however, dipole lengths of 500 and 1,000 m are too long to detect the outcropping conductor, thus causing a loss of lateral resolution.

In response to current channeling imposed by the outcropping conductor in Figure 1-1, a profile of the secondary surface electric field perpendicular to strike exhibits positive and negative values as one marches past the conductor. These electric field variations may be described as due to surface distributions of electric charge "sieved" along the lateral boundaries of the conductor as the conduction current forces its way through them. In the DC limit, Faraday's law shows that positive and negative secondary electric field variations will balance if averaged along a line drawn across the conductor and beyond points where the secondary electric field has negligible amplitude. The electric field value that remains from such a line average primarily contains the inductive response of geoelectric features buried below the conductor. This principle is illustrated in Figure 1-3.

Even though it is advisable to use the longest possible dipoles in field surveys, this is not a general solution because the voltage difference measured with the longer dipole may itself have a static distortion caused by an even larger geoelectric feature in the subsurface. A measure of the averaging distance required to outweigh the local secondary DC electric field distortion is the adjustment distance (Ranganayaki and Madden, 1980.) For confined bodies, normally this distance is only a few times longer than the size of the body itself (Robertson, 1983), but it may be of tens of kilometers if the distortion is due to a semiinfinite slab, or an ocean-continent boundary, for instance (Mackie et al., 1988).

Due to the frequency scaling property intrinsic to MT fields, geoelectric structures that at one frequency respond in an almost exclusively inductive fashion may be the source of static distortion at a lower frequency, with their DC effect superimposed on the inductive response of even deeper targets. Lacking a better name to describe this phenomenon, in this thesis the term static effect is used in a very broad sense to include frequency-dependent static distortion. Static effects may also affect the surface magnetic field response; however, in most practical cases the electric static effect is much more significant and definitely exhibits more lateral variability than the magnetic static effect (Wannamaker et al., 1984).

1.3 Sampling requirements

In magnetotellurics, spectral estimation techniques are used to obtain a frequency and space dependent, 2x2, surface impedance matrix, $\underline{Z}$, linearly relating orthogonal electric and magnetic field values measured at the same point. Traditionally, inference of the electrical characteristics of the subsurface stems from samples of $\underline{Z}$ made at a number of locations within the survey area. Often, this inference is aided by the measurement of a

tipper vector, **T**, linearly relating the vertical magnetic field with the two horizontal magnetic field components measured at the same point. For practical reasons, the interpretation of the frequency-dependent and time-invariant transfer functions $\underline{Z}$ and **T** is almost always preferred to the direct interpretation of the electric and magnetic fields: the random nature of both source strength and polarization makes it prohibitive to simultaneously record the electric and magnetic signals at all sounding locations within the survey area.

From a fundamental viewpoint, however, the actual electric and magnetic field behavior is easier to understand than the local impedances and tipper vectors. By way of example, consider the subsurface resistivity model shown in Figure 1-4. This example includes local 2-D features as well as a regional 1-D background medium, the latter composed of exactly three layers. Two of the 2-D features outcrop to the surface of the model, and a third one is a buried block with square section. For reference, the x-axis is normal to strike and points to the right of the section, whereas the z-axis points downward. Figures 1-5 through 1-8 are profiles of the different electric and magnetic field components that describe the surface MT response along the direction normal to strike. All field quantities in these figures are displayed as ratios with respect to the corresponding 1-D background field (E_0 for the electric field components and H_0 for the magnetic field components) at the frequencies of 1000, 0.1, and 0.001 Hz. The scale on the left-hand side of the electric field plots corresponds to the logarithmic amplitude of the electric field ratio, whereas on the right-hand side of the same plots the scale is linear phase. In contrast, the lateral amplitude variations of the magnetic fields are much smaller than those of the electric fields, and are thus best described along a linear axis and as real and imaginary parts instead of amplitude and phase components. Surface lateral variations of the TM-mode magnetic field component are constant in all cases (d'Erceville and Kunetz, 1962), and are thus omitted from this study. For reference, similar field plots for the case in which near-surface conductors are not present in the model example are shown in Figures 1-9 through 1-12.

Several basic properties of MT fields can be observed in Figures 1-3 through 1-8. For instance, at 1000 Hz the lateral electric and magnetic field variations reflect the nature of the lateral variations of surface resistivity. However, the amplitude variations of both electric field components are much more prominent than those of the magnetic field components. Laterally, the TM electric field profile is discontinuous across the surface blocks. On the other hand, the TE electric field profile is smooth and, in fact, appears as a

low-pass filtered version of the TM profile. In both cases the phase profiles exhibit only slight variations. At 0.1 Hz, the TE electric field profile is mostly affected by the buried conductive block (cf. to Figure 1-10), whereas the TM electric field profile continues to show the same lateral discontinuities observed at 1000 Hz, although the discontinuity over the thicker surface conductor becomes more accentuated at the new frequency. The lateral profile of TM impedance phase at 0.1 Hz, on the other hand, develops variations that suggest the influence of both the thicker surface conductor and the buried block (cf. Figure 1-10). At the same frequency, the TE magnetic field components show their maximum amplitude (larger for the horizontal than for the vertical component) exactly over the buried conductive block, but this anomaly is also emphasized by the magnetic response of the thicker surface conductor (cf. Figure 1-10). Finally, at 0.001 Hz only the TM electric field component exhibits significant lateral amplitude variations (the phase variations of the same component are practically null at this frequency). The fact that all other field components show almost flat profiles indicate that their 2-D inductive range has virtually disappeared at this point in the frequency spectrum.

In Figure 1-6, the persistency even at 0.001 Hz of lateral amplitude variations in the TM electric field response associated with the surface features is due to distortion of static nature. In contrast, the TE electric and magnetic field components have, using Fourier analysis jargon, a band-limited 2-D response along the frequency axis consistent with the depth of penetration of an inductive process. Because of these characteristics, in the presence of highly variable (laterally) and unknown surface and subsurface resistivity structure, the static effect dictates as short as possible spacings between adjacent electric field sampling locations. This ensures that lateral bounds for the discontinuities can be recognized and not misinterpreted as deeper geoelectric structure. Spatial sampling requirements for the measurement of the TE electric field are less severe because of the absence of a static component. The magnetic field components, on the other hand, exhibit much less significant lateral variations than either electric field component and are therefore less troublesome to sample.

Over three-dimensional (3-D) geoelectric media the nature of the MT fields is more akin to that of 2-D TM fields (Swift, 1962, Wannamaker et al., 1984, and Torres-Verdín and Bostick, 1990a) although some amount of 2-D TE-type field behavior may be observed in regions with substantial current channeling.

1.4 Sampling techniques and model recovery: the problem

In most cases, economic limits impose a maximum number of MT stations that can be used for the exploration of a given target. A major task then consists of selecting sampling locations that as a set can maximize the amount of information recovered about the characteristics of the subsurface. Ways in which this can be accomplished largely depend on the "expected" characteristics that can best describe the target. By way of example again, consider the Long Valley Caldera (Mammoth Lakes, California) work recounted by Park and Torres-Verdín (1988), where regular to good-quality data from 77 MT stations scattered in an area of approximately 20x17 km, were used to ascertain the existence, and if so, the characteristics of magmatic bodies thought to underlie the volcanic sediments within the caldera. The Long Valley Caldera is a complex 3-D geoelectric environment, and in due respect the authors decided to use both a 3-D simulation code and all available complementary geophysical and geological data to carry out the interpretation. This strategy of interpretation shed some light on the general distribution of electrical conductivity within the caldera, but the spacing between adjacent stations was not short enough to eliminate dramatic sensitivity to 3-D surface features. Despite the larger than usual number of MT soundings available for the interpretation, such a near-surface sensitivity masked the evidence for massive magmatic bodies seated deep below the volcanic sediments. Had the data been acquired following the established Nyquist criterion for spatial sampling, much less uncertainty would have been introduced regarding the nature of near-surface effects and, consequently, more certainty about the surface response from deeply buried magmatic bodies.

A data acquisition strategy that recognizes the need for continuous sampling of the electric field is known as Electromagnetic Array Profiling (EMAP) (Bostick, 1986, Torres-Verdín and Bostick, 1990b, see also Chapters V and VI). In this technique, the surface electric field is sampled by deploying electric dipoles end-to-end continuously along a survey path. Electric field data acquired along the line of measurements are referred to the primary magnetic field components estimated within the survey area for subsequent processing and inversion. The field procedure used by EMAP not only reduces the likelihood of aliasing effects but also lends itself to spatial filtering of the measured electric field variations along the survey path in order to reduce distortions of static nature.

Field procedures such as EMAP open a whole new window of opportunities for the processing and subsequent inversion of MT data into estimates of subsurface resistivity. Traditionally, the inversion of MT data taken along a profile has been approached by model

parameterization schemes in which the subsurface is represented as a mesh of rectangular blocks. On the basis of this parameterization, a theoretical MT response is simulated numerically and the electrical resistivity of the blocks adjusted in an iterative fashion until a tolerable difference is found between the simulated and field data sets (Jupp and Vozoff, 1977, Rodi et al., 1984, Sasaki, 1989, Madden and Mackie, 1989, Wannamaker et al., 1989b, Oldenburg and Ellis, 1990, deGroot-Hedlin and Constable, 1990, and Smith and Booker, 1990). Unfortunately, the forward problem involved in this approach, that of deriving the wave impedances for arbitrary distributions of subsurface resistivity, can be very complicated and may, at the least, require extensive numerical computations. Another normally unrecognized complication is that stiff model parameterizations can sometimes demand excessive lateral structure within the model in order for the data to be satisfied within the desired accuracy. Even though excessive lateral complexity in the inverted parameterized model may "best fit" the field data, the results may project a wrong idea of the resolution with which features in the surface can be resolved from MT data taken on the surface. An imposing, although often disregarded, complication in solving the inverse problem is the effect of excessive separation between sampling locations. Whenever the distance between measurement locations fails to properly describe the lateral extent of local variations of both electric and magnetic fields, there is a potential risk in interpreting their wavenumber harmonics beyond the Nyquist wavenumber as false geoelectric structure in the subsurface.

A spatially continuous data set may lend itself not only to model parameterization-type inversions, but also to fast and relatively accurate inversion procedures similar to those employed in seismic data interpretation under the name of migration and field continuation (Zhdanov and Frenkel, 1983, Lee et al., 1987, and Zhdanov, 1988, for instance), or, to use more modern terminology (although not for this reason more precise), seismic imaging. Despite the limitations involved in their approximate nature, these techniques share the common theme of being consistent with the resolving power implicit in the physics of the forward problem.

Unfortunately, at least two decades of continued field and interpretation practices have demonstrated that a single MT station is not sufficient to provide a profile of electrical resistivity vs. depth. Seismological practices, by contrast, show an evolution process in which the necessity of dense spatial sampling (even vectorial) is amply recognized in any effort to provide an adequate image of the subsurface. Justifiable as it may sound, the excuse for magnetotellurics not to go in the same direction has been the underlying

assumption that, although lower in information content, a single MT station is inherently cheaper than a simple seismic survey in which, instead, a layout of many sensors is needed to unfold vertical information about the earth. Nowadays, however, with the emergence of a new front of electronic and computer technology, the economical excuse becomes less and less factual.

The feasibility of more aggressive spatial sampling technique is best appreciated from few of the most recent accounts of MT case histories. For instance, Word et al. (1986), describe an EMAP field transect across the Rocky Mountains. Shoemaker et al., (1989), introduce a variant of the EMAP technique applied to a sedimentary basin project in Oregon, including calibration with well-log data. Takasugi et al. (1989) narrate the probably most comprehensive MT survey yet undertaken in which all electric and magnetic field components were measured over a 13x13 rectangular grid in the Hokkaido Island, Japan. Pelton and Furgerson (1989), describe dense MT sampling techniques referred to as swath MT and grid MT with an example from Railroad Valley, Nevada. Morrison et al. (1990), report a continuous MT profiling technique over a mineral prospect in Nevada. Warren and Srnka (1990) describe a multiple-line hydrocarbon survey over the volcanics of the Columbia River basalt plain, and finally, Torres-Verdín and Bostick (1990c) recount a three-line EMAP survey carried out over a geothermal reservoir in northern Honshu Island, Japan (see Chapter VI).

1.5 Scope of work

This thesis can be considered a collection of research works related to the general topic of MT profiling. The arrangement in which these works are presented reflects by no means a historical progression, but rather an effort to coherently mesh them together. However, a main thrust should be clear: the attempt to understand what are the characteristics of the surface MT response that determine how subsurface structure can be resolved beneath the profile of surface measurements. Even though this is pursued under the basis of a mathematical treatment, the pragmatic aspect of the problem is left as a central aspect of the exposition. Thus, in addition to establishing physical criteria as to how to sample and interpret MT data gathered in the field, at least two methods are presented for the fast interpretation of those data.

Chapter II is an exposition of the mathematical work leading to the Born approximation of the surface electric and magnetic fields that result from exciting the earth with a normally incident plane wave. The results of this work have been the subject of

previous work by the author (Torres-Verdín, 1985, and Torres-Verdín and Bostick, 1990a), and thus only a brief summary is presented including the latest findings on the subject. The objective is to lay out the framework for the development of topics reported in subsequent chapters of the thesis.

In Chapter III, a Born, or linearized 1-D inversion method is introduced with the objective of understanding the vertical resolution bounds of data sampled in the frequency dimension. The work presented here parallels and expands that by Bostick et al. (1979).

A linearized inversion procedure applicable to 2-D data sets is introduced in Chapter IV. The material presented here can be considered a natural extension of the ideas exposed in Chapter III. Complications pertinent to this case of analysis comprise one new coordinate variable as well as three more field quantities. The inversion is carried out in the wavenumber domain and special emphasis is given to the lateral resolution bounds with which geoelectric structure can be resolved when the inversion is performed on each of the field quantities involved or, else, on appropriate combinations of them. Synthetic tests of the inversion are presented as well as a field example.

The elements of Electromagnetic Array Profiling (EMAP) are presented in Chapter V. Work related to EMAP actually comprised the earlier aspects covered in the course of the thesis research. However, having been involved in the initial development aspects of the technique, it is the author's opinion that the ideas put forth by EMAP can be best understood once the material covered in Chapters II, III, and IV has been thoroughly assimilated. Also, inasmuch as EMAP is a technique developed for and applicable to 3-D environments, it seems logical to present it following Chapter IV.

Chapter VI is an account of some of the properties of EMAP as applied to 2- and 3-D environments. In particular, in two dimensions, a procedure is introduced whereby both TE and TM impedances can be estimated from a field configuration in which the survey traverse is oblique with respect to strike. Simulation and field data examples are used to examine the performance of EMAP over 3-D environments.

Finally, Chapter VII is a compendium of conclusions to the thesis work as well as an outline of suggested topics for further research.

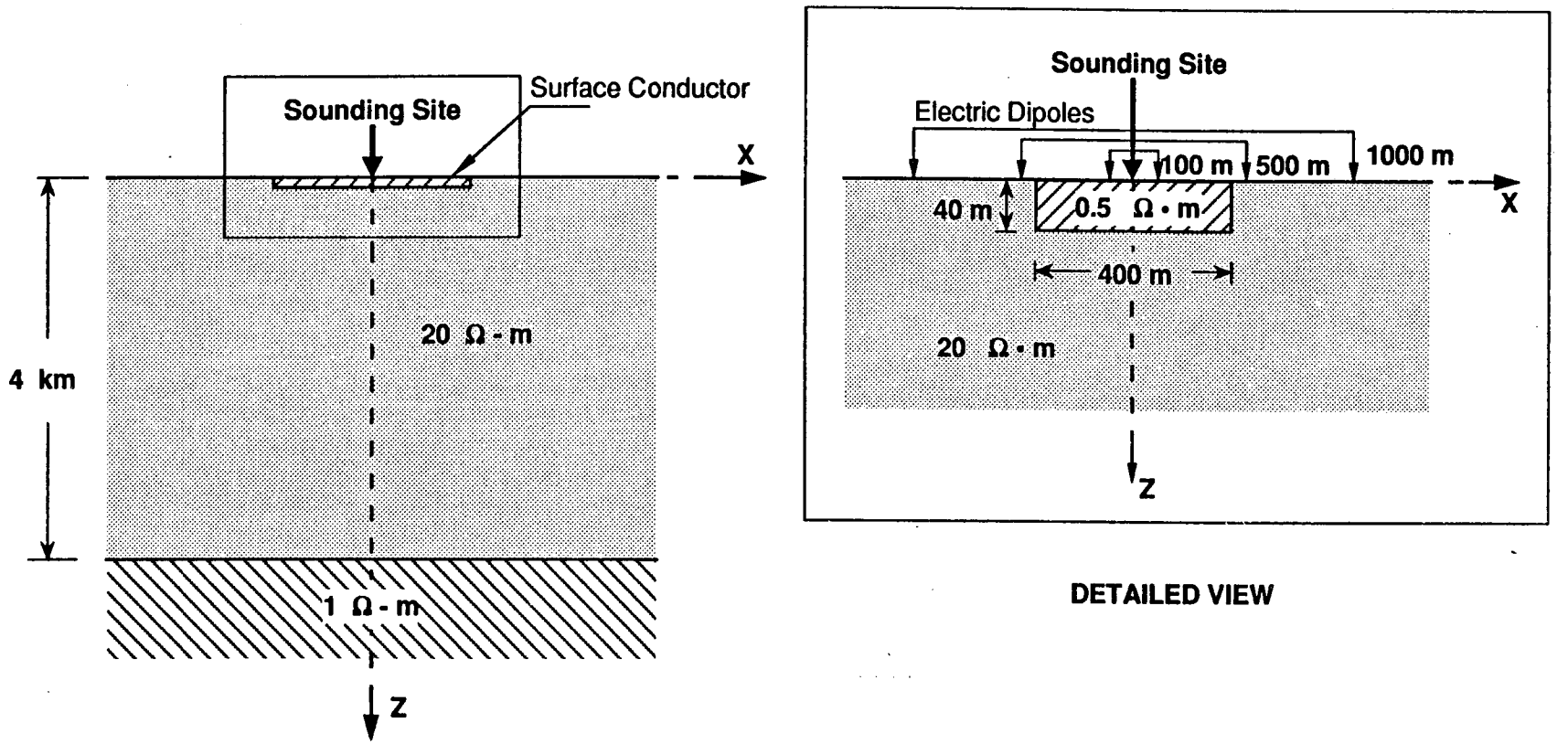

Figure 1-1. A 2-D model for the study of dipole length effects including a surface conductor embedded in an otherwise 1-D medium.

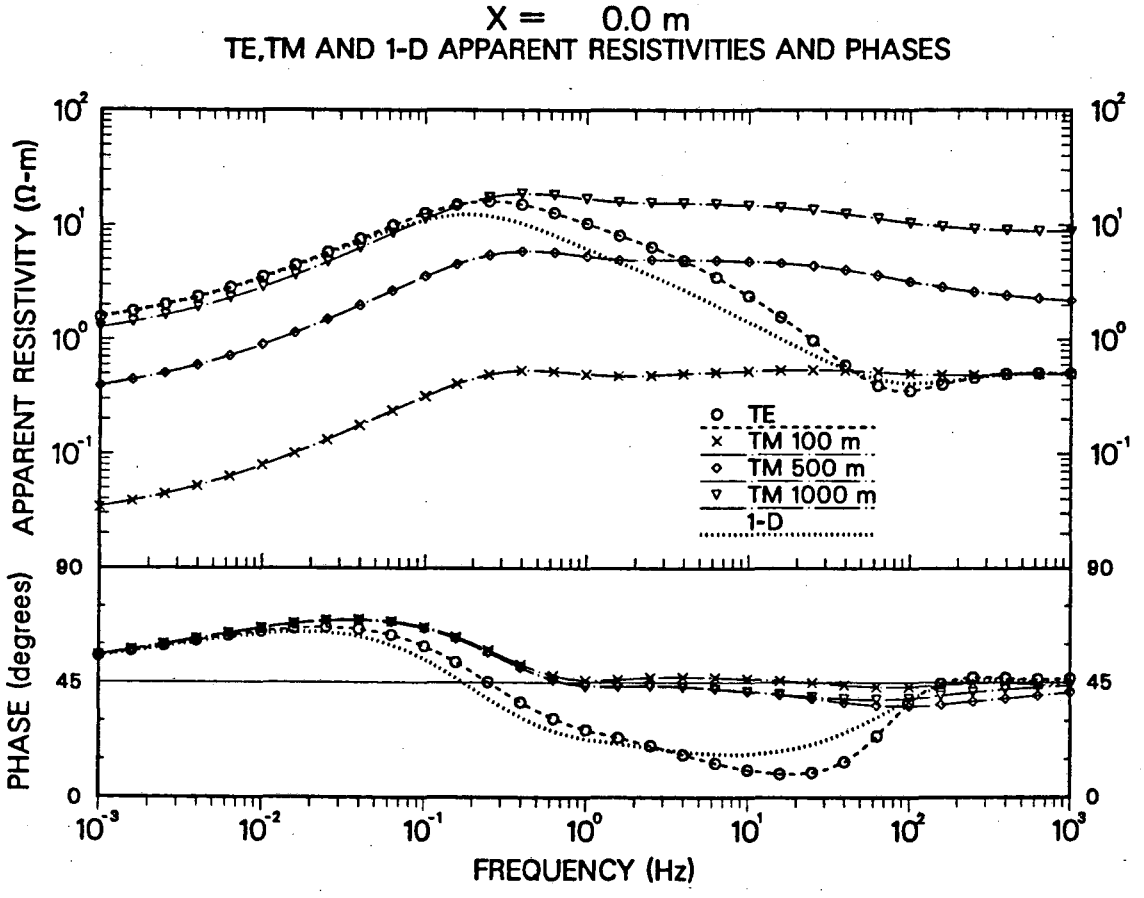

Figure 1-2. The effect of dipole length when the MT sounding site is centered within the surface conductor of Figure 1-1. Curves are shown of the TE, TM, and 1-D apparent resistivity and impedance phases simulated at the sounding site. The three different TM curves correspond to an equal number of dipole lengths, i.e., 100, 500 and 1000 m. For comparison, 1-D response curves are shown which are associated with the model shown in Figure 1-1 except that the surface conductor has infinite lateral extent.

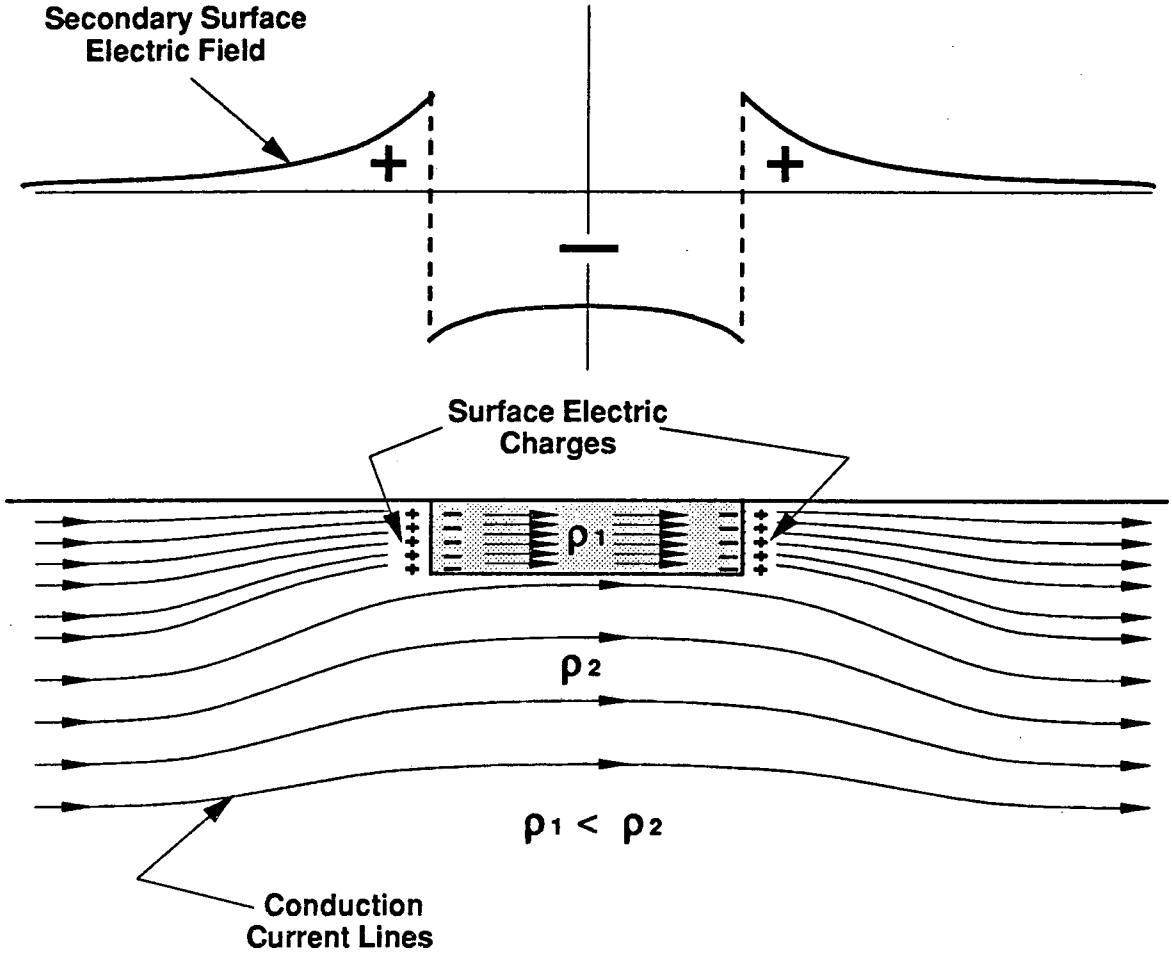

Figure 1-3. DC-limit TM electric field response of the outcropping conductor in Figure 1-1. The lower diagram depicts how some amount of the otherwise laterally uniform conduction current is bent upward and channeled through the surface conductor. This channeling effect is manifested on the surface as the surge of a secondary electric field with positive and negative lateral variations across the conductor, as shown in the upper curve. Because of Faraday's law, an average of these lateral variations will tend to zero as the observations of the secondary electric field are extended infinitely away from the conductor.

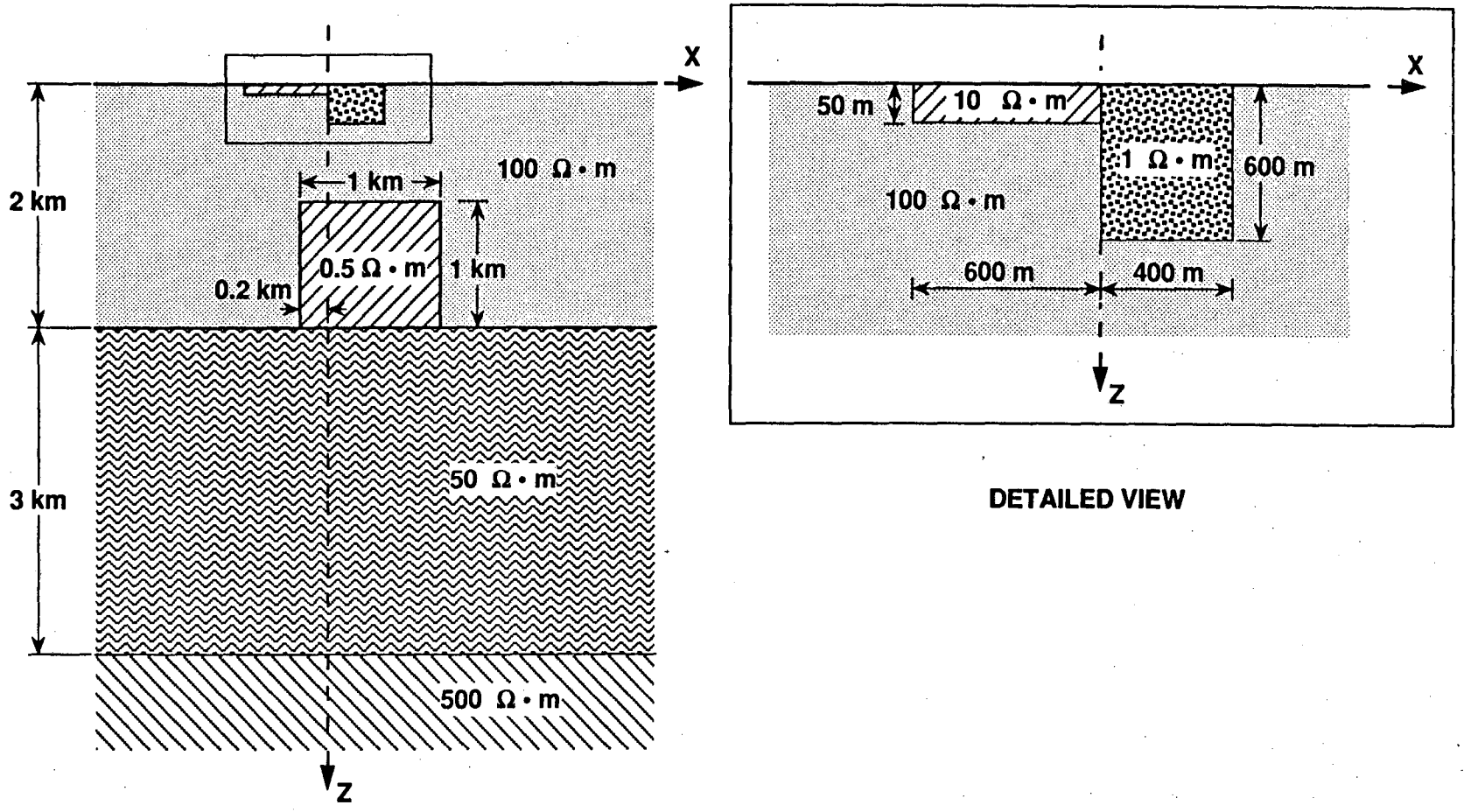

Figure 1-4. A 2-D model example for the study of lateral surface electric and magnetic field variations. The model consists of a regional 1-D background medium with exactly three layers. Features of 2-D nature are a buried block with square section and two surface conductors.

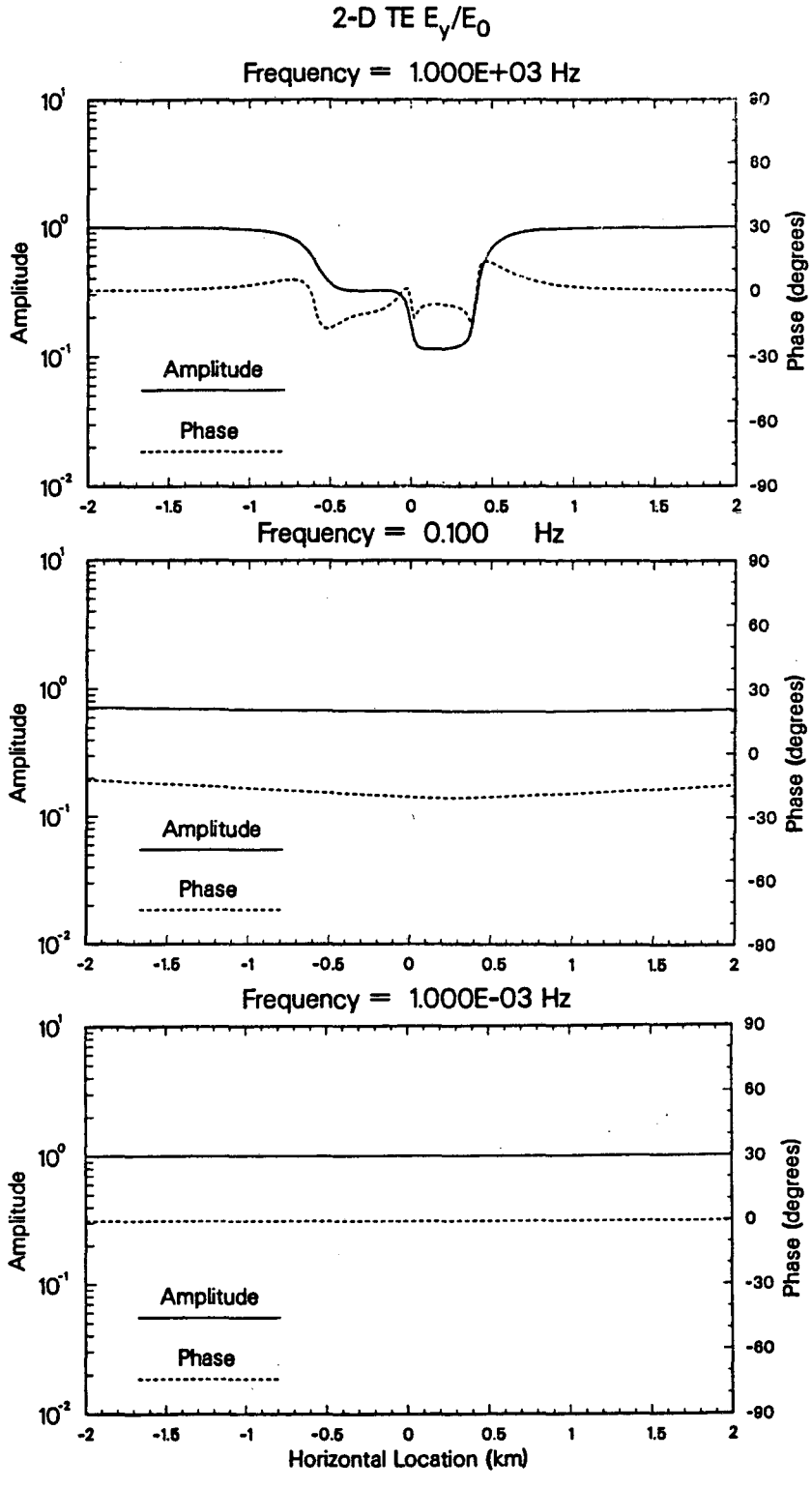

Figure 1-5. TE-mode E_y electric field component along the direction normal to strike for the model shown in Figure 1-4. Both amplitude and phase components are normalized with respect to the primary electric field, E_0, associated with the 1-D background medium. Profiles are shown at frequencies values of 1000, 0.1, and 0.001 Hz.

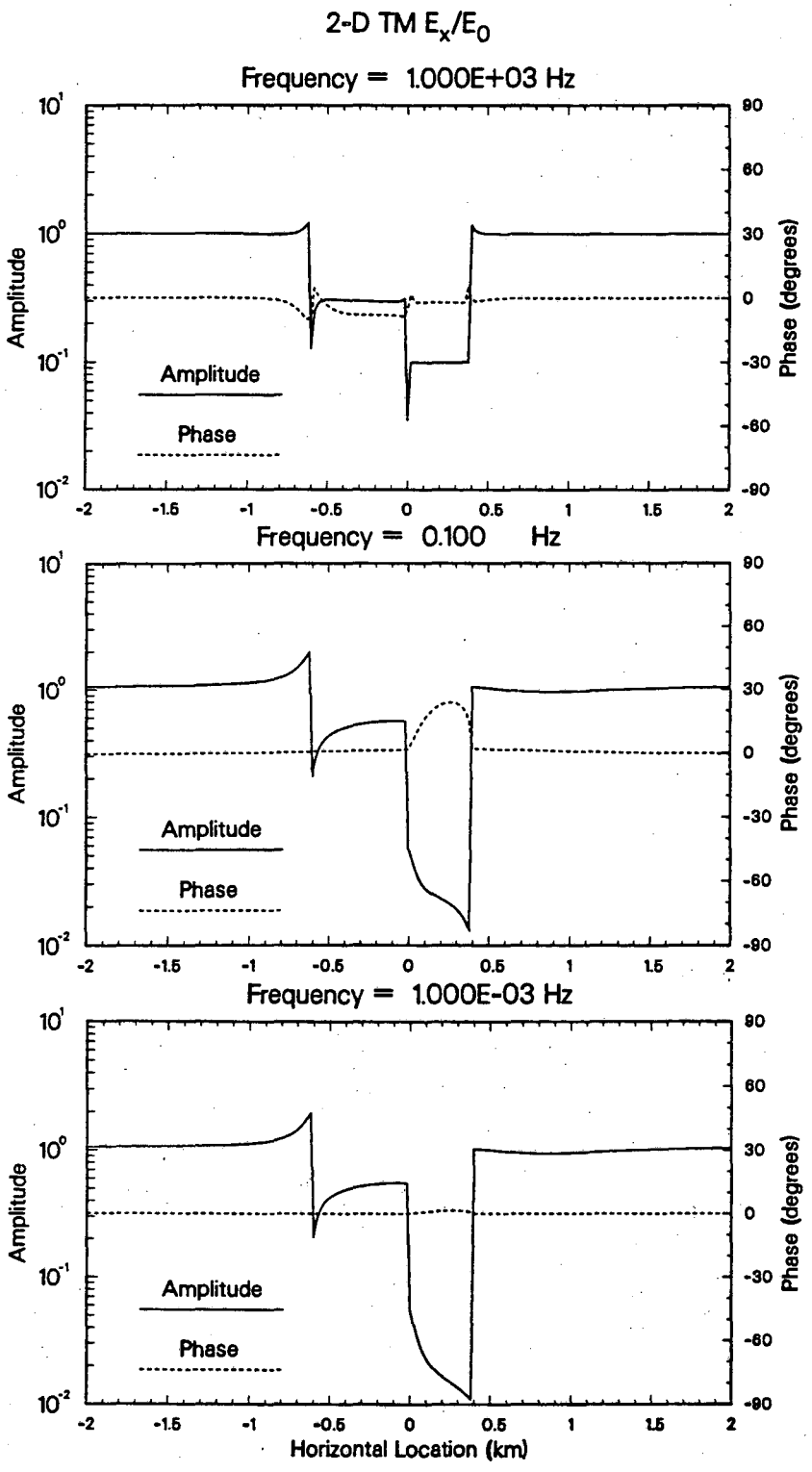

Figure 1-6. TM-mode E_x electric field component along the direction normal to strike for the model shown in Figure 1-4. Both amplitude and phase components are normalized with respect to the primary electric field, E_0, associated with the 1-D background medium. Profiles are shown at frequencies values of 1000, 0.1, and 0.001 Hz.

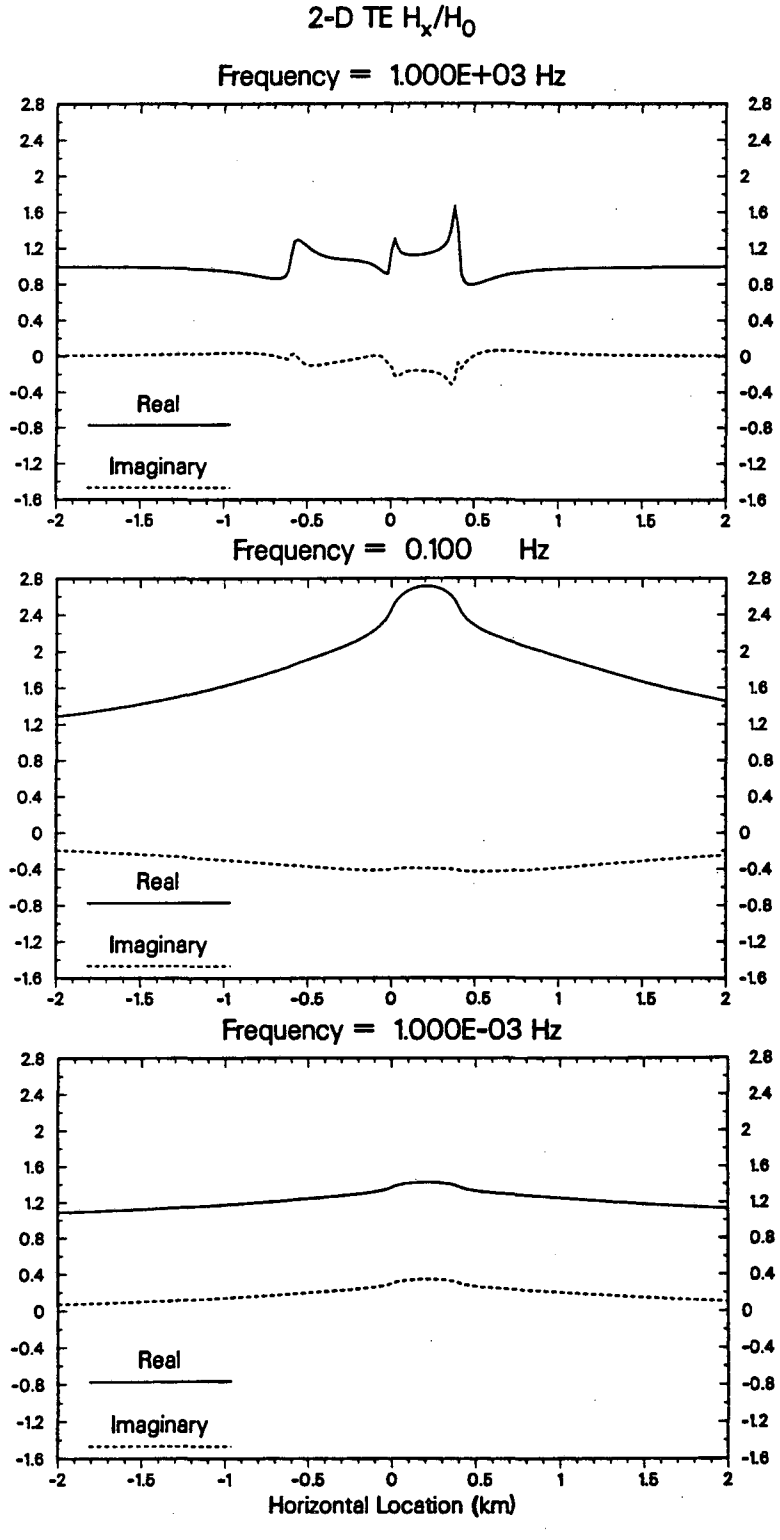

Figure 1-7. TE-mode H_x magnetic field component along the direction normal to strike for the model in Figure 1-4. Both real and imaginary components are normalized with respect to the primary magnetic field, H_0, associated with the 1-D background medium. Profiles are shown at frequencies values of 1000, 0.1, and 0.001 Hz.

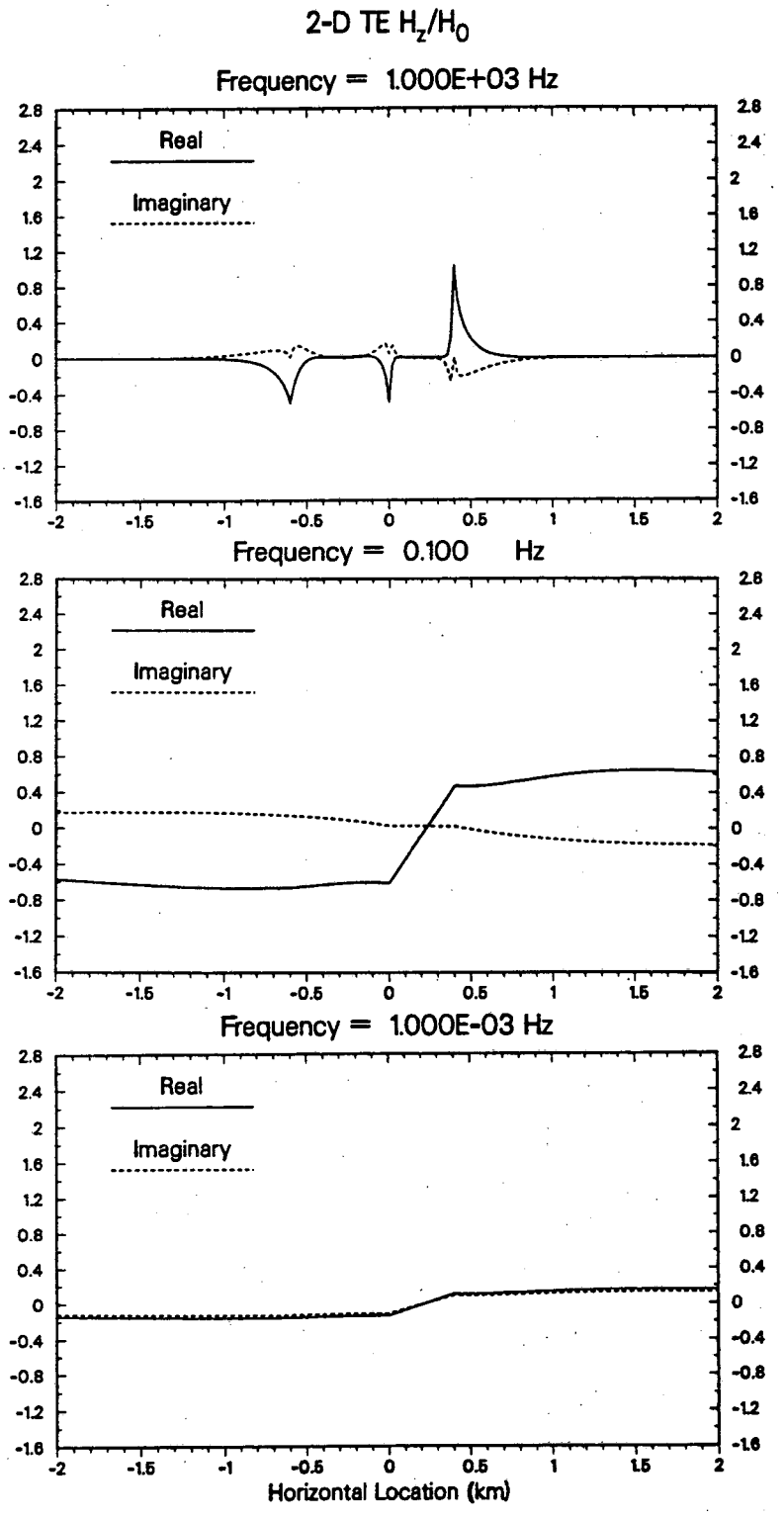

Figure 1-8. TE-mode H_z magnetic field component along the direction normal to strike for the model shown in Figure 1-4. Both real and imaginary components are normalized with respect to the primary magnetic field, H_0, associated with the 1-D background medium. Profiles are shown for the frequencies of 1000, 0.1, and 0.001 Hz.

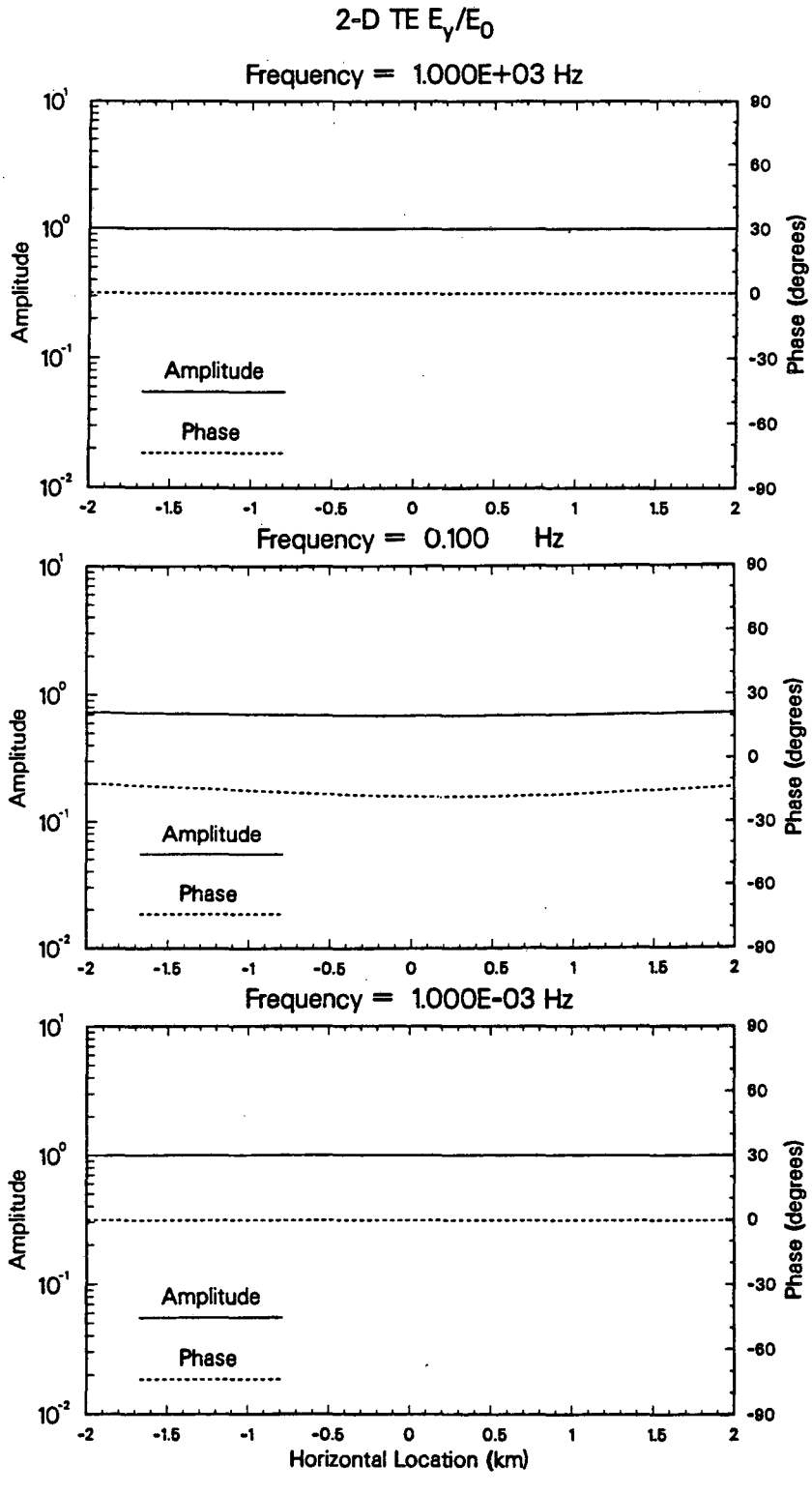

Figure 1-9. TE-mode E_y electric field component along the direction normal to strike for the model shown in Figure 1-4 assuming no surface conductors. Both amplitude and phase components are normalized with respect to the primary electric field, E_0, associated with the 1-D background medium. Profiles are shown at frequencies values of 1000, 0.1, and 0.001 Hz.

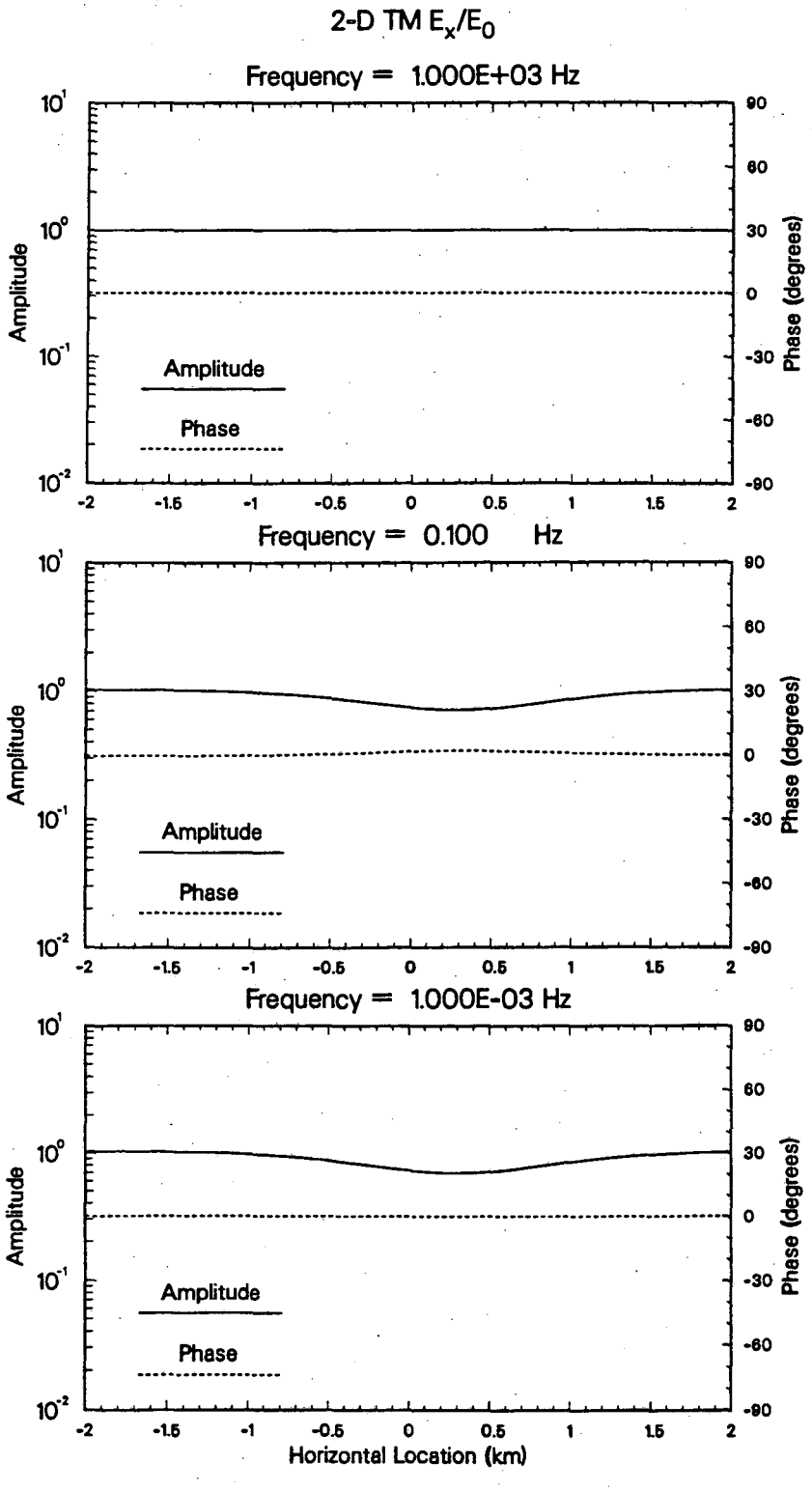

Figure 1-10. TM-mode E_x electric field component along the direction normal to strike for the model shown in Figure 1-4 assuming no surface conductors. Both amplitude and phase components are normalized with respect to the primary electric field, E_0, associated with the 1-D background medium. Profiles are shown at frequencies values of 1000, 0.1, and 0.001 Hz.

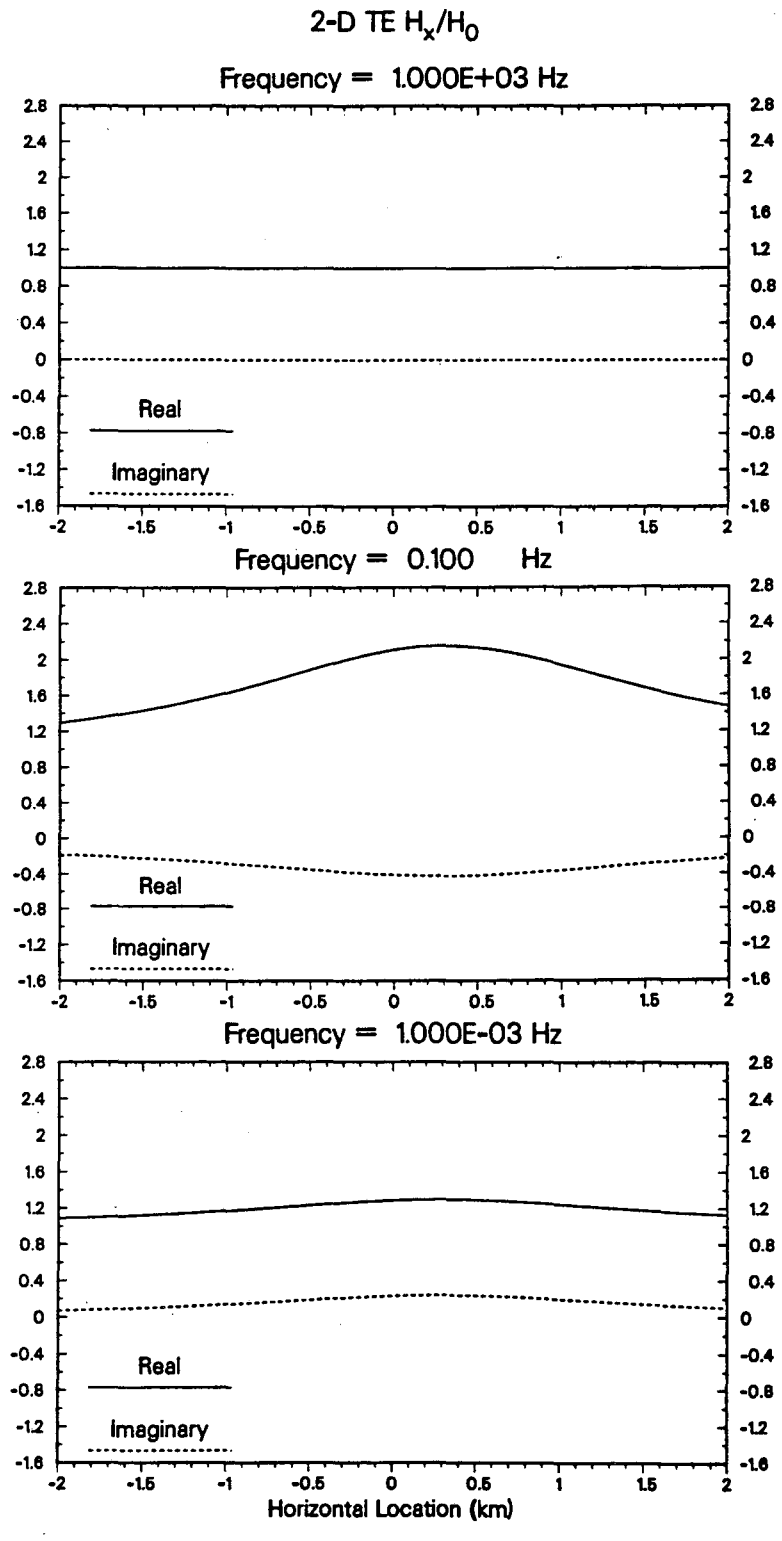

Figure 1-11. TE-mode H_x magnetic field component along the direction normal to strike for the model in Figure 1-4 assuming no surface conductors. Both real and imaginary components are normalized with respect to the primary magnetic field, H_0, associated with the 1-D background medium. Profiles are shown at frequencies values of 1000, 0.1, and 0.001 Hz.

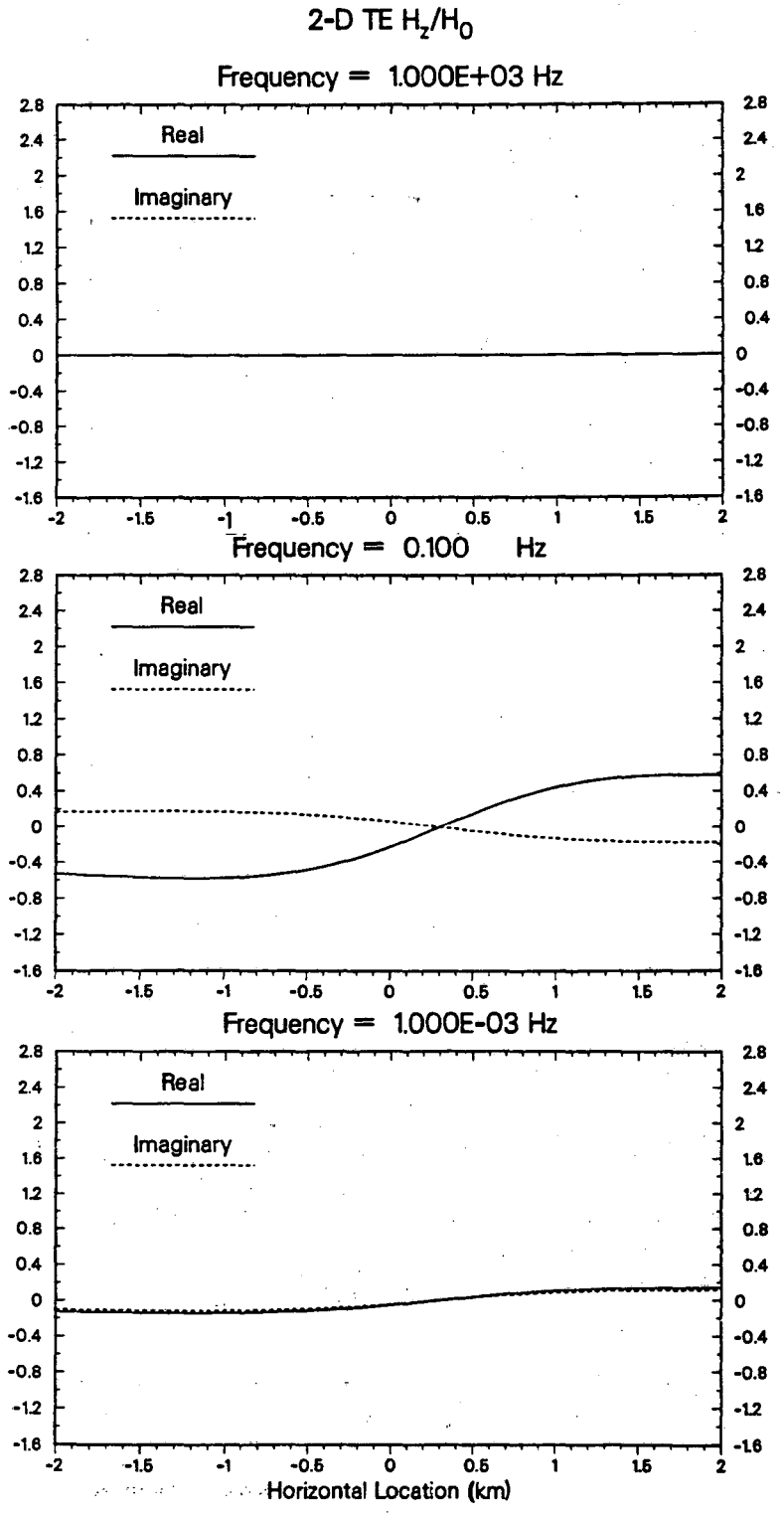

Figure 1-12. TE-mode H_z magnetic field component along the direction normal to strike for the model shown in Figure 1-4 assuming no surface conductors. Both real and imaginary components are normalized with respect to the primary magnetic field, H_0, associated with the 1-D background medium. Profiles are shown for the frequencies of 1000, 0.1, and 0.001 Hz.

CHAPTER II

BORN APPROXIMATION OF THE SURFACE MT FIELDS

2.1 Introduction

The mathematical developments presented in this chapter originated with a Master's thesis (Torres-Verdín, 1985). Also, a more comprehensive presentation of the same subject has been recently accepted for publication (Torres-Verdín and Bostick, 1990a). Since the results from these two studies serve as a foundation for the material presented in subsequent chapters, a succinct version of them is included here.

The Born approximation provides a mathematical model that is consistent with the qualitative characteristics of the surface MT fields over any type of geometrical complexity within the subsurface. Quantitatively, however, the assumptions implicit in the Born approximation restrict its numerical accuracy to those situations in which either the subsurface resistivity contrasts are small, or in which the scattered fields are only a small fraction of the primary field. Even though these restrictions may not always apply rigorously, the ensuing approximations may be used to test the MT method in inhomogeneous media and with an analysis that produces results as simple closed-form expressions. As detailed below, these expressions clearly show the characteristic response functions under inhomogeneous conditions.

2.2 Integral formulation and first-order Born approximation

The earth is described as a set of conductivity anomalies embedded in a homogeneous half-space of conductivity σ_0 and occupying the region $z \geq 0$. The air space is modelled with a non-conductive half-space in the region $z<0$, and the source of excitation provides electromagnetic (EM) energy throughout the entire range of frequencies relevant to magnetotellurics. Each frequency component of the excitation is assumed to be in the form of a plane wave, linearly polarized and propagating vertically downward onto the surface of the earth at z=0. Cartesian axes are chosen with the x-axis pointing in the direction of polarization of the incident plane wave (Figure 2-1). Unit vectors in the x, y and z directions are identified as $\hat{\mathbf{i}}$, $\hat{\mathbf{j}}$ and $\hat{\mathbf{k}}$, respectively.

At any observation point in the earth, the total MT fields may be written as

$$\mathbf{E} = \mathbf{E}_0 + \mathbf{e}, \text{ and} \tag{2.1}$$

$$\mathbf{H} = \mathbf{H}_0 + \mathbf{h}, \tag{2.2}$$

where the vectors $\mathbf{E}_0$ and $\mathbf{H}_0$ are primary electric and magnetic fields, respectively, associated with the propagation of the incident plane wave in the homogeneous half-space. The vector components **e** and **h**, on the other hand, designate secondary, or scattered fields. Similarly, the conductivity distribution in the earth may be expressed as

$$\sigma = \sigma_0 + \Delta\sigma, \tag{2.3}$$

where $\Delta\sigma$ identifies departures in conductivity away from the homogeneous half-space. In equation (2.3), the spatial function $\Delta\sigma$ is arbitrary except for two restrictions. The first is that $\Delta\sigma$ be such that σ is positive, and the second that $\Delta\sigma$ be absolutely integrable over the half-space $z \geq 0$. This last restriction insures the existence of the Fourier transform of $\Delta\sigma$, and allows the estimation of σ_0 from the spatial average of σ.

The link between the total fields **E** and **H** is determined by the source free Maxwell equations, written as

$$\nabla \times \mathbf{E} = -i\omega\mu\mathbf{H}, \text{ and} \tag{2.4}$$

$$\nabla \times \mathbf{H} = \sigma\mathbf{E}, \tag{2.5}$$

in which $i = \sqrt{-1}$, a time-harmonic variation of the form $e^{i\omega t}$ is assumed, displacement currents are neglected, and the permeability μ is set to its free space value. A similar set of equations to that of (2.4) and (2.5) is satisfied by the primary electric and magnetic fields, except that σ is replaced by σ_0.

Equations (2.1) through (2.3) substituted into (2.4) and (2.5) yield

$$\nabla^2\mathbf{e} + \kappa^2\mathbf{e} = i\omega\mu\Delta\sigma\mathbf{E}, \tag{2.6}$$

where κ is the propagation constant for the homogeneous half-space, given by

$$\kappa^2 = -i\omega\mu\sigma_0 . \tag{2.7}$$

The inhomogeneous Helmholtz equation (2.6) may be cast in the integral form

$$\mathbf{e}(\mathbf{r}) = \int_{\tau_0} \underline{G}(\mathbf{r},\mathbf{r}_0)\, \Delta\sigma(\mathbf{r}_0)\, \mathbf{E}(\mathbf{r}_0)\, d\tau_0 \tag{2.8}$$

(Morse and Feshbach, 1953), where $\mathbf{r}=(x,y,z)$ is the observation point, and the volume τ_0 corresponds to the set of source points $\mathbf{r}_0=(x_0,y_0,z_0)$ in the half-space $z\geq 0$ where $\Delta\sigma \neq 0$. In equation (8) the function $\underline{\mathbf{G}}$ is the Green's tensor satisfying

$$\nabla^2\underline{\mathbf{G}}(\mathbf{r},\mathbf{r}_0) + \kappa^2\underline{\mathbf{G}}(\mathbf{r},\mathbf{r}_0) = i\omega\mu\,\delta(\mathbf{r}-\mathbf{r}_0)\,\underline{\mathbf{I}}\,, \tag{2.9}$$

and which also complies with the boundary conditions inherent to the homogeneous half-space model; the function $\delta(\mathbf{r})$ denotes the Dirac delta, and the symbol $\underline{\mathbf{I}}$ is the unity tensor.

Within the homogeneous half-space, the primary fields are described by the pair

$$\mathbf{E}_0(z_0) = E_0\, e^{-i\kappa z_0}\,\hat{\mathbf{i}}\,, \text{ and} \tag{2.10}$$

$$\mathbf{H}_0(z_0) = H_0\, e^{-i\kappa z_0}\,\hat{\mathbf{j}}\,, \tag{2.11}$$

for which the ratio

$$\frac{E_0}{H_0} = Z_0(\omega) = \sqrt{\frac{i\omega\mu}{\sigma_0}}\,, \tag{2.12}$$

corresponds to the surface plane-wave impedance looking down into the homogeneous half-space.

First-order Born approximation of the Fredholm integral equation of the second kind (2.8) is obtained by substituting the total field $\mathbf{E}$ that appears under the integral sign in that equation by the incident field $\mathbf{E}_0$ (Morse and Feshbach, 1953.) This substitution yields j-th secondary electric field components expressed as

$$e_j(\mathbf{r}) \approx \int_{\tau_0} G_j(\mathbf{r},\mathbf{r}_0)\,\Delta\sigma(\mathbf{r}_0)\,E_0\,e^{-i\kappa z_0}\,d\tau_0\,, \qquad j = x, y, z \tag{2.13}$$

where the scalar function G_j, with units of electric field strength per dipole moment, describes the j-th component of the electric field vector due to an infinitesimal electric dipole. The latter is centered at $\mathbf{r}_0$ and oriented parallel to the x-axis.

Equation (2.13) is an accurate solution for the secondary electric field, $\mathbf{e}$, within a medium in which $|\Delta\sigma| \ll \sigma_0$. Besides this limitation, the small departures $\Delta\sigma$ away from

the homogeneous earth model preserve the attribute of three-dimensionality in the subsurface conductivity distribution.

Further simplification of equation (2.13) is done as follows. Introducing the variables ρ_0 and $\Delta\rho$, defined as

$$\rho_0 = \frac{1}{\sigma_0}, \text{ and, } \Delta\rho = \frac{1}{\Delta\sigma}, \tag{2.14}$$

respectively, one can show that under the assumption that $|\Delta\sigma| << \sigma_0$, the approximation

$$-\frac{\Delta\sigma}{\sigma_0} \approx \frac{\Delta\rho}{\rho_0}$$

holds true. Using this property, the ratio $\Delta\rho/\rho_0$ is hereafter referred to as the normalized resistivity function, and assigned the symbol ρ_n, i.e.,

$$\rho_n = \frac{\Delta\rho}{\rho_0}. \tag{2.15}$$

Equation (2.13) may thus be rewritten as

$$\frac{e_j(\mathbf{r})}{E_0} \approx \int_{\tau_0} \rho_n(\mathbf{r}_0)\, K_{ej}(\mathbf{r},\mathbf{r}_0)\, d\tau_0, \tag{2.16}$$

where

$$K_{ej}(\mathbf{r},\mathbf{r}_0) = -\sigma_0\, G_j(\mathbf{r},\mathbf{r}_0)\, e^{-i\kappa z_0}. \tag{2.17}$$

In similar fashion, a Born approximation solution for the secondary magnetic field, **h**, may be expressed as

$$\frac{h_j(\mathbf{r})}{H_0} \approx \int_{\tau_0} K_{hj}(\mathbf{r},\mathbf{r}_0)\, \rho_n(\mathbf{r}_0)\, d\tau_0, \tag{2.18}$$

where

$$K_{hj}(\mathbf{r},\mathbf{r}_0) = -\frac{1+i}{\delta}\, \Delta_j(\mathbf{r},\mathbf{r}_0)\, e^{-i\kappa z_0}, \tag{2.19}$$

and

$$\delta = \sqrt{\frac{2}{\omega\mu\sigma_0}}.$$

The variable δ above is the skin depth of the homogeneous half-space at the particular frequency under consideration. In equation (2.19), the function Δ_j is analogous to G_j,

except that Δ_j describes the magnetic field components due to the x-oriented electric dipole, and has units of magnetic field strength per electric dipole moment.

Equations (2.16) and (2.18) express the secondary MT fields as weighted averages of the subsurface resistivity distribution. They are linear approximations to the forward MT problem in which a perturbation in subsurface resistivity translates to a perturbation of the surface MT fields. The main difference between the weighting functions, K_e and K_h, in equations (2.16) and (2.19) and their primitive electric and magnetic field forms, G and Δ, respectively, is an additional vertical attenuation factor, $e^{-i\kappa z_0}$, in the former. Furthermore, it is not difficult to show that, when the observation point is located on the surface, both K_e and K_h are space shift-invariant, namely,

$$K(\mathbf{r},\mathbf{r}_0) = K(\mathbf{r}-\mathbf{r}_0) \quad (z=0,\ z_0 \geq 0) .$$

Hence, in Cartesian coordinates equations (2.16) and (2.18) may be specialized to read as

$$\frac{e_j(x,y,0)}{E_0} \approx \int_0^\infty [K_{ej}(x,y,z_0) * \rho_n(x,y,z_0)]\, dz_0, \text{ and} \tag{2.20}$$

$$\frac{h_j(x,y,0)}{H_0} \approx \int_0^\infty [K_{hj}(x,y,z_0) * \rho_n(x,y,z_0)]\, dz_0, \tag{2.21}$$

where the symbol "$*$" denotes 2-D convolution with respect to x and y. The functions $K(x,y,z_0)$ in these last two equations can be thought of as depth-dependent horizontal MT "wavelets." At a given depth, z_0, the MT wavelets describe the source-coordinate variations of equations (2.17) and (2.19) when the observation point is fixed at the origin.

Equations (2.20) and (2.21) may be transformed into the wavenumber domain with the Fourier transform pair

$$\mathcal{F}\{f(x,y)\} = F(\xi,\eta) = \int\int_{-\infty}^{\infty} f(x,y)\, e^{+i(\xi x + \eta y)}\, dx\, dy, \text{ and}$$

$$\mathcal{F}^{-1}\{F(\xi,\eta)\} = f(x,y) = \frac{1}{(2\pi)^2} \int\int_{-\infty}^{\infty} F(\xi,\eta)\, e^{-i(\xi x + \eta y)}\, d\xi\, d\eta,$$

to read as

$$\frac{E_j(\xi,\eta)}{E_0} \approx \int_0^\infty \Lambda_{ej}(\xi,\eta,z_0)\, P(\xi,\eta,z_0)\, dz_0, \text{ and} \tag{2.22}$$

$$\frac{H_j(\xi,\eta)}{H_0} \approx \int_0^\infty \Lambda_{hj}(\xi,\eta,z_0)\, P(\xi,\eta,z_0)\, dz_0\,, \tag{2.23}$$

respectively, where

$E_j(\xi,\eta) = \mathcal{F}\{e_j\ (x,y,0)\}$,
$H_j(\xi,\eta) = \mathcal{F}\{h_j(x,y,0)\}$,
$P(\xi,\eta,z_0) = \mathcal{F}\{\rho_n(x,y,z_0)\}$, and
$\Lambda(\xi,\eta,z_0) = \mathcal{F}\{K(x,y,z_0)\}$.

The functions Λ above are the transfer functions for the linearized forward MT problem. Because of the important fact that these functions can be written as simple algebraic expressions, analysis of the forward MT problem can be done much more easily in the wavenumber domain than in the space domain. This objective is pursued in the following sections.

2.3 The MT transfer functions

Equations for the MT transfer functions Λ_e and Λ_h introduced in the previous section follow from the Cartesian plane-wave vector solutions of the electric and magnetic fields excited by a buried electric dipole. These solutions are derived in Appendix A (equations A.19 through A.24).

Special cases for the electric and magnetic field transfer functions appropriate for 1- and 2-D earth models can be obtained from the expressions of the 3-D transfer functions with the substitutions ξ=0 and η=0, or both. In a 1-D earth, for instance, the resistivity of the subsurface is constant with respect to both x and y, and therefore contains only the DC wavenumber components ξ=0 and η=0. Hence, the transfer functions that relate to this particular case are obtained by setting both ξ=0 and η=0 in the 3-D transfer function equations. Over 2-D media, one may set ξ=0 if the resistivity of the subsurface is constant in the x-direction (E-parallel, or TE polarization mode), or η=0 if the resistivity of the subsurface is constant in the y-direction (E-perpendicular, or TM polarization mode.) This

exercise yields the following equations for the electric transfer functions, Λ_{ex}, over 1-, 2-, and 3-D geoelectric media:

$$\Lambda_{ex}\ \textbf{1-D}\ (\omega) = \frac{i\omega\mu\sigma_0}{i\kappa}(1)\, e^{-i(\kappa+\kappa)z_0} \tag{2.24}$$

$$\Lambda_{ex}\ \textbf{2-D TE}\ (\omega,\eta) = \frac{i\omega\mu\sigma_0}{i\zeta}\left(\frac{i\zeta}{|\eta|+i\zeta}\right) e^{-i(\zeta+\kappa)z_0} \tag{2.25}$$

$$\Lambda_{ex}\ \textbf{2-D TM}\ (\omega,\xi) = \frac{i\omega\mu\sigma_0}{i\zeta}(1)\, e^{-i(\zeta+\kappa)z_0} + \frac{\xi^2}{i\zeta} e^{-i(\zeta+\kappa)z_0} \tag{2.26}$$

$$\Lambda_{ex}\ \textbf{3-D}\ (\omega,\xi,\eta) = \frac{i\omega\mu\sigma_0}{i\zeta}\left[\frac{\xi^2+\eta^2\left(\frac{1+R_\Psi}{2}\right)}{\xi^2+\eta^2}\right] e^{-i(\zeta+\kappa)z_0} + \frac{\xi^2}{i\zeta} e^{-i(\zeta+\kappa)z_0}, \tag{2.27}$$

where

$$\zeta = -i\sqrt{i\omega\mu\sigma_0 + \xi^2+\eta^2}\ ,$$

and,

$$R_\Psi = \frac{\zeta + i\sqrt{\xi^2+\eta^2}}{\zeta - i\sqrt{\xi^2+\eta^2}}\ .$$

Tables 1 through 4 summarize the MT transfer functions operating over 1-, 2-, and 3-D geoelectric media for the remaining electric and magnetic field components; as for the case of equations (2.24) through (2.27) above, the expressions in these tables have been written in forms that facilitate their term-to-term comparison.

EARTH MODEL	
1-D and 2-D	**null**
3-D	$\frac{i\omega\mu\sigma_0}{i\zeta}\left[\frac{\xi\eta}{\xi^2+\eta^2}\left(\frac{1-R_\Psi}{2}\right)\right] e^{-i(\zeta+\kappa)z_0} + \frac{\xi\eta}{i\zeta} e^{-i(\zeta+\kappa)z_0}$

Table 2-1. E_y electric transfer function, Λ_{ey}.

EARTH MODEL	
1-D and 2-D	**null**
3-D	$-\sqrt{i\omega\mu\sigma_0}\ \left[\frac{\xi\eta}{\xi^2+\eta^2}\left(\frac{1-R_\Psi}{2}\right)\right]\ e^{-i(\zeta+\kappa)z_0}$

Table 2-2. H_x magnetic transfer function, Λ_{hx}.

EARTH MODEL		
1-D	**null**	
2-D	TE	$-\sqrt{i\omega\mu\sigma_0}\ \left[\frac{\lvert\eta\rvert}{\lvert\eta\rvert+i\zeta}\right]\ e^{-i(\zeta+\kappa)z_0}$
2-D	TM	**null**
3-D	$-\sqrt{i\omega\mu\sigma_0}\ \left[\frac{\eta^2}{\xi^2+\eta^2}\left(\frac{1-R_\Psi}{2}\right)\right]\ e^{-i(\zeta+\kappa)z_0}$	

Table 2-3. H_y magnetic transfer function, Λ_{hy}.

EARTH MODEL		
1-D	**null**	
2-D	TE	$\sqrt{i\omega\mu\sigma_0}\ \left[\frac{i\eta}{\lvert\eta\rvert+i\zeta}\right]\ e^{-i(\zeta+\kappa)z_0}$
2-D	TM	**null**
3-D	$\sqrt{i\omega\mu\sigma_0}\ \left[\frac{\eta}{\zeta}\left(\frac{1+R_\Psi}{2}\right)\right]\ e^{-i(\zeta+\kappa)z_0}$	

Table 2-4. H_z magnetic transfer function, Λ_{hz}.

Close examination of equations (2.24) through (2.27) as well as of the equations in Tables 2-1 through 2-4 reveals that, qualitatively, all transfer functions are consistent with the properties of the MT fields known to hold over 1- and 2-D earths; e.g., (a) the surface vertical electric field is null, (b) no secondary field components are generated when the earth is 1-D except for the electric field component in the x-direction, (c) no y- and x-component of the secondary electric and magnetic fields, respectively, arise over 2-D geoelectric media, and (d) the TM mode of propagation in a 2-D earth is not accompanied by a secondary surface magnetic field component. Also, an interesting correlation is pointed out between the electric transfer functions for 2-D TM and 3-D geoelectric media, for which the two additive terms involved in their expressions have similar properties. This correlation is consistent with the notion that the TM response of a 2-D earth is in some ways similar to that of a 3-D earth (Swift, 1967, and Wannamaker et al., 1984), and will be further studied in the following section. Sections 2.4 through 2.7 are devoted to a more in-depth analysis of the characteristics of the electric and magnetic transfer functions.

2.4 The electric transfer functions

Inspection of equations (2.24) and (2.25) shows similarities between the electric transfer functions for 1-D and 2-D TE earths. The two transfer functions differ in that certain factors that are constant in the 1-D transfer function are functions of the wavenumber η in the TE transfer function. Specifically, the complex coefficient

$$r_1(\eta) = \frac{i\zeta}{|\eta| + i\zeta} \qquad (\zeta = -i\sqrt{i\omega\mu\sigma_0 + \eta^2}) \tag{2.28}$$

in equation (2.25) does not approach zero with increasing values of the η wavenumber, and this dependence on η causes the TE electric response to have the characteristics of a low-pass wavenumber filter. Also, because of the exponential factor in equation (2.25), the cutoff wavenumber gets progressively lower with increasing depth, z_0. This means that the TE-mode electric field has a progressive loss of response, with respect to depth, to the spatial detail in the resistivity distribution that is contained in the large wavenumber components. Otherwise the behavior of the TE-mode transfer function is similar to that of the 1-D earth; conventional interpretation procedures used with magnetotellurics are known to yield quite reasonable results in both cases, and neither case suffers from the electric static effect. Likewise, because of the low-pass filter characteristics of the 2-D TE transfer

functions, aliasing effects will be reduced when the electric field is sampled at recording locations spaced some distance apart from each other.

Consider now both 2-D TE and TM electric transfer functions Λ_{ex}. The first additive term of the sum in the TM transfer function is non-zero only for the case of time varying ($\omega>0$) fields, and for this reason it is hereafter referred to as the **induction component**. This term has a form similar to that of the TE mode, except that evaluation of the complex coefficient,

$$r_2(\xi, \eta) = \frac{\xi^2 + \eta^2\left(\frac{1 + R_\Psi}{2}\right)}{\xi^2 + \eta^2} \qquad \left(\zeta = -i\sqrt{i\omega\mu\sigma_0 + \xi^2 + \eta^2}\right), \tag{2.29}$$

in equation (2.27) yields $r_2(\xi,0)=1$ for the TM mode, whereas for the TE mode r_2 is rendered a function of η (r_1 in equation 2.28). In addition, ζ is a function of ξ for the TM mode instead of η as is the case for TE. It can also be shown that the amplitude of r_2 is bounded such that

$$\frac{1}{2} \le \left| r_2(\xi,\eta) \right| \le 1 \tag{2.30}$$

for $-\infty < \xi < +\infty$ and $-\infty < \eta < +\infty$, implying that the amplitude difference between the two terms, $r_2(\xi,0)$ and $r_2(0,\eta)$, is at most of a factor of 2.

Amplitude curves for the electric response of both the TE mode and the induction component of the TM mode are plotted in Figure 2-2. The response curves in this figure have been normalized with respect to the amplitude of the 1-D transfer function at the same depths of response, z_0, and are plotted with respect to the normalized wavenumber $\xi/\sqrt{\omega\mu\sigma_0}$. It can be seen that, like the TE-mode response, the TM induction response is characteristic of a low-pass filter with a depth dependent cutoff wavenumber.

The second additive component in the TM-mode electric transfer function Λ_{ex} has no counterpart in either the 2-D TE or the 1-D responses. In allusion to the fact that this second additive component does not vanish in the DC limit ($\omega\rightarrow 0$), this component is hereafter referred to as the **static component.** Because of this second term, the TM-mode electric response from the subsurface may differ significantly from that of the TE mode. The difference in amplitude response between the two components depends on

specific values of frequency, ω, and wavenumber, ξ. To clarify this point, Figure 2-3 shows amplitude response curves computed for the TM electric static component at different depths of response, z_0, and normalized with respect to the 1-D amplitude response measured at the same depths; abscissas for the plots shown are normalized wavenumbers $\xi/\sqrt{\omega\mu\sigma_0}$. The behavior for the TM electric static component evidenced by the curves in Figure 2-3 is that of a band-pass wavenumber filter with a double zero in its response at ξ=0. Decreasing values of depth of response, z_0, widen the pass band of the wavenumber filter. In fact, at z_0=0 the TM static component becomes a perfect high-pass filter of the lateral variations of subsurface resistivity. Because the lateral variations of surface resistivity are normally rich in large wavenumber components, the high-pass filter nature of the TM static component opens the possibility of significant aliasing effects if the electric field is undersampled in the measurement process.

Equations (2.26) and (2.27) show similarities between the electric transfer functions for the 2-D TM and 3-D cases. Both transfer functions contain induction and static components in their expressions. Except for the complex factor $r_2(\xi,\eta)$, the induction component of the 3-D electric transfer function is symmetric in ξ and η, but the magnitude of the asymmetry is at most a factor of 2 by virtue of the inequality (2.30). The induction component of the 3-D electric transfer function is characteristic of a 2-D low-pass wavenumber filter for which the cutoff wavenumbers are determined by the depth of response: an increase in the depth of response causes a decrease in the cutoff wavenumbers. The static component of the 3-D electric transfer function, on the other hand, is highly asymmetric in ξ and η. Significant response from this component, however, is developed only for the large ξ wavenumbers.

When the coefficient $r_2(\xi,\eta)$ in equation (2.29) is unheeded, simple algebra shows that the amplitude ratio of the static component to the induction component of the 3-D electric function equals $\xi^2/\omega\mu\sigma_0$. This ratio indicates that relative to the induction component, the 3-D static component functions as a band-pass filter of the wavenumber harmonics of subsurface resistivity in the x-direction (the direction of primary electric-field polarization.) In contrast, the 3-D static component is a low-pass filter with respect to the η wavenumber harmonics of subsurface resistivity. The directional wavenumber properties of the 3-D static component are illustrated in Figure 2-4, wherein 2-D surfaces describe the amplitude response of the static component of Λ_{ex} (equation 2.27) normalized with respect to the 1-D amplitude response for the depths of response, z_0, of 0 and 0.25 skin depths, and plotted as functions of the normalized wavenumbers $\xi/\sqrt{\omega\mu\sigma_0}$ and $\eta/\sqrt{\omega\mu\sigma_0}$.

In consistency with the characteristics of the static effect described in section 1.2, the static component of Λ_{ex} causes no distortion in the frequency-domain phase response of the surface electric fields. However, non-inductive phase distortions in the electric response from the subsurface can be anticipated in 3-D geoelectric media by inspection of the Λ_{ey}, or cross-coupling electric transfer function. This problem is discussed next.

2.5 The cross-coupling electric transfer function

The electric transfer function Λ_{ey} is similar to Λ_{ex} in the sense that over 3-D media both transfer functions contain static and induction components in their response. However, unlike Λ_{ex}, Λ_{ey} exhibits symmetric dependence on the wavenumbers ξ and η in both its induction and static components. This property intuitively suggests that Λ_{ey} is responsible for the cross-coupling between the secondary fields due to incident electric fields polarized in the x and y directions. Moreover, the wavenumber behavior of Λ_{ey} shows that neither its static component nor its induction component exhibit sensitivity to the $\xi=0$ and $\eta=0$ wavenumber harmonics of the subsurface resistivity distribution. In other words, Λ_{ey} is insensitive to the lateral average of subsurface resistivity that exists at any given depth in the subsurface.

Another interesting observation about the DC limit ($\omega\rightarrow 0$) response of Λ_{ey} is that its static component can develop a larger amplitude response than the static component of Λ_{ex} when the subsurface resistivity distribution contains wavenumber harmonics in the neighborhood of $\eta=\pm\xi$. The availability of wavenumber harmonics in this region opens the possibility of lateral DC current channeling effects, which can cause deflection of the secondary electric field vector about the direction of primary electric-field polarization. This deflection of the electric field vector may lead to non-inductive distortion of the phase response between the secondary electric and primary magnetic fields. In some situations, this may even result in distortion of the otherwise minimum-phase property of the surface electric field response.

The inductive and static components of Λ_{ey} are shown in separate plots in Figure 2-5. At a fixed depth of response, z_0, of 0 skin depths, these plots describe amplitude response variations (normalized with respect to the 1-D electric response at the same depth) with respect to the normalized wavenumbers $\xi/\sqrt{\omega\mu\sigma_0}$ and $\eta/\sqrt{\omega\mu\sigma_0}$. Although the band-pass characteristics of the transfer function Λ_{ey} are not precisely the same as those of Λ_{ex},

methods used to suppress the surface static response of Λ_{ex} can also be used to suppress the surface static response of Λ_{ey}, as explained in section 2.7.

2.6 The magnetic transfer functions

Tables 2.2 through 2.4 show no static component in the magnetic transfer functions comparable to those of the 2-D TM or 3-D electric transfer functions. This remark is probably best understood with the aid of Figure 2-6, where the amplitude response of the TE magnetic transfer function, Λ_{hy}, is plotted with respect to the normalized wavenumber $\eta/\sqrt{\omega\mu\sigma_0}$ at various depths of response, z_0, where the values shown along the vertical axis have been normalized with respect to the 1-D electric amplitude response at the same depths. The response curves in Figure 2-6 are characteristic of a band-pass wavenumber filter (the plots are representative of the wavenumber properties for the remaining 2- and 3-D magnetic transfer functions as well) for which the pass-band is progressively wider for decreasing values of the depth of response, z_0.

The band-pass filter properties of the magnetic transfer functions open the possibility of surface magnetic field distortion by way of current channeling, not only inductive at high frequencies, but also in the DC limit ($\omega \rightarrow 0$)[1] . However, because of the fact that the primary electric field at any depth is proportional to the product $Z_0(\omega)e^{-i\kappa z_0}$ (equations 2.10 and 2.12, and also reflected in the factor $\sqrt{i\omega\mu\sigma_0}$ that appears in the magnetic transfer functions summarized in Tables 2.2 through 2.4), even on the surface of the earth (where the effect of the magnetic transfer functions is most emphasized), the amount of conduction current available for channeling will decrease in proportion to $\sqrt{\omega}$ for decreasing values of frequency (Wannamaker et al., 1984). With this reduction in the conduction current available for channeling, the only way to increase the surface magnetic field effect at decreasing values of frequency is by simultaneous attrition of the area where the conduction takes place; this rather pathological situation is not to be expected in practical field studies. Moreover, partly because of their lack of lateral surface discontinuities and partly because of their relatively smaller amplitude compared to the amplitude of the primary magnetic field, secondary surface magnetic field variations do not impose as stiff sampling requirements as their electric field counterparts do in the MT probing of the subsurface.

---

[1] DC surface magnetic field effects are a subject of interest to the magnetometric resistivity method. Edwards (1974), for instance, has studied the surface magnetic response of a DC current filament buried in a conductive half-space.

An important property of the secondary surface magnetic fields variations also implicit in the Born approximation results is that they exhibit absolutely no sensitivity to the average value of subsurface resistivity. This can be demonstrated by substituting $\xi=\eta=0$ in the expressions for the 3-D magnetic transfer functions shown in Tables 2.2 through 2.4 (in fact, the result of this substitution is already expressed as the 1-D magnetic transfer function in each table.) The consequences of this property in any attempt to infer a cross-section of subsurface resistivity exclusively from measurements of the surface magnetic field are discussed in detail in Chapter IV. For the moment, it is stressed that the same property can be used to obtain an estimate of the primary magnetic field.

The fact that the secondary surface magnetic field measurements have a perfectly null DC wavenumber harmonic indicates that their horizontal spatial average taken simultaneously in the x and y directions must approach zero for increasingly long averaging distances. In the limit, the outcome of such a horizontal average will be an estimate of the plane-wave primary magnetic field. This property suggests that when the magnetic field is sampled at a number of locations within the survey area, one may first estimate the primary magnetic field by areal spatial averaging of these measurements and then compute MT impedances solely reflecting the spatial variability of the electric field response from the subsurface. Such a procedure contrasts with the standard MT field method in which the local electric-to-magnetic field ratio (local wave impedance) is measured at all sampling locations. More specific techniques that can be used for the practical estimation of secondary-to-primary field ratios using the same principle are described in Chapters IV and V.

2.7 Suppressing the electric static effect

A foremost conclusion that stems from section 2.4 above is that the effect of the static component in the 2-D TM and 3-D electric transfer functions can be reduced by inverting its wavenumber behavior, i.e., by spatially low-pass filtering the surface electric field. Where this can be accomplished, the remaining low-pass characteristics of the electric transfer functions will cause the measured electric field components to contain contributions from subsurface resistivity variations that are averaged with respect to depth as well as both horizontal directions, x and y. Subject to the restrictions of the Born approximation, a bench mark for the cutoff wavenumber, ξ_c, required to suppress static effects may be determined from equations (2.26) and (2.27) as the value of ξ below which the induction

component in those expressions produces a larger surface amplitude response than the static component at the same frequency. Excluding the effects of $r_2(\xi,\eta)$, this occurs when

$$\xi^2 = \omega\mu\sigma_0 = \frac{\omega\mu}{\rho_0} . \qquad (2.31)$$

Cutoff wavenumbers below this critical value increase the suppression of the electric static component but decrease the lateral resolution of the induction component. Conversely, cutoff wavenumbers greater than this value produce just the opposite effect.

As emphasized in section 2.4, the induction component of the 3-D electric transfer function has the characteristics of a spatial low-pass filter for which the cutoff wavenumbers in orthogonal horizontal directions are inversely related to the depth of response. Because a low-pass filter is an averaging operator, it follows that the magnitude of the response derived from the induction component is determined by the distribution of local lateral averages of subsurface resistivity where the size of the region over which the resistivity is averaged increases with increasing depth. Furthermore, similarities between the induction component of the 3-, 2- and 1-D electric transfer functions suggest that the induction component responds to the lateral variations of subsurface resistivity much as if operating over a horizontally stratified medium with the resistivity at each depth level equal to a local lateral resistivity average taken at the same depth. This property suggests that, with their electric static component suppressed by way of spatial filtering, 2-D TM and 3-D surface electric field data can be interpreted using methods appropriate for the interpretation of 1-D or 2-D TE (both inductive modes of surface electric response) electric field data.

Thus, the resistivity ρ_0 in equation (2.31) should be interpreted as a local spatial average of the subsurface resistivity distribution at an effective depth of response determined by the operating frequency. To link the three parameters, frequency, ω, average resistivity, ρ_0, and effective depth of response, the right-hand side of equation (2.31) is now expressed in terms of the Bostick (1977) depth of penetration, z_B, namely,

$$\frac{1}{z_B^2} = \frac{\omega\mu}{\rho_0} .$$

This equality suggests that the cutoff wavenumber of the filter required to reduce the effect of the static component on the surface electric response may be estimated from

$$\xi_c \approx \frac{1}{z_B} ,$$

or, in general, from

$$\xi_c = \frac{1}{c\, z_B} \quad , \tag{2.32}$$

where c is a real constant that can be arbitrarily adjusted to control the extent of the spatial filtering below (c<1) or above (c>1) that consistent with equation (2.31).

As discussed in section 2.4, the high-pass characteristics of the electric static component almost exclusively operate on the ξ wavenumber harmonics of the subsurface resistivity distribution. Because of this, any filtering operation intended to suppress surface static effects must have directional properties in order to comply with the requirements suggested by equation (2.32). The easiest and most natural way to comply with such a requirement is to extend the directional spatial filtering performed by the electric field sensors themselves (see section 1.3) in a controlled fashion.

For a preset filtering direction, it is essential that electric dipoles be deployed tangential to it. In so doing, there are two variables that control the sampling of the surface electric field response from the subsurface, and hence its subsequent inversion into an estimate of subsurface resistivity: one is the separation distance between adjacent dipoles and the other is the dipole length. The separation distance should be chosen in accordance to the well established sampling theorem so as to minimize aliasing effects (potentially damaging given the high-pass characteristics of the 3-D electric static component.) As for the dipole length, it should be remembered that although long dipoles may provide a useful amount of suppression of local static effects, excessively long dipoles may cause undesired lateral smoothing. A method that offers a good compromise between sampling distance and dipole length is the one in which electric dipoles are deployed end-to-end along the filtering path. This arrangement of electric dipoles has the important characteristic that the length of the electric field average at a given point can be increased with decreasing values of frequency as required for the application of equation (2.32). Both the implementation characteristics of such a survey technique as well as the practical evaluation of spatial filtering for the MT sounding of the subsurface are the central discussion matters in Chapters V and VI.

2.8 Summary

First-order Born approximation of the MT scattering equations yields a linear solution for the relation between a perturbation in subsurface resistivity and the ensuing surface response. The linear system solutions derived from this approach apply only to cases of low resistivity contrasts, but do retain many of the characteristics of the forward and inverse MT problems as they can be applied to any geometrical complexity in subsurface. In fact, the linearized forward solutions yield a set of response equations that can be easily specialized to the cases of 1-, 2-, and 3-D subsurface resistivity distributions, and which are consistent with all the qualitative properties of magnetotellurics that are known to hold over these environments.

Wavenumber analysis of the linear system solutions suggests that the electric response from 2-D TM and 3-D geoelectric media can be described as the additive interplay of induction and static components. The induction component has a zero DC-limit response, and operates over the lateral variations of subsurface resistivity in the form of a low-pass wavenumber filter whose cutoff wavenumber decreases with decreasing values of frequency. These characteristics exemplify the response properties of the purely inductive 2-D TE and 1-D transfer functions, and which imply a selective deepening of the zone of response with decreasing values of frequency. The static component, on the other hand, does not have a zero DC-limit response and operates over the lateral variations of subsurface resistivity in the form of band-pass wavenumber filter whose cutoff wavenumber increases with decreasing values of frequency. Because of these wavenumber properties, the static component may eventually outweigh the amplitude response derived from the induction component below some value of frequency, at which point the amplitude of the surface electric response will not truly reflect a selective deepening of the zone of response with decreasing values of frequency. This is a common and highly adverse situation in the exploration of the subsurface with the MT method.

Fortunately, the linear system analysis also suggests that a way to enhance the amplitude response of the depth-sensitive induction component over the amplitude response of the depth-insensitive static component is to spatially low-pass filter the surface electric field. The cutoff wavenumber of the filter required for this operation decreases with decreasing values of frequency and is therefore insensitive to the induction component. After filtering, the electric field variations can be subject to procedures suitable for the inversion of the inductive part of the MT response into a cross-section of subsurface resistivity.

The practical procedure suggested herein for the sampling of the electric field is the one in which electric dipoles are deployed end-to-end continuously along a curvilinear survey path. This arrangement of dipoles lends itself to a spatial filtering procedure whereby the length of the electric field average is increased with decreasing values of frequency. Although the suggested field procedure includes only the sampling of electric field data tangential to the line of measurements, the use of spatial filtering is consistent with the response characteristics of 3-D geoelectric media. It is envisioned that detailed exploration work over complicated 3-D targets may demand the deployment of electric dipole arrays in more than one direction.

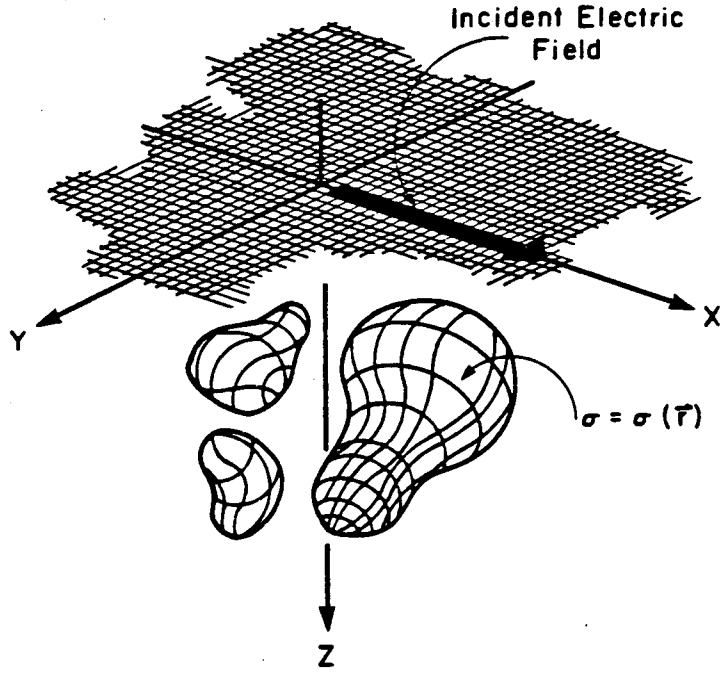

Figure 2-1. Theoretical model: the earth is described as a homogeneous half-space with confined conductivity anomalies. Incident electromagnetic energy is in the form of normal plane waves polarized in the x-direction.

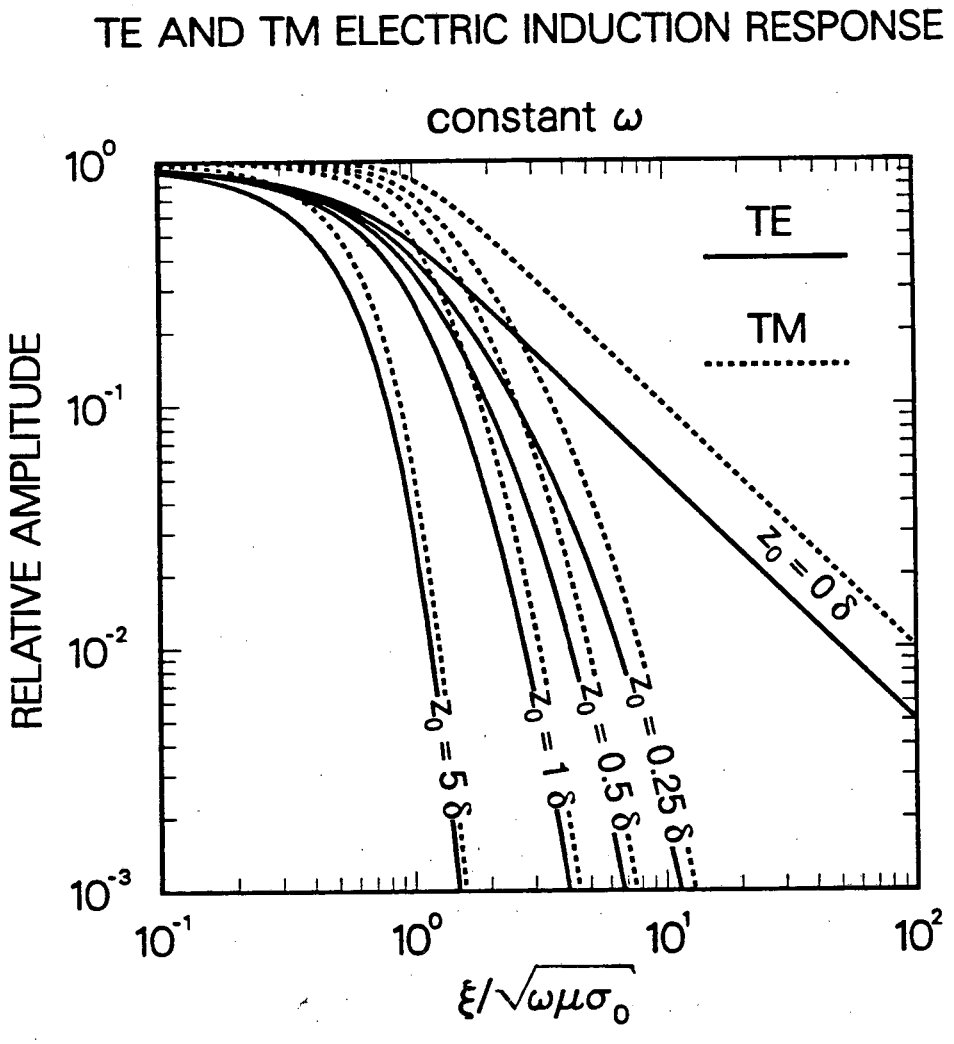

Figure 2-2. Amplitude response of the 2-D electric induction components. Solid and dashed curves describe the amplitude response of the TE and TM-induction transfer functions, respectively, evaluated at different depths of response, z_0. The curves are normalized with respect to the 1-D electric amplitude response calculated at the same depths of response, and are plotted with respect to the normalized wavenumber $\xi/\sqrt{\omega\mu\sigma_0}$.

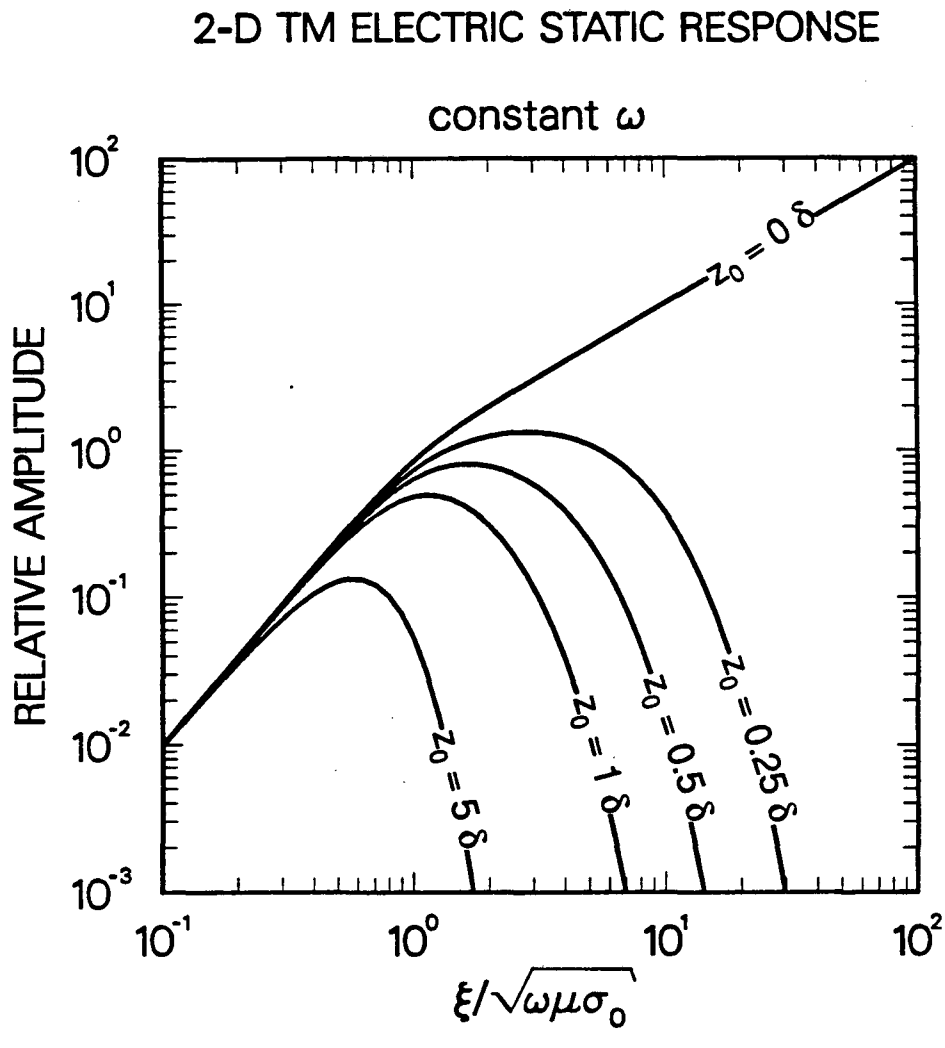

Figure 2-3. Amplitude response of the TM-mode electric static component. Response curves are shown for various depths of response, z_0, normalized with respect to the 1-D response at the same depths, and plotted with respect to the normalized wavenumber $\xi/\sqrt{\omega\mu\sigma_0}$.

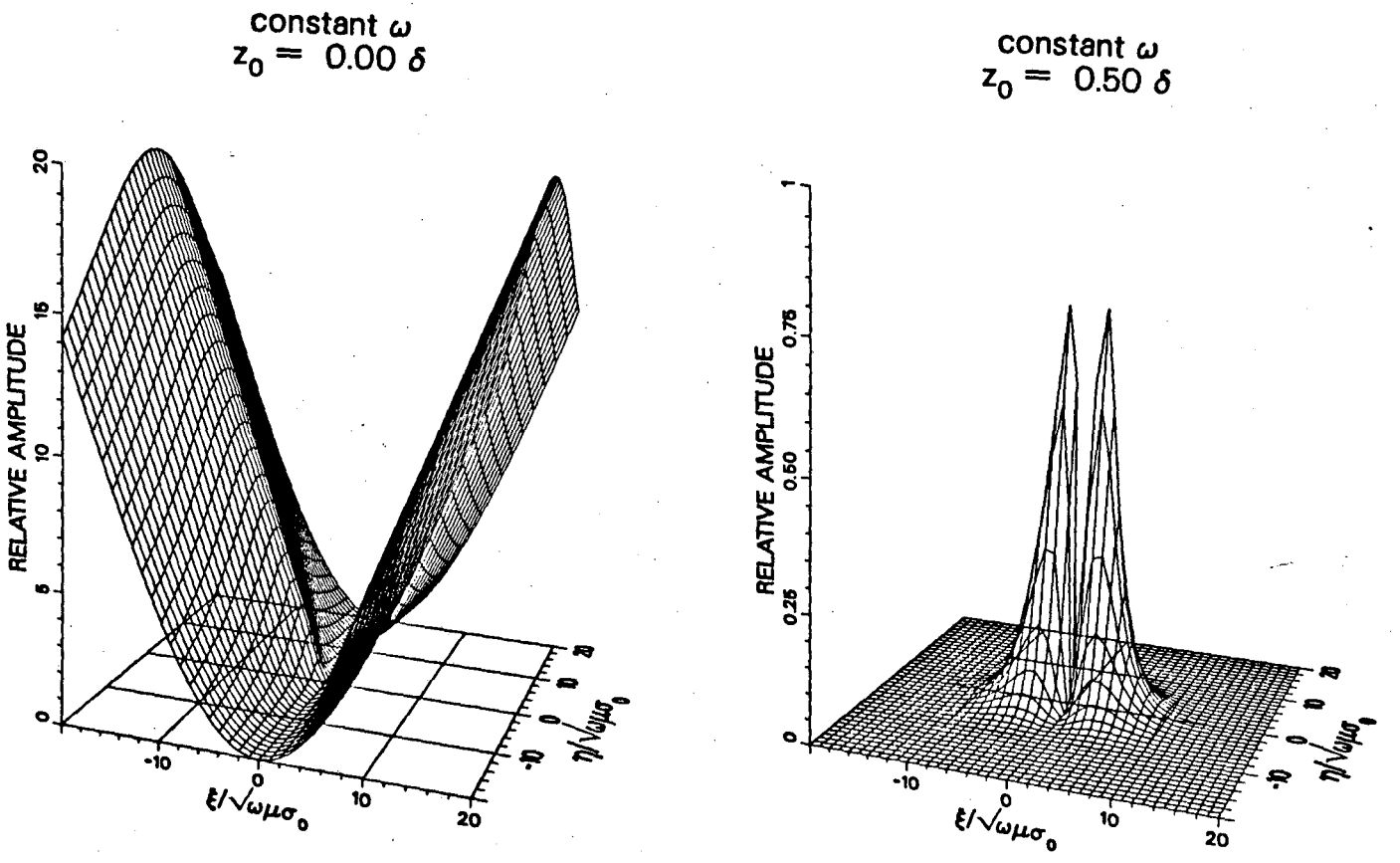

Figure 2-4. Amplitude response of the 3-D electric static component. Response values are normalized with respect to the 1-D response at the same depth and are plotted with respect to the normalized wavenumbers $\xi/\sqrt{\omega\mu\sigma_0}$ and $\eta/\sqrt{\omega\mu\sigma_0}$. Plots are shown for depth of response values, z_0, of 0.0, and 0.25 skin depths.

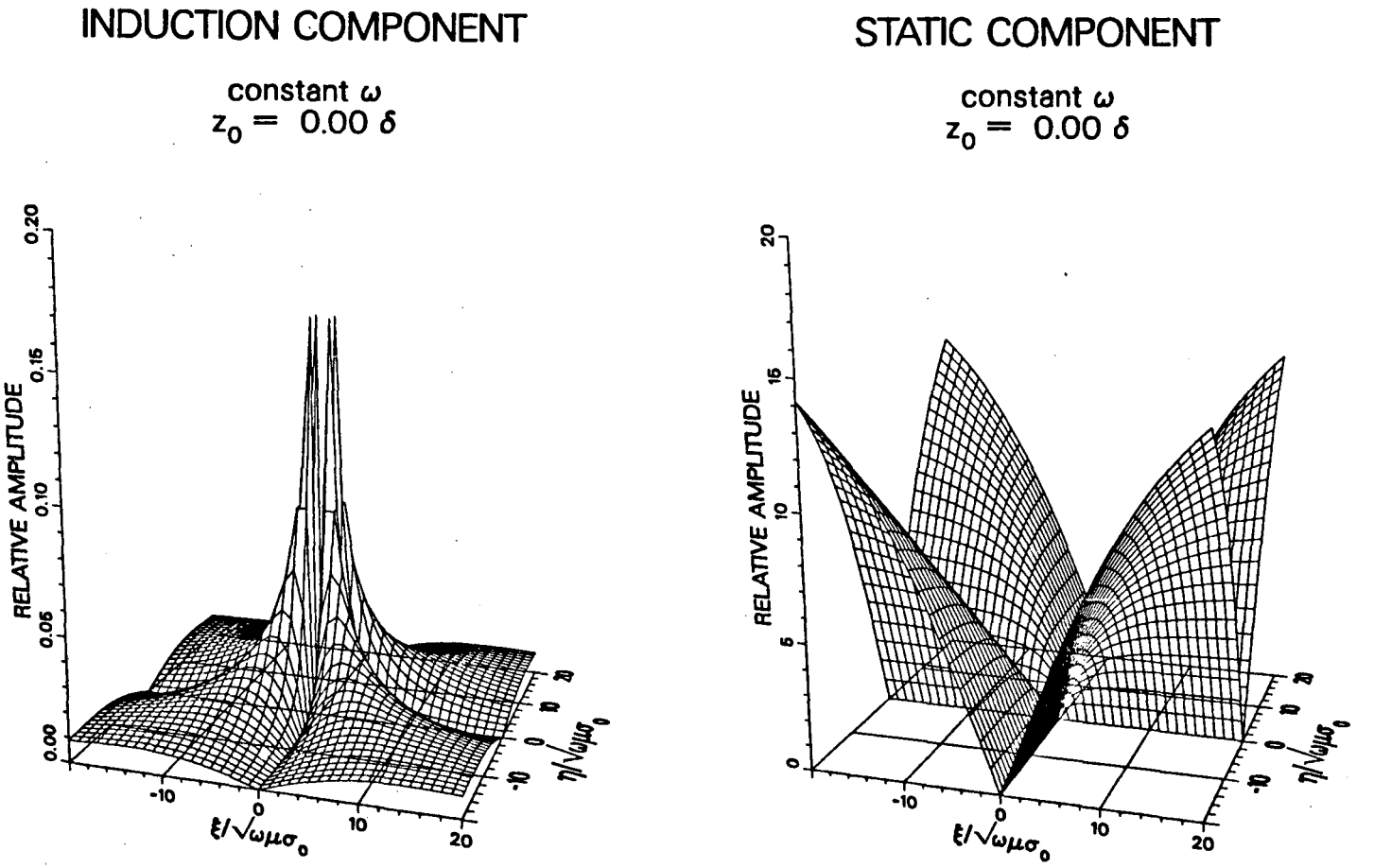

Figure 2-5. Amplitude response of the 3-D cross-coupling electric transfer function. Response values are normalized with respect to the 1-D electric response at the same depth and are plotted with respect to the normalized wavenumbers $\xi/\sqrt{\omega\mu\sigma_0}$ and $\eta/\sqrt{\omega\mu\sigma_0}$. Separate plots are shown for both induction and static components at the depth of response, z_0, of 0.0 skin depths.

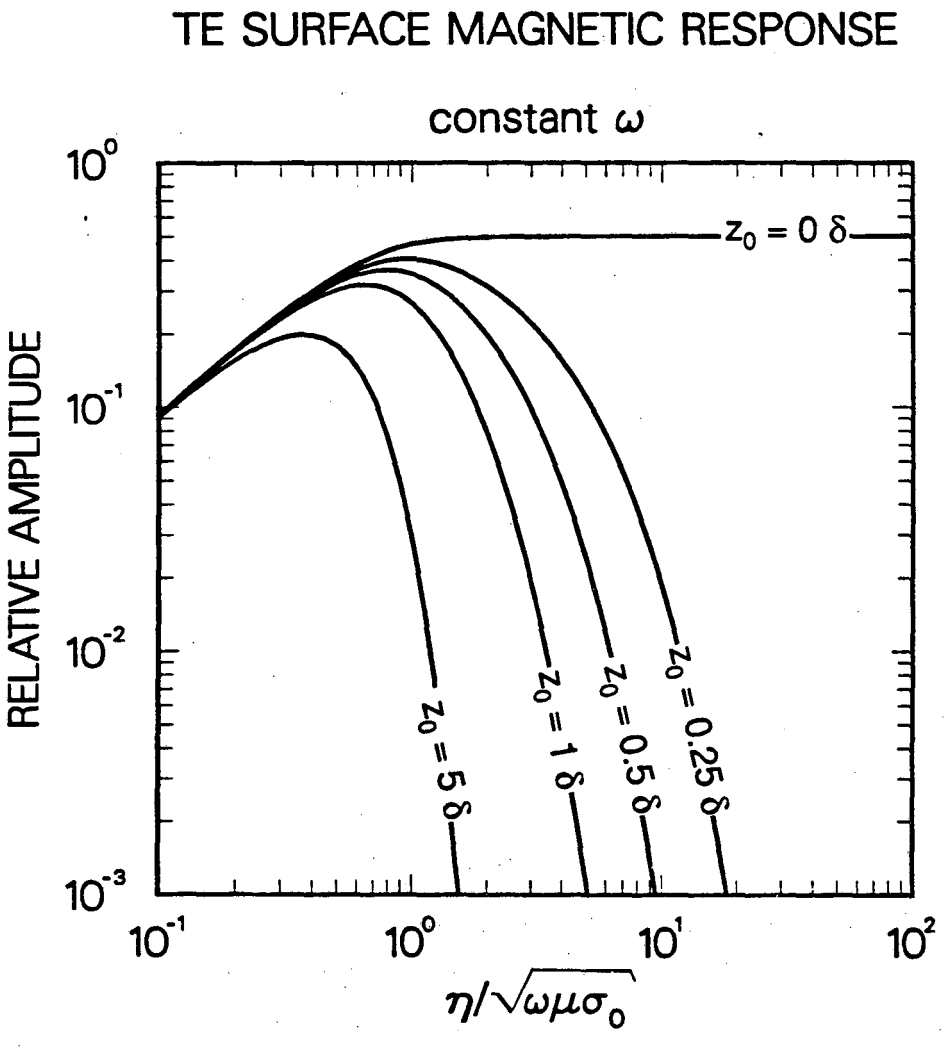

Figure 2-6. Amplitude response of the TE magnetic transfer function. Response curves are shown for various depths of response, z_0, normalized with respect to the 1-D electric response at the same depths, and are plotted with respect to the normalized wavenumber $\eta/\sqrt{\omega\mu\sigma_0}$.

CHAPTER III

BORN INVERSION OF 1-D MT DATA

3.1 Introduction

Inversion of 1-D MT data has been a subject of extensive research, with contributions dating as far back as the curve matching techniques suggested by Cagniard (1953) in his seminal paper on magnetotellurics. The abundance of material related to this interesting topic is no mere coincidence: the situation in which a normally incident plane wave excites a stratified medium to date remains the simplest of all analytical problems for the EM probing of the subsurface. It is this simplicity that makes the 1-D MT inverse problem amenable to a fairly large class of formulations, ranging from computer-intensive, nonlinear iterative techniques, to much simpler direct (although sometimes only approximate) procedures. Regardless of the method of solution, however, the common theme to all 1-D MT inverse techniques is the problem of extracting a resistivity profile in the rather adverse situation of exponentially decreasing sensitivity with increasing depth.

This chapter introduces a linearized solution for the inference of a profile of subsurface resistivity from surface electric field data gathered at a number of frequencies. The linearized inverse directly stems from the Born approximation solutions derived in Chapter II particularized for a medium in which the resistivity is solely a function of depth. In considering this rather simplified view to the inverse problem, however, the intention is not to devise a practical tool for the interpretation of MT data, but to shed light on the factors that control the vertical resolution characteristics of 1-D MT data.

The linearized 1-D MT inverse problem is studied here by extensively exploring the properties of the associated weighting kernels. For this purpose, a change of variables is introduced whereby both frequency and depth are expressed as logarithmic quantities. Likewise, a modification of the data and model representations is used which is consistent with the expressions for the first-order Rytov approximation of the surface MT fields. It is shown that the logarithmic parameterization of both frequency and depth transforms the kernel of the linear system solution into a depth-shift invariant operator. With this property, the characteristics of the linear system are studied in the wavenumber domain, leading to simple formulas describing the wavenumber range along which noisy data can be mapped

into practically undistorted vertical variations of subsurface resistivity. Finally, numerically simulated data are used to test the linearized inverse solution in cases where the assumptions implicit in the Born approximation are unjustified. The objective of these tests is to ascertain in a most pragmatic way the extent to which the linearized inverse is a useful tool for understanding the actual nonlinear inverse problem. In so doing, various practical ℓ_2- and ℓ_1-norm model estimation procedures are examined and their results contrasted against those obtained with a popular nonlinear estimation procedure.

A study in some ways related to the objectives of this chapter has been reported by Bostick et al. (1979). Their work stemmed from direct linearization of the second-order nonlinear Ricatti equation governing the variations of EM wave impedance with respect to depth. In spite of a different starting point, however, Bostick et al.'s basic equations are equivalent to those serving as foundation to this chapter, not to mention some of their original concepts as well. Unfortunately, their work has been never formally written and their ideas remain largely unknown. Thus, in the measure to which this chapter represents an outgrowth of Bostick et al,'s work, care has been exercised to point out where ideas and concepts are borrowed from their work.

Finally, the topics studied in this chapter are important for understanding the developments of Chapter IV leading to the formulation of a Born inversion procedure applicable to 2-D MT data.

3.2 The linearized forward problem

Secondary surface magnetic field variation both laterally and with respect to frequency are constant over 1-D media (Kaufman and Keller, 1981). This property of the surface MT response is consistent with the characteristics of the linearized magnetic transfer functions (Tables 2.2 and 2.3) derived in Chapter II, and indicates that the nature of the 1-D vertical variations of subsurface resistivity can only be determined from the secondary frequency variations of the surface electric field.

Following the notation introduced in Chapter II, the electric field, E, on the surface of a 1-D earth may be expressed as

$$E(\omega) = E_0(\omega) + e(\omega)\,, \tag{3.1}$$

where ω is the radian frequency, E_0 is the primary electric field dictated by a homogeneous half-space of resistivity ρ_0, and e is the secondary surface electric field that arises with

variations of subsurface resistivity away from the homogeneous half-space. Similarly, the resistivity, ρ, in the subsurface may be written as

$$\rho(z) = \rho_0 + \Delta\rho(z) , \tag{3.2}$$

where z is depth measured downward from the surface and $\Delta\rho$ describes the vertical variations of subsurface resistivity away from the homogeneous half-space.

In the presence of band limited and noisy surface measurements, the mapping of $E(\omega)$ into $\rho(z)$ is perforce non-unique (Bailey, 1970). In addition, the relationship between these two functions is in general nonlinear and thus difficult to analyze without specific knowledge of the subsurface. To ease the understanding of how $E(\omega)$ maps into $\rho(z)$, consider the test case in which the assumptions

$$e(\omega) << E_0(\omega), \text{ or/and} \tag{3.3}$$
$$\Delta\rho(z) << \rho_0 \tag{3.4}$$

are met. For this situation, the relationship between $e(\omega)$ and $\Delta\rho(z)$ can be expressed as suggested by equations (2.20) and (2.24), namely,

$$\frac{e}{E_0}(\omega) = \sqrt{i\omega\mu/\rho_0} \int_0^\infty \frac{\Delta\rho(z_0)}{\rho_0} e^{-2z_0\sqrt{i\omega\mu/\rho_0}}\, dz_0 . \tag{3.5}$$

Customarily, surface electric field measurements made over 1-D media are disguised in the form of an impedance, $Z(\omega)$, relating orthogonal electric and magnetic field values. Assuming that the electric field vector, **E**, points in the x-direction and that the magnetic field vector, **H**, points in the y-direction, the 1-D MT impedance can be expressed in terms of the secondary-to primary electric field ratio as

$$Z(\omega) = \frac{E(\omega)}{H(\omega)} = \frac{E_0(\omega) + e(\omega)}{H_0(\omega)} = Z_0(\omega)[\, 1 + \frac{e(\omega)}{E_0(\omega)}\,] , \tag{3.6}$$

where $Z_0(\omega)$ is the surface wave impedance associated with the reference homogeneous half-space (equation 2.12).

Equation (3.5) can be rewritten in the more familiar notation of linear inverse problems (Parker, 1977) as

$$d(\omega) = \int_0^\infty m(z_0)\, f(\omega,z_0)\, dz_0 \,, \tag{3.7}$$

where

$$d(\omega) = 2\frac{e}{E_0}(\omega) \quad \text{are the data,} \tag{3.8}$$

$$m(z) = \frac{\Delta\rho(z)}{\rho_0} \quad \text{is the model, and} \tag{3.9}$$

$$f(\omega,z) = 2\sqrt{i\omega\mu/\rho_0}\, e^{-2z\sqrt{i\omega\mu/\rho_0}} \quad \text{is the kernel.} \tag{3.10}$$

In this notation, the factor 2 is arbitrarily introduced in the data and kernel definitions with the objective of rendering the real part of $f(\omega,z_0)$ unimodular (see section 3.7).

The kernel $f(\omega,z_0)$ in equation (3.10) may be thought of as an adaptive operator that, at a given depth, z, locally averages the vertical model variations to produce the data measured at the frequency ω. The vertical extent of the average performed by the kernel is adapted in response to variations in both frequency, ω, and depth, z. Analysis of the averaging characteristics of the kernel is best done if both model and data variables are expressed in forms that truly express the vertical resolution characteristics of magnetotellurics; this objective is pursued in sections 3.3, 3.4, and 3.5 below.

3.3 Linearized forward problem under the first-order Rytov approximation

Often, practical MT exploration problems call for exponential representations of both data and resistivity variations in the form

$$E(\omega) = e^{\Phi(\omega)} = e^{\Phi_0(\omega) + \Delta\Phi(\omega)} \,, \text{ and} \tag{3.11}$$

$$\rho(z) = e^{\psi(z)} = e^{\psi_0 + \Delta\psi(z)} \,, \tag{3.12}$$

where Φ and ψ are auxiliary complex and scalar functions, respectively. This representation for $E(\omega)$ and $\rho(z)$ envisions both functions as logarithmic oscillations about their average logarithmic values. In fact, because the two functions occur over such large amplitude ranges they are both customarily plotted with a logarithmic scale (see Figures 1.4 and 1.5), for which a description in the form of equation (3.11) and (3.12) is best suited.

Exponential function representations such as those of equations (3.11) and (3.12) lend themselves to a recursive series expansion known as the Rytov series. This representation is in some ways similar to the additive Born series expansion for which first-order terms were derived in Chapter II. Studies of the relationship between the terms in both expansions have been presented in the solution of wave propagation problems (Sancer and Varvatsis, 1970, and Mano, 1971). A simple relation between the first-order terms involved in both series expansions for the MT problem can be obtained in the following way. With the equivalences

$$e^{\Phi_d(\omega)} = E_0(\omega) \text{ , and}$$
$$e^{\psi_0} = \rho_0 \text{ ,}$$

as well as the assumptions that $|\Delta\psi| << |\psi_0|$ and $|\Delta\Phi| << |\Phi_0|$, substitute the right-hand side of equations (3.11) and (3.12) into equations (3.1) and (3.2), to get

$$\frac{e}{E_0}(\omega) = \Delta\Phi(\omega) = \Delta \ln E(\omega) \text{ , and}$$
$$\frac{\Delta\rho(z)}{\rho_0} = \Delta\psi(z) = \Delta \ln \rho(z) \text{ .}$$

These expressions suggest modified data and model representations for the linearized 1-D MT forward problem in the form

$$d(\omega) = \Delta \ln E^2(\omega) = \Delta \ln |E(\omega)|^2 + i \arg[2\frac{E(\omega)}{E_0(\omega)}], \text{ and} \qquad (3.13)$$

$$m(z) = \Delta \ln \rho(z), \qquad (3.14)$$

respectively, where the assumption is implied that $E(\omega)$ is never zero, a fact perfectly justified by the minimum-phase property of 1-D MT data (Kunetz, 1972, and Weidelt, 1972). Notice that the model definition in equation (3.14) has the advantage of naturally enforcing the positivity of $\rho(z)$ in any attempt to solve for $m(z)$ via equation (3.7).

It becomes evident that under the first-order Rytov approximation both the data and the model possess different expressions compared to those of the first-order Born approximation. However, the kernel for the linear system equations is exactly the same in both situations. The physical significance attached to $d(\omega)$ under the first-order Rytov approximation is explored in the following section.

3.4 Relationship between the ratio e/E_0 and apparent resistivity and impedance phase data under the first-order Rytov approximation

Once again, consider the 1-D MT impedance, $Z(\omega)$, defined in equation (3.6), although this time expressed in the additive form

$$Z(\omega) = Z_0(\omega) + \Delta Z(\omega),$$

where $\Delta Z(\omega)$ is the perturbation of surface wave impedance reflecting the variations $\Delta\rho(z)$ of $\rho(z)$ about ρ_0. Disregarding second-order terms of $\Delta Z(\omega)$, the square of $Z(\omega)$ can be approximated with the expression

$$Z^2(\omega) = Z_0^2(\omega)\left[1 + 2\frac{\Delta Z(\omega)}{Z_0(\omega)}\right].$$

Taking the complex logarithm on both sides of this last identity and retaining only the first-order terms in $\Delta Z(\omega)$ for the expression within brackets yields

$$\ln[Z^2(\omega)] = \ln[Z_0^2(\omega)] + 2\frac{\Delta Z(\omega)}{Z_0(\omega)}.$$

Collecting real and imaginary components results in the two identities

$$\ln|Z(\omega)|^2 = \ln|Z_0(\omega)|^2 + \mathrm{Real}\left[2\frac{\Delta Z(\omega)}{Z_0(\omega)}\right], \text{ and}$$

$$2\arg[Z(\omega)] = 2\arg[Z_0(\omega)] + \mathrm{Imag}\left[2\frac{\Delta Z(\omega)}{Z_0(\omega)}\right].$$

Adding $-\ln(\omega\mu)$ to both sides of the first identity and substituting the exact expressions for $|Z_0(\omega)|$ and $\arg[Z_0(\omega)]$ (equation 2.12) yields

$$\ln\rho_A(\omega) = \ln\rho_0 + \mathrm{Real}\left[2\frac{\Delta Z(\omega)}{Z_0(\omega)}\right], \text{ and} \qquad (3.15)$$

$$2\arg[Z(\omega)] = \frac{\pi}{2} + \mathrm{Imag}\left[2\frac{\Delta Z(\omega)}{Z_0(\omega)}\right], \qquad (3.16)$$

where $\rho_A(\omega)$ is the 1-D apparent resistivity function (Cagniard, 1953). Now, from equation (3.6) it becomes clear that

$$2\frac{e}{E_0}(\omega) = 2\frac{\Delta Z(\omega)}{Z_0(\omega)},$$

in which case, by simple inspection of equations (3.15) and (3.16), one finally obtains

$$\text{Real}[2\frac{e}{E_0}(\omega)] = \Delta \ln \rho_A(\omega), \text{ and} \tag{3.17}$$

$$\text{Imag}[2\frac{e}{E_0}(\omega)] = 2\arg[Z(\omega)] - \frac{\pi}{2}. \tag{3.18}$$

These are simple expressions that relate both apparent resistivity and impedance phase with the real and imaginary parts of $d(\omega)$. As detailed in section 3.11, equation (3.17) also provides a simple means to estimate the background resistivity, ρ_0, directly from apparent resistivity data.

3.5 Reparameterization and convolutional response

Because of the very large frequency range over which electric and magnetic field measurements are made, MT signals are normally processed to yield frequency samples evenly distributed in logarithmic fashion. Both the reason and repercussion of a sampling procedure of this nature as to the way in which vertical variations of subsurface resistivity can be resolved from the data is best understood if both model and data variables are expressed in equivalent forms. A way to accomplish this is by writing both skin depth, δ, and depth, z, in terms of exponential variables; more precisely, let

$$\delta = \sqrt{\frac{2\rho_0}{\omega\mu}} = e^{-v}, \text{ and} \tag{3.19a}$$

$$z = e^{-u}, \tag{3.20a}$$

such that,

$$v = -\ln \delta = \ln \sqrt{\omega} + \ln \sqrt{\frac{\mu}{2\rho_0}}, \text{ and} \tag{3.19b}$$

$$u = -\ln z \tag{3.20b}$$

(Bostick et al. 1979.) Equation (3.19b) above is a double transformation that links the two variables, background resistivity and frequency, to map the original frequency samples into the same natural log depth axis that is used to describe the vertical variations of subsurface resistivity (equation 3.20b).

Substitution of equations (3.19a) and (3.20a) into equation (3.5) gives rise to a well-known convolutional representation form, i.e.,

$$d(v) = \int_{-\infty}^{\infty} m(u)\, f(v-u)\, du\ , \tag{3.21}$$

where

$$f(u) = g(u) + i\, h(u), \tag{3.22}$$

$$g(u) = [\cos(2e^u) + \sin(2e^u)]\, 2e^{u-2e^u}, \text{ and} \tag{3.23}$$

$$h(u) = [\cos(2e^u) - \sin(2e^u)]\, 2e^{u-2e^u}. \tag{3.24}$$

Thus, under the logarithmic parameterization of δ and z, the new kernel, f(u), in equation (3.21) adopts the properties of a depth-shift invariant operator. In a way, the simplicity of equation (3.21) suggests that the logarithmic scale for both the sampling of the data and the inference of the model are an optimal combination to deal with the exponential decay that the kernel $f(\omega,z)$ (equation 3.5) experiences with increasing depth. Smith and Booker (1988) in their own nonlinear study advocate a parameterization of this nature because they show it works as a natural "prewhitening" process of the observational errors. The function f(u) defined in equations (3.22) through (3.24) is the impulse response (or Green's function) for the 1-D MT forward problem and, borrowing the terminology used in linear-system theory, can be meritoriously referred to as the 1-D MT wavelet (Bostick et al., 1979).

Figure 3-1 shows both real and imaginary components of the reversed 1-D MT wavelet, f(-u), plotted as a function of -u, such that depth actually increases to the right of the plot. The reversed wavelet is shifted over the resistivity model at increasing values of depth to produce the data measured at decreasing values of frequency. The resulting apparent resistivity and phase curves (real and imaginary components of the data under the Rytov approximation) thus appear as smooth versions of the original resistivity profile after the wavelet has been shifted through it (Figure 3-2). A study of the smoothing characteristics of the 1-D MT wavelet is carried out in section 3.8 with the aid of the Fourier transform.

3.6 Causality and minimum phase

For the seemingly unrealistic, although theoretically appealing situation in which the linearized data have been gathered at all points along the logarithmic frequency axis, their real and imaginary components remain linear combinations of each other. This linear dependence is due to the linearity in turn exhibited by the real and imaginary parts of the

1-D MT kernel themselves In fact, both components are related by the Hilbert transform, defined as

$$h(u) = \frac{1}{\pi} \int_{-\infty}^{+\infty} \frac{g(u_0)}{u_0 - u} du_0 \text{ , and} \tag{3.25}$$

$$g(u) = -\frac{1}{\pi} \int_{-\infty}^{+\infty} \frac{h(u_0)}{u_0 - u} du_0 \tag{3.26}$$

(Bracewell, 1965).

To demonstrate that equations (3.25) and (3.26) hold true for the linearized 1-D MT forward problem, consider the auxiliary integral, $I_1(\omega)$, defined as

$$I_1(u) = \int_{-\infty}^{+\infty} \frac{e^{+i2e^{u_0}} e^{u_0} - 2e^{u_0}}{u_0 - u} du_0 .$$

The Cauchy principal value of $I_1(u)$ can be found by closed contour integration in the upper half of the complex plane. For this purpose, the contour of integration is chosen to contain both the real axis and a semicircle of infinite radius. Given that the complex function,

$$\alpha(w) = e^{+i2e^{w}} e^{w} - 2e^{w},$$

vanishes for

$$w = R\cos\theta + i\sin\theta; \; R \rightarrow \infty, \text{ and } 0 < \theta < \pi ,$$

it can be shown that the contribution from the integral taken along the infinite semicircle reduces to zero. Along the real axis, on the other hand, the path of integration can be drawn such that the singular point $u=u_0$ is not contained within the region enclosed by the contour of integration. Thus, with no other singularities to take care of, the Cauchy principal value of $I_1(u)$ is $-i\pi$ times the residue of the integrand at $u=u_0$ (Marsden, 1973), whereupon,

$$I_1(u) = -i\pi e^{+i2e^{u}} e^{u} - 2e^{u} .$$

Similarly, a second auxiliary integral,

$$I_2(u) = \int_{-\infty}^{+\infty} \frac{e^{-i2e^{u_0}} e^{u_0} - 2e^{u_0}}{u_0 - u} du_0 \ ,$$

is solved with the aid of a closed contour drawn in the lower half of the complex plane. The Cauchy principal value of $I_2(u)$ is now $+i\pi$ times the residue of the integrand at $u=u_0$, i.e,

$$I_2(u) = +i\pi e^{+i2e^u} e^u - 2e^u \ .$$

By combining the results for $I_1(u)$ and $I_2(u)$ above one finds the expressions

$$\int_{-\infty}^{+\infty} \frac{\cos(2e^{u_0})\ e^{u_0} - 2e^{u_0}}{u_0 - u} du_0 \ = -\pi\sin(2e^u) \ , \text{ and}$$

$$\int_{-\infty}^{+\infty} \frac{\sin(2e^{u_0})\ e^{u_0} - 2e^{u_0}}{u_0 - u} du_0 \ = \pi\cos(2e^u) \ .$$

These last two formulas are now used in the substitution of equations (3.23) and (3.24) into equations (3.25) and (3.26) to finally showing that, in effect, both g(u) and h(u) are analytic components of each other.

The Hilbert transform relation that exists between g(u) and h(u) is consistent with the property of causality inherent to the electrical response of a 1-D earth upon normal plane-wave excitation (Kunetz, 1972, and Weidelt, 1972). In the case of the first-order Rytov approximation, equations (3.25) and (3.26) directly enforce the even more specialized minimum-phase property of the response. Boehl et al. (1977) have advantageously used this minimum-phase property in the interpretation of noisy and biased apparent resistivity data.

Even though both real and imaginary components of the data are related by a causal linear transformation, there are properties of the subsurface resistivity variations that cannot be recovered by the imaginary component alone. This is shown in sections 3.7 and 3.8 below.

3.7 Depth of penetration in a homogeneous half-space

When operating over a homogeneous perturbation of subsurface resistivity, the electrical response from the subsurface obtained via equation (3.21) is determined by the

DC values of the real and imaginary components of the 1-D MT wavelet. Direct integration of the right-hand side of equations (3.23) and (3.24) reveals that such DC values are given by

$$\int_{-\infty}^{+\infty} g(u)\, du = 1, \text{ and}$$

$$\int_{-\infty}^{+\infty} h(u)\, du = 0.$$

In plain words, these results indicate that only the real component of the data is sensitive to the average value of subsurface resistivity. Also, notice that the unimodularity of g(u) comes as a consequence of the factor 2 arbitrarily introduced in the definitions for the data and kernel functions in equations (3.8) and (3.10), respectively.

Because of the fact that h(u) has a zero DC value, the imaginary part of the electrical response is useless in helping establish a difference among all homogeneous distributions of subsurface resistivity and, therefore, cannot be used in an independent determination of depth of penetration. For this purpose, attention is focused solely on the real component of the data.

Consider now the integrated response function, I(-u), defined as

$$I(-u) = \int_{-\infty}^{-u} g(-u_0)\, du_0 = 1 - e^{-2e^{-u}} \cos\left(2e^{-u}\right).$$

Inspection of this last expression reveals that $I(-u)\rightarrow 0$ for $u\rightarrow -\infty$, whereas $I(-u)\rightarrow 1$ for $u\rightarrow +\infty$. The way in which I(-u) asymptotes the value of 1 determines the depth range down from the surface where most of the weighting exercised by g(-u) takes place. This is illustrated in Figure 3-3, where the integrated responses of the real and imaginary components of the 1-D MT wavelet are plotted with respect to -u, i.e., with depth increasing to the right of the plot.

The first point, -u, where I(-u) becomes 1 is -u=0.242 (0.78δ). For comparison, the Bostick depth of penetration (Bostick, 1977) in the homogeneous half-space coincides with the point -u=0.346 (0.71δ). Beyond the value -u=0.242, toward the positive portion of the -u axis, the function I(-u) continuously oscillates about 1, with the oscillations progressively smaller for increasing values of -u. This oscillatory behavior of I(-u) indicates that, for given frequency, or v value, the surface electric response is insensitive to any half-space buried below the critical point v-u=0.242. Although the result obtained here

is consistent with the results reported in his study, Spies (1989) examines more conservative estimates of the depth of penetration in an effort to account for practical noise levels in the measured data. As shown below, the effect that noisy measurements have in the estimation of a resistivity model is probably best understood in the vertical wavenumber domain.

3.8 Vertical harmonic behavior

Owing to the depth-shift invariance property of the 1-D MT wavelet, the characteristics of the linearized response can be easily studied in the Fourier domain. To this effect, define the Fourier transform pair of f(u) as

$$F(\lambda) = \mathcal{F}\{f(u)\} = \int_{-\infty}^{+\infty} f(u)\, e^{+i2\pi\lambda u}\, du, \text{ and} \tag{3.27}$$

$$f(u) = \mathcal{F}^{-1}\{F(\lambda)\} = \int_{-\infty}^{+\infty} F(\lambda)\, e^{-i2\pi\lambda u}\, d\lambda, \tag{3.28}$$

where the variable λ is the linear vertical wavenumber. Thus, in the Fourier transform domain, equation (3.21) takes on the multiplicative form

$$D(\lambda) = M(\lambda)\, F(\lambda)\,, \tag{3.29}$$

where,

$D(\lambda) = \mathcal{F}\{d(v)\}$, and
$M(\lambda) = \mathcal{F}\{m(u)\}$.

In order to obtain the Fourier transform of the 1-D MT wavelet, first substitute equation (3.23) into equation (3.27) together with the change of variable $\varphi = 2e^{u}$. The result is

$$G(\lambda) = \mathcal{F}\{g(u)\} = 2^{-i2\pi\lambda} \int_0^{\infty} (\cos\varphi + \sin\varphi)\, \varphi^{i\,2\pi\lambda} e^{-\varphi}\, d\varphi\,.$$

Further substitution of Euler's formulas for sine and cosine into this last expression plus a few algebraic steps yields

$$G(\lambda) = 2^{-1\,-\,i2\pi\lambda} \{(1 - i) \int_0^{\infty} \varphi^{i\,2\pi\lambda}\, e^{-\varphi(1\,-\,i)}\, d\varphi + (1 + i) \int_0^{\infty} \varphi^{i\,2\pi\lambda}\, e^{-\varphi(1\,+\,i)}\, d\varphi\}\,.$$

The integrals involved in this last expression can be solved in terms of the complex-valued gamma function, Γ. Using the integral formula

$$\int_0^\infty t^{\nu-1} e^{-\mu t} dt = \frac{1}{\mu^\nu}\Gamma(\nu)$$
$$[\text{Real } \mu>0, \text{ Real } \nu>0]$$

(Abramowitz and Stegun, 1972, 6.1.1), one finally obtains

$$G(\lambda) = 2^{-i3\pi\lambda} \cosh\left(\frac{\pi^2\lambda}{2}\right) \Gamma(1+i2\pi\lambda) . \qquad (3.30)$$

Similarly, the Fourier transform, $H(\lambda)$, of the imaginary part of the 1-D MT wavelet, h(u), takes on the form

$$H(\lambda) = -i2^{-i3\pi\lambda} \sinh\left(\frac{\pi^2\lambda}{2}\right) \Gamma(1+i2\pi\lambda) . \qquad (3.31)$$

Amplitude values of both G and H can be computed with use of the identity

$$|\Gamma(1+i2\pi\lambda)|^2 = \Gamma(1+i2\pi\lambda)\,\Gamma(1-i2\pi\lambda) = \frac{2\pi^2\lambda}{\sinh(2\pi^2\lambda)}$$

(Abramowitz and Stegun, 1972, 6.1.31).

The low-pass filter nature of both G and H is illustrated in Figure 3-4 with plots of amplitude response versus linear wavenumber, λ. In these plots, the upper scale consists of wavenumber values in the units of cycles/decade. Such units are particularly useful in magnetotellurics since the sampling interval with which data are acquired in the frequency axis is normally a submultiple of a log10 decade. Notice that, in agreement with the depth-domain analysis carried out in section 3.7, $H(\lambda)$ annihilates the DC wavenumber harmonic of the vertical variations of subsurface resistivity.

3.9 Model deconvolution and vertical resolution

In the wavenumber domain, a simple algebraic step is all that is required to estimate a resistivity model from the data via equation (3.29), namely,

$$M(\lambda) = \frac{1}{F(\lambda)} \cdot D(\lambda), \qquad (3.32)$$

provided that $|F(\lambda)| \neq 0$ for all values of λ. However, the asymptotic decay of $|F(\lambda)|$ (Figure 3-4), together with the potentially damaging presence of noise in the data, render the above equation unstable in any practical attempt to recover $M(\lambda)$. To understand this problem, assume that the data are contaminated with additive noise whose Fourier transform is denoted as $N(\lambda)$. Thus, in the wavenumber domain the measured data, $\tilde{D}(\lambda)$, can be written as

$$\tilde{D}(\lambda) = D(\lambda) + N(\lambda) . \tag{3.33}$$

Resorting to the basic tenet of linearity, one can obtain a model estimate, $\widehat{M}(\lambda)$, from the noisy data by way of the expression

$$\widehat{M}(\lambda) = S(\lambda)\, \tilde{D}(\lambda), \tag{3.34}$$

in which the transfer function $S(\lambda)$ is deliberately introduced to describe the way in which noise in the data projects into a distortion of the true model solution, $M(\lambda)$. The way in which the true model solution is modified in response to the presence of noise in the data is determined by the characteristics of both $F(\lambda)$ and $N(\lambda)$. Unfortunately, in practical applications only a few of the characteristics of the noise, $N(\lambda)$, are known a priori, and, consequently, the estimation of $M(\lambda)$ from noisy data is rendered non-unique.

A common procedure to solve the model estimation problem is the one for which the difference between $M(\lambda)$ and $\widehat{M}(\lambda)$ is minimized in a least-squares, or ℓ_2-norm sense. To this end, consider a stationary, zero-mean model, $M(\lambda)$ (if the mean of the model is not zero one subtracts the mean from it prior to performing this analysis). Likewise, assume that the noise in the measurements is stationary, has zero mean and is uncorrelated with the model. Hence, the least-squares, or Wiener estimate of $S(\lambda)$ is

$$S(\lambda) = \frac{1}{F(\lambda)} \frac{|F(\lambda)|^2}{|F(\lambda)|^2 + NSR^2(\lambda)} , \tag{3.35}$$

where $NSR(\lambda)$ is the function that describes the noise-to-signal ratio, expressed as

$$NSR(\lambda) = \frac{|N(\lambda)|}{|M(\lambda)|} \tag{3.36}$$

(see, for instance, Papoulis, 1965, and Franklin, 1970). With this solution for $S(\lambda)$, a measure of the difference between $M(\lambda)$ and $\widehat{M}(\lambda)$ is obtained by substituting equations (3.32), (3.33), and (3.35) into equation (3.34), i.e.,

$$\widehat{M}(\lambda) = \frac{|F(\lambda)|^2}{|F(\lambda)|^2 + NSR^2(\lambda)} \bullet M(\lambda) . \qquad (3.37)$$

Equations (3.32) and (3.34) reduce to equivalent expressions when $NSR(\lambda)=0$. It is remarked also that the definition of the noise-to-signal ratio in equation (3.36), which considers the model variations as signal, tacitly assumes that $|M(\lambda)|\neq 0$ for all values of λ. This assumption has a practical reason: it allows one to study the resolving power of the linear system solution embodied in equation (3.34) when the model is potentially capable of exciting all wavenumber harmonics in the surface electric field response.

In equation (3.37), the ratio

$$R(\lambda) = \frac{|F(\lambda)|^2}{|F(\lambda)|^2 + NSR^2(\lambda)}$$

is normally referred to as the resolution window. The latter function is a zero-phase low-pass filter that describes the distortion of model harmonics in the presence of noise; the larger the value of $NSR(\lambda)$ the lower the cutoff wavenumber of $R(\lambda)$.

Within the assumption of stationarity, the Wiener estimate of $S(\lambda)$ is indeed the best estimate when the noise, $N(\lambda)$, is white and is described by a Gaussian probability distribution (Menke, 1984). To understand the resolution characteristics of the 1-D MT wavelet, consider a "white" model, m(u), with variance s^2, and hence described in terms of the Dirac delta function, $\delta(u)$, as $s^2\delta(u)$. Assume also that the noise is white and is described by a Gaussian probability distribution of zero mean and variance equal to n^2. Under these conditions, the function $NSR(\lambda)$ (equation 3.36) is constant and equal to

$$NSR(\lambda) = \frac{n}{s} .$$

Figure 3-5 shows the "white" model amplitude response, $D(\lambda)$, of the linear system described by $F(\lambda)$ upon excitation of a unity-variance model, $\delta(u)$. This figure also shows a white noise amplitude response, $N(\lambda)$, with a 10% standard deviation. Graphically, it is easy to understand for this particular situation that, beyond approximately 1.5 cycles/decade, the noise response has completely flooded the natural signal level from the

subsurface. For a given noise-to-signal ratio, the maximum wavenumber harmonic that can be recovered from the subsurface without distortion is described in the plots of resolution window, $R(\lambda)$ shown in Figure 3-6, for both real and imaginary components of the data.

Even in computer simulated data, when the only likely sources of noise are accumulated 32-bit computer roundoff errors, a noise-to-signal ratio of approximately 10^{-4} remains a good minimum bound. For this situation, Figure 3-6 indicates that 3.5 cycles/decade is the maximum wavenumber with which the model, $M(\lambda)$, can be recovered without significant harmonic distortion. Assuming that this wavenumber is the actual Nyquist wavenumber with which the data have been sampled along a $\log_{10}$ frequency axis, it becomes apparent that 7 or 8 frequency samples per decade should be the maximum necessary to optimally recover the vertical variations of subsurface resistivity (other sources of noise in the data actually bring this minimum number of samples per decade to a lower value.) Inverse simulation studies carried out with single-precision arithmetic on a 32-bit computer show that a more practical lower bound for noise-to-signal ratio is approximately 0.01 (sections 3.12 and 3.13), for which the optimal number of frequency samples per decade is in the neighborhood of 5.

In the sections below, deconvolution examples are presented to illustrate the characteristics of, and problems faced by practical 1-D MT inverse problem formulations. The objective of those examples is to ascertain whether the linear system representation discussed above has any practical use in situations where the assumptions of small secondary resistivity and electric field variations are clearly unjustified. Likewise, in the simple framework of the linearized forward solution, procedures are examined whereby the inversion of a resistivity profile is affected by the choice of model functional, smoothing parameters and, ultimately, model norm.

Even though deconvolution procedures in the wavenumber domain can be used in practical inversion problems, often depth-domain procedures offer a greater degree of flexibility, as is shown below.

3.10 Model deconvolution in practice

Inversion procedures for the estimation of the model, m(u), from the data, d(u), for which the relationship is of a linear nature have been amply studied in the context of geophysical applications (see, for instance, the excellent tutorial paper by Oldenburg, 1984.) For the particular case in which the kernel is shift invariant, such as that of the

linearized forward MT problem, Treitel and Lines (1982), have explored the relationship between the Wiener deconvolution and Backus and Gilbert (1967, 1968, 1970) model estimation procedures.

The approach taken here for the model estimation is equivalent to the constrained Wiener inverse solution described by Treitel and Lines (1982). For this purpose, equation (3.21) is discretized in the form

$$d(v_i) = \begin{cases} \sum_{j=1}^{N} m(u_j) g(v_i - u_j)\, \Delta u_j & \text{for } 1 \le i \le M \\ \sum_{j=1}^{N} m(u_j) h(v_i - u_j)\, \Delta u_j & \text{for } M+1 \le i \le 2M \end{cases}$$

Using the abbreviated notation,

$d_i = d(v_i)$,

$m_j = m(u_j)$, and

$$f_{ij} = \begin{cases} g(v_i - u_j)\, \Delta u_j & \text{for } 1 \le i \le M \\ h(v_i - u_j)\, \Delta u_j & \text{for } M+1 \le i \le 2M \end{cases},$$

a simple matrix notation for the discrete linear forward problem is

$$\underline{d} = \underline{\underline{F}}\, \underline{m}\,, \tag{3.38}$$

where

$$\underline{d} = \begin{pmatrix} d_1 \\ d_2 \\ \vdots \\ d_M \end{pmatrix}, \quad \underline{m} = \begin{pmatrix} m_1 \\ m_2 \\ \vdots \\ m_N \end{pmatrix}, \quad \text{and}$$

$$\underline{\underline{F}} = \begin{pmatrix} f_{11} & f_{12} & \cdots & f_{1N} \\ f_{21} & f_{21} & \cdots & f_{2N} \\ \vdots & \vdots & \ddots & \vdots \\ f_{M1} & f_{M2} & \cdots & f_{MN} \end{pmatrix}.$$

For simplicity, and without sacrifice of generality, here attention is paid to the well-posed inverse problem in which the number of frequency samples is exactly the same as the number of model unknowns, i.e., M=N. Likewise, it is assumed that the data are evenly sampled and that there are not missing data between the first and the last samples. The

variable Δu is thus independent of the column index in equation (3.38). Finally, even though in practice the data are seldom sampled continuously with respect to frequency, the linearity between real and imaginary components predicted by the Hilbert transform pair in equations (3.25) and (3.26) still holds to a large extent. For this reason, the model estimation procedures examined in this chapter are based solely on the real component of the data. Model inference from the imaginary component of the data alone is not studied because, as it was shown in sections 3.7 and 3.8, such data are unable to resolve the DC component of the resistivity profile. To circumvent this difficulty one could think of a procedure whereby the DC component of the resistivity profile would be extracted from the real component of the data and the remaining vertical wavenumber harmonics inferred from the imaginary component alone. However, the advantages and disadvantages of such a procedure are not explored in this thesis.

Consider now the practical situation in which the measured data, $\underline{\tilde{d}}$, are contaminated with additive noise, $\underline{n}$, i.e.,

$$\underline{\tilde{d}} = \underline{d} + \underline{n} \,. \tag{3.39}$$

An estimate of the model, $\underline{\hat{m}}$, can be found from the noisy data with use of the linear equation

$$\underline{\hat{m}} = \underline{S}\,\underline{\tilde{d}} \,, \tag{3.40}$$

where the inverse operator $\underline{S}$ describes the way in which noise in the measured data is projected into the estimated model solution. Once again, a solution for $\underline{S}$ may be found by minimizing the least-squares difference between $\underline{\hat{m}}$ and $\underline{m}$, written as

$$r(\underline{m}) = (\underline{\hat{m}} - \underline{m})^T (\underline{\hat{m}} - \underline{m}), \tag{3.41}$$

where the superscript T is used to symbolize matrix transpose. The minimization of this model functional is the basis of the Wiener or stochastic inverse (Franklin, 1970, and Aki and Richards, 1980), in which both model and noise vectors are assumed realizations of a stochastic process. In this vein, assume also that both the model and the noise are uncorrelated and have zero means (if their means are not zero then they are subtracted prior to performing this analysis.) With these assumptions, equations (3.38) through (3.40) substituted into equation (3.41) yield a set of normal equations for the entries of $\underline{S}$ whose final solution is

$$\underline{S} = (\underline{F}^T \underline{C}_M \underline{F} + \underline{C}_N)^{-1} \underline{C}_M \underline{F}^T,$$

where

$$\underset{\sim}{C}_M = \underline{m}\,\underline{m}^T, \text{ and}$$

$$\underset{\sim}{C}_N = \underline{n}\,\underline{n}^T$$

are the model and noise covariance matrices, respectively (Aki and Richards, 1980). For the case in which both the model and the noise are white Gaussian processes with zero means and standard deviations equal to s^2 and n^2, respectively, their covariance matrices can be written as

$$\underset{\sim}{C}_M = s^2\,\underset{\sim}{I}, \text{ and}$$

$$\underset{\sim}{C}_N = n^2\,\underset{\sim}{I},$$

respectively, where $\underset{\sim}{I}$ is the identity matrix. Under these assumptions, the solution for $\underset{\sim}{S}$ above can be specialized to read as

$$\underset{\sim}{S} = (\underset{\sim}{R} + nsr^2\,\underset{\sim}{I})^{-1}\underset{\sim}{F}^T, \tag{3.42}$$

where

$$\underset{\sim}{R} = \underset{\sim}{F}^T\,\underset{\sim}{F}$$

is the autocorrelation matrix of the linear system, symmetric and Toeplitz (the latter characteristic being a result of the shift-invariance property of the 1-D MT wavelet); also,

$$nsr = \frac{n}{s}$$

is the noise-to-signal ratio. Incidentally, the solution for $\underset{\sim}{S}$ in equation (3.42) is the space-domain equivalent of the wavenumber domain inverse filter $S(\lambda)$ derived in section 3.9.

Alternatively, a solution for the operator $\underset{\sim}{S}$ introduced in equation (3.40) can be found by casting the model functional, $r(\underline{m})$, in the form of data residuals, i.e.,

$$r(\underline{m}) = (\tilde{\underline{d}} - \underline{d})^T (\tilde{\underline{d}} - \underline{d}), \tag{3.43}$$

together with the condition that this model functional be minimized in conjunction with the model energy constraint that

$$\underline{m}^T\underline{m} = c$$

remain constant. An augmented model functional for this situation can be written as

$$r(\underline{m}) = (\underline{\tilde{d}} - \underline{d})^T (\underline{\tilde{d}} - \underline{d}) + \alpha (\underline{m}^T \underline{m} - c) , \qquad (3.44)$$

where α, the Lagrange multiplier, becomes a new variable sought after in the minimization process leading to the model estimate. Treitel and Lines (1982) have shown that the critical model value for which this augmented model functional is minimized is identical to that derived from the Wiener inverse (equations 3.41 and 3.42). The physical significance attached to the Lagrange multiplier, α, in equation (3.44), however, is best understood with the use of the noise-to-signal ratio concept of the Wiener inverse formulation.

An interesting modification to the model functional in equation (3.44) is the one for which the first derivative of the model is minimized concomitantly with the minimization of the data residuals, namely,

$$r(\underline{m}) = (\underline{\tilde{d}} - \underline{d})^T (\underline{\tilde{d}} - \underline{d}) + \alpha \sum_{i=2}^{N} (m_i - m_{i-1}) . \qquad (3.45)$$

The model estimate that results from the minimization of this new model functional is

$$\underline{\hat{m}} = (\underline{\underline{R}} + \alpha \underline{\underline{D}}^T \underline{\underline{D}})^{-1} \underline{\underline{F}}^T \underline{\tilde{d}} , \qquad (3.46)$$

where $\underline{\underline{D}}$ is the first-order difference matrix, written in expanded form as

$$\underline{\underline{D}} = \begin{pmatrix} 0 & 0 & 0 & \cdots & 0 & 0 \\ -1 & 1 & 0 & \cdots & 0 & 0 \\ 0 & -1 & 1 & \cdots & 0 & 0 \\ \vdots & \vdots & \vdots & \ddots & \vdots & \vdots \\ 0 & 0 & 0 & \cdots & 1 & 0 \\ 0 & 0 & 0 & \cdots & -1 & 1 \end{pmatrix}_{NxN} .$$

In equation (3.46), the Lagrange multiplier, α, controls the degree of smoothness in the inferred model solution. A small value of α produces a highly oscillatory model solution; conversely, a large value of α produces a smooth model solution. Even though their solution includes an optimal search for the Lagrange multiplier, α, whereby the data residuals are kept as close as possible to a preset data misfit value, Constable et al. (1987) have applied this modification of the Wiener inverse solution under their own denomination of Occam's inverse. Similar model functionals can be formulated in like manner for the minimization of higher-order model derivatives.

Minimization of model functionals such as those written in equations (3.44) and (3.45) can also be done via quadratic programming techniques (Lawson and Hanson,

1974, and Gill et al., 1981). The advantage of quadratic programing is that model range constraints, known a priori from sources of information other than the measured data themselves, can be enforced in the minimization of the model functional. In section 3.14 examples are shown that illustrate the effect of adding this type of model range constraints to the minimization of the model functional. Also, section 3.15 illustrates the use of an alternative ℓ_1-norm model functional.

3.11 Estimation of the background resistivity

Application of the inverse procedures described in the previous two sections assumes that the background resistivity is known beforehand. Within the assumption of linearity, accurate knowledge of the background resistivity is important to reduce shifting errors in the mapping whereby measurements made along the $\log_{10}$ frequency axis are transported into the $\log_{10}$ depth scale describing the inverted resistivity profile. This mapping is governed by equation (3.19b).

Assuming again that the model can be described as the realization of an ergodic stochastic process, the background resistivity can be thought of as the expected value of this stochastic process. Accordingly, because of the linear relationship between the model and the data also assumed in the analysis above, the average value of the data (i.e., its zero-lag autocorrelation value) should reflect the expected model value. With this idea in mind, substitute the value of Real($2e/E_0$) given by equation (3.17) into equations (3.21) and (3.15) and express both frequency and depth in terms of the logarithmic variables v (for any given background resistivity) and u, respectively, to get

$$\ln \rho_A(v) = \ln \rho_0 + \int_{-\infty}^{\infty} \Delta \ln \rho(u)\, f(v-u)\, du \; .$$

Integrating both sides of this expression with respect to v from $-\infty$ to $+\infty$ yields

$$\lim_{L \to \infty} \left(\frac{1}{2L} \int_{-L}^{+L} \ln (\rho_A(v))\, dv \right) = \ln (\rho_0) + \int_{-\infty}^{+\infty} \left[\int_{-\infty}^{+\infty} \Delta \ln \rho(u)\, f(v-u)\, du \right] dv \; .$$

Finally, interchanging the order of integration on the right-hand side integral, and assuming that $\Delta \ln \rho(u)$ has zero mean, one obtains

$$\rho_0 = e^{\overline{\ln \{\rho_A[\ln(\omega)]\}}}, \qquad (3.47)$$

where the bar over the logarithmic apparent resistivity is used to denote expected value. In short, equation (3.47) indicates that the background resistivity is the expected value of apparent resistivity taken over a logarithmic frequency axis.

Needless to say, an error in the estimated background resistivity, ρ_0, will be responsible for a change in the v-value range with which the data are projected onto the logarithmic depth scale that is used in the inversion of $\rho(z)$. The way in which an error in the estimated background resistivity distorts the logarithmic depth scale is best expressed by the derivative of v with respect to $\ln(\rho_0)$. From equation (3.19b), this derivative is found to be

$$\frac{\partial v}{\partial \ln \rho_0} = -\frac{1}{2} \ .$$

Thus, as a result of a small perturbations of $\ln(\rho_0)$, the ensuing perturbation of the v value is given by

$$\Delta v \approx -\frac{1}{2} \Delta \ln \rho_0 \ .$$

This approximation indicates that a perturbation in the background resistivity will merely cause a shift of the data along the logarithmic depth scale. A positive perturbation of ρ_0 will uniformly shift the depth scale deeper in the subsurface; conversely, a negative perturbation in ρ_0 will uniformly bring the logarithmic depth scale closer to the surface.

3.12 Example of inversion with the Born approximation of the data

The standard synthetic example analyzed here is the one described along with its MT response in Figure 3-2. This model corresponds to the layered example used in the nonlinear inversion study of Oldenburg (1979), although here the resistivity profile plotted on a $\log_{10}$ depth scale has been shifted to the next higher decade to reflect a relatively more practical exploration situation. The MT response plotted in Figure 3-2 was numerically simulated with an exact 1-D transmission line algorithm, including 10 frequency samples per decade in the band from 0.0005 to 1,000 Hz (a total of 64 samples). For the Born approximation of the data, the function $d(\omega)$ in equation (3.7) is constructed from the simulated impedances with the formula

$$d(\omega) = \text{Real}\left[2\frac{Z(\omega)}{Z_0(\omega)}\right] - 2$$

(see equation 3.6). The value for background resistivity used henceforth in this chapter is 4.0 Ω•m; this value is approximately equal to the average of the fluctuations of logarithmic apparent resistivity along the logarithmic frequency axis within the simulated frequency range.

Plots of the inverted resistivity profiles are shown in Figure 3-7. The algorithm employed for the inversion is the constrained Wiener deconvolution governed by equations (3.41) and (3.42), including results for three values of noise-to-signal ratio, i.e., 0.01, 0.1, and 1. Also, for comparison, the Bostick (1977) pseudoinverse is included in the same figure. As evidenced by these results, a high noise-to-signal ratio translate to smooth resistivity profiles, whereas a low noise-to-signal ratio produces a more oscillatory behavior in the inverted profile. Noise-to-signal ratios lower than those considered in Figure 3-7 (0.001, for instance) are tested here because their associated resistivity profiles undergo very unrealistic oscillations. In fact, from the simulation studies related in this chapter, it appears that a noise-to-signal ration of 0.01 is the lowest feasible value when the synthetic data are calculated on a 32-bit single-precision machine.

Besides the model oscillations controlled by the noise-to-signal ratio, the excessive undershoot near the first downward step of the layered model is a prominent feature exhibited by the three inverted resistivity profiles. The nature of this undershoot will become clearer when results are presented in the following section using the Rytov approximation of the data. In advance, however, it is noted that such a situation occurs at points where the data exhibit the most sensitivity to a change in subsurface resistivity, that is to say, about low-resistivity variations. A decrease in subsurface resistivity is the easiest way to render the assumption of small secondary-to-primary field ratios inappropriate. On the other hand, the resistivity contrasts considered in this example by no means adhere to the low-contrast assumption that is the basis of the linearized inverse. The fact that this assumption is not as stiff an operation requirement is to a large extent due to the use of the logarithmic model representation (equation 3.14).

Figure 3-7 also shows that resistivity profiles inverted with a noise-to-signal ratio below 1.0 display slightly more vertical resolution than the profile inverted with the Bostick pseudoinverse. However, the asymptotic nature of the Bostick pseudoinverse is better suited to account for the abrupt termination of the data at 0.0005 Hz than the Born inversion procedure, which at the same point develops a highly oscillatory behavior.

3.13 Example of inversion with the Rytov approximation of the data

Consider now the expression for the data under the first-order Rytov approximation of the 1-D MT response, given by

$$d(\omega) = 2 \ln \left| \frac{Z(\omega)}{Z_0(\omega)} \right|$$

(equations 3.8 and 3.13). With the simulated results described in the previous section as input data, Figure 3-8 shows the resistivity profiles inverted via the constrained Wiener inverse for values of noise-to-signal ratio of 0.01, 0.1, and 1.

Inspection of the results shown in Figures 3-7 and 3-8 reveals that even at the lowest noise-to-signal ratio, the resistivity profile inverted with the Rytov representation of the data is more stable and closer to the true model than the one inverted with the Born representation of the data. Of interest is also the fact that in the two methods resistive anomalies are better resolved than conductive ones, albeit for the model example studied here the former anomalies exhibit much larger contrasts than the latter. This situation is explained by recalling that the measured surface MT data is less sensitive to high-resistivity variations than to low-resistivity variations, in which case the linearized inverse works under much favorable circumstances over resistive than over conductive variations of subsurface resistivity.

Noise-to-signal ratios above 0.01 show almost no trace of the thin (keeping in mind the logarithmic nature of the depth scale, of course) conductive layer buried at a depth of 700 m in the model plot of Figure 3-8.

Additional inversion examples that illustrate the discrepancies between the Born and Rytov representations of the data are shown in Appendix B. In the following sections, the estimation of a vertical profile of subsurface resistivity is approached with slightly different model functionals.

3.14 Model range constraints

Model range constraints are but a class of a priori information that is sometimes available regarding the nature of the model sought after. These constraints originate from sources of information other than the data themselves (at least the data supported by the physical system related to the inversion.) For instance, suppose that prior to inverting for

the model whose MT response is shown in Figure 3-2, it is known that all resistivity values fall above 1 Ω•m. Starting with equation (3.2), this constraint can be cast in the form

$$\frac{\Delta\rho(z)}{\rho_0} > \frac{1}{\rho_0} .$$

Enforcing this inequality in the minimization of the model functional is best done if instead of the logarithmic formula (3.12), the resistivity profile is written in algebraic form in terms of the ratio $\Delta\rho/\rho_0$, namely

$$\rho(z) = \rho_0(1 + \frac{\Delta\rho(z)}{\rho_0}).$$

For the case in which the desired resistivity profile has a preset upper bound, a more stable algebraic expression for the resistivity $\rho(z)$ is

$$\rho(z) = \frac{\rho_0}{1 - \frac{\Delta\rho(z)}{\rho_0}}.$$

For instance, if the resistivity profile shown in Figure 3-2 is known not to take on values above 100 Ω•m a model range constraint may be enforced with the inequality

$$\frac{\Delta\rho(z)}{\rho_0} < \frac{\rho_0}{100} - 1.$$

Figures 3-9 and 3-10 show the results of inverting the synthetic data described in Figure 3-2 with the model range constraints that $\rho(z)>1$ Ω•m, and $\rho(z)<100$ Ω•m, respectively, assuming the three standard values of noise-to-signal ratio of 0.01, 0.1, and 1. The results shown where obtained with the quadratic programming algorithm of the HARWELL FORTRAN library (subroutine VE04A, Hopper, 1979) in conjunction with the Rytov representation of the data.

In Figure 3-9, the lower bound model constraint causes the inversion to be overly sensitive to the low-resistivity variations, and for which the data actually exhibit the largest response. This sensitivity is somewhat quelled only when the noise-to-signal ratio is larger than 0.1, but when this is done the inverted resistivity profile shows no added benefit from the inclusion of the model range constraint. However, in other situations, such as those shown in Appendix B, this type of model range constraint may prove useful to reduce the

sidelobe activity, or Gibb's phenomenon, that is often characteristic of the standard ℓ_2-norm minimization procedures.

On the other hand, the use of an upper bound model constraint for the inversion of the same data shows more interesting features in the estimated resistivity profile. For this new case, high-resistivity variations become more emphasized than their low-resistivity counterparts. However, in like manner as with the lower bound model constraint, equal values of noise-to-signal ratios cause much more variable resistivity profiles than with the enforcement of no constraints at all. Also, even though some sidelobe activity is successfully diminished with the use of the upper bound constraint (especially near low-resistivity layers), the inverted resistivity profiles do not descended to quite as low a resistivity value over conductive layers as the profiles for the unconstrained case do. More examples that illustrates the advantages and disadvantages of using model range constraints in conjunction with the minimization of the model functional in equation (3.44) are shown in Appendix B.

3.15 Constrained ℓ_1-norm deconvolution

To evaluate the effects of different measures of length and size in the estimation of a subsurface resistivity profile, consider now the ℓ_1-norm model functional

$$r(\underline{m}) = \| \underline{\tilde{d}} - \underline{F}\underline{m} \| + \alpha \sum_{i=2}^{N} |m_i - m_{i-1}| , \qquad (3.48)$$

where the double vertical bar, ||, is used to denote ℓ_1 norm, i.e.,

$$\| \underline{m} \| = \sum_{i=1}^{N} |m_i| ,$$

and α is a prewhitening parameter (or Lagrange multiplier). The model functional in equation (3.48) can be compared, at least in principle, to the ℓ_2-norm functional described by equation (3.44). However, because of the poor smoothing characteristics of the ℓ_1 norm, the simultaneous minimization of the first-order model differences (first derivative) is more appropriate in this case than the model energy constraint used previously with the ℓ_2-norm (in which case equation 3.48 is akin to equation 3.45.)

The minimization of an ℓ_1-norm model functional that includes an ℓ_1-norm model energy constraint is more appropriate for the inference of a model characterized by a

sequence of spikes (Taylor et al., 1979). In magnetotellurics, this type of minimization finds a natural application for the D^+ inverse formulation advanced by Parker (1980), and Parker and Whaler (1981). Hybrid formulations of the model functional may include an ℓ_1-norm minimization of the data residuals subject to the constraint that the ℓ_2-norm of the model remains constant in the process (Gill et al., 1981). The ℓ_1-norm minimization of the data residuals can be used to deal with model estimation problems in which the data have been contaminated with non-Gaussian noise. In fact, this type of minimization is ideal for the case in which the noise in the data is described by an exponential probability distribution (Menke, 1984).

In practice, however, the minimization of the model functional expressed in equation (3.48) entails much more elaborate and time consuming procedures than the use of an ℓ_2-norm model functional does. This minimization is customarily approached using linear programming techniques (Claerbout and Muir, 1973). The procedure used in this section for the estimation of $\rho(z)$ via equation (3.48) makes use of the algorithm devised by Barrodale and Roberts (1973) whereby the first-order model difference constraint is included via an augmented transformation matrix.

Figure 3-11 shows the resistivity profiles inverted by minimization of the model functional in equation (3.48) with the three standard values of smoothing parameter α (and for this reason termed the noise-to-signal ratio as in the case of the ℓ_2-norm minimization) of 0.01, 0.1, and 1. For the minimization, both the model and the data were expressed as dictated by their first-order Rytov representations. In Figure 3-11, the blocky nature of the inverted profiles is intrinsic to the ℓ_1 norm itself when used in conjunction with the first-difference model norm, and should not be viewed as a natural way to extend the wavenumber range that can be obtained with the ℓ_2 norm. In fact, it is precisely where the ℓ_2-norm results fail to provide the high wavenumber harmonics necessary to recover sharp boundaries in the subsurface resistivity, that the ℓ_1-norm profiles contract or expand their blocky nature.

Even though for the model example analyzed in this chapter the resistivity profiles inverted with the ℓ_1-norm model functional do not show dramatic differences with respect to the profiles inverted with the ℓ_2-norm, often the use of the ℓ_1-norm minimization scheme justifies its higher operational in extreme noise conditions.

3.16 Nonlinear inversion (does it provide a larger wavenumber content?)

For completeness, consider now the nonlinear inverse procedure put forth by Constable et al. (1987) under the name of Occam's inversion in reference to its objective to find the simplest (smoothest) possible model solution that satisfies the data within a prescribed data misfit value. Constable et al. minimize the model functional described by equation (3.45) at every linear step of their nonlinear algorithm. In so doing, they choose the lowest value of Lagrange multiplier, α, that can accommodate the prescribed data misfit value (the χ^2 error). The smaller the χ^2 error, the lower the value of α, and hence the more oscillatory the estimated model solution. Conversely, the larger the χ^2 error, the larger the value of α and the smoother the model solution.

However, Constable et al.'s (1987) approach becomes rather unstable when, instead of the first derivative, one opts to minimize the ℓ_2-norm of the model. This instability could be somewhat reduced if, in addition to the χ^2 error, a cutoff value for α were prescribed as well in their algorithm (such as the model energy constraint of the Wiener inverse). Nevertheless, in the absence of a better way to compare the linearized inversion results with those of a similar nonlinear method, the comparison is here done with Constable et al.'s algorithm. In support for this exercise, however, it may be added that resistivity profiles inverted with the linearized equations and a first-derivative model functional (equation 3.45) show practically no difference with respect to the profiles inverted using the model energy constraint (equation 3.44).

In the implementation of Constable et al.'s (1987) algorithm, the model was parameterized with a sequence of uniformly distributed layer thicknesses (in logarithmic fashion). Locations for the layers were obtained with the mapping of frequency values into logarithmic depths dictated by equation (3.19b) and assuming a background resistivity of 4 Ω•m, and the layers remained fixed thereafter throughout the inversion. The number of layers was the same as the number of frequency samples and the inversion was carried out using both apparent resistivity and impedance phase data (this is twice the actual number of data used in the linearized inverse solutions studied above.)

With 10 linear iterations, the results of the inversion are shown in Figure 3-12 for the prescribed data misfit, or rms values of 1, 1.5, and 2. The rms misfit value is defined as

$$\text{rms} = \sqrt{\frac{1}{M}\sum_{i=1}^{M}\frac{(\tilde{d}_i - d_i)^2}{s_i^2}} \quad ,$$

where $\tilde{d}_i$ and d_i are the measured and simulated data, respectively, and s_i is the standard deviation of the measured data (assumed unity for all data samples here). In contrast, the linearized Rytov inversion in Figure 3-8 has an rms value of approximately 1 at a noise-to-signal ratio of 0.01.

The profiles inverted with the nonlinear procedure are in excellent agreement with the true model for rms data misfit values below 1.5. In fact, at a noise-to-signal ratio of 0.1, the Rytov inversion results correlate well with the profile inverted in nonlinear fashion at an rms value of 1.5. However, the nonlinear inversion has done a much better job in: (1) adjusting the lateral locations of the various layers, (2) contracting the resistivity profile about low-resistivity variations, and (3) expanding the resistivity profile within high resistivity variations in the layered model. These three interesting features, together with the physical construct of the 1-D MT wavelet, permit one to visualize the way in which a nonlinear inverse works: within low-resistivity variations, the wavelet contracts because in these zones the average resistivity is lower than the background (or global average) resistivity; within high resistivity variations, on the other hand, the wavelet expands because in their immediate vicinity the average resistivity is larger than the average. A contraction of the wavelet signifies a larger wavenumber content, whereas an expansion of it produces a narrower wavenumber content. Also, because of the localized nature of these averages, the exact mapping location for the frequency samples along the logarithmic depth scale is determined by the local and not global average of $\rho(z)$. This explains why the inverted variations of subsurface resistivity are better positioned with the nonlinear inverse than with the the linearized inverse.

The degree to which the wavenumber content in the inverted resistivity profile is different from that of the linearized inverse is determined by the presence and number of low-resistivity zones in the subsurface. These low-resistivity zones are more prone to cause a violation of the assumptions implicit in the linearized inverse than high-resistivity zones are. However, over and above a noise-to-signal ratio of 0.01, the characteristics of the resolution windows in Figure 3-6 should not significantly depart from those of a practical nonlinear situation.

3.17 Discussion and concluding remarks

The inversion examples related in the previous sections indicate that the Rytov expression for both data and model functions significantly outperforms their alternative Born expression. This conclusion is more evident in situations where the frequency-

domain MT data exhibits the largest amplitude variations, that is to say, in response to conductive features in the subsurface.

Use of the Rytov approximation generates acceptable linear inverse solutions in the presence of resistivity contrasts of at most 20:1 approximately. However, given the logarithmic depth scale which is natural to magnetotellurics, a large decrease in resistivity at a particular depth can only have a significant surface response if the depth range where this variation occurs has a large logarithmic thickness (the thickness itself may be large but unless the logarithmic thickness is large compared to its logarithmic depth there will be a measurable surface response). Hence, even highly conductive zones can be unheeded in the surface MT response depending on their depths of burial. Conversely, in response to resistive features, the Rytov approximation yields an acceptable inverse solution for resistivity contrasts of up to 1:100 approximately. Again, the reason why the linearized inverse works better over resistive than over conductive zones is directly related to the fact that MT data are more sensitive to the latter. Because of this, the requirement that secondary electric fields be small compared to the primary field implicit in the Born approximation is more appropriate over resistive than over conductive zones, thus the difference in performance. In fact there are situations wherein the linearized inverse outperforms the Bostick (1977) pseudoinverse.

The inclusion of positivity constraints in the least-squares model functional somewhat extends the wavenumber range of the inferred resistivity profile, and this is especially noticeable as a reduction of sidelobe, or Gibb's phenomenon activity. However, in order to warrant a stable inverse solution, the use of this type of constraints requires larger noise-to-signal ratios (or Lagrange multiplier values) than for the case in which no model range constraints are enforced in the minimization process. Also, the use of an ℓ_1-norm model functional remains an attractive procedure for the inversion of resistivity profiles from data contaminated with non-Gaussian noise. This type of minimization is also suitable for the recovery of sparse delta-like conductance profiles such as those of the D^+ inverse of Parker (1980) and Parker and Whaler (1981).

Despite the aforementioned positive characteristics of the linearized inverse, it should be pointed out that in situations where the logarithmic thicknesses are both large an sparse and the resistivity contrasts are large, this approximate procedure may easily break down. A more practical idea that seems worth exploring as a natural outgrowth of the developments presented in this chapter is the iterative Rytov inversion. For this situation, either the resistivity profile is continuously updated by fixed point iteration of the electric

fields in the subsurface or, at every step of the iteration a new resistivity profile is linearly inverted and then updated to minimize the differences between the observed and numerically simulated data. Albeit in a different context, these two procedures have been successfully used under the name of iterative and distorted Born inversion methods, respectively, by Habashi and Mittra (1987). Finally, the linearized inverse procedures studied in this chapter may be easily adapted to be used with the exact nonlinear formulation put forth by Gómez-Treviño (1987), in which the model functionals are expressed in terms of the resistivity distribution rather than in terms of a perturbation of it.

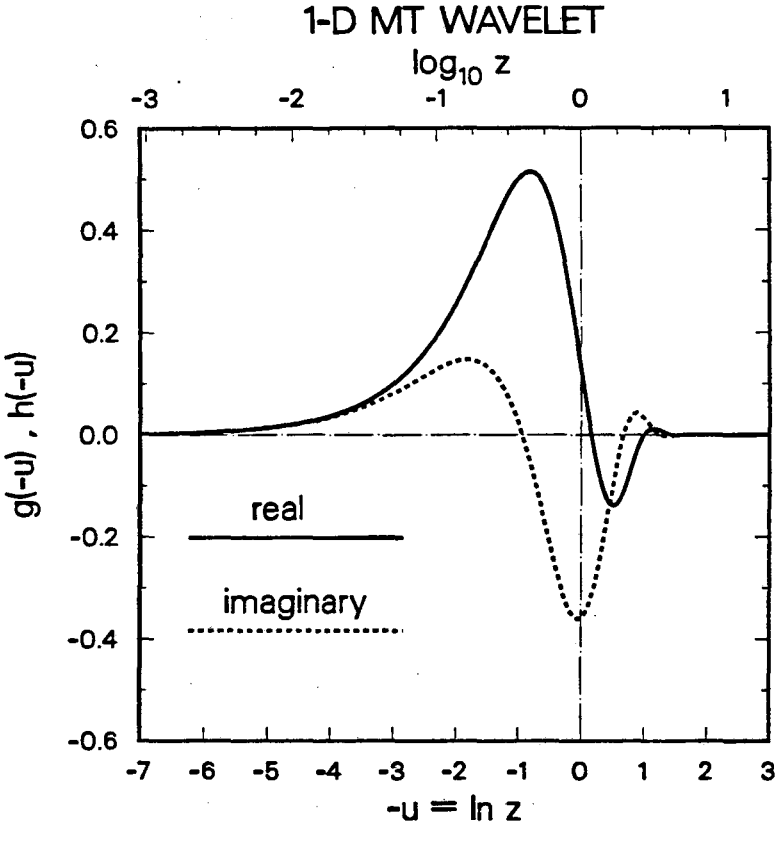

Figure 3-1. Real and imaginary components of the reversed 1-D MT wavelet.

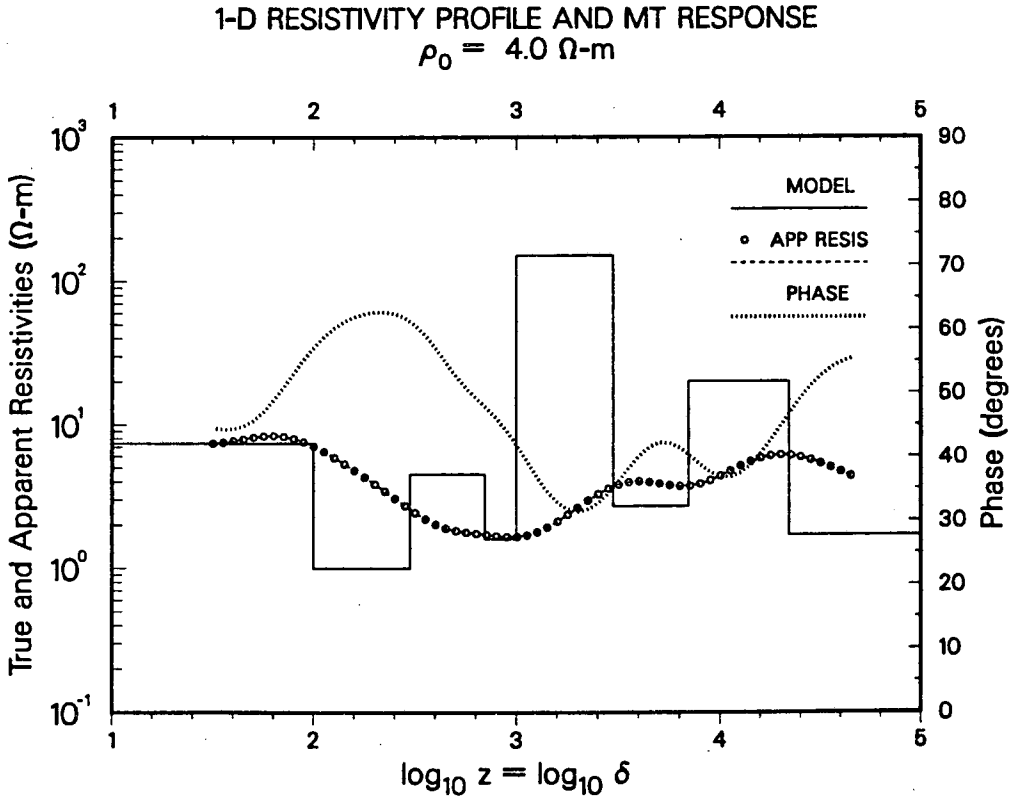

Figure 3-2. 1-D model and MT response curves (apparent resistivity and impedance phase) displayed with the logarithmic parameterization of both frequency and depth that corresponds to a background resistivity of 4 Ω•m (equations 3.19b and 3.20 b).

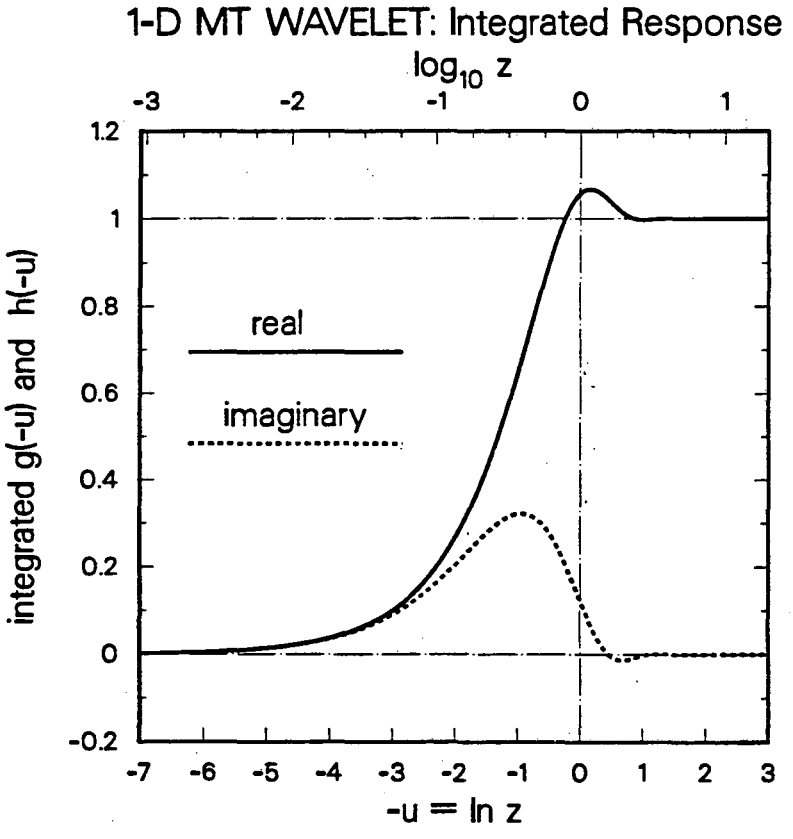

Figure 3-3. Integrated responses of the real and imaginary parts of the 1-D MT wavelet. The depth range for the integration is from $-\infty$ to -u.

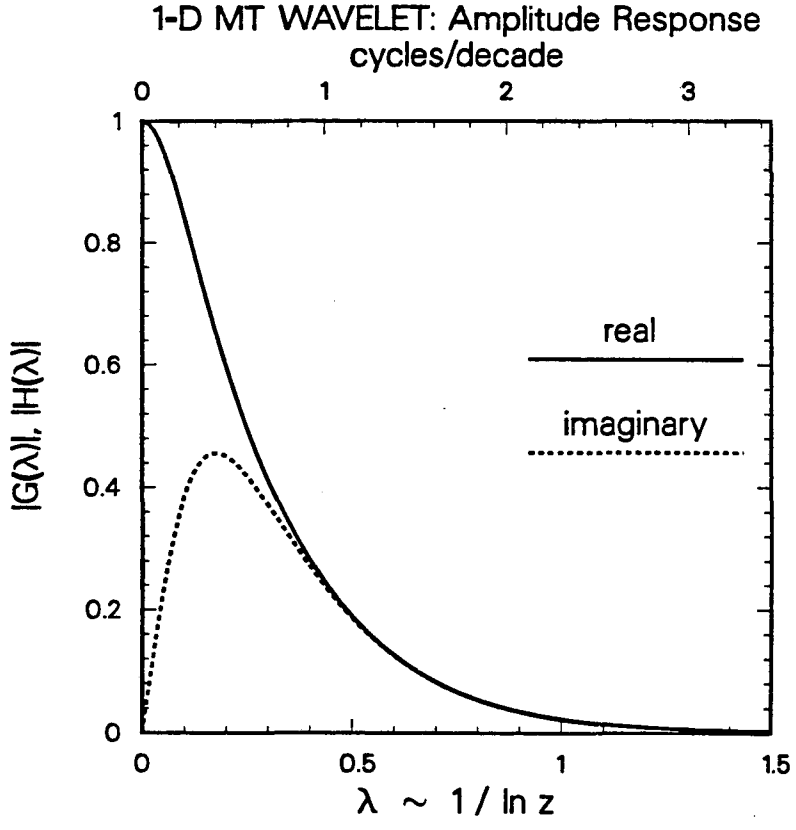

Figure 3-4. Amplitude response of the real and imaginary parts of the 1-D MT wavelet (G and H, respectively) plotted with respect to the linear vertical wavenumber, λ.

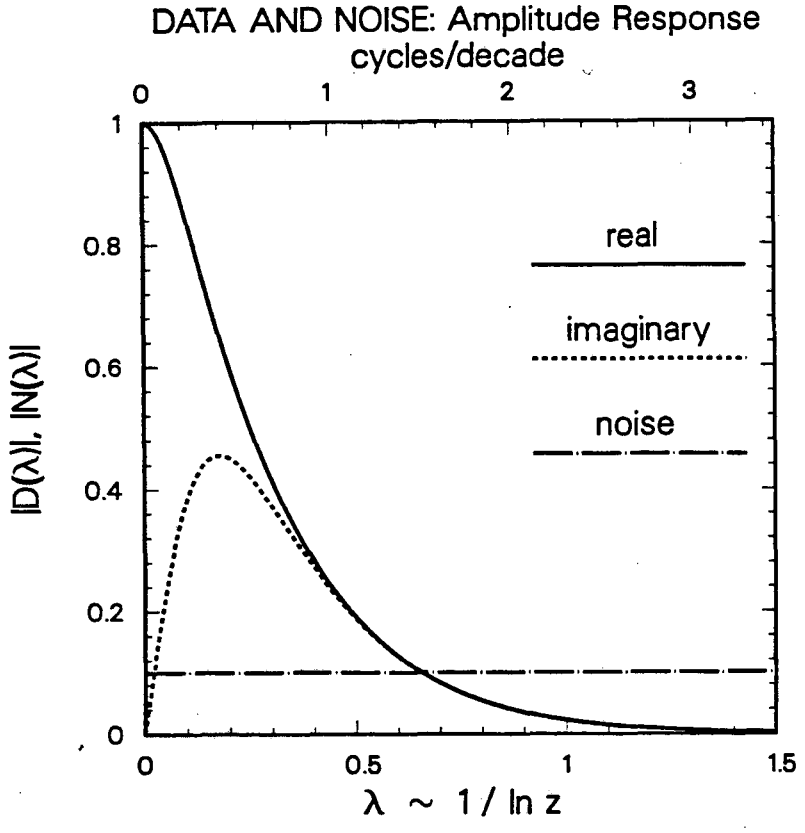

Figure 3-5. The data and the noise in the vertical wavenumber domain: the data are the amplitude response output of the 1-D MT wavelet to a unity-variance "white" model. The noise, on the other hand, is characterized as a 0.01-variance, zero-mean, and Gaussian-distributed white stochastic process.

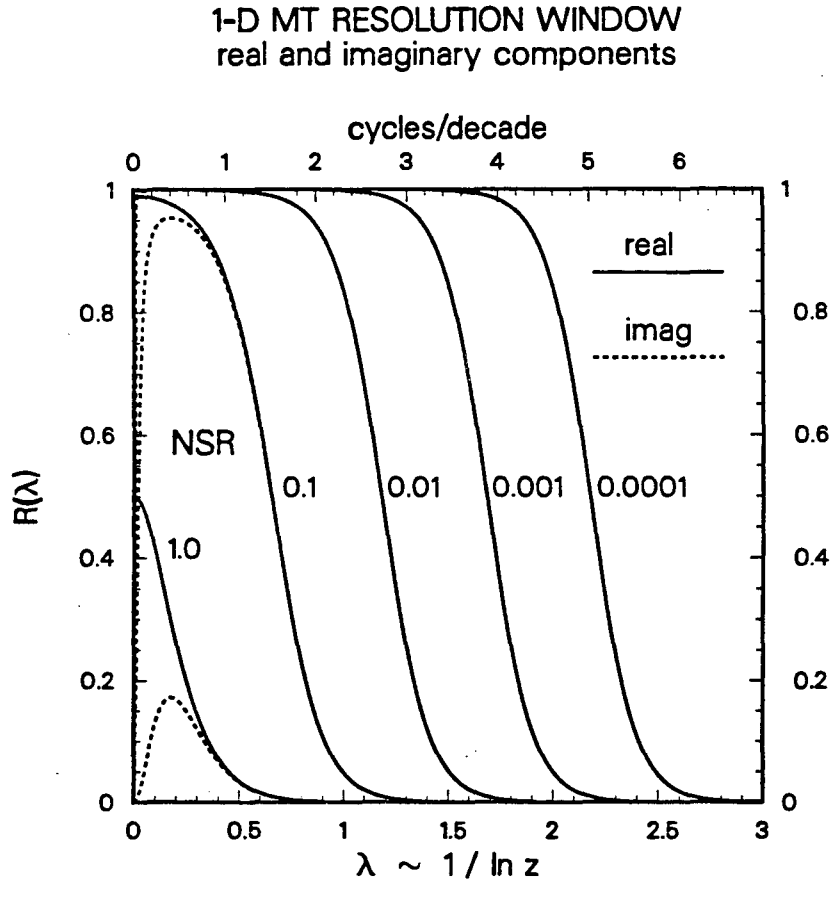

Figure 3-6. Wavenumber resolution windows, R(λ), for the 1-D MT linear inverse problem at various noise-to-signal ratios.

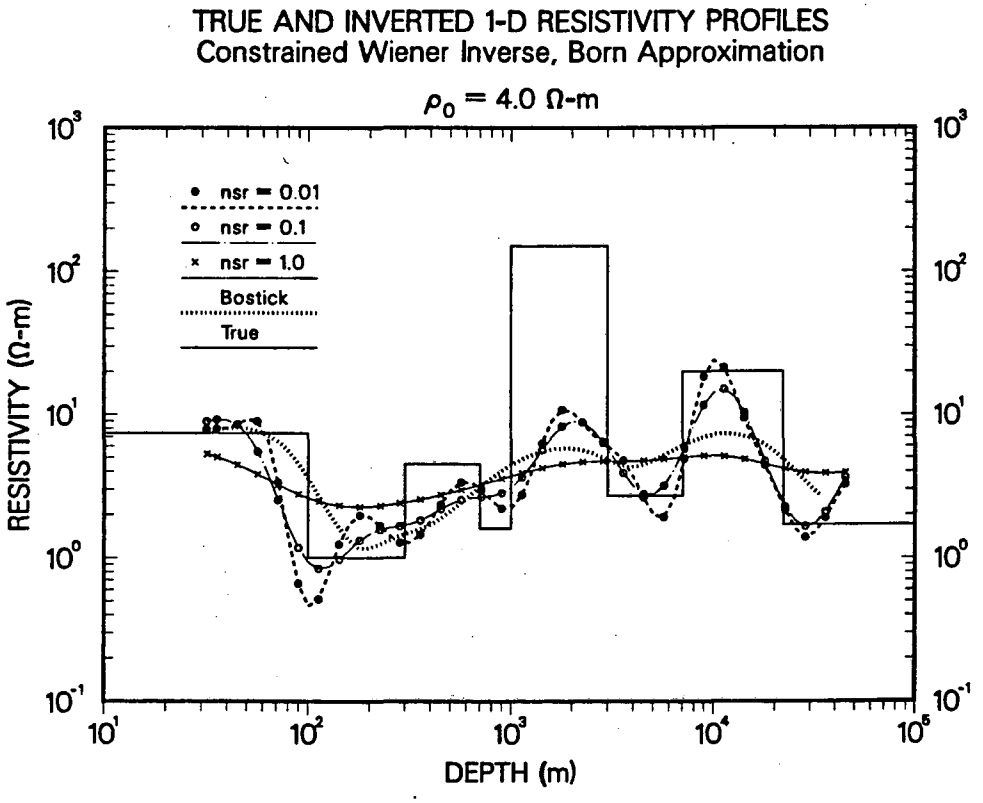

Figure 3-7. Resistivity profiles inverted from the data shown in Figure 3-2 using the constrained Wiener method. The data were input into the inversion with their expression for the first-order Born approximation considering three values of noise-to-signal ratio, i.e., 0.01, 0.1, and 1.

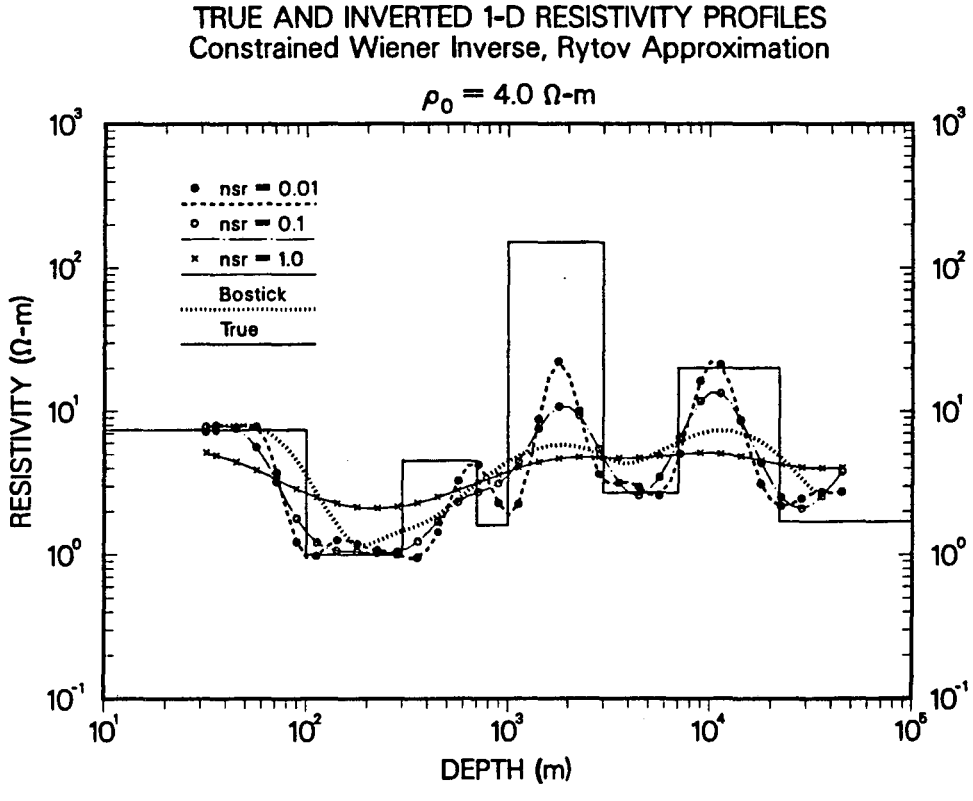

Figure 3-8. Resistivity profiles inverted from the data shown in Figure 3-2 using the constrained Wiener method. The data were input into the inversion with their expression for the first-order Rytov approximation considering three values of noise-to-signal ratio, i.e., 0.01, 0.1, and 1.

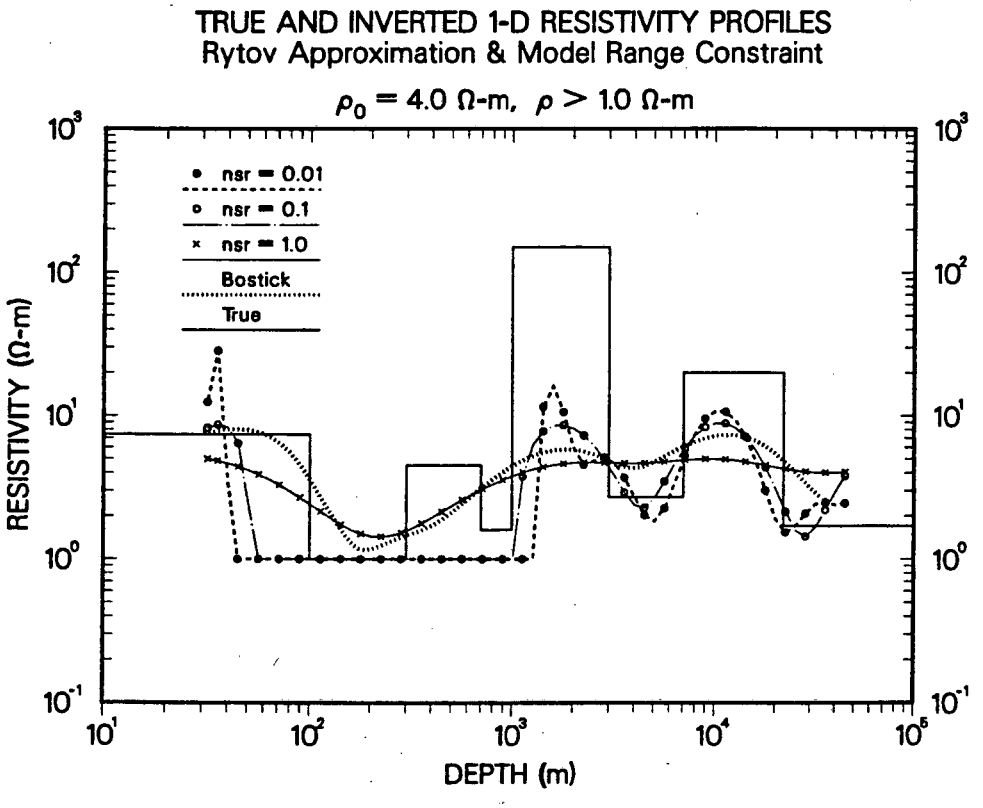

Figure 3-9. Resistivity profiles inverted from the data shown in Figure 3-2 using the constrained Wiener method. The data were input into the inversion with their expression for the first-order Rytov approximation. In addition, the model range constraint that $\rho(z)>1$ Ω•m was enforced in the inversion considering three values of noise-to-signal ratio, i.e., 0.01, 0.1, and 1.

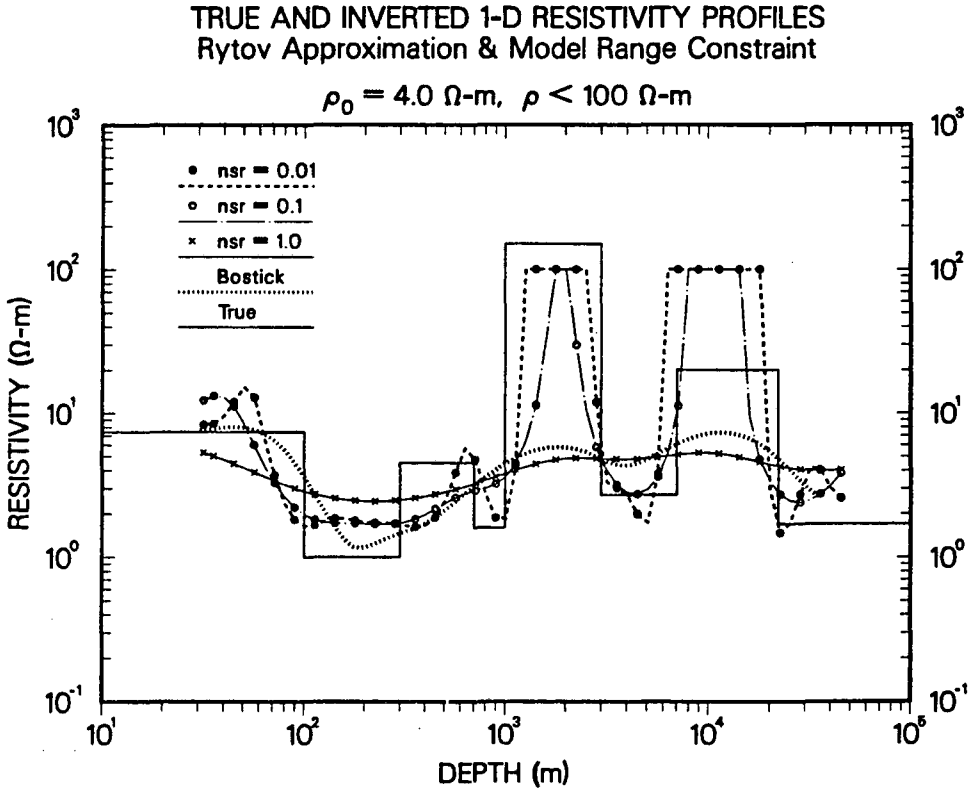

Figure 3-10. Resistivity profiles inverted from the data shown in Figure 3-2 using the constrained Wiener method. The data were input into the inversion with their expression for the first-order Rytov approximation. In addition, the model range constraint that $\rho(z)<100$ Ω•m was enforced in the inversion considering three values of noise-to-signal ratio, i.e., 0.01, 0.1, and 1.

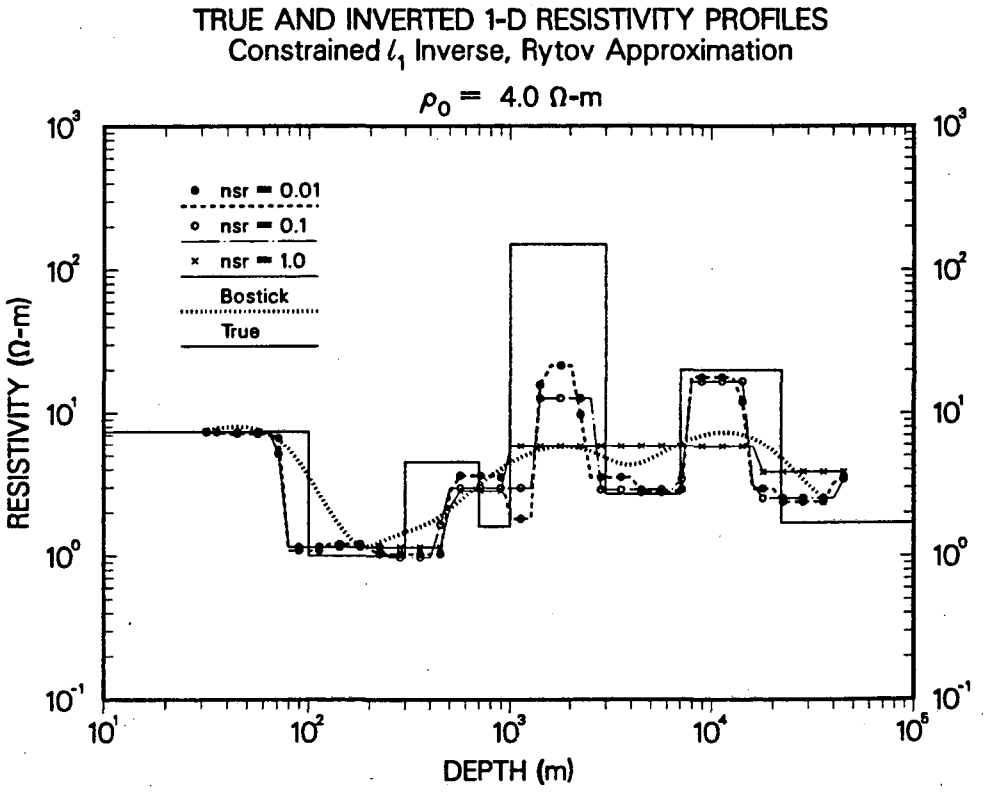

Figure 3-11. Resistivity profiles inverted from the data shown in Figure 3-2 using the constrained ℓ_1-norm method. The data were input into the inversion with their expression for the first-order Rytov approximation considering three values of noise-to-signal ratio (or smoothing parameter), i.e., 0.01, 0.1, and 1.

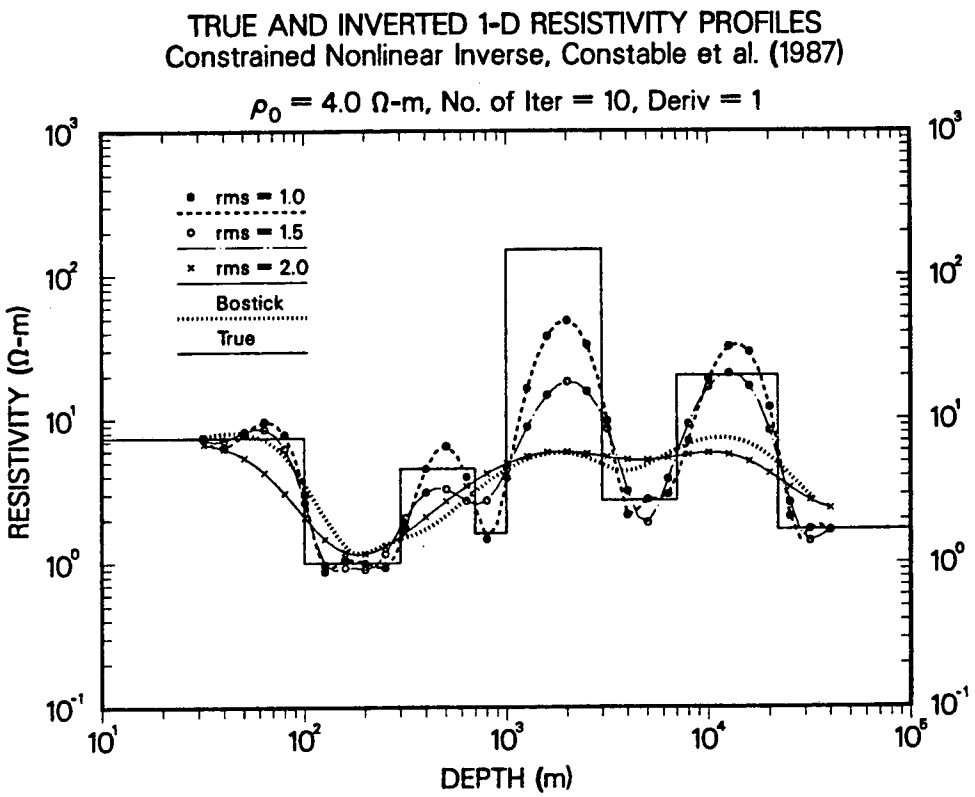

Figure 3-12. Resistivity profiles inverted from the data shown in Figure 3-2 using the constrained nonlinear procedure of Constable et al. (1987). A first-derivative, least-squares model functional was minimized after 10 linear iterations. Results are shown for three different values of the prescribed rms data misfit error, i.e., 1, 1.5, and 2.

CHAPTER IV

BORN INVERSION OF 2-D MT DATA

4.1 Introduction

The last few years have seen a revived interest in the development of procedures for the inversion of 2-D MT data. By and large, this interest has been propelled by the advent of powerful and compact computer resources that can cope in a more or less economic fashion with the severe memory and time demands exacted by practical exploration situations. A second and perhaps more dramatic factor has been the recent introduction of field procedures wherein the sampling distance is short enough to reduce a large degree of the uncertainty caused by otherwise unheeded near-surface scatterers. In consequence, new methods of inversion also face the need to deal with amounts of data never thought of before. Fast simulation procedures are required that can be repeatedly performed in conjunction with nonlinear iterative inversion techniques within reasonable CPU times (see, for instance, Smith and Booker, 1990). Stabilization procedures are also needed that can guarantee the extraction of subsurface geoelectric features within the lateral and vertical resolution bounds imposed by the underlying diffusion equation in the presence of noise. The success of this second important aspect of the 2-D MT inverse problem is largely determined by the general understanding one can have of the frequency- and space-domain properties of surface electric and magnetic fields. This is the main thrust of this chapter: to shed light to the controlling factors that cause the surface MT fields to respond to lateral and vertical variations of subsurface resistivity, and to advantageously use these factors in an attempt to invert 2-D MT data.

The material presented in this chapter in some ways stems from the 1-D linearized inverse formulation described in Chapter III. A 2-D geoelectric model is assumed in which both lateral and vertical variations of resistivity are described as small perturbations about a constant value. This simplifying assumption causes the relationship between a perturbation of subsurface resistivity and the ensuing surface field perturbation to be expressed as the output of a linear system. Accordingly, since the MT excitation of a 2-D earth can be decoupled into two independent modes of propagation, TE (electric field parallel to strike) and TM (magnetic field parallel to strike), the way in which geoelectric features can be

recognized in the subsurface bears a one-to-one relationship with the type of electric or magnetic field quantity used in the inversion. Thus, the analysis presented here is aimed at understanding what specific information of the subsurface resistivity distribution is borne by each field component, and how this information can be used to invert a cross-section of subsurface resistivity under the pragmatic assumption that the measured data are corrupted with noise.

Because of its algebraic simplicity, the linearized 2-D MT forward problem is approached in the lateral wavenumber domain. Further, as with the 1-D linear problem, a logarithmic parameterization of frequency and depth is implemented in the wavenumber-domain equations. Both data and model variables are expressed with their Rytov (logarithmic) expressions for the inversion of electric field data. For the inversion of magnetic field data, given their relatively low dynamic range, a Born (algebraic) data representation is more appropriate. The drawback of inverting surface magnetic field data is that they are not sensitive to the 1-D background, and hence magnetic field measurements must be complemented with electric field data if the former are to be transformed into a cross-section of subsurface resistivity. In the same context, it is shown that all three surface TE electric and magnetic field components are linearly related to each other, implying that from a purely theoretical standpoint, it is unnecessary that all three components be measured at exactly the same points.

A practical limitation imposed by an inversion procedure wherein input data are field values rather than standard MT impedances, is that the former have to be somehow estimated prior to inversion. Thus, a field procedure is introduced here whereby secondary electric and magnetic field variations about a constant background can be estimated from measurements of auxiliary base impedances and magnetic transfer functions. The suggested field procedure requires that the magnetic field be constantly monitored at a fixed station (the magnetic base station) while electric and magnetic field data are being acquired at sampling locations along the survey line.

A central objective pursued with the wavenumber-domain formulation advanced herein is the estimation of the lateral wavenumber content of the lateral subsurface resistivity variations that can be recovered from noisy data. It is shown that, in direct consequence of the underlying diffusion equation, the inferred lateral wavenumber content diminishes with decreasing values of frequency, i.e., with increasing values of the depth of burial. In fact, the wavenumber-domain analysis predicts that, with 1% noise in the data, the maximum wavenumber that can be recovered is approximately equal to the reciprocal of

the Bostick depth of penetration. It is also shown that this wavenumber bound is consistent with the stability criterion that is required for the inversion of TM electric field data.

A final topic presented here concerns the details of a practical inversion procedure. This procedure is implemented directly in the wavenumber domain and consists of repeated 1-D inversion at each wavenumber followed by inverse Fourier transformation of the inverted wavenumber-domain model. It is emphasized that a data prewhitening, or spatial filtering step is a natural way to guarantee stability in the inversion of TM electric field data. In physical terms, this data processing step can be understood as a way to suppress the non-inductive response from the subsurface. Synthetic examples are used to test the proposed inversion procedure mainly with the intent of ascertaining whether the 2-D forward linear equations have any bearing on realistic situations in which the resistivity contrasts are significant. These examples also prove helpful to corroborate the lateral and vertical resolution properties of each surface field component, electric or magnetic, and in general of magnetotellurics. The wavenumber-domain inversion is also tested on tangential field data acquired along a continuous transect over a geothermal target in northern California.

4.2 The 2-D linear forward problem

Assume a right-hand Cartesian coordinate frame with its origin on the surface, its x-axis normal to strike, and its z-axis pointing down into the 2-D earth (Figure 4-1). The surface electric and magnetic field variations can thus be described with the equations

$$E_x(x,\omega) = E_0(\omega) + e_x(x,\omega), \tag{4.1}$$

$$E_y(x,\omega) = E_0(\omega) + e_y(x,\omega), \tag{4.2}$$

$$H_x(x,\omega) = H_0(\omega) + h_x(x,\omega), \text{ and} \tag{4.3}$$

$$H_z(x,\omega) = h_z(x,\omega), \tag{4.4}$$

where E_0 and H_0 are primary electric and magnetic fields, respectively, related to a homogeneous half-space of resistivity ρ_0, and e and h are secondary electric and magnetic field, respectively, that arise with lateral and vertical variations of subsurface resistivity away from the homogeneous half-space. The E_y, H_x, and H_z fields are associated with TE propagation in the 2-D earth, whereas the E_x component is associated with TM propagation. Only the TM magnetic field, H_y, is constant with respect to both frequency and position regardless of the subsurface resistivity distribution (d'Erceville and Kunetz,

1962), and for this reason such component is not expressed here in terms of secondary field variations.

Similarly, the resistivity distribution in the subsurface, ρ, may be written as

$$\rho(x,z) = \rho_0 + \Delta\rho(x,z), \tag{4.5}$$

where the scalar function $\Delta\rho$ describes the lateral and vertical variations of subsurface resistivity away from the homogeneous half-space. A vertical variation of $\Delta\rho$ causes only frequency variations of the e_x and e_y fields. On the other hand, a lateral variation of $\Delta\rho$ causes both frequency and lateral variations of all secondary fields.

In general, the mapping of $\Delta\rho(x,z)$ into frequency and space variations of the secondary fields -the 2-D MT forward problem- is nonlinear and hence highly dependent on the specific characteristics of this function. A model-independent analysis of the physics underlying the mapping of $\Delta\rho(x,z)$ into surface field variations can only be made in light of certain assumptions. The specific assumptions made here about $\Delta\rho(x,z)$ and the secondary surface fields for which this function is responsible are:

$$e(x,\omega) << E_0(\omega), \tag{4.6}$$

$$h(x,\omega) << H_0(\omega), \text{ or/and} \tag{4.7}$$

$$\Delta\rho(x,z) << \rho_0. \tag{4.8}$$

These inequalities cause the relationship between the secondary surface fields and the function $\Delta\rho(x,z)$ to be expressed as suggested by equations (2.20) and (2.21), namely,

$$\frac{e(x,\omega)}{E_0(\omega)} = \int_0^\infty K_e(x,z_0,\omega) * \frac{\Delta\rho(x,z_0)}{\rho_0}\, dz_0, \text{ and} \tag{4.9}$$

$$\frac{h(x,\omega)}{H_0(\omega)} = \int_0^\infty K_h(x,z_0,\omega) * \frac{\Delta\rho(x,z_0)}{\rho_0}\, dz_0, \tag{4.10}$$

where the symbol "*" indicates convolution with respect to x, and the kernel functions K_e and K_h are defined by equations (2.17) and (2.19), respectively. Equations (4.9) and (4.10) are simple linear expressions for the 2-D MT forward problem, such that the underlying physics for the mapping of $\Delta\rho(x,z)$ into secondary surface fields is fully

contained in the mathematical properties of the kernels. Notice that when the inequality (4.8) is satisfied the inequalities (4.6) and (4.7) are also satisfied, but the opposite is not always true because in some cases a large value of $\Delta\rho(x,z)$ may not significantly affect the secondary surface field response. The fact that the integration involved in equations (4.9) and (4.10) is only performed in the vertical direction indicates that the local MT response from the subsurface is largely determined by the characteristics of $\Delta\rho(x,z)$ below the observation point.

Even though explicit formulas for the space-domain kernels K_e and K_h exist, in this chapter the algebraic simplicity of their wavenumber-domain expressions is used with the intent to expose the physics of the 2-D MT forward problem in the clearest possible way.

4.3 The 2-D linear forward problem in the wavenumber domain

Following the convention introduced in Chapter II for the forward and inverse Fourier transforms, the lateral Fourier transform pair is here defined as

$$F(k) = \mathcal{F}\{f(x)\} = \int_{-\infty}^{\infty} f(x)\, e^{+\,i2\pi kx}\, dx, \text{ and}$$

$$f(x) = \mathcal{F}^{-1}\{F(k)\} = \int_{-\infty}^{\infty} F(k)\, e^{-\,i2\pi kx}\, dk,$$

where k is the linear wavenumber in the x direction. Thus, in the lateral wavenumber domain, equations (4.9) and (4.10) can be written in the general form

$$D(k,\omega) = \int_{0}^{\infty} M(k,z_0)\, \Lambda(k,z_0,\omega)\, dz_0, \qquad (4.11)$$

where

$$D(k,\omega) = \begin{cases} \mathcal{F}\{2\frac{e_x}{E_0}(x,\omega)\} & \text{TM mode} \\ \mathcal{F}\{2\frac{e_y}{E_0}(x,\omega)\} & \text{TE mode} \\ \mathcal{F}\{2\frac{h_x}{H_0}(x,\omega)\} & \text{TE mode} \\ \mathcal{F}\{2\frac{h_z}{H_0}(x,\omega)\} & \text{TE mode} \end{cases} \quad \text{are the data,} \qquad (4.12)$$

$$M(k,z) = \mathcal{F}\{\frac{\Delta\rho}{\rho_0}(x,z)\} \quad \text{is the model, and} \qquad (4.13)$$

$$\Lambda(k,z,\omega) = \begin{cases} 2(i\zeta)\, e^{-i(\zeta+\kappa)z} & (e_x \text{ TE mode}) \\ 2(i\zeta - 2\pi|k|)\, e^{-i(\zeta+\kappa)z} & (e_y \text{ TE mode}) \\ i(1+i)\delta\, 2\pi|k|\,(i\zeta - 2\pi|k|)\, e^{-i(\zeta+\kappa)z} & (h_x \text{ TE mode}) \\ (1+i)\delta\, 2\pi k\,(i\zeta - 2\pi|k|)\, e^{-i(\zeta+\kappa)z} & (h_z \text{ TE mode}) \end{cases} \quad \text{is the kernel.} \tag{4.14}$$

The wavenumber-domain kernels in equation (4.14) are the MT transfer functions introduced in section 2.3, and the functions ζ and κ in their expressions are given by

$$\zeta(k,\omega) = -\frac{1+i}{\delta}\sqrt{1 - i\left(\frac{2\pi k\delta}{\sqrt{2}}\right)^2}\,, \text{ and} \tag{4.15}$$

$$\kappa(\omega) = \frac{1-i}{\delta}\,, \tag{4.16}$$

where δ is skin depth, i.e.,

$$\delta(\omega) = \sqrt{\frac{2\rho_0}{\omega\mu}}\,. \tag{4.17}$$

It is also noted that the factor 2 that has been arbitrarily included in the data and kernel definitions above serves for the same unimodularity purposes discussed in Chapter III in connection with the 1-D MT wavelet.

The expressions included in equation (4.14) can be further simplified with the aid of equations (4.15) through (4.17). First, define

$$\gamma(k,\omega) = \frac{\delta}{\sqrt{2}}\,2\pi k\,, \tag{4.18}$$

and introduce the function

$$A(\gamma) = a(\gamma) - ib(\gamma) = \sqrt{1 - i\gamma^2}\,, \tag{4.19}$$

where $a(\gamma)$ and $b(\gamma)$ are real and positive functions. Simple trigonometry shows that

$$a(\gamma) = \sqrt{\frac{\sqrt{1+\gamma^4}+1}{2}}\,, \text{ and} \tag{4.20}$$

$$b(\gamma) = \sqrt{\frac{\sqrt{1+\gamma^4}-1}{2}}\,. \tag{4.21}$$

Substitution of equations (4.18) and (4.19) together with (4.15) into equation (4.14) yields the following simplified form for the 2-D wavenumber domain kernel

$$\Lambda(k,z,\omega) = W(\gamma)\ \frac{2(1+i)}{\delta}\ e^{-[(1+a(\gamma)+b(\gamma)) + i(1+a(\gamma)-b(\gamma))]z/\delta}, \qquad (4.22)$$

where

$$W(\gamma) = \begin{cases} \sqrt{1 - i\gamma^2} & e_x \ \text{TM mode} \\ \sqrt{1 - i\gamma^2} - \sqrt{-i}\ |\gamma| & e_y \ \text{TE mode} \\ [\sqrt{1 - i\gamma^2} - \sqrt{-i}\ |\gamma|]\ (\sqrt{-i}\ |\gamma|) & h_x \ \text{TE mode} \\ [\sqrt{1 - i\gamma^2} - \sqrt{-i}\ |\gamma|]\ (i\sqrt{-i}\ \gamma) & h_z \ \text{TE mode} \end{cases} \qquad (4.23)$$

Finally, substitution of equation (4.23) into equation (4.11) yields

$$D(k,\omega) = W(\gamma) \int_0^{\infty} M(k,z_0)\ 2\frac{(1+i)}{\delta}\ e^{-\{[1+a(\gamma)+b(\gamma)] + i[1+a(\gamma)-b(\gamma)]\}z_0/\delta} dz_0. \qquad (4.24)$$

Notice that the definition of the function $\gamma(k,\omega)$ in equation (4.18) suggests that the wavenumber and frequency dependency of the Λ transfer functions (equation 4.14) is jointly assimilated in the product δk rather than by independent algebraic terms. As shown in a subsequent section, this property of the transfer functions becomes an important consideration in the study of the lateral resolution characteristics of 2-D MT data. Incidentally, the ratio $\delta/\sqrt{2}$ in the definition of γ is equal to the Bostick (1977) depth of penetration in the homogeneous background. In equation (4.24), $W(\gamma)$ is independent of the variable u and this is why it can be taken outside of the integral. This depth-independent function plays the role of a wavenumber prefilter whose properties are set by the particular field quantity in use. A detailed study of both the prefilter and the integrand of equation (4.24) is reserved for the following sections.

4.4 Logarithmic parameterization and pseudo-convolutional response

Using the logarithmic variables v and u introduced in Chapter III, equations (3.19) and (3.20), in place of δ and z_0 in equation (4.24), respectively, gives rise to

$$D(k,v) = W(\gamma)\int_{-\infty}^{+\infty} M(k,u)\, 2(1+i)\, e^{v-u - [(1+a+b) + i(1+a-b)]e^{v-u}} du\ .$$

Further algebraic manipulation leads to the more familiar form

$$D(k,v) = W(\gamma)\int_{-\infty}^{+\infty} M(k,u)\, F(\gamma, v-u) du, \tag{4.25}$$

where

$$F(\gamma,u) = G(\gamma,u) + i\, H(\gamma,u), \tag{4.26}$$

$$G(\gamma,u) = \{\cos[(1+a-b)e^u] + \sin[(1+a-b)e^u]\}\, 2e^{u-(1+a+b)e^u}, \text{ and} \tag{4.27}$$

$$H(\gamma,u) = \{\cos[(1+a-b)e^u] - \sin[(1+a-b)e^u]\}\, 2e^{u-(1+a+b)e^u}. \tag{4.28}$$

The functions G and H above are intimately related to the real and imaginary components of the 1-D kernel, respectively (see equations 3.22 through 3.24). In fact, it is trivial to show that equation (4.25) reduces to equation (3.21) under the substitution k=0 for both TE and TM electric fields. The same substitution yields a null result when specialized for the TE magnetic fields. However, the main difference between the 1-D kernel, f(u), and the 2-D wavenumber domain kernel, F(γ,u), is that the latter is no longer depth-shift invariant. Because of this, the function F(γ,u) is hereafter referred to as the **2-D MT pseudowavelet**. The relationship between the 1-D MT wavelet and the 2-D MT pseudowavelet is explored next.

4.5 1-D factorization of the 2-D MT pseudowavelet

Equations (4.27) and (4.28) can be factored in such way that one of the factors is the 1-D depth-shift invariant kernel, f(u), defined by equation (3.22). To this end, express

$$\cos[(1+a-b)e^u] = \cos(2e^u)\cos[(a-b-1)e^u] - \sin(2e^u)\sin[(a-b-1)e^u],$$

$$\sin[(1+a-b)e^u] = \sin(2e^u)\cos[(a-b-1)e^u] + \cos(2e^u)\sin[(a-b-1)e^u], \text{ and}$$

$$e^{-(1+a+b)e^u} = e^{-2e^u}e^{-(a+b-1)e^u},$$

and substitute into equations (4.27) and (4.28) to get

$$F(\gamma,u) = f(u)\, Q(\gamma,u), \tag{4.29}$$

where

$$Q(\gamma,u) = e^{-[(a+b-1) + j(a-b-1)e^u}. \tag{4.30}$$

The 2-D factor, $Q(\gamma,u)$, defined above is governed by independent expressions of u and v rather than by their difference, v-u, alone as the functions a and b are determined by v but not by u (see equations 4.20 and 4.21); in other words, as opposed to f(u), $Q(\gamma,u)$ is not depth-shift invariant. Notice that $F(\gamma,u)$ and f(u) reduce to equivalent expressions when k=0 (the DC wavenumber), whereas for large values of k, $F(\gamma,u) \rightarrow f(u)\, e^{-\sqrt{2}\gamma e^{u}}$. This indicates that the 2-D factor Q is an exponential damping term whose effect is emphasized by either increasing the wavenumber, k, or by decreasing the frequency, ω. In essence, the exponential damping inflicted by Q upon f in equation (4.29) translates to a progressive loss of sensitivity to lateral features in the subsurface with increasing values of γ.

Figure 4-2 shows both real and imaginary components of the reversed 2-D MT pseudowavelet, $F(\gamma,-u)$, plotted with respect to -u. Four different panels are included in the same figure for an equal number of γ values of 1, 2, 4, and 6. Clearly, in relation to the 1-D MT wavelet plotted in Figure 3-1, the 2-D MT is subject to severe attenuation when the γ variable is larger than 1.

Aside from the lateral resolution characteristics of the 2-D MT pseudowavelet, the lateral resolution of MT data is to some extent dictated by the prefilter $W(\gamma)$ defined in equation (4.23). Ways in which the choice of field data affects the characteristics of the prefilter are studied next.

4.6 The wavenumber prefilter

From equation (4.23) one can show that $W(\gamma)\rightarrow 1$ for $|\gamma|\rightarrow 0$ with the use of TE and TM electric field data. On the other hand, $W(\gamma)\rightarrow 0$ as $|\gamma|\rightarrow 0$ with the use of TE magnetic field data. This DC wavenumber behavior of the magnetic prefilter is consistent with the known fact that the surface magnetic fields are insensitive to the 1-D background medium (see also section 2.6). Also interesting is the behavior of $W(\gamma)$ for large values of γ. For the TE electric field, $|W(\gamma)|$ monotonically decreases as $1/(\sqrt{2}|\gamma|)$ with increasing values of γ, and this causes the prefilter to have the characteristics of a low-pass wavenumber filter. Conversely, the amplitude of the TM prefilter increases as $|\gamma|/\sqrt{2}$ with increasing values of γ, and this causes $W(\gamma)$ to have the characteristics of a high-pass wavenumber amplifier. The high-pass nature of the TM prefilter may significantly emphasize the response of local near-surface variations of resistivity (rich in large wavenumber harmonics) over the response of deeper and usually smoother lateral variations of subsurface resistivity. Such is precisely the action of the electric static component studied in Chapter II. In equation

(4.23), however, the effects of both TM electric static and induction components are combined in a single expression.

Finally, besides their single-zero at $\gamma=0$, both TE magnetic prefilters are all-pass wavenumber filters with a constant amplitude response of 1/2, and hence their effect over the subsurface resistivity distribution is that of a 1/2 flat gain attenuator. Figures 4-3 through 4-5 are amplitude response plots of the TM electric and TE electric and magnetic prefilters, $W(\gamma)$. Notice that because the sole difference between the h_x and h_z prefilters is that the h_z prefilter is asymmetrical about $\gamma=0$, a single amplitude plot suffices to display the characteristics of the TE magnetic prefilters.

Another important property of the TE prefilters, electric and magnetic, is that they are related by simple linear formulas. This can be shown directly by inspection of the expressions included in equation (4.23), from which it can be established that

$$W(\gamma)_{hx} = -\sqrt{-i}\, U(\gamma)\, \gamma\, W(\gamma)_{ey}, \text{ and} \tag{4.31}$$

$$W(\gamma)_{hz} = i\, U(\gamma)\, W(\gamma)_{hx}, \tag{4.32}$$

where

$$U(\gamma) = \begin{cases} -1 & \text{if } \gamma<0 \\ 1 & \text{if } \gamma>0 \end{cases} . \tag{4.33}$$

Because the remaining factors of the 2-D MT forward linear system (equation 4.25) are the same for all field components, the preceding formulas convey a spatial linear dependence among the three TE field components. Equation (4.32), for instance, indicates that the horizontal and vertical magnetic field components are Hilbert transforms of each other in the space domain (Bracewell, 1965). The relationship between the electric and horizontal magnetic field components in equation (4.31), on the other hand, points to the fact that the horizontal magnetic field component can be obtained by high-pass wavenumber filtering of the electric field component, where the filter is a single-pole linear ramp. Conversely, except for its DC wavenumber harmonic, the electric field component can be obtained by low-pass wavenumber filtering of the horizontal magnetic field component. A proof that the linear dependence among TE fields expressed by equations (4.31) and (4.32) remains valid even beyond the domain of the Born approximation solutions is included in Appendix C.

4.7 Vertical harmonic behavior of the 2-D MT pseudowavelet

Both the 2-D MT pseudowavelet and the wavenumber prefilter are responsible for the attenuation of the lateral wavenumber spectrum of the surface electric and magnetic fields. This loss of lateral response is primarily controlled by the γ variable. Even though the properties of the prefilter are set by the particular type of field component, a field-independent study of lateral resolution properties of 2-D MT data can be performed by examination of the 2-D pseudowavelet. Following the vertical wavenumber analysis presented in section 3.8, the objective here is to derive a vertical wavenumber expression of the 2-D MT pseudowavelet, $F(\gamma,u)$, and to explore how this expression becomes affected by specific values of the γ variable. Strictly speaking, the vertical wavenumber study carried out in connection with the 1-D linear inverse problem was made possible by the depth-shift invariance of the 1-D MT wavelet. As shown earlier, the 2-D MT pseudowavelet does not share the same property and therefore the vertical wavenumber analysis is not valid in a formal sense. To circumvent this difficulty, the approximation is made here that the variable γ is simply a constant that conditions the characteristics of the otherwise depth-shift invariant wavelet. Even under this approximation, the ensuing vertical wavenumber expression sheds considerable insight to the vertical resolution characteristics of 2-D MT data.

The Fourier transform pair for the u (-log(depth)) $\rightarrow \lambda$ (vertical wavenumber) transformation is given by equations (3.27) and (3.28). Using those equations, define the vertical wavenumber-domain functions $\tilde{G}(\gamma,\lambda)$, $\tilde{H}(\gamma,\lambda)$, and $\tilde{F}(\gamma,\lambda)$ as

$$\begin{aligned}
&\tilde{G}(\gamma,\lambda) = \mathcal{F}\{G(\gamma,u)\},\\
&\tilde{H}(\gamma,\lambda) = \mathcal{F}\{H(\gamma,u)\}, \text{ and}\\
&\tilde{F}(\gamma,\lambda) = \tilde{G}(\gamma,\lambda) + i\,\tilde{H}(\gamma,\lambda),
\end{aligned} \tag{4.34}$$

where the functions G and H are the real and imaginary components of the 2-D MT pseudowavelet, respectively.

To obtain the vertical Fourier transform of the 2-D MT pseudowavelet, $F(\gamma,u)$, first substitute equation (4.27) into equation (3.27) together with the change of variable $\varphi = (1+a-b)e^{u}$. The result is

$$\tilde{G}(\gamma,\lambda) = \frac{2}{(1+a-b)^{1+i2\pi\lambda}} \int_0^{\infty} (\cos\varphi + \sin\varphi)\, \varphi^{i\,2\pi\lambda}\, e^{-\varphi(1+a+b)/(1+a-b)}\, d\varphi\,.$$

Making use of the same algebraic steps detailed in section 3.8 as well as of the integral expression for the complex gamma function, Γ, yields the explicit formula

$$\widetilde{G}(\gamma,\lambda) = \Gamma(1+i2\pi\lambda)\left\{\frac{1-i}{[(1+a+b)-i\,(1+a-b)]^{1+i2\pi\lambda}} + \frac{1+i}{[(1+a+b)+i\,(1+a-b)]^{1+i2\pi\lambda}}\right\}. \quad (4.35)$$

Similarly, the vertical Fourier transform, $\widetilde{H}(\gamma,\lambda)$, of the imaginary part of the 2-D MT pseudowavelet takes on the form

$$\widetilde{H}(\gamma,\lambda) = \Gamma(1+i2\pi\lambda)\left\{\frac{1+i}{[(1+a+b)-i\,(1+a-b)]^{1+i2\pi\lambda}} + \frac{1-i}{[(1+a+b)+i\,(1+a-b)]^{1+i2\pi\lambda}}\right\}. \quad (4.36)$$

In the DC wavenumber limit, $\gamma=0$, whereupon $a=1$, and $b=0$. Substitution of these values for a and b into equations (4.35) and (4.36) leads to vertical wavenumber-domain expressions that are identical to those of the 1-D MT wavelet (equations 3.30 and 3.31, respectively). On the other hand, large values of γ cause the a and b functions to be both equal to $\gamma/\sqrt{2}$, and this dictates that the $\widetilde{G}$ and $\widetilde{H}$ functions monotonically decrease in amplitude as $1/(\sqrt{2}|\gamma|)$ for large γ values. Figure 4-6 shows amplitude response curves of both functions $\widetilde{G}$ and $\widetilde{H}$ plotted against the linear vertical wavenumber, λ, for γ values of 1, 2, 4, and 6. The four panels displayed in this figure are analogous to the one shown in Figure 3-4 in connection with the 1-D MT wavelet. An interesting remark concerning the characteristics of the function $\widetilde{H}$ is that, contrary to what occurs with the 1-D MT wavelet, its $\lambda=0$ wavenumber harmonic (the vertical DC response) does not vanish so long γ is not zero.

Clearly, the vertical low-pass filter nature of the 2-D MT pseudowavelet severely constrains the recovery of lateral detail in the subsurface resistivity distribution. This is felt most dramatically in situations where the measured data are corrupted with noise. A way to ascertain the largest lateral wavenumber that can be recovered of the subsurface resistivity distribution from noisy data is outlined below.

4.8 Vertical resolution of lateral structure in the presence of noise

Following the Wiener deconvolution procedure introduced in section 3.9, under the assumption of a "white" model, M(k,u), both with respect to u (-log(depth)) and x (lateral distance), the lateral resolution properties of the pseudowavelet can be described with the aid of the spectral resolution window relating the true model with the estimated model in the

presence of noise. Accordingly, let $\widetilde{M}(k,\lambda)$ and $\widehat{\widetilde{M}}(k,\lambda)$ denote the zero-mean true and estimated model solutions in the vertical wavenumber domain, respectively, and let

$$NSR(k,\lambda) = \frac{|N(k,\lambda)|}{|M(k,\lambda)|} \tag{4.37}$$

describe the noise-to-signal ratio inherent to the measured data. The function $\widetilde{N}(k,\lambda)$ in this last expression embodies the spectral characteristics of the zero-mean noise process that additively contaminates the data. In the present analysis, $\widetilde{N}(k,\lambda)$ is further assumed to be uncorrelated with the model. Disregarding the effect of the prefilter, $W(\gamma)$, in equation (4.25), the ℓ_2-norm, or Wiener model estimate, $\widehat{\widetilde{M}}(k,\lambda)$, can be written in terms of the true model, $\widetilde{M}(k,\lambda)$, with the formula

$$\widehat{\widetilde{M}}(k,\lambda) = \widetilde{R}(\gamma,\lambda) \bullet \widetilde{M}(k,\lambda), \tag{4.38}$$

where

$$\widetilde{R}(\gamma,\lambda) = \frac{|\widetilde{F}(\gamma,\lambda)|^2}{|\widetilde{F}(\gamma,\lambda)|^2 + NSR^2(k,\lambda)} \tag{4.39}$$

is the resolution window. As emphasized in section 3.9, the resolution window is a zero-phase low-pass filter that describes the distortion of vertical model harmonics in the presence of noise; the larger the value of $NSR(k,\lambda)$ the lower the cutoff wavenumber of $\widetilde{R}(\gamma,\lambda)$.

The simplest way that exists to quantify the lateral harmonic distortion incurred on in the estimation of $\widetilde{M}(k,\lambda)$ from noisy measurements is to consider both the model and the noise to be realizations of a "white" Gaussian stochastic process, in which case the noise-to-signal ratio defined in equation (4.37) takes on the constant value of

$$NSR(k,\lambda) = \frac{n}{s},$$

where n and s are the standard deviations of the noise and the model, respectively. Plots of the resolution window, $\widetilde{R}(\gamma,\lambda)$ with respect to λ are shown in Figure 4-7 for different combinations of noise-to-signal ratio and γ values. In each panel of this figure a noise-to-signal ratio is fixed while values of γ are varied. The vertical wavenumber values, λ, are described in cycles/decade so that the resolution curves are in effect comparable to those shown in Figure 3-6 for the 1-D MT wavelet. Clearly, the largest vertical

wavenumber harmonic that can be recovered from the model is highly dependent on the assumed noise-to-signal ratio. For instance, at a noise-to signal ratio of 0.01 the maximum value of γ that guarantees no vertical harmonic distortion in the inferred model is between 6 and 8 (at γ=8, even the λ=0 harmonic is slightly distorted). For the same value of noise-to-signal ratio, however, a γ value of 1 allows the recovery of λ harmonics of at most 1.5 cycles/decade. Larger values of noise-to-signal ratio cause more significant distortion effects on the λ harmonics.

In practice, the largest lateral wavenumber, k, that can be inferred from the subsurface resistivity distribution is determined by the distance between contiguous field sampling locations. This largest k value is the Nyquist wavenumber, given by

$$k_N = \frac{1}{2\,\Delta x},$$

where Δx is the sampling distance. In conventional MT profiling surveys, Δx varies anywhere from 0.5 to 10 km, so that k_N varies from 1 to 0.05 km^{-1}. With continuous electric field sampling techniques such as EMAP, the Nyquist wavenumber is inversely proportional to twice the length of the dipole. In fact, for this type of surveys the maximum lateral wavenumber is also conditioned by the length of the dipole (see section 5.2), but since the dipole length is at most equal to the sampling distance, the Nyquist wavenumber will still remain the largest wavenumber that can be accounted for. Below such an upper bound, Figure 4-7 shows that the largest wavenumber harmonic that can have a measurable effect is dictated by both the noise-to signal ratio inherent to the data and the particular γ value. Given that γ is directly proportional to the Bostick depth of penetration, it follows that the largest lateral wavenumber harmonic of the subsurface resistivity distribution that can have a recognizable effect on the frequency-domain data (reflected on the λ variable) is inversely proportional to the depth of penetration.

In summary, the largest lateral wavenumber, k_{max}, that can be recovered from the subsurface resistivity distribution at the frequency ω is given by the expression

$$k_{max} = \min[k_N, k(\gamma_{max})], \tag{4.40}$$

where

$$k(\gamma_{max}) = \frac{\gamma_{max}}{2\pi\, z_B}, \text{ and} \tag{4.41}$$

z_B is the Bostick (1977) depth of penetration in the homogeneous background. At a noise-to-signal ratio of 0.01, Figure 4-4 shows that $\gamma_{max} \approx 6.0$, in which case $k_{max} \approx 1/z_B$.

To understand the practical meaning of this result, consider the 2-D synthetic model whose cross-section perpendicular to strike is shown in Figure 4-8. The model consists of a single 5 Ω•m rectangular block with lateral and vertical dimensions of 2 km x 600 m, respectively, and which is buried at a depth of 400 m. A homogeneous 80 Ω•m half-space is the background medium. Figure 4-9 is a wavenumber-domain amplitude response plot of TM secondary electric field response across strike. The response has been normalized with respect to the primary electric field, $E_0(\omega)$, and multiplied by 2 as required by equation (4.12). Simulated field values are shown at 10 Hz, which is the point in the frequency spectrum where the buried block develops a maximum inductive response. Also, and merely for comparison, a normalized wavenumber-domain plot of the 2 km-wide block is shown with a dashed line in the same figure. Inspection of the data amplitude response curve in Figure 4-5 shows that the largest lateral wavenumber for which there would be appreciable surface response at a noise-to-signal ratio of 1% is approximately 2.3 km^{-1}. On the other hand, at 10 Hz, the Bostick depth of penetration computed from the actual apparent resistivity data is approximately equal to 400 m. Assuming that the value $\gamma_{max} \approx 6$ is adequate for the hypothetical 1% noise-to-signal ratio (which is probably slightly optimistic given the unavoidable numerical errors incurred on the simulation of the electric and magnetic fields), equation (4.41) yields a k_{max} value equal to 2.5 km^{-1}, which is in reasonable agreement with the upper bound determined by visual inspection of the amplitude response curve. Similar wavenumber-domain plots for the remaining TE electric and magnetic fields are shown in Figures 4-10 through 4-12. Notice that these plots indeed evidence the fact that the TE electric wavenumber response has a shorter operating band than the TM response, and that in effect the TE magnetic field response has a null at k=0

When the effect of the wavenumber prefilter, $W(\gamma)$, is included in equation (4.39), the actual value of k_{max} below that predicted by equation (4.41) is determined by the cutoff characteristics of $W(\gamma)$. For instance, knowing that $W(\gamma)$ is a low-pass filter for the TE electric field and a high-pass filter for the TM electric field, one can intuitively understand why the lateral resolution characteristics of TM electric field data are superior to those of TE electric field data. The following sections are devoted to integrating the lateral wavenumber characteristics of both the prefilter and the 2-D MT pseudowavelet into a practical procedure to invert surface MT data.

4.9 Prewhitening of the TM electric field data

Assuming that $W(\gamma)\neq 0$, equation (4.25) can be modified to read as

$$D(k,v) \bullet \frac{1}{W(\gamma)} = \int_{-\infty}^{+\infty} M(k,u)\, F(\gamma, v-u)du \; . \tag{4.42}$$

The multiplication involved in the left-hand side member of this new expression can be thought of as a data "prewhitening" step. The prewhitening operator, $1/W(\gamma)$, is a wavenumber filter whose cutoff wavenumber is controlled by both the background resistivity, ρ_0, and the frequency, ω. Notice that when TE electric fields are the data the prefilter is a low-pass wavenumber filter, and hence the data prewhitening step becomes an inherently unstable process. On the other hand, owing to the fact that the TE magnetic prefilter has a null at k=0, prewhitening of magnetic field data will become unstable in the neighborhood of such wavenumber.

The only case for which the multiplication on the left-hand side of equation (4.42) is rendered stable for all wavenumber values is when the data are TM electric fields. This is so because for such data $W(\gamma)$ is a high-pass filter. To clarify this important point, consider the amplitude response curve of the inverse TM prefilter, $1/W(\gamma)$, shown in Figure 4-13. The curve in this figure illustrates an essential low-pass wavenumber behavior. In fact, it can be shown that the cutoff wavenumber of the $1/W(\gamma)$ filter decreases as $1/(\sqrt{2}|\gamma|)$ for increasing values of γ. Purely in terms of frequency, the cutoff wavenumber of $1/W(\gamma)$ decreases as $\sqrt{\omega}$ for decreasing values of ω. It is also emphasized that because the 2-D MT pseudowavelet, $F(\gamma,u)$, exhibits exactly the same $1/(\sqrt{2}|\gamma|)$ decay for large values of γ, the prewhitening of TM electric field data as indicated by equation (4.42), will not unbalance the lateral resolution characteristics on either side of the linear system equation.

The preceding analysis reveals that prewhitening of TM electric field data is a desirable processing step to help stabilize the inversion of equation (4.25). For the inversion of TE electric and magnetic field data, however, the stabilization seems more natural if the prefilter, $W(\gamma)$, is absorbed in the low-pass wavenumber properties of the 2-D MT pseudowavelet, $F(\gamma,u)$. Practical details involved in the subsequent inversion of prewhitened and non-prewhitened data are discussed below.

4.10 Model estimation in practice

Attention is now shifted to the problem of how lateral and frequency variations in the data can be inverted into a cross-section of subsurface resistivity with the linearized inverse. The procedure studied here is based on the discretization of the linear integral equation (4.25) for the TE electric and magnetic fields and of equation (4.42) for the TM electric field.

In consideration to the prewhitening step described in the previous section, one can rewrite equation (4.25) as

$$\hat{D}(k,v) = \int_{-\infty}^{+\infty} M(k,u)\, K(\gamma, v-u)\, du\,, \tag{4.43}$$

where

$$\hat{D}(k,v) = \frac{D(k,v)}{W(\gamma)}\,, \text{ and}$$

$$K(\gamma, v-u) = F(\gamma, v-u)$$

for TM electric field data, and

$$\hat{D}(k,v) = D(k,v), \text{ and}$$

$$K(\gamma, v-u) = W(\gamma)\, F(\gamma, v-u)$$

for TE electric and magnetic field data. In general, the wavenumber-domain model, M(k,u), is complex-valued and can thus be expressed as

$$M(k,u) = M_R(k,u) + i\, M_I(k,u). \tag{4.44}$$

Likewise, the kernel $K(\gamma, v-u)$ in the integrand of equation (4.43) can be written as

$$K(\gamma, v-u) = K_R(\gamma, v-u) + i\, K_I(\gamma, v-u). \tag{4.45}$$

The product $M(k,u)K(\gamma, v-u)$ in the integrand of equation (4.43) can then be expressed in the expanded form

$$MK = K_R\,[M_R + i\, M_I] + i\, K_I\,[M_R + i\, M_I].$$

In view of the fact that the real and imaginary components of $F(\gamma,v-u)$ are linearly related[1], and so are the real and imaginary components of $W(\gamma)$, the imaginary part of the product MK above provides only redundant information to that furnished by its real complement. In addition, when $\gamma=0$, the function $K_I(\gamma,v-u)$ is identical to zero for all field components, in which case only the function $K_R(\gamma,v-u)$ can be used to estimate the DC wavenumber harmonic of M(k,u). Notice also that because the complex-valued kernel $K(\gamma,v-u)$ is symmetric with respect to γ, when only the real part of the space-domain data, e/E_0, or h/H_0, is used for inversion (see equations 4.9 and 4.10), the imaginary kernel, $K_I(\gamma,v-u)$, becomes unnecessary. The only case for which $K(\gamma,v-u)$ is asymmetric with respect to γ is when the linear equation (4.43) is specialized for the vertical magnetic field. Therefore, if only the real part of the space-domain h_z/H_0 data is used for inversion, use of the real kernel, $K_R(\gamma,v-u)$ becomes unnecessary.

With the use of only the real part of the kernel $K(\gamma,v-u)$, equation (4.47) can be separated into two independent expressions involving the real and imaginary parts of the model, namely,

$$\text{Real}[\widehat{D}(k,v)] = \int_{-\infty}^{+\infty} M_R(k,u)\, K_R(\gamma,v-u)\, du \text{ , and} \tag{4.46}$$

$$\text{Imag}[\widehat{D}(k,v)] = \int_{-\infty}^{+\infty} M_I(k,u)\, K_R(\gamma,v-u)\, du. \tag{4.47}$$

To solve for M_R and M_I from the discretized versions of equations (4.46) and (4.47), respectively, one can resort, for instance, to any of the ℓ_2-norm estimation procedures discussed in section 3.10. The advantage here is that the autocorrelation matrix of the kernel $K_R(\gamma,v-u)$ is the same for both equations. This is indeed a useful property considering that, as was found with the simulation studies of Chapter III, most of the computer time involved in the estimation of the model is spent in assembling such a matrix. The disadvantage, though, is that contrary to what occurred with the 1-D MT wavelet, the 2-D MT pseudowavelet is not depth-shift invariant and hence the new autocorrelation matrix is no longer Toeplitz. In consequence, the inversion of the autocorrelation matrix (plus the prewhitening diagonal matrix) for the discretized versions of equations (4.46) and

---

[1] A proof of this linear dependence can be done following the same analytical steps used in Chapter III to prove the linear dependence between the real and imaginary components of the 1-D MT wavelet (section 3.7)

(4.47) cannot be carried out with simple Levinson recursions as it was done in Chapter III (Robinson and Treitel, 1980).

The specific procedure chosen here to estimate both M_R and M_I from equations (4.46) and (4.47), respectively, is the constrained Wiener inverse described in Chapter III (equations 3.44 and 3.42). With single inversions performed at each wavenumber between 0 and the Nyquist wavenumber, k_N, the inverted real and imaginary model harmonics can then be inverse Fourier transformed to recover the space-domain version of the model, m(x,z). In addition, the inversion of magnetic field data should rely on an estimate of the DC wavenumber harmonic of the model. The latter can be derived from electric field data.

It was shown in Chapter III that the Rytov representation for both model and data variables is a good combination to use in the inversion of electric field data. The reason for this is that the electric field response often exhibits large oscillations (laterally and also with respect to frequency) about and average value. For the case of the magnetic field response, however, the developments included in Chapter II show that the magnetic field ratio H/H_0 exhibits only minor lateral oscillations in the presence of lateral variations of subsurface resistivity. Specifically, the horizontal magnetic field ratio, H_x/H_0, laterally oscillates about 1, whereas the vertical magnetic field ratio, H_z/H_0, oscillates about 0. These properties intuitively suggest that the Born representation of the data is better suited than the Rytov representation in dealing with magnetic fields. The Rytov representation for the model is still the most appropriate choice in dealing with either electric or magnetic field data. Examples that illustrate the performance of the linearized 2-D inverse are presented in a subsequent section. For the moment, attention is focused on two important preliminary details: (1) the estimation of secondary-to-primary field ratios from impedances and magnetic transfer functions, and (2) the estimation of a background resistivity value.

4.11 Field procedure for the estimation of secondary electric and magnetic field variations

The linear model estimation procedures discussed thus far rely on specific values for the secondary-to-primary field ratios. In contrast, owing to the fact that MT signals do not behave as stationary processes whereas wave impedances do, conventional MT sampling procedures are based on the measurement of wave impedances instead of actual field quantities. The problem of calculating secondary electric and magnetic fields solely arising from MT backscattering from the earth has been contemplated before. In particular, Berdichevsky and Zhdanov (1984) studied a separation of the external (source) and internal

(backscattering from the earth) parts of the EM field based on the Stratton-Chu integration formulas (these formulas are similar to those of the Green's theorem on a closed surface; see for instance, Harrington, 1961). Their separation procedure, however, can be used only when conventional MT impedances are densely sampled over the surface of the earth.

A field procedure that can be used to overcome the need for densely sampled MT impedances in the estimation of secondary electric and magnetic field variations away from those of a homogeneous 1-D background is depicted in Figure 4-14. As shown there, a magnetic base station is deployed at a locality within the survey area which is kept fixed at times when electric and magnetic field data are acquired at different points along the survey line. Base impedances are calculated as the ratio between the total electric field measured along the survey line and the magnetic field measured at the base station. To show how the base impedances can yield estimates of the secondary-to-primary field ratios, assume a coordinate frame as described in Figure 4-1, and let $H_x^B(\omega)$ and $H_y^B(\omega)$ denote the x and y magnetic field components, respectively, measured at the base station. Likewise, let $E_x(\omega)$ and $E_y(\omega)$ designate the TM and TE electric fields, respectively, measured at a given point along the line the survey line, and for the sake of simplicity assume that the latter is laid out normal to strike. Thus, the TM and TE base impedances are given by the formulas

$$\hat{Z}_{TM}(\omega) = \frac{E_x(\omega)}{H_y^B(\omega)}, \text{ and} \tag{4.48}$$

$$\hat{Z}_{TE}(\omega) = -\frac{E_y(\omega)}{H_x^B(\omega)}, \tag{4.49}$$

respectively, with the x-dependency of all quantities tacitly implied. Similarly, horizontal and vertical magnetic transfer functions relating the TE magnetic fields measured along the line of measurements with the $H_x^B(\omega)$ field measured at the base station are given by the formulas

$$T_x(\omega) = \frac{H_x(\omega)}{H_x^B(\omega)}, \text{ and} \tag{4.50}$$

$$T_z(\omega) = \frac{H_z(\omega)}{H_x^B(\omega)}, \tag{4.51}$$

respectively.

For the TM mode, the H_y field is spatially constant, and $H_y^B(\omega)$ is equal to the primary magnetic field, $H_0(\omega)$. For the TE mode, however, the H_y field is not spatially constant, but since its DC wavenumber is null, the primary magnetic field in the same direction can be estimated from the spatial average of the magnetic transfer functions T_x along the line of measurements (see section 2.6).

From equations (4.1) and (4.2) it then follows that

$$\frac{e_x(\omega)}{E_0(\omega)} = \frac{\hat{Z}_{TM}(\omega)}{Z_0(\omega)} - 1, \text{ and} \tag{4.52}$$

$$\frac{e_y(\omega)}{E_0(\omega)} = \frac{\hat{Z}_{TE}(\omega)}{Z_0(\omega)\,\overline{T}_x(\omega)} - 1, \tag{4.53}$$

where

$$Z_0(\omega) = \sqrt{i\omega\mu\rho_0},$$

and $\overline{T}_x(\omega)$ is the spatial average of $T_x(\omega)$ along the survey line. Therefore, with knowledge of the background resistivity, ρ_0, equations (4.52) and (4.53) can be used to estimate the secondary-to-primary electric field ratios from the measured TM and TE base impedances, $\hat{Z}_{TM}(\omega)$, and $\hat{Z}_{TE}(\omega)$, respectively, and the magnetic transfer functions, $T_x(\omega)$. In like fashion, the secondary-to-primary TE magnetic field ratios can be calculated from the expressions

$$\frac{h_x(\omega)}{H_0(\omega)} = \frac{T_x(\omega)}{\overline{T}_x(\omega)} - 1, \text{ and} \tag{4.54}$$

$$\frac{h_z(\omega)}{H_0(\omega)} = \frac{T_z(\omega)}{\overline{T}_x(\omega)}, \tag{4.55}$$

which, incidentally, do not imply knowledge of the background resistivity. A procedure that can be used for the estimation of the background resistivity, ρ_0, directly from the measured electric field data is presented next.

4.12 Estimation of the background resistivity

For the 2-D linearized inversion, accurate knowledge of the background resistivity is important not only to reduce shifting errors in the $\log_{10}$ depth scale but also to adjust the

cutoff wavenumber characteristics of the prefilter. The procedure described here for the estimation of the background resistivity stems from the same principles used with the linearized 1-D inversion. Assuming that the model can be described as the realization of an ergodic stochastic process in both x and z directions, the background resistivity can be thought of as the expected value of this stochastic process. In consequence, because of the linear relationship between the model and the data in equations (4.9) and (4.10), the average value of the data should reflect the expected model value. However, because the spatial average of magnetic field data tends to zero, the background resistivity can only be estimated from electric field data.

To express the electric field data in a form that conveys information about the lateral and vertical variations of subsurface resistivity, consider the modified impedance, $\tilde{Z}$, defined as

$$\tilde{Z}(x,\omega) = \frac{E(x,\omega)}{H_0(\omega)},$$

where $H_0(\omega)$ is the primary magnetic field associated with the homogeneous half-space whose resistivity is sought after. For the TM mode the modified impedance, $\tilde{Z}$, is identical to the TM impedance, whereas for the TE mode, it is given by

$$\tilde{Z}(x,\omega) = \frac{\hat{Z}_{TE}(x,\omega)}{\overline{T}_x(\omega)},$$

where $\hat{Z}_{TE}$ and $\overline{T}_x$ are the base impedance and average magnetic transfer function, respectively, calculated by means of the field procedure described in section 4.11. An apparent resistivity function, ρ_A, can then be defined from the modified impedances as

$$\rho_A(x,\omega) = \frac{1}{\omega\mu}|\tilde{Z}(x,\omega)|^2$$

(Cagniard, 1953). The resistivity of the homogeneous background can then be estimated from

$$\rho_0 \approx e^{\overline{\ln\{\rho_A[x,\ln(\omega)]\}}}, \qquad (4.56)$$

where the bar over the logarithmic apparent resistivity is used to denote expected value with respect to both x and log(ω). This equation is completely analogous to that derived for the 1-D linearized forward problem, except that the new expected value considers an addition lateral average of the data. The sensitivity of the depth mapping functional to a change in

the estimated background resistivity has been studied in section 3.11. For the 2-D linearized forward problem, a change in the estimated background resistivity will also "untune" the cutoff wavenumber characteristics of the prefilter. A large value of ρ_0 will cause excessive lateral smoothing by the prefilter, whereas a small value of ρ_0 will be responsible for insufficient prewhitening which in turn can be the source of vertical conductive leakage in the inverted resistivity section.

4.13 Synthetic examples of inversion

In summary, the linearized 2-D MT inverse problem can be approached according to the following steps:

(1) Estimate the background resistivity (see section 4.12),
(2) Estimate the secondary-to-primary field ratios to be inverted (see section 4.11); use Rytov and Born representations for electric and magnetic field ratios, respectively (see section 3.3),
(3) Fourier transform the estimated field ratios with respect to lateral location, frequency by frequency (one may opt to Fourier transform only the real part of the estimated field ratios),
(4) If inverting TM electric field data, prewhiten the wavenumber domain ratios obtained with step 3 (see section 4.9),
(5) Perform pseudo 1-D inverses at each wavenumber for both real and imaginary components of the wavenumber-domain model (see section 4.10); the model should be expressed with its Rytov representation formula (see section 3.3),
(6) If inverting magnetic field data, estimate the DC wavenumber harmonic of the model from electric field data, and
(7) Inverse Fourier transform the estimated real and imaginary wavenumber components of the model. The result is an estimate of the cross-section of subsurface resistivity.

The subsections below contain a suite of synthetic examples that attest to both advantages and shortcomings of the linearized 2-D procedure itemized in the steps above. It is pointed out that the intent of these exercises is simply to ascertain whether the lateral and vertical resolution properties studied in the previous sections are valid in situations where the assumptions underlying the Born approximation are violated. The synthetic data were simulated with the finite-element code of Wannamaker et al. (1987), and the frequency range was from 0.001 to 1000 Hz, including 10 frequency samples per decade. In all field

simulations, the standard station separation of 100 m was assumed, and this same distance was used to replicate the dipole responses of TM electric field data. A radix-8 fast Fourier transform algorithm (Bergland and Dolan, 1979) was used to carry out the forward and inverse Fourier transforms involved in steps 3 and 7 above. Finally, the pseudo 1-D inverses of step 5 were solved with the constrained Wiener inverse procedure introduced in section 3.10, which was implemented with a simple matrix inversion algorithm specialized for symmetric and positive-definite matrices (HARWELL FORTRAN library, subroutine MA22A, Hopper, 1979). A noise-to-signal ratio of 0.08 was assumed in all the examples presented here, as it was found that this value not only was in agreement with the numerical accuracy of the simulated data but also prevented excessive vertical and lateral oscillations in all of the inverted models. Owing to the fact that all three surface TE electric and magnetic field components are linearly related (see Appendix 3), the linearized inverse is tested here only on electric field data.

4.13.1 A single buried block

A description of the resistivity model using a logarithmic depth scale is included in Figure 4-15a. Both the relatively low resistivity contrast of the single-block scatterer as well as its intermediate-range depth of burial, constitute favorable conditions for the linearized inverse. Plots of the inverted resistivity sections are shown in Figures 4-15 and 4-16 for the TM and TE electric field components, respectively. The results shown were inverted from 60 frequency samples simulated at each one of a total of 61 sounding locations, so that in effect the traverse length is 6 km. To conform to the total number of spatial sampling locations required by the fast Fourier transform, the first and last data points along the traverse were extended symmetrically outside the lateral limits of the assumed survey traverse. This generated a total of 128 spatial sampling locations and thus 65 wavenumber harmonics were independently inverted before performing the final inverse Fourier transformation leading to the model estimate.

The background resistivity was estimated directly from the electric field data as suggested in section 4.12 and this was 45 Ω•m. Both resistivity sections obtained from the inversion of the TE and TM electric field data are in good agreement with the true model section. In fact, the resistivity recovered in the central portion of the block is only slightly lower than the actual value of 5 Ω•m. Most interesting is the difference in lateral resolution in these two cases. The model cross-section inverted from the TM electric field data is laterally concentrated whereas the TE electric section shows a significant amount of "lateral

conductive leakage." Conversely, vertically, the TE electric section is more concentrated than the TM section, which in this sense is affected by "vertical conductive leakage." The latter effect is no doubt the result of unsuppressed static distortion caused by the conductive block at frequencies below its inductive range. The TE electric field response is not affected by static distortion but in exchange does not possess the lateral resolving power that the TM response does. Notice also that the vertical positioning of the conductive block is in both cases only slightly shifted downward with respect to the true model. A lower background resistivity could reduce this downward shift in the vertical scale in exchange for a larger amount of unsuppressed vertical conductive leakage in the TM section. As a parenthetical note, the computation time incurred on the inversion of each one of the resistivity sections was approximately 24 minutes on a Sun Spark 1^+ workstation.

4.13.2 A single buried block and a conductive basement

The model is described in Figure 4-17a. A single 2-D scatterer is buried in a 1-D background composed of an upper resistive layer and a conductive basement. Lateral and vertical dimensions of the conductive block are 1.6 km x 700 m, respectively. The objective of this example is to evaluate the performance of the linearized inverse in a situation where the concept of a constant vertical background is not applicable. The estimated background resistivity from the DC lateral and vertical wavenumber harmonics of the data is 20 Ω•m, and a total of 61 electric field sampling locations were assumed along the survey line.

Figures 4-17b and 4-18b are plots of the resistivity cross-sections inverted from the TM and TE electric field data, respectively. Laterally, the inverted resistivity cross-sections show the resolution characteristics expressed in the single-block model example examined in section 4.13.2 above. The TE section exhibits lateral conductive leakage whereas the TM section is subject to some amount of vertical conductive leakage. In consequence, the 1-D background is slightly better resolved with TE than with TM data.

4.13.3 A vertical fault and a conductive basement

The vertical fault model is particularly interesting because it allows one to easily appreciate the loss of lateral resolution with respect to depth in both TE and TM electric field data. Figure 4-19a details the geometrical characteristics of this test case. The fault extends from the surface down to a depth of 3 km, at which point the model is terminated with a conductive basement. In contrast with the examples presented in the previous two

sections, the concept of background resistivity here loses its meaning both laterally and vertically because there is no predominant geoelectric feature in the model in either direction. An average of the electric field data yields for this test case a background resistivity of 130 Ω•m. Figures 4-19b and 4-20b display the inverted resistivity cross-sections for the TM and TE electric field data, respectively. Data simulated at a total number of 61 sampling locations were used to produce the results shown. In the inverted TE section, the vertical fault appears much smoother, laterally, than in the TM section. However, despite the difference in lateral smoothness with which the vertical fault is resolved in each case, the results cast no doubt that the degree of smoothness increases with depth. In addition to the fact that a background resistivity of 130 Ω•m is more appropriate on the right-hand side of the vertical fault, the difference in lateral conductive leakage between the two sections evidently causes a discrepancy as to how, vertically, the conductive basement is resolved in each case.

4.13.4 A semiinfinite buried slab and a surface inhomogeneity

As shown in the Figure 4-21a, perhaps the most interesting feature of this example is the 500 m-wide and 100 m-thick surface conductor located exactly in the middle of the geoelectric cross-section. In addition, a 300 m-thick semiinfinite horizontal slab has been included on the right-hand side of the section at a depth of 1.4 km. Despite its reduced thickness, the semiinfinite nature of this second feature produces a TM electric field distortion whose influence on the surface can be felt several kilometers away from the leftmost sampling location (+3 km.) By contrast, the same feature causes a more localized distortion on the surface TE response. On the other hand, the resistive basement provides a large enough contrast to prevent the vertical smearing of the conductive slab.

In order to optimize the function of the TM prewhitening filter in suppressing the expected static distortion by the surface conductor, the background resistivity for this example was deliberately made equal to the resistivity of its surrounding layer, that is to say, 100 Ω•m. Figures 4-21a and 4-22b are plots of the resistivity cross-section inverted from the TE and TM electric field data, respectively. Both sections provide indication of all of the features included in the original geoelectrical model but there are clear differences between them. For instance, laterally, the horizontal slab is smoother in the TM section than in the TE section. Likewise, vertically, the same feature is more concentrated in the TM section than in the TE section. The surface conductor, on the other hand, is much better resolved vertically in the TE section that in the TE section. Vertical conductive leakage

caused by the same conductor on the TM section spreads out to longer distances with increasing values of depth to eventually blend with the lateral conductive imprint of the buried slab.

4.13.5 Symmetric resistive and conductive blocks

This test case is a modified version of the two-block calibration model used by Smith and Booker (1990) and Oldenburg and Ellis (1990) in their own inversion studies. Separated by a distance 0f 3 km, the two blocks have the same geometrical dimensions (1.5 km x 1.5 km) and are buried at a common depth of 1.5 km. Also, both blocks share the same resistivity contrast with the surrounding layer. A conductive basement at a depth of 10 km incorporates an additional vertical contrast of the same magnitude into the model. The characteristics of this example permit one to compare the resolution properties of both TM and TE electric field responses in a perfectly symmetric geometrical model that contains resistive as well as conductive 2-D features.

Figures 4-22 and 4-23 display the true and inverted resistivity resistivity cross-sections derived from the TM and TE electric fields, respectively. The traverse length assumed for the simulated data was 12 km and, with use of a sampling distance of 100 m, the total number of stations input to the inversion was 121. The first and last data points were extended laterally outward to complete a total of 256 points, each including 61 frequencies. Approximately 40 minutes of CPU time were spent to produce each of the inverted resistivity cross-section in a Sun Spark 1^+ workstation.

At a noise-to-signal ratio of 0.08 and an estimated background resistivity of 40 Ω•m, the resistivity cross-section inverted from the TM electric fields evidences both resistive and conductive blocks. At the same time, the conductive basement is almost perfectly recovered. Laterally, the conductive block appears less localized than the resistive block, but the resistivity value recovered for the latter is less accurate than the one recovered for the former. In contrast, the resistivity cross-section inverted from the TE electric fields not only has unheeded the resistive block, but also show the conductive block as a highly smeared feature. The difference in the performance of the linearized inverse for the two electric field modes can be traced back to the MT response characteristics of each mode. In fact, the reason why the resistive block has a negligible imprint on the TE section compared to that of the conductive block is that the former causes a reduction of conduction current as opposed to the increase of current introduced by the conductive block. On the other hand, the TM-mode conduction current exhibits vertical distortion patterns directed

both away from the resistive block and toward the conductive block. Even though the outward current deflection effect introduced by the resistive block is much less pronounced than the channeling effect imposed by the conductive block, the surface response in the first case is large enough to cause a measurable anomaly in the surface electric field.

4.14 Field example of inversion

During the Summer of 1990, an expedition crew formed by staff and students of both Engineering Geoscience, U.C. Berkeley, and Lawrence Berkeley Laboratory, embarked upon an unconventional MT survey for the exploration of the Surprise Valley Geothermal prospect in northern California. A location map including the description of the field procedure as well as of the survey parameters employed in such geophysical adventure are included in Figure 4-24. The project was financed by both Trans-Pacific Geothermal Co. and the Department of Energy. Both a detailed geological description and a historical semblance of the geothermal activity in Surprise Valley are reserved for a later section in Chapter V. For the moment, just a brief description is presented insofar as what the data mean in terms of the linearized inverse procedure introduced in the previous sections of this chapter.

A 4.2 km-long electric field transect was laid out perpendicular to the predominant geologic strike as inferred from the available geological and geophysical data. This transect consisted of 100 m tangential electric dipoles placed end-to-end along the total survey length. Additionally, orthogonal electric dipoles and pairs of induction coils were positioned at regular spacings. To comply with the requirements of the field procedure suggested in section 4.11 above, a magnetic base station was situated approximately 3.5 km away from the transect. This magnetic station served also as a remote site for noise reduction purposes. The electric field data recorded at each one of the tangential dipoles were referred to the synchronous magnetic fields acquired at the magnetic base station and this procedure yielded TM-like base impedances for subsequent inversion (see sections 4.11 and the more general discussion of this topic in section 5.3). Lateral magnetic field variations measured along the transect were found negligible for all practical purposes, whereupon the magnetic field measured at the base station was assumed an unbiased sample of the background magnetic field in the area. Apparent resistivity and phase pseudosections for the calculated TM-like base impedances are shown in Figure 5-23. The topographic profile included in those figures shows a maximum altitude gain of 400 m toward the west end of the transect.

Notwithstanding that the inverse procedure introduced in this chapter does not account for variations in topography along the line of measurements, the objective of this section is to evaluate the performance, and possibly the shortcomings, of the underlying assumption of linearity made here for the MT response. Figure 4-25a shows the inverted resistivity section derived from the Surprise Valley TM-like base impedances using a background resistivity of 6 Ω•m and a noise-to-signal ratio of 0.2, which is in fact a slightly higher value than the actual noise-to-signal ratio estimated independently from the electric and magnetic field measurements. For comparison, a resistivity section inverted from the same data is shown in a contiguous figure. The latter section was derived using a data-adaptive spatial filtering procedure which allows for lateral and frequency variations of the cutoff wavenumber characteristic of the prewhitening filter discussed in section 4.9 above. Subsequently, a 1-D Bostick (1977) pseudoinverse was applied to the filtered base impedances and the results were "stitched" together to yield the resistivity cross-section shown in Figure 4-25b. Additionally, an elevation correction was applied to the inverted resistivity profile to account for the topographic variations along the transect. A thorough description of all of these processing and inversion steps are main subjects of discussion in Chapter V; the results shown here are advanced merely to establish a measure of comparison.

Even though there exist marked differences between the two inverted resistivity sections shown in Figure 4-25, there are also common features that correlate well. For instance, the prominent resistor on the right-hand side of the sections shows the same upward dip in both cases. This resistor is found in both the apparent resistivity and impedance phase pseudosections of Figure 5-23. Below the resistor, the presence of a conductive layer can be expected by inspection of the phase pseudosection. In Figure 4-25b, however, the same layer is somewhat blurred partly because of the approximate nature of the Bostick pseudoinverse, although indeed the tendency of the section is toward a conductive feature at depth. The most significant discrepancy between the resistivity sections, however, occurs at the shallowest depths, where the resistivity distribution is highly conductive and for this reason causes a large surface electric field response which the linearized inverse is simply unable to account for. This is why toward the right-hand side of section obtained with the linearized inverse the resistivity distribution exhibits a drastic and highly unnatural downward dip toward the sedimentary valley. That this behavior is in effect unnatural can be explained by recalling the deficiency of the 1-D linearized inverse introduced in Chapter III to recover large conductive segments in the vertical resistivity profiles. In contrast, the Bostick pseudoinverse provides a much better

resistivity estimate in the same situation. Ways in which the lateral variations of topography may be responsible for some of the differences between the two sections at their upper right-hand corners are actually more difficult to understand, but there is no doubt that some distortion is introduced thereby.

4.15 Discussion and concluding remarks

The synthetic examples above show that the resolution properties inherent in the linearized 2-D inverse hold even in situations where the low resistivity contrast assumption is not valid. As in the case of the 1-D linearized inverse, the parameter that effectively controls the validity of the linearized inverse is the amplitude of the secondary-to-primary field ratio fed into the inversion. Regardless of the resistivity contrast, lateral dimensions and depth of burial of the MT scatterer(s), a low secondary-to-primary field response ratio justifies the use of the inversion. In fact, this is why, for instance, the linearized inverse performed especially well at recovering resistive features and buried conductors. It should also be pointed out that the merit of the linearized inverse resides in using Rytov and Born representations for the electric and magnetic field data, respectively, which are the most appropriate data parameterization schemes in either case. Needless to say, the merits of the linearized inverse should not be judged entirely by its practical promise. The Surprise Valley field example, for instance, is but one of a great many situations where the linearized inverse may support only marginal credence to the assumption of a low-contrast electric field response. Instead, the analytical results and numerical experiments presented in this chapter indicate that the importance of the linearized inverse is that it provides valuable insight on the many details that can make a more practical inverse method truly successful.

Foremost among these details is the use of a "prewhitening" operator in the inversion of TM electric field data. This operator spatially low-pass filters the data without sacrificing their lateral resolution, and it also turns out to be a natural way to stabilize the inversion. As a useful corollary, it can be stated that the relative success with which the prewhitening operator can be used in the inversion of TM data will be determined by the separation distance between contiguous measurements. Short sampling intervals will allow an optimal application of the low-pass wavenumber filter and will also improve the stability of the inversion. In plain physical terms, the prewhitening operator helps remove the frequency dependent static effects mentioned in Chapter II. Thus, in the presence of near-surface inhomogeneities, the success of the inversion will be largely determined by the accuracy with which the prewhitening operator can be adjusted in response to lateral

changes in the near-surface resistivity distribution. A large near-surface effect demands a low cutoff wavenumber from the prewhitening operator. Conversely, in the absence of near-surface effects, the low-pass wavenumber filter should not suppress valuable lateral information in the surface response. It was shown that one of the characteristics of the prewhitening filter is that its cutoff wavenumber decreases with decreasing values of frequency. However, because the linearized inverse assumes a constant background resistivity, no lateral adjustments of its cutoff wavenumber can be made to suppress lateral variations in the intensity of static effects. A way to enforce prewhitening with lateral sensitivity to static effects will be discussed in Chapter V.

As for the remaining TE electric and magnetic field data (including the prewhitened TM electric field data), the linearized inverse formulation indicates that their sensitivity to laterally varying features in the subsurface decreases with increasing depths of burial. More specifically, it was found that the largest lateral wavenumber harmonic in the subsurface that can be detected at a given frequency is inversely proportional to the corresponding Bostick depth of penetration. This reduction of lateral resolution with depth is actually more severe on the TE electric and magnetic fields than on the TM electric field, as can be seen in the synthetic examples presented here. Also, it was shown that only electric field data can resolve the DC wavenumber harmonic of the subsurface resistivity distribution, and that for this very reason magnetic field data are insufficient to extract specific values of resistivity and depth. Therefore, any inverse scheme that contemplates the use of magnetic field data should not overlook the need for adequately sampled electric fields. The linearized inverse also shows that the TE electric and magnetic fields are linearly related to each other (actually, this property holds even in nonlinear environments), thus implying that over a strictly 2-D earth one does not need to continuously sample all three TE components to infer a cross-section of subsurface resistivity. However, as shown in Chapter VI, more realistic exploration situations call for measurements of the magnetic field to recognize 3-D induction effects along the line of measurements.

From the properties of the linearized inverse one could think of an actual nonlinear method of inversion as one that continuously adjusts the lateral and vertical changes in background resistivity to position the resistivity and depth estimates in more precise locations than with the use of a constant background resistivity. In the inversion of TM electric field data, these adjustments include lateral and frequency changes in the cutoff wavenumber properties of the prewhitening operator that in turn result in better vertical positioning of the inverted resistivity values. A decrease in the average background

resistivity increases the cutoff wavenumber of the prewhitening operator and this also shifts the estimated resistivity values to shallower depths. Exactly the opposite effect occurs when the local background resistivity is larger than its assumed global value.

The wavenumber inversion presented in this chapter could also be approached directly in the space domain. In retrospect, the choice of a wavenumber-domain method over a space-domain formulation was made because of the algebraic simplicity of the former. One of the stronger disadvantages of the wavenumber formulation is that model constraints are very difficult, if not impossible, to incorporate in the numerical solution. On the other hand, the role of the prewhitening operator is much easier to understand in the wavenumber domain than in the space domain. Thus, it appears that the space-domain formulation could offer a great deal of flexibility provided that the prewhitening step is accounted for. Notably, the role of the prewhitening operator has been unrecognized in all of the parametric nonlinear inverse formulations reported so far in the literature.

A 3-D version of the ideas developed in this chapter seems a natural way to continue the line of research into linearized solutions to the MT inverse problem. Even though some of the concepts dealing with this subject have already been touched upon in Chapter II, detailed work remains to be done on specific characteristics that can make practical inverse methods tractable. A wavenumber inversion, for instance, could be formulated in terms of the 2-D Fourier transform of the model, at which point stability criteria could be investigated in view of the lateral characteristics of the MT response. Evidently, the practicality of a 3-D inverse solution will be highly determined by the availability of 2-D surface data. This is by itself a major undertaking that perhaps will only become feasible in the future. For the moment, the remaining chapters of this thesis concentrate on the study and interpretation of 2- and 3-D properties of the MT response that could be sampled along a continuous line of electric field measurements such as the Surprise Valley transect introduced in section 4.14.

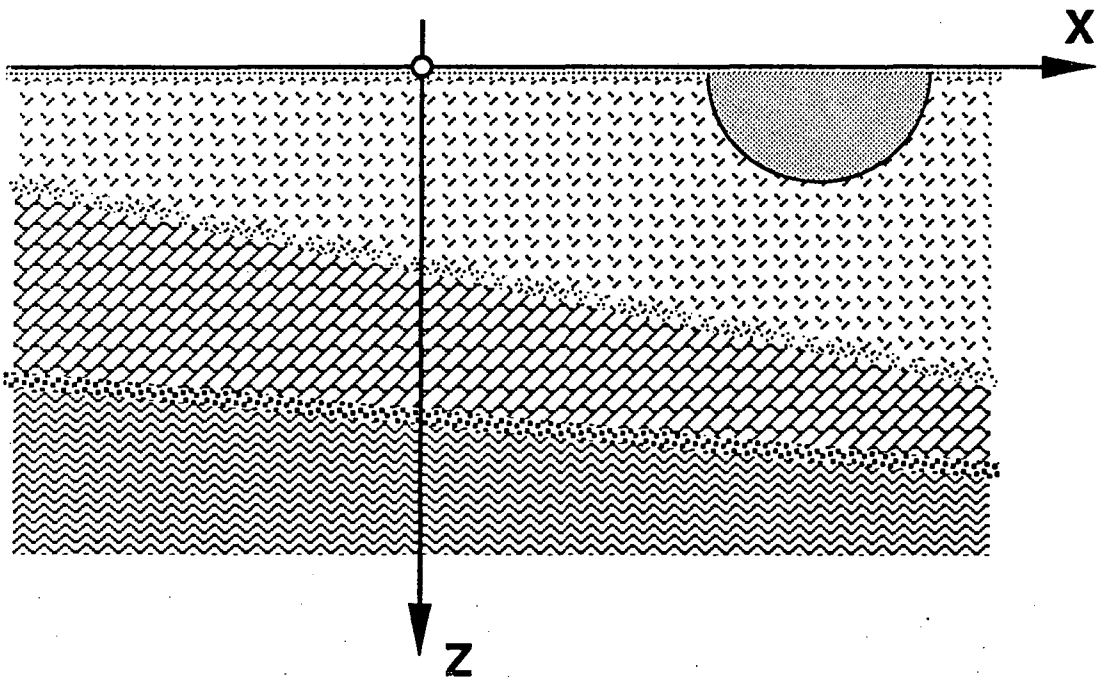

Figure 4-1. Cartesian coordinate frame for the 2-D forward and inverse MT problems.

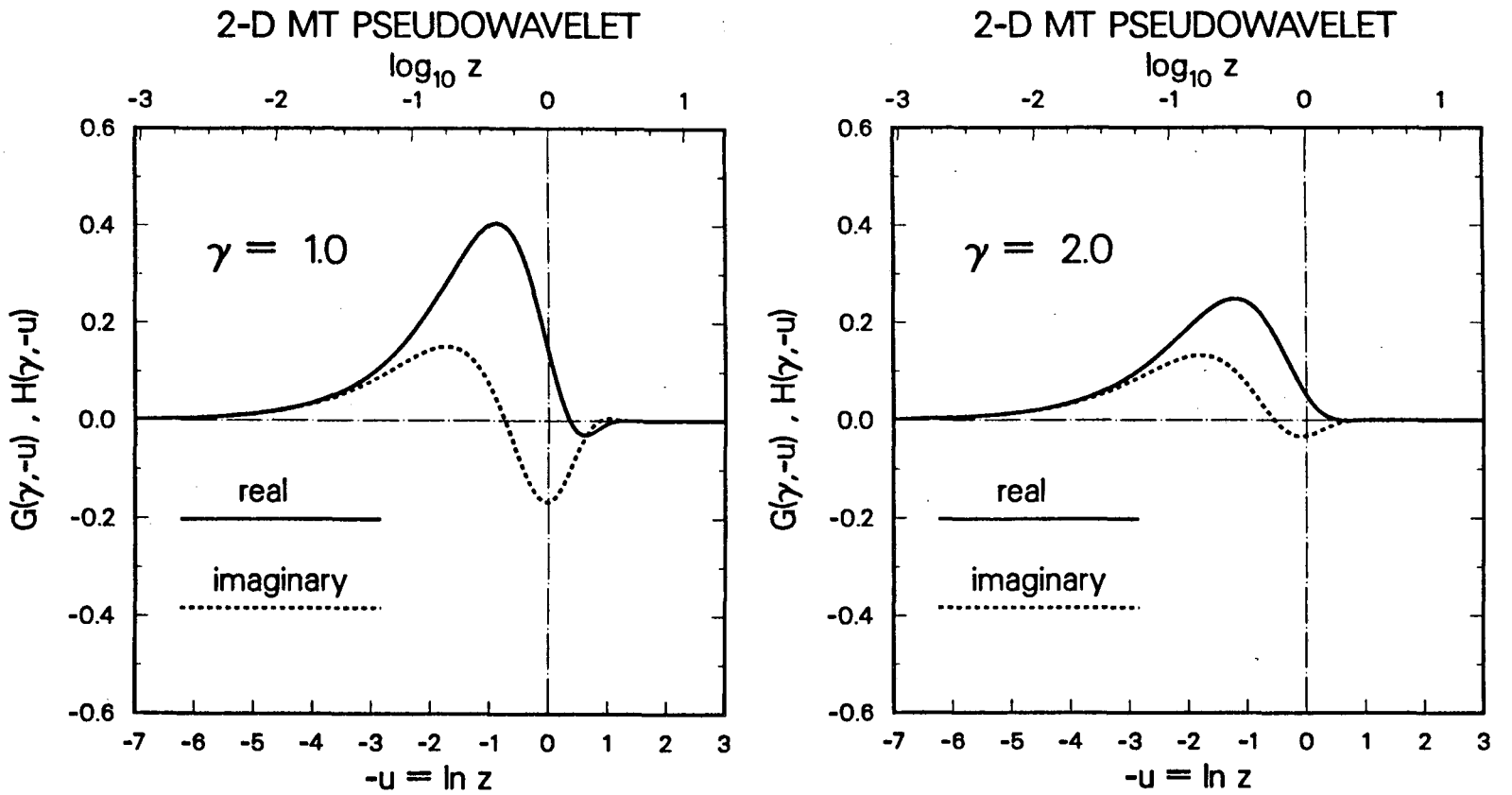

Figure 4-2. Real and imaginary components of the reversed 2-D MT pseudowavelet. In each panel, a pseudowavelet is shown for a particular value of the γ variable ($\gamma=2\pi k z_B$, where k is the lateral linear wavenumber and z_B is the Bostick depth of penetration in the homogeneous background at a given frequency.)

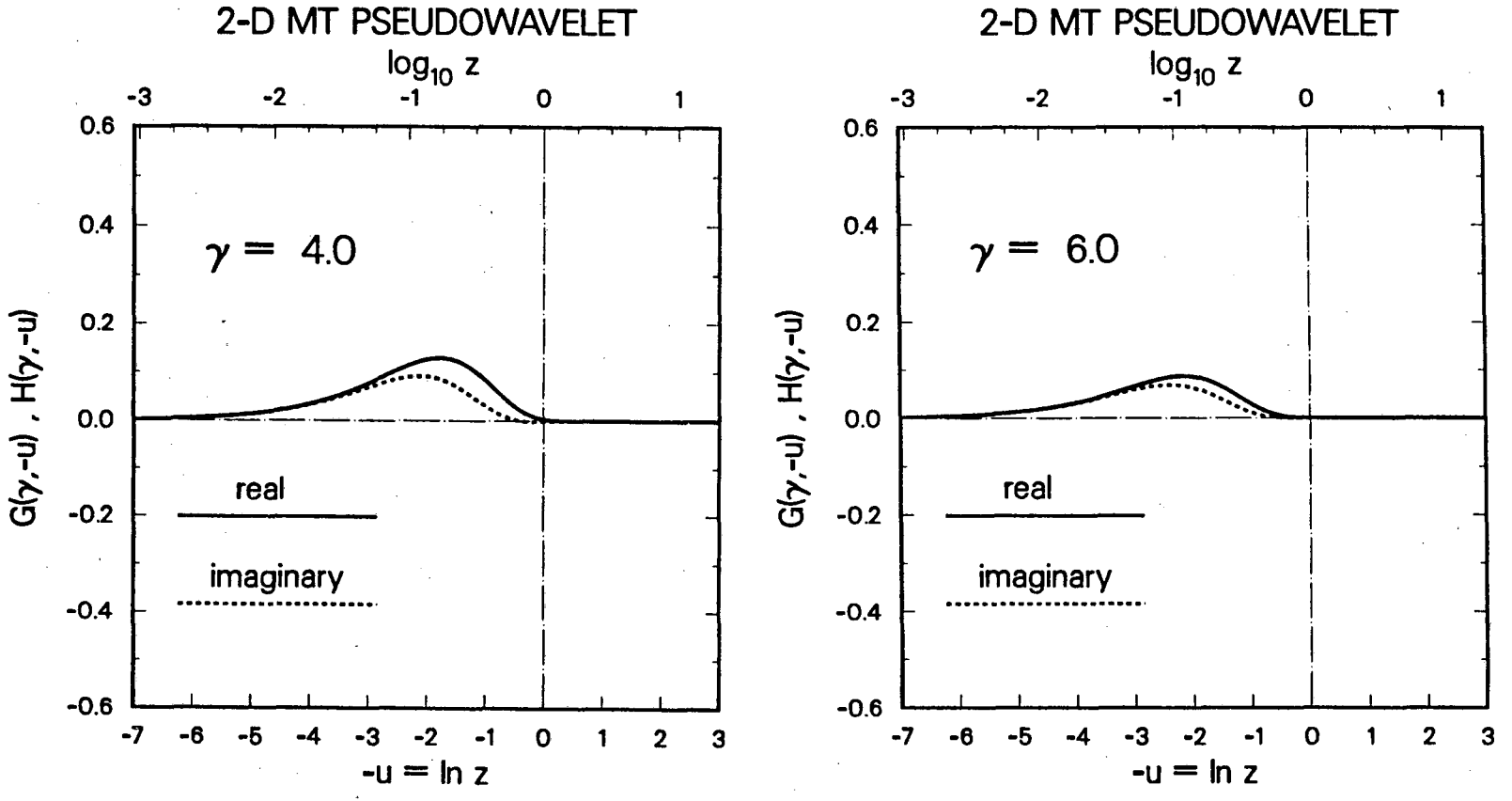

Figure 4-2 (continued). Real and imaginary components of the reversed 2-D MT pseudowavelet. In each panel, a pseudowavelet is shown for a particular value of the γ variable ($\gamma=2\pi k z_B$, where k is the lateral linear wavenumber and z_B is the Bostick depth of penetration in the homogeneous background at a given frequency.)

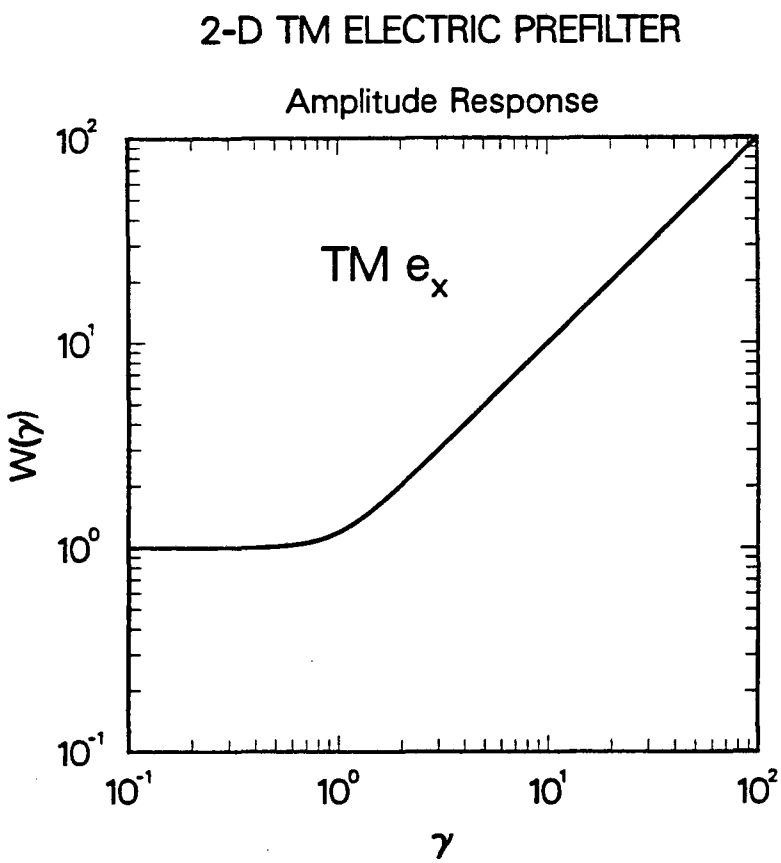

Figure 4-3. Amplitude response of the TM electric field prefilter plotted with respect to the γ variable ($\gamma=2\pi k z_B$, where k is the lateral linear wavenumber and z_B is the Bostick depth of penetration in the homogeneous background at a given frequency.)

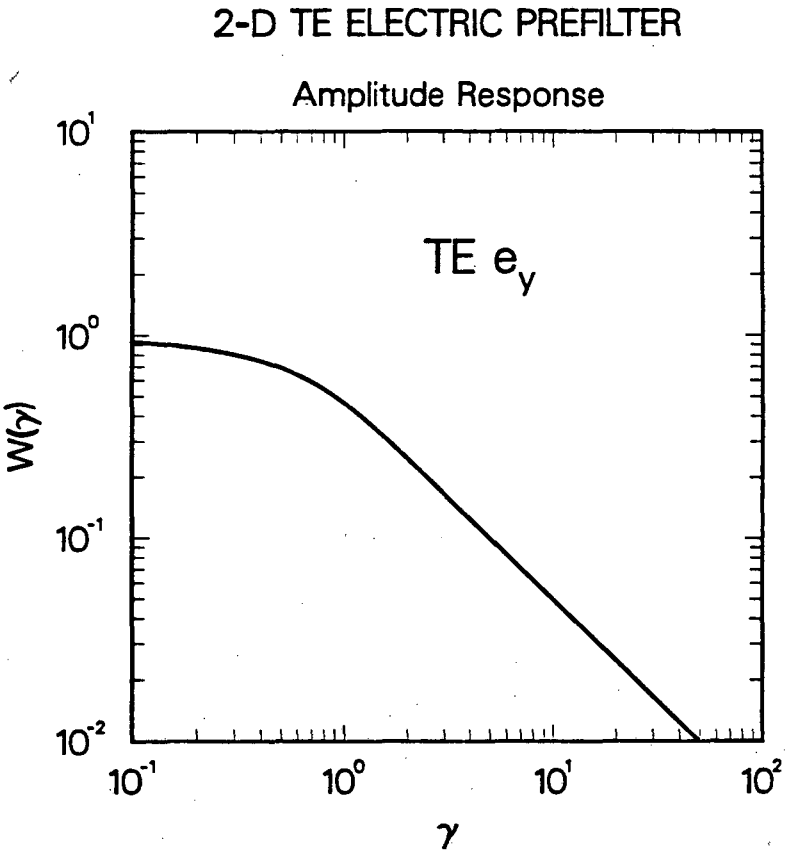

Figure 4-4. Amplitude response of the TE electric field prefilter plotted with respect to the γ variable ($\gamma=2\pi k z_B$, where k is the lateral linear wavenumber and z_B is the Bostick depth of penetration in the homogeneous background at a given frequency.)

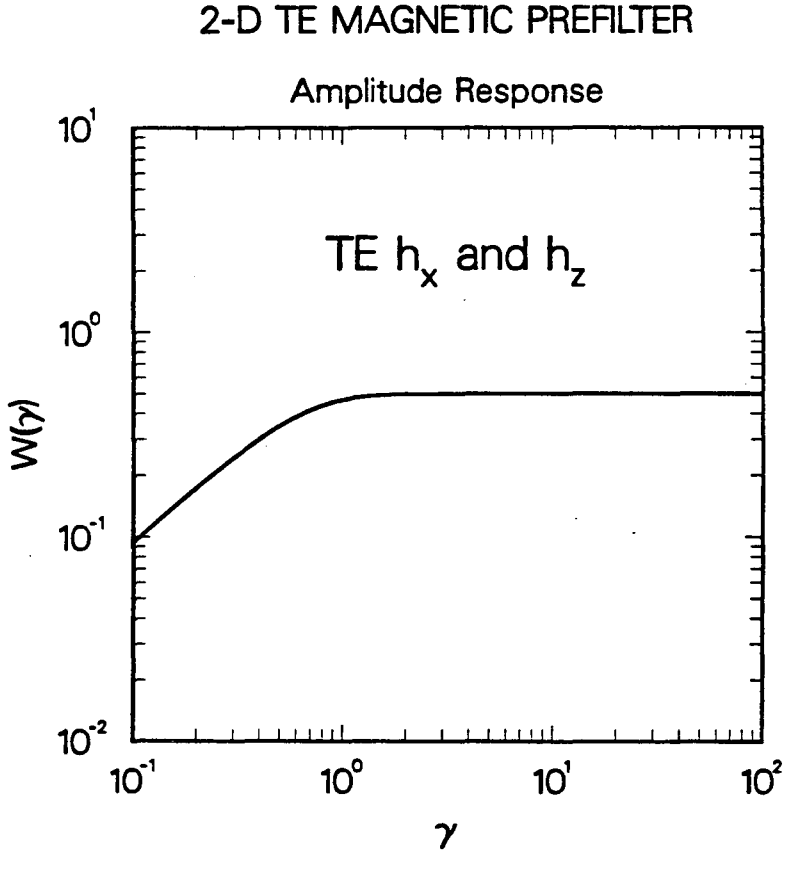

Figure 4-5. Amplitude response of the TE magnetic field prefilter plotted with respect to the γ variable ($\gamma=2\pi k z_B$, where k is the lateral linear wavenumber and z_B is the Bostick depth of penetration in the homogeneous background at a given frequency.)

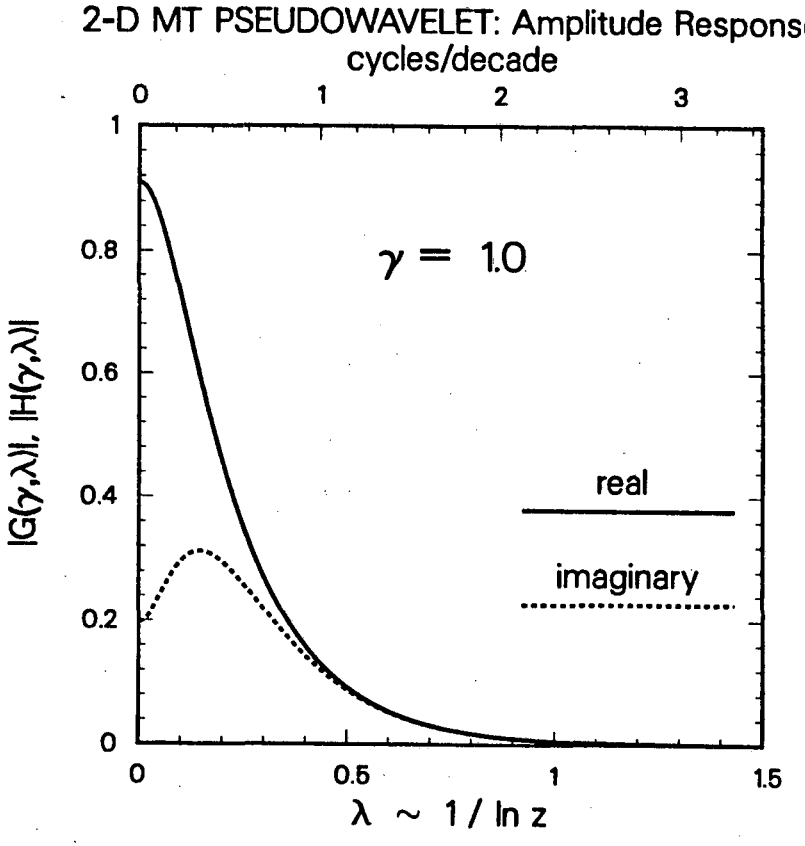

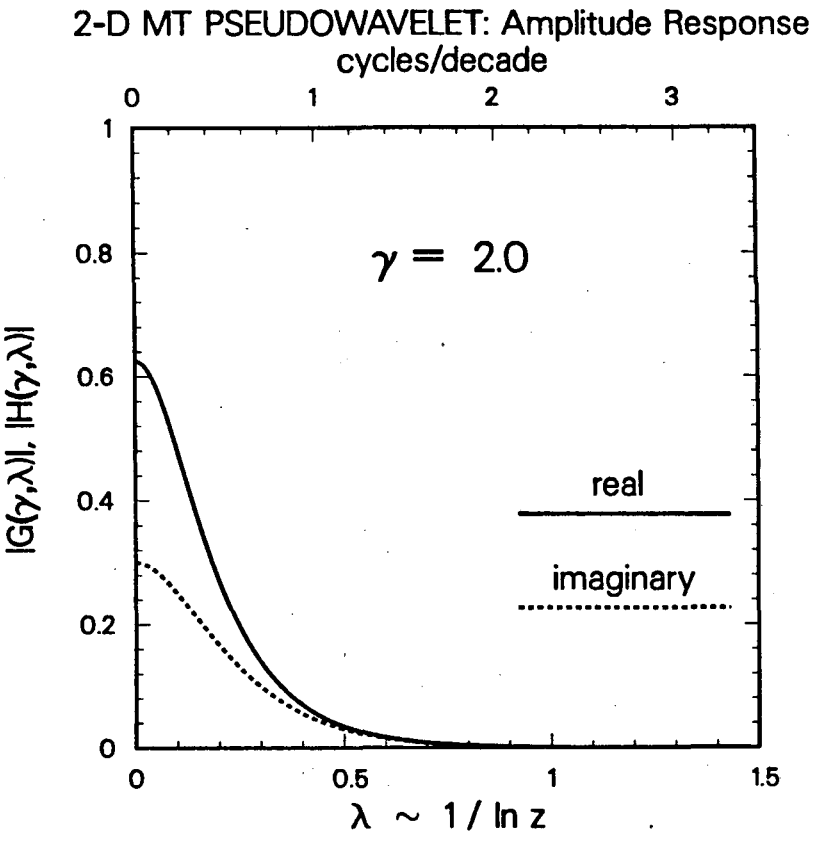

Figure 4-6. Amplitude response curves of the real and imaginary components of the 2-D MT pseudowavelet (G and H, respectively) plotted with respect to the linear vertical wavenumber, λ. In each panel, response curves are shown for a particular value of the γ variable ($\gamma=2\pi k z_B$, where k is the lateral linear wavenumber and z_B is the Bostick depth of penetration in the homogeneous background at a given frequency.)

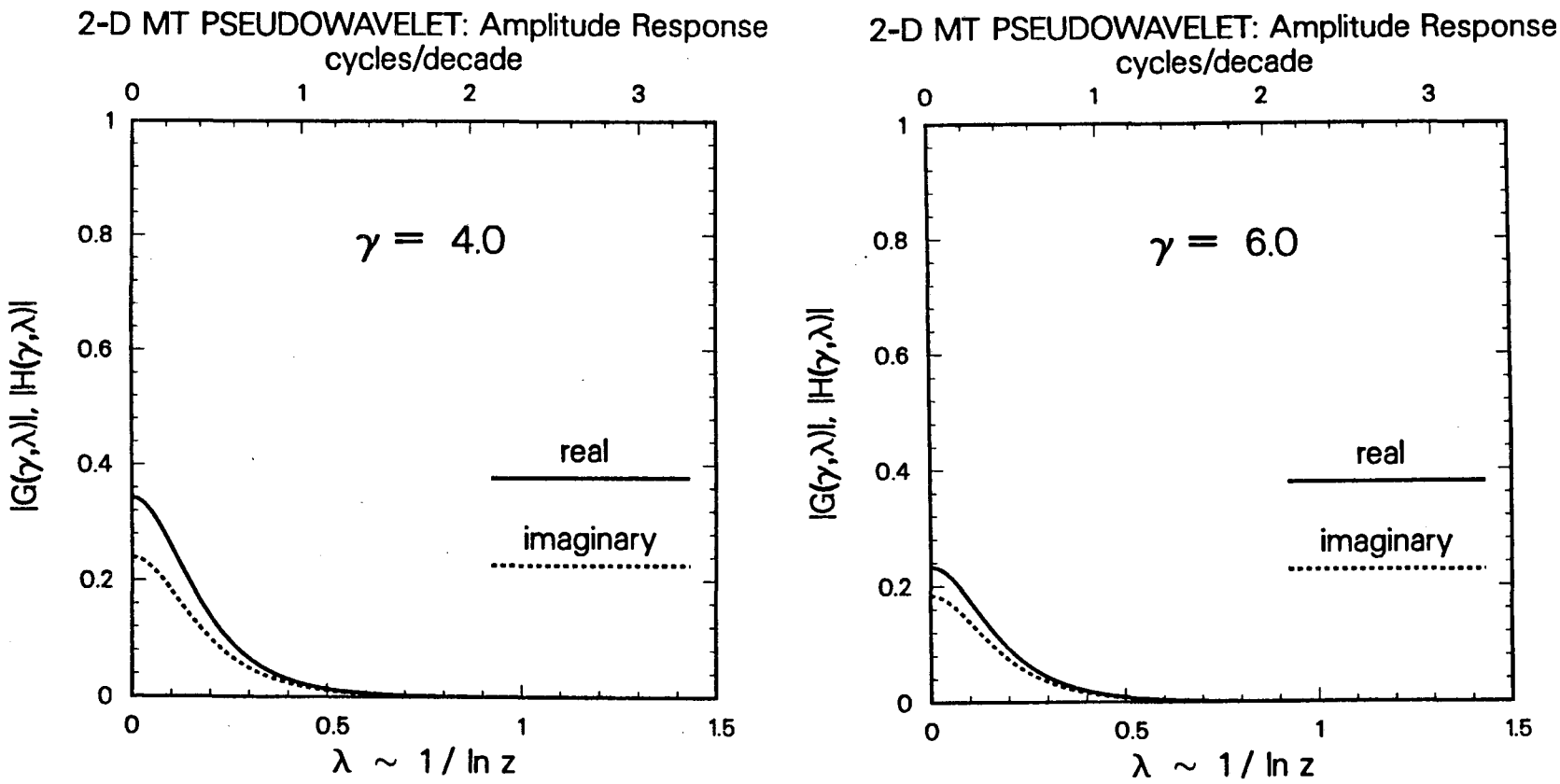

Figure 4-6 (continued). Amplitude response curves of the real and imaginary components of the 2-D MT pseudowavelet (G and H, respectively) plotted with respect to the linear vertical wavenumber, λ. In each panel, response curves are shown for a particular value of the γ variable ($\gamma=2\pi k z_B$, where k is the lateral linear wavenumber and z_B is the Bostick depth of penetration in the homogeneous background at a given frequency.)

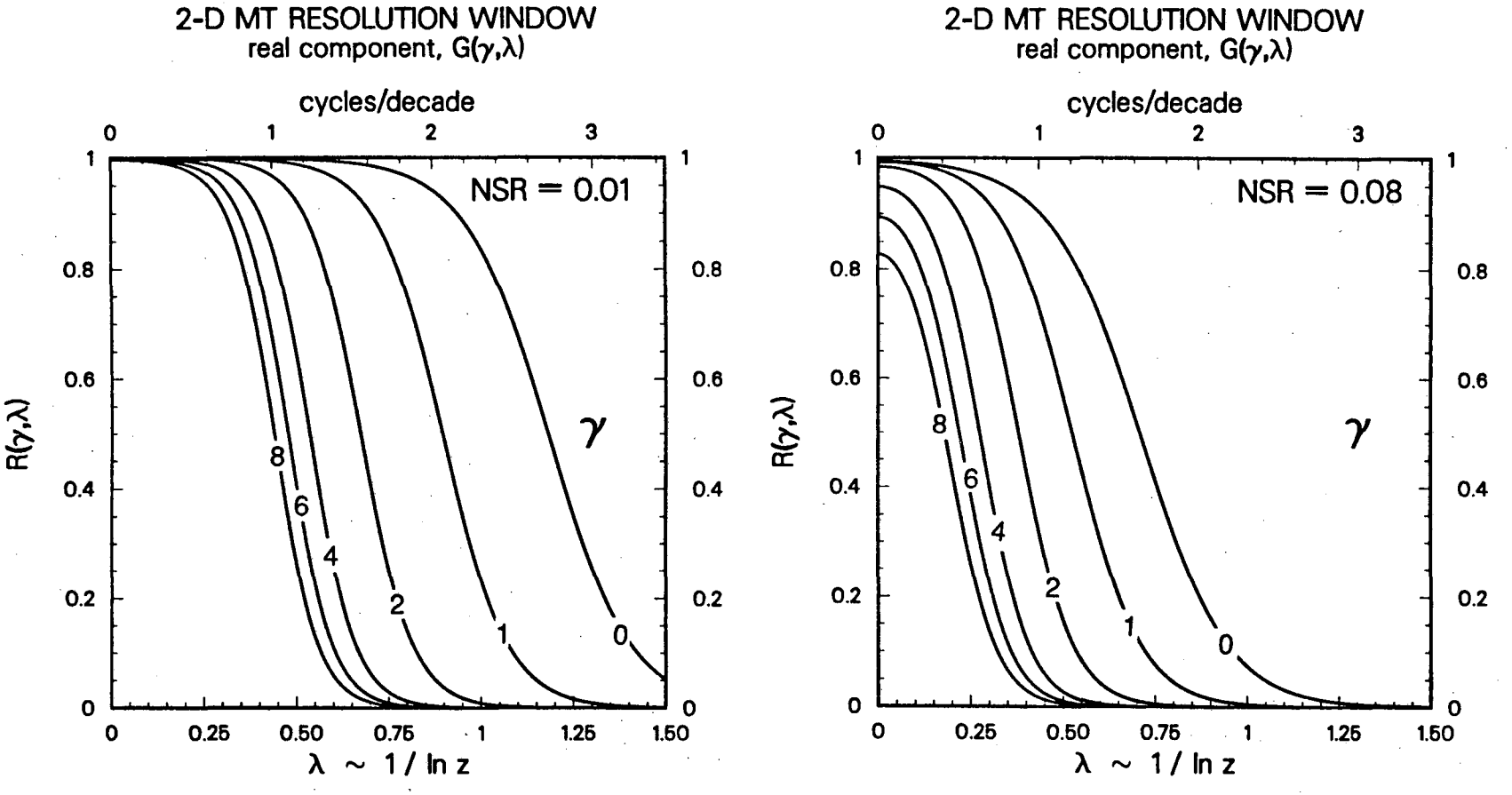

Figure 4-7. Wavenumber resolution windows, $R(\gamma,\lambda)$, for the 2-D MT linear inverse problem at various noise-to-signal ratios. In each panel, plots of the resolution window are shown for a fixed noise-to-signal ratio and different values of the γ variable ($\gamma=2\pi k z_B$, where k is the lateral linear wavenumber and z_B is the Bostick depth of penetration in the homogeneous background at a given frequency.)

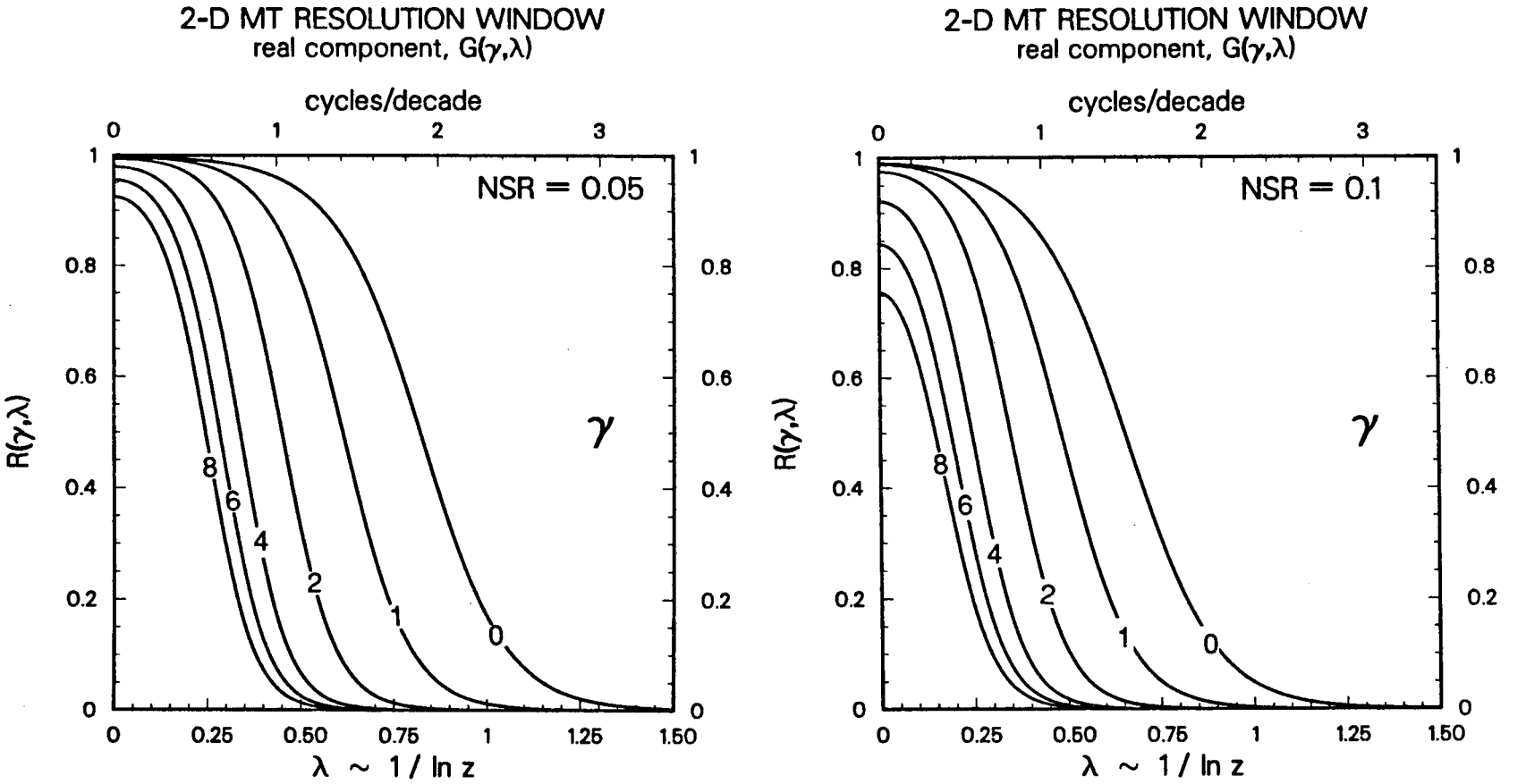

Figure 4-7 (continued). Wavenumber resolution windows, $R(\gamma,\lambda)$, for the 2-D MT linear inverse problem at various noise-to-signal ratios. In each panel, plots of the resolution window are shown for a fixed noise-to-signal ratio and different values of the γ variable ($\gamma=2\pi k z_B$, where k is the lateral linear wavenumber and z_B is the Bostick depth of penetration in the homogeneous background at a given frequency.)

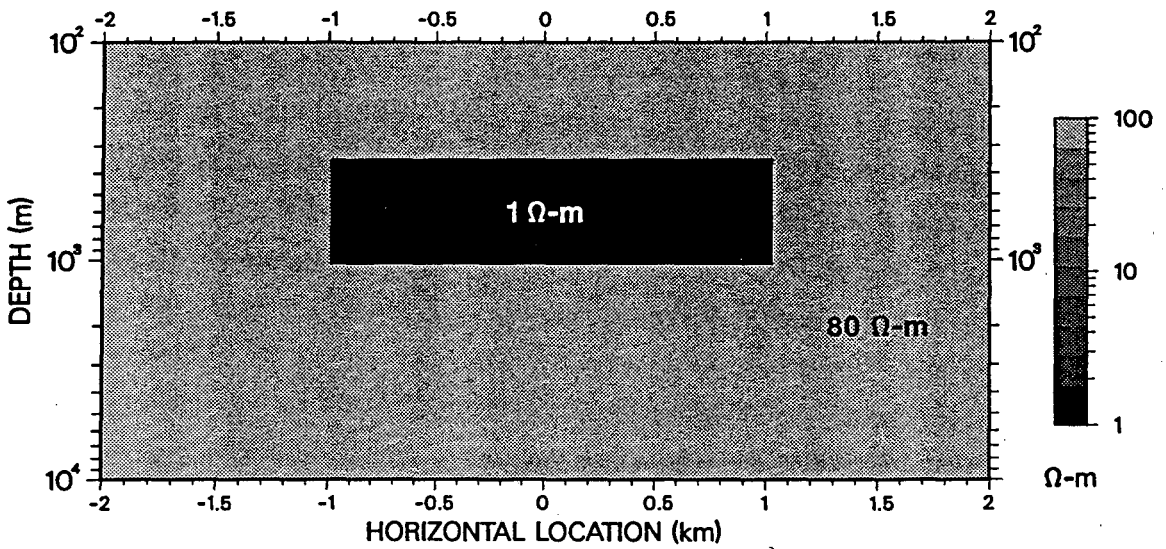

Figure 4-8. Cross-section perpendicular to strike of a rectangular conductor buried in a homogeneous background. Figures 4-9 through 4-12 are lateral wavenumber-domain plots of the MT response simulated for this model at 10 Hz.

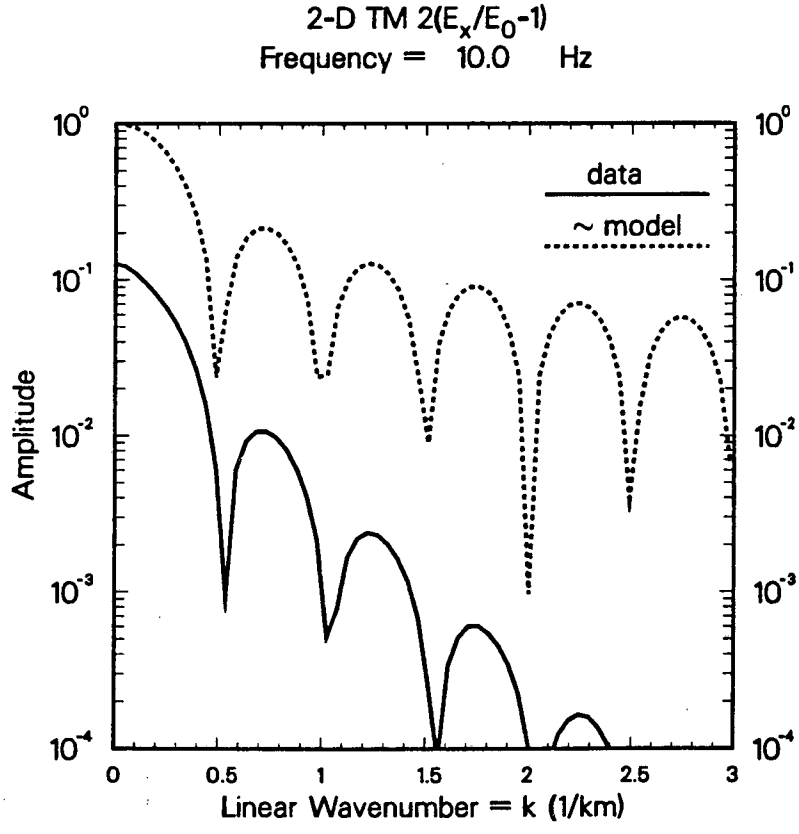

Figure 4-9. Amplitude response plot of the secondary-to-primary TM electric field ratio at 10 Hz for the single conductor model of Figure 4-8. For comparison, a normalized amplitude plot of the lateral Fourier transform of the conductive block is shown as well.

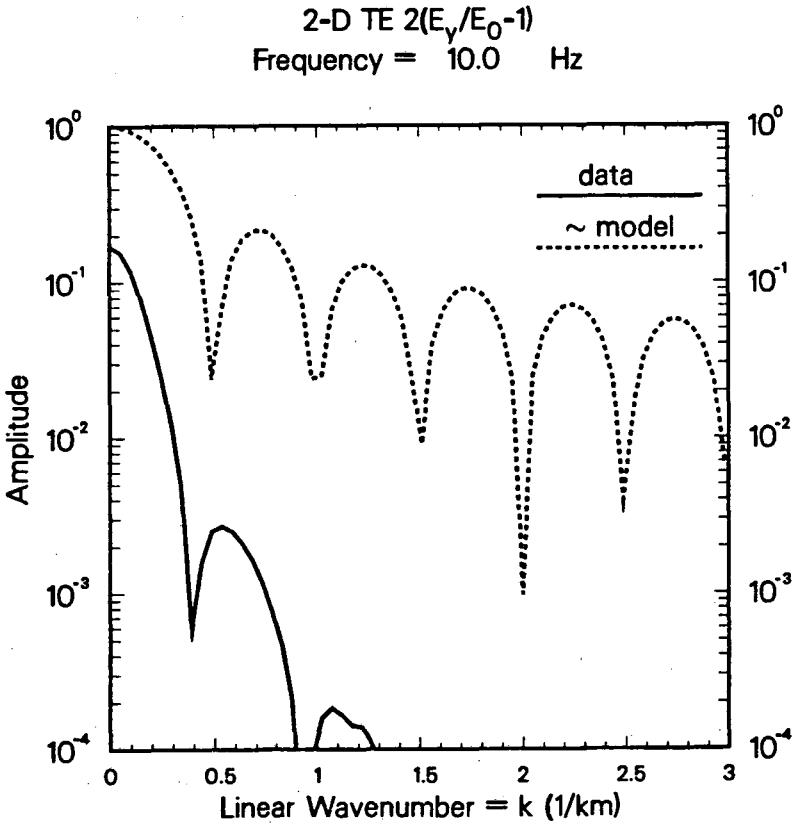

Figure 4-10. Amplitude response plot of the secondary-to-primary TE electric field ratio at 10 Hz for the single conductor model of Figure 4-8. For comparison, a normalized amplitude plot of the lateral Fourier transform of the conductive block is shown as well.

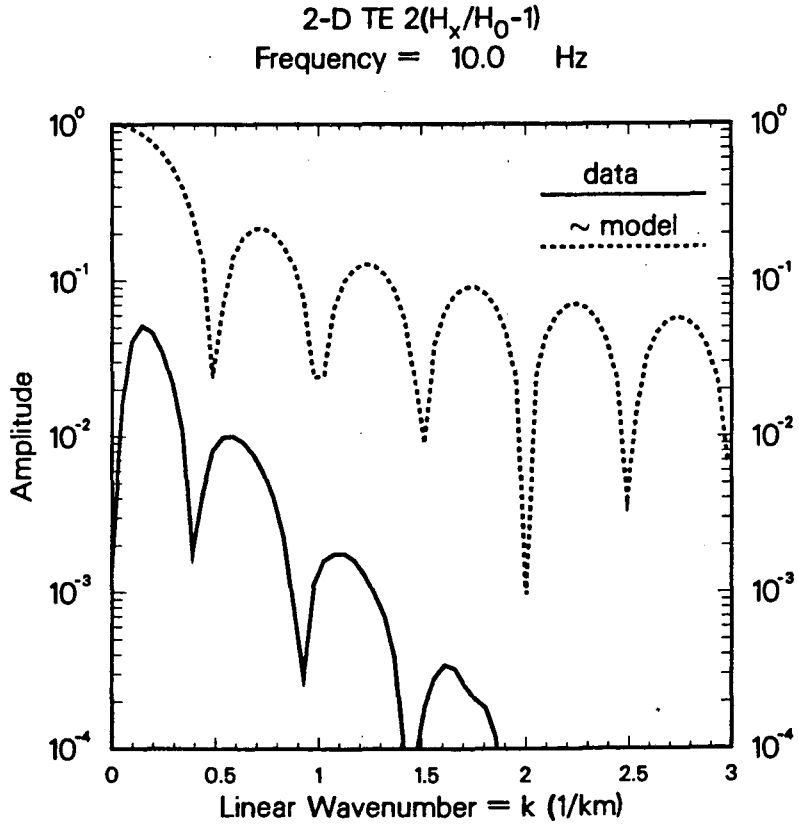

Figure 4-11. Amplitude response plot of the secondary-to-primary TE horizontal magnetic field ratio at 10 Hz for the single conductor model of Figure 4-8. For comparison, a normalized amplitude plot of the lateral Fourier transform of the conductive block is shown as well.

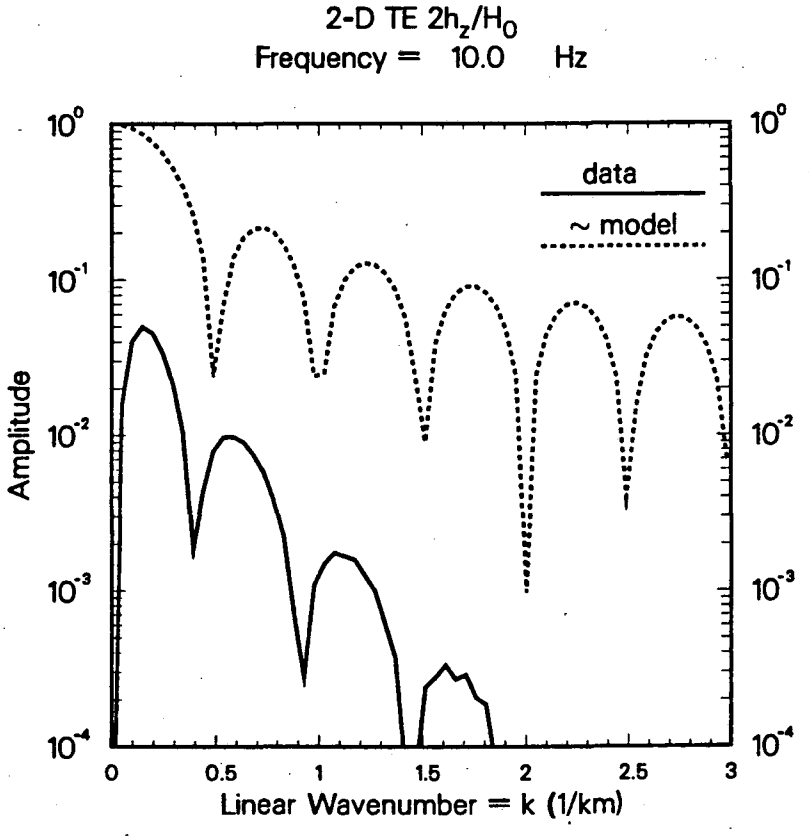

Figure 4-12. Amplitude response plot of the secondary-to-primary TE vertical magnetic field ratio at 10 Hz for the single conductor model of Figure 4-8. For comparison, a normalized amplitude plot of the lateral Fourier transform of the conductive block is shown as well.

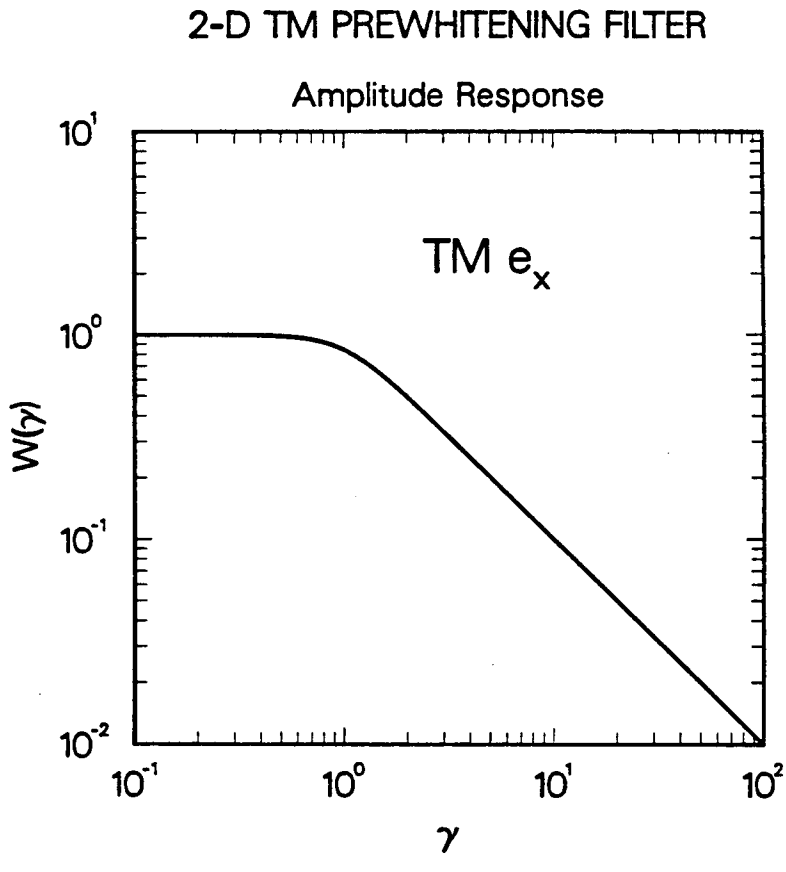

Figure 4-13. Amplitude response of the TM electric field "prewhitening" filter plotted with respect to the γ variable ($\gamma=2\pi k z_B$, where k is the lateral linear wavenumber and z_B is the Bostick depth of penetration in the homogeneous background at a given frequency.)

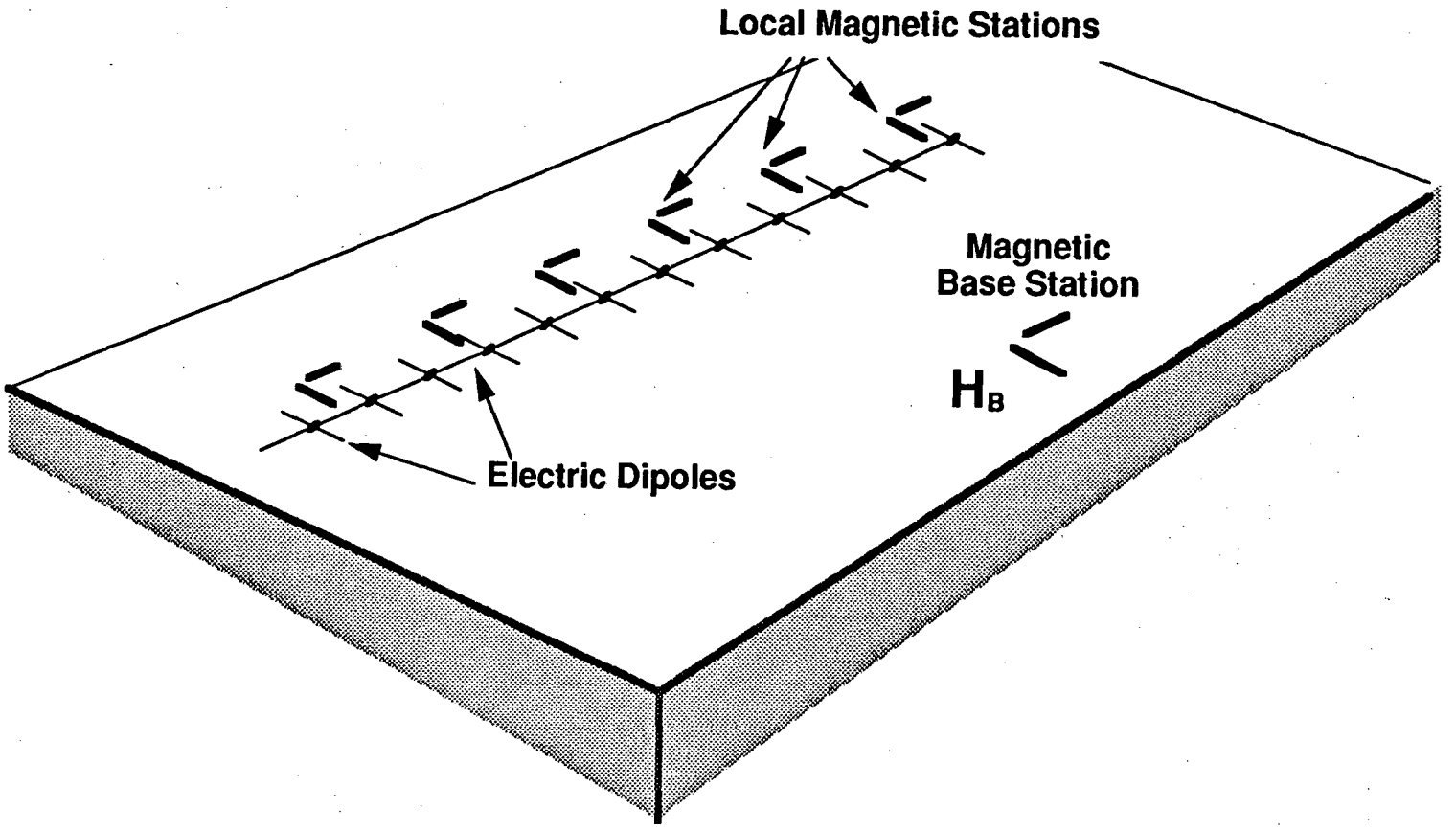

Figure 4-14. Graphical description of the suggested field procedure for the estimation of secondary-to-primary field ratios rather than conventional MT impedances. A magnetic base station is kept at a fixed location while electric and magnetic field are gathered at different points along the survey line.

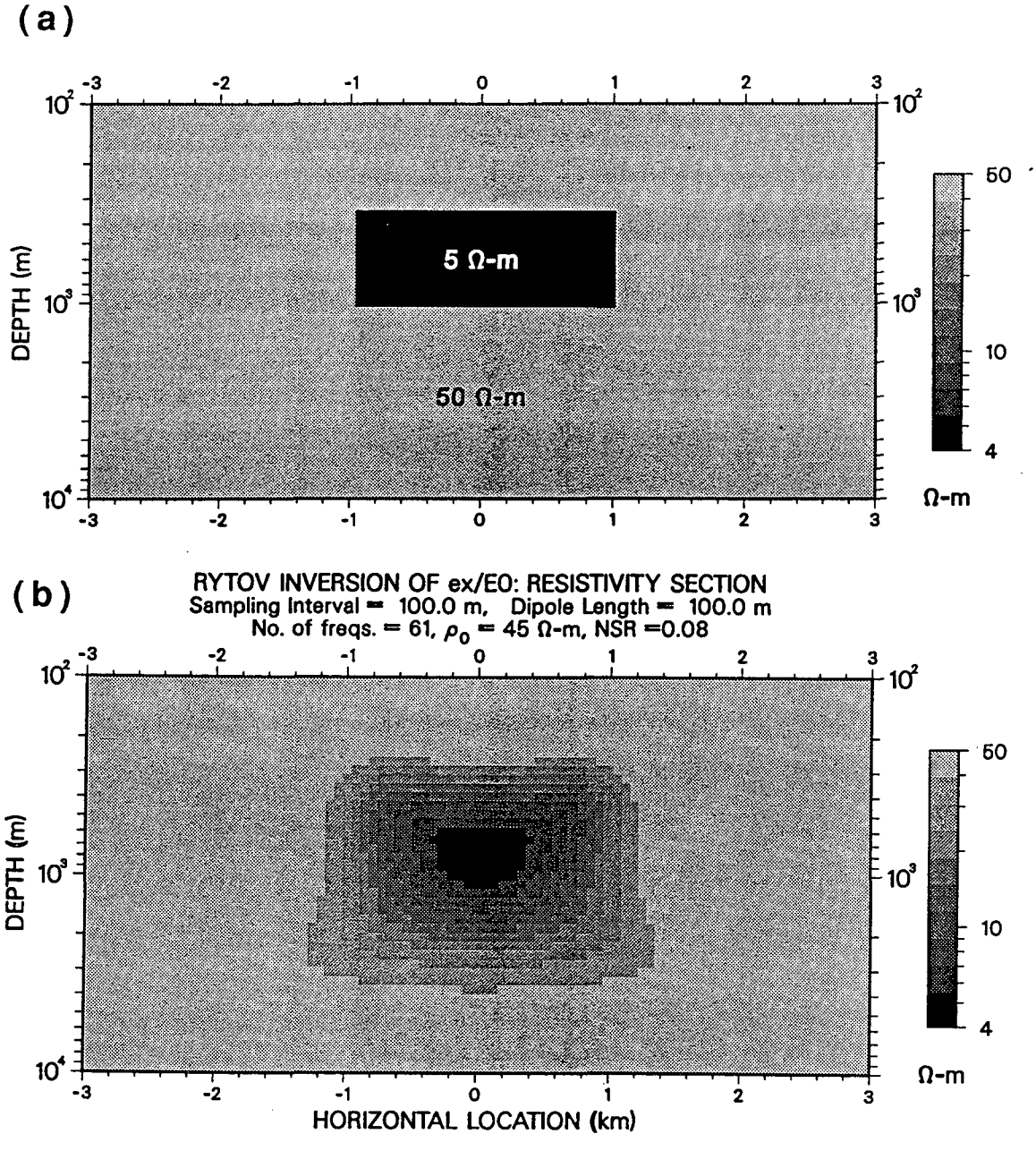

Figure 4-15. A single conductive block buried in a homogeneous background. **(a)** is the resistivity section across strike, and **(b)** is the resistivity section inverted from the TM electric field data. A total of 61 stations and 60 frequencies were used in the inversion. Both station separation and dipole length were made constant and equal to 100 m. The assumed noise-to-signal ratio was 0.08.

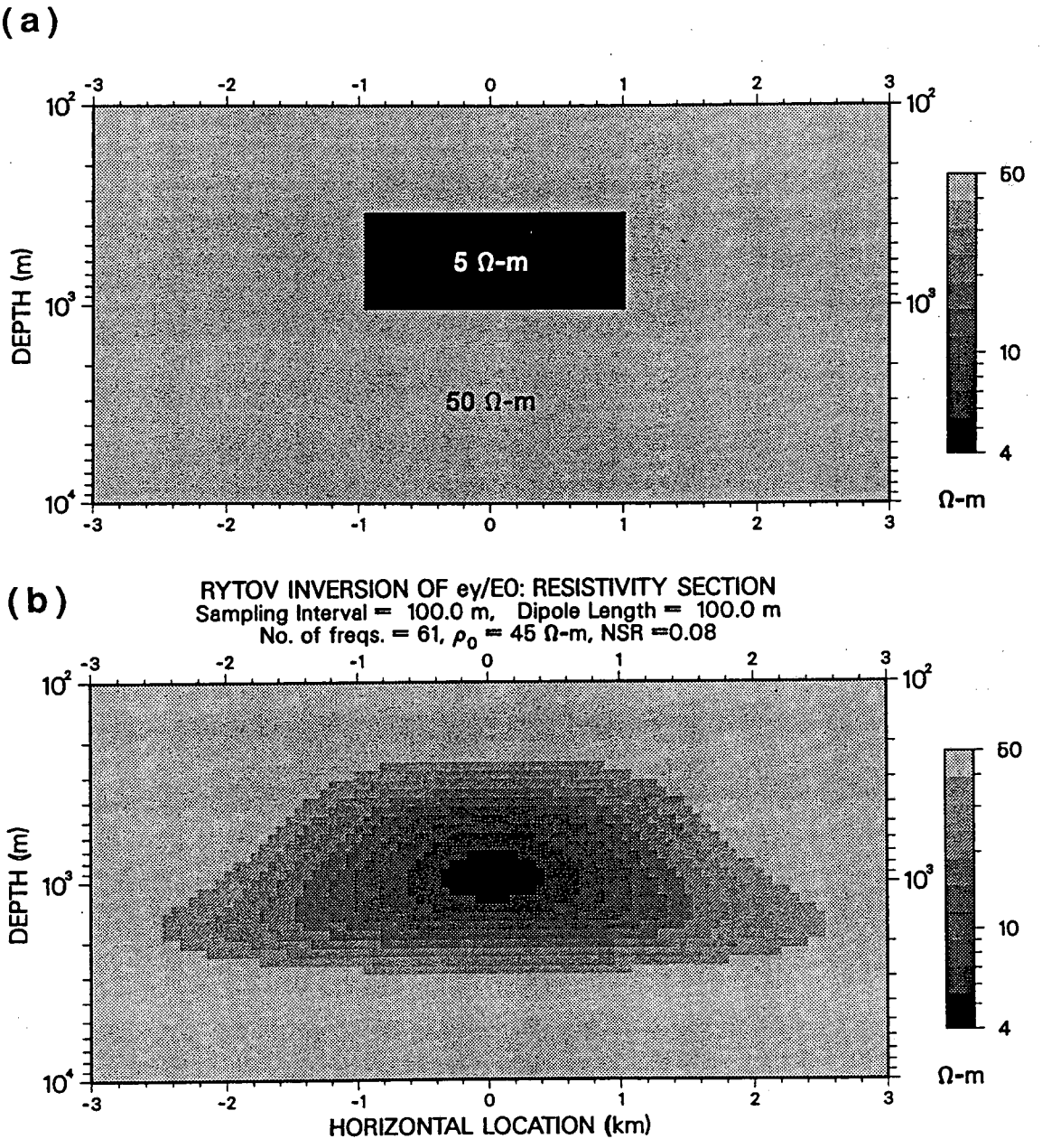

Figure 4-16. A single conductive block buried in a homogeneous background. **(a)** is the resistivity section across strike, and **(b)** is the resistivity section inverted from the TE electric field data (cf. Figure 4-15b). A total of 61 stations and 60 frequencies were used in the inversion. Stations were spaced at 100 m intervals, and the assumed noise-to-signal ratio was 0.08.

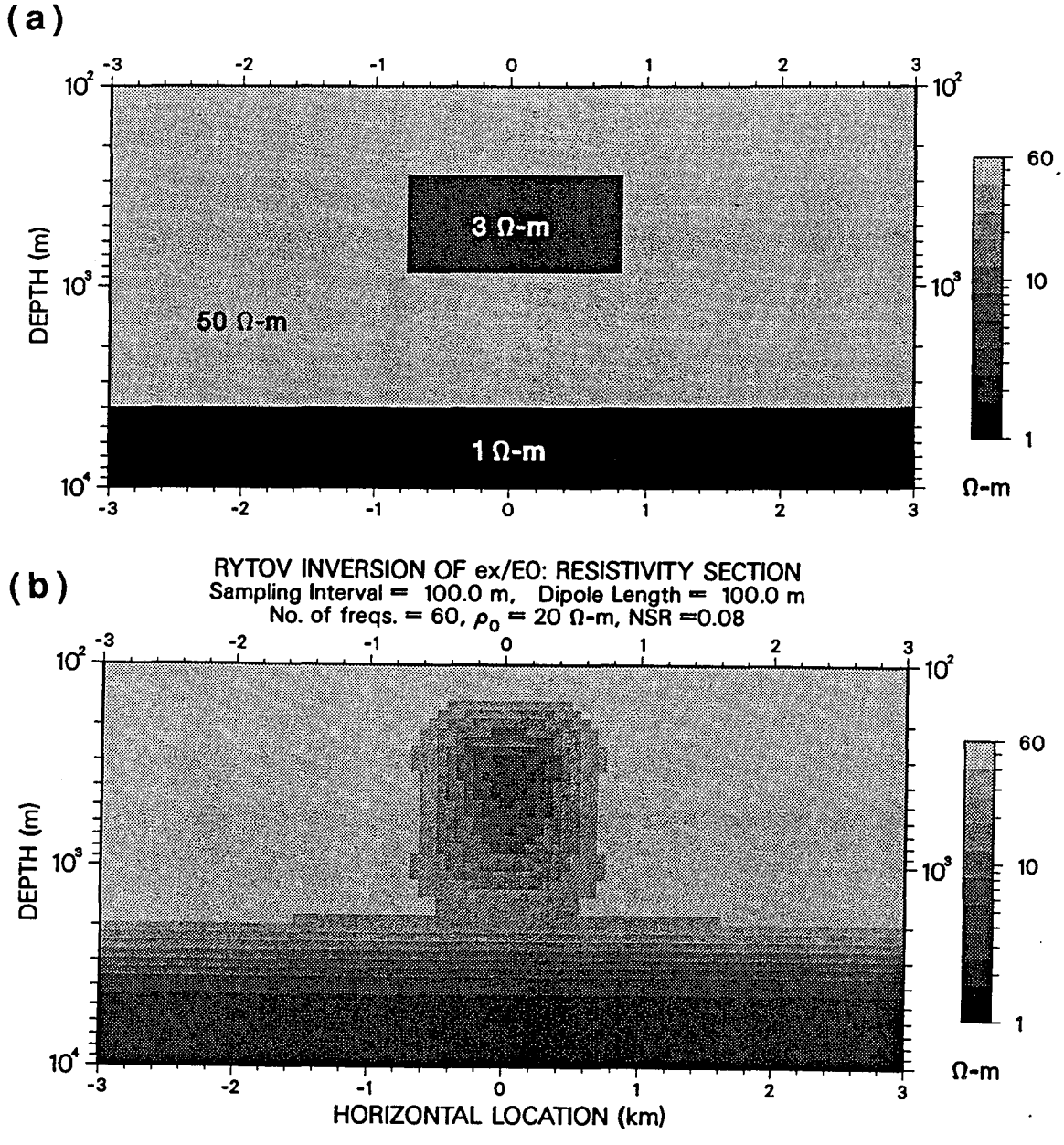

Figure 4-17. A single buried block and a conductive basement. (a) is the resistivity section across strike, and (b) is the resistivity section inverted from the TM electric field data. A total of 61 stations and 61 frequencies were used in the inversion. Both station separation and dipole length were made constant and equal to 100 m. The assumed noise-to-signal ratio was 0.08.

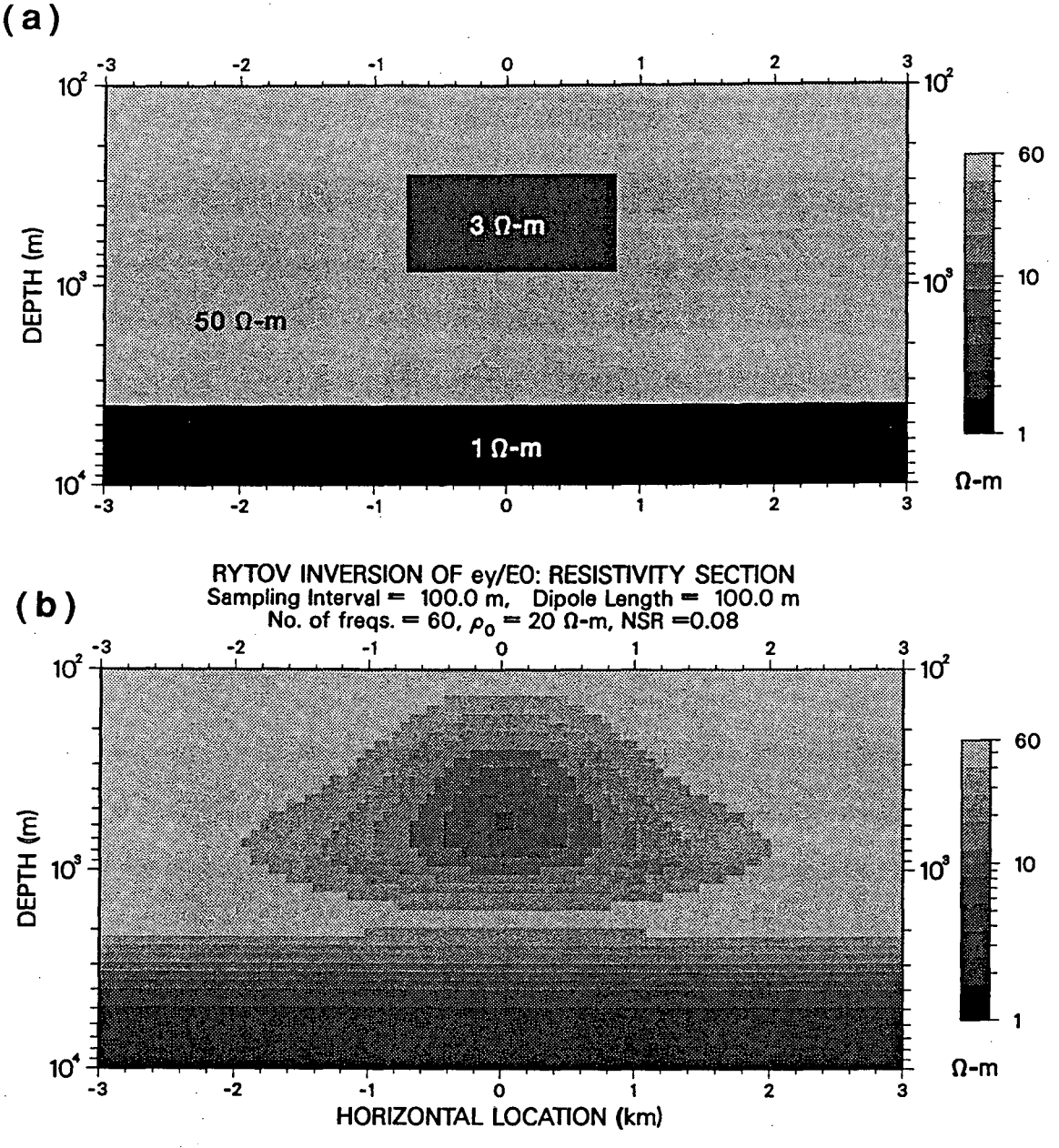

Figure 4-18. A single buried block and a conductive basement. (a) is the resistivity section across strike, and (b) is the resistivity section inverted from the TE electric field data (cf. Figure 4-19b). A total of 61 stations and 61 frequencies were used in the inversion. Stations were spaced at 100 m intervals, and the assumed noise-to-signal ratio was 0.08.

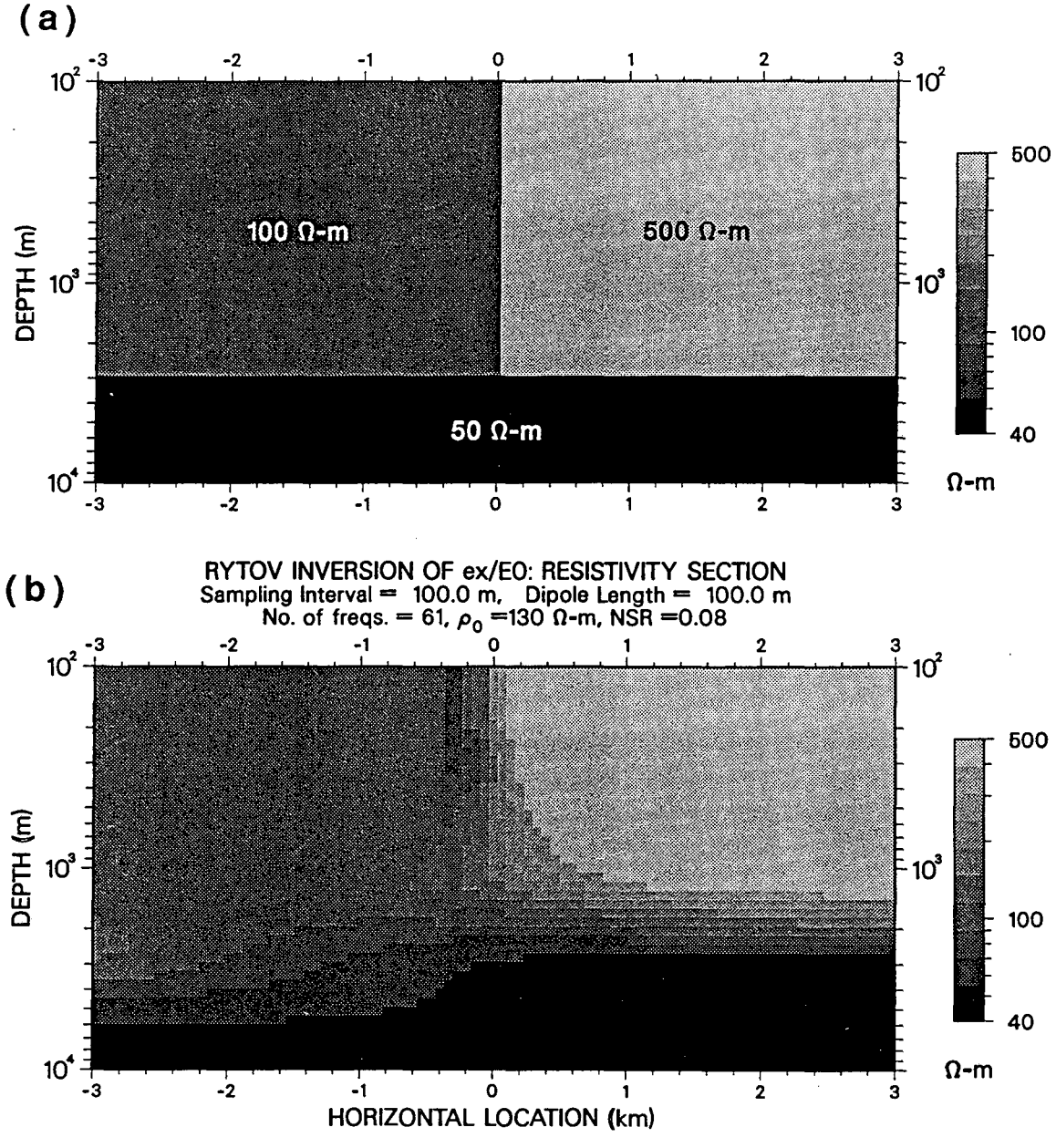

Figure 4-19. A vertical fault and a conductive basement. **(a)** is the resistivity section across strike, and **(b)** is the resistivity section inverted from the TM electric field data. A total of 61 stations and 61 frequencies were used in the inversion. Both station separation and dipole length were made constant and equal to 100 m. The assumed noise-to-signal ratio was 0.08.

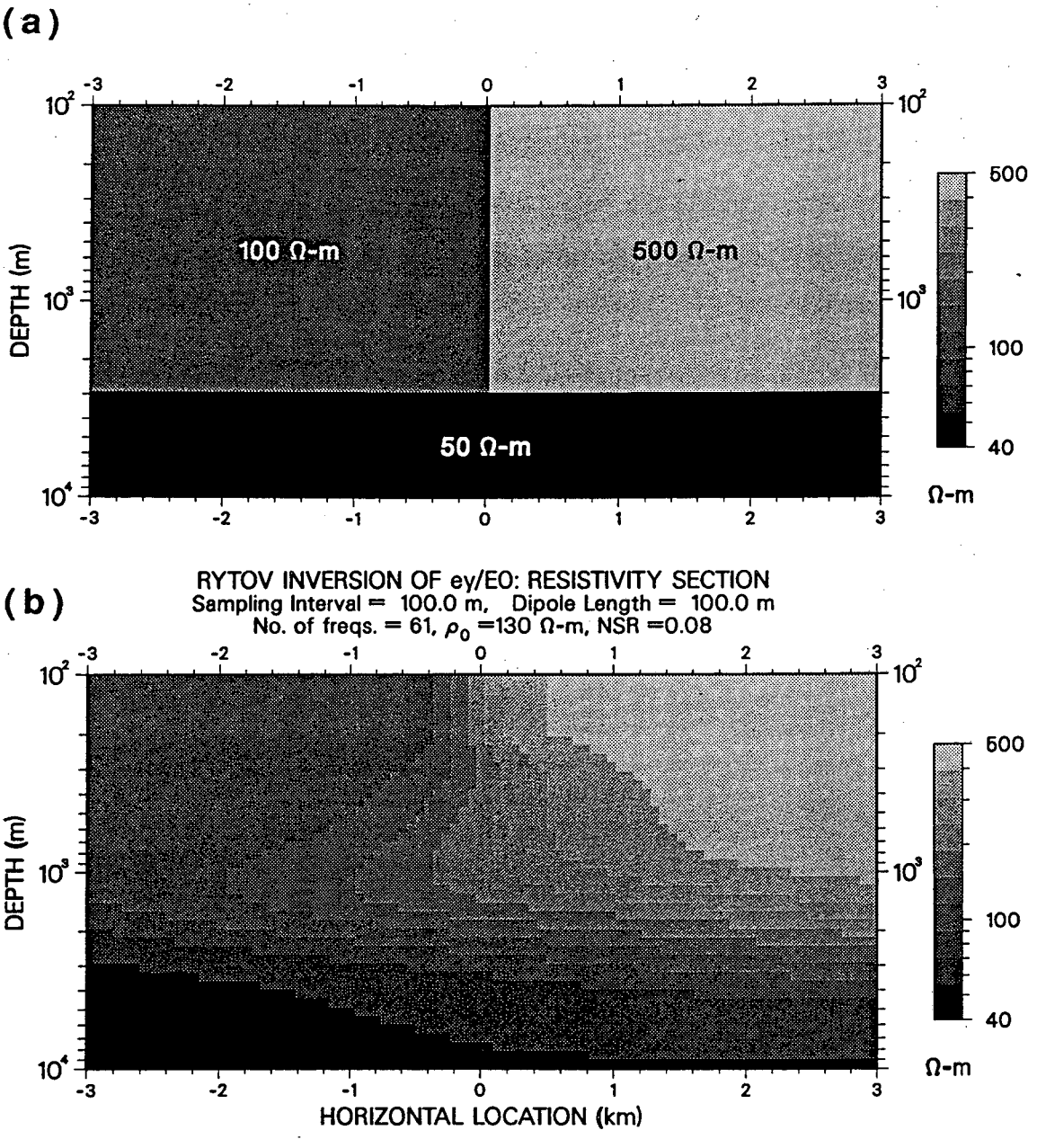

Figure 4-20. A vertical fault and a conductive basement. (a) is the resistivity section across strike, and (b) is the resistivity section inverted from the TE electric field data (cf. Figure 4-23b). A total of 61 stations and 61 frequencies were used in the inversion. Stations were spaced at 100 m intervals, and the assumed noise-to-signal ratio was 0.08.

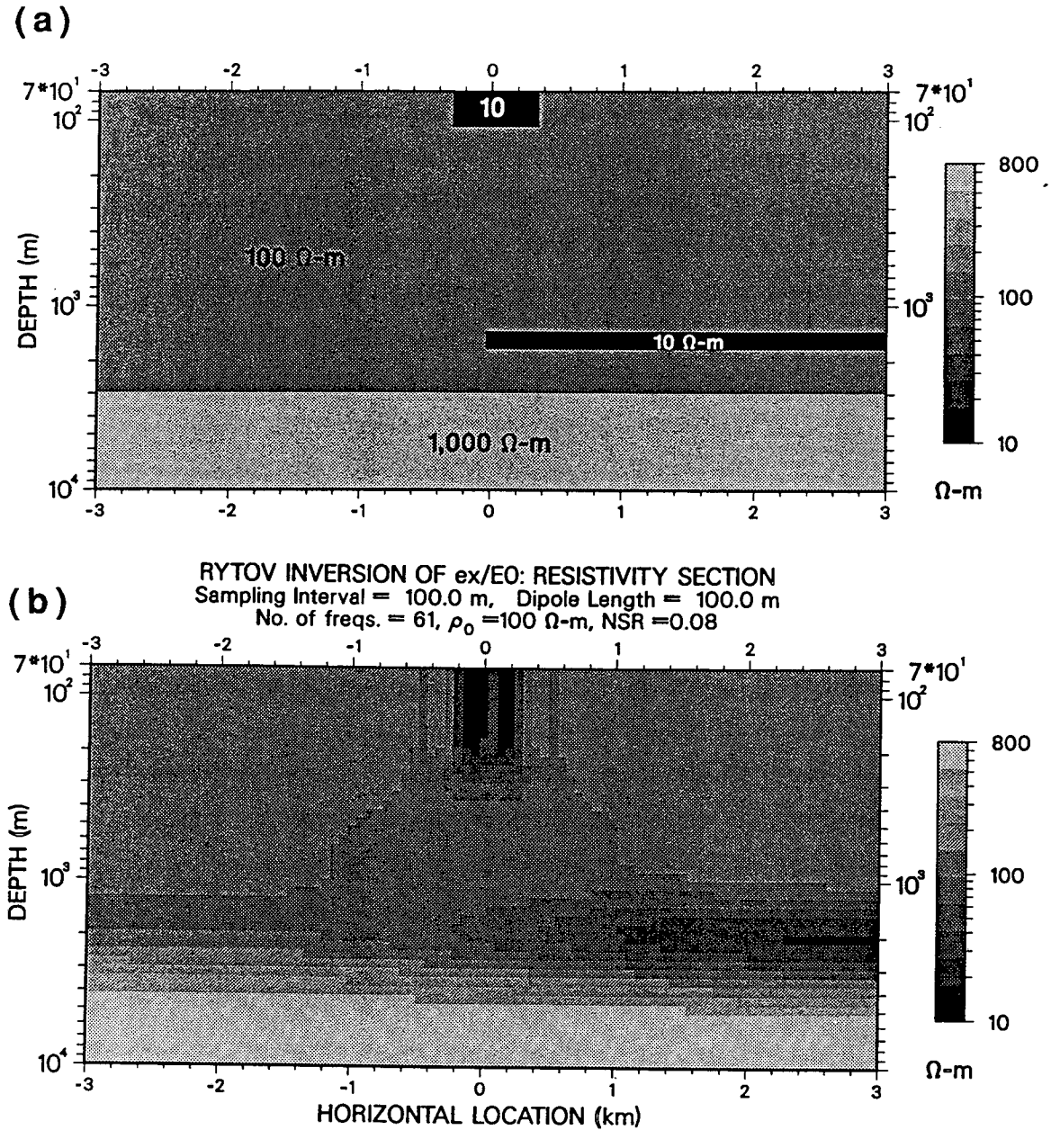

Figure 4-21. A semiinfinite buried slab and a surface inhomogeneity. (a) is the resistivity section across strike, and (b) is the resistivity section inverted from the TM electric field data. A total of 61 stations and 61 frequencies were used in the inversion. Both station separation and dipole length were made constant and equal to 100 m. The assumed noise-to-signal ratio was 0.08.

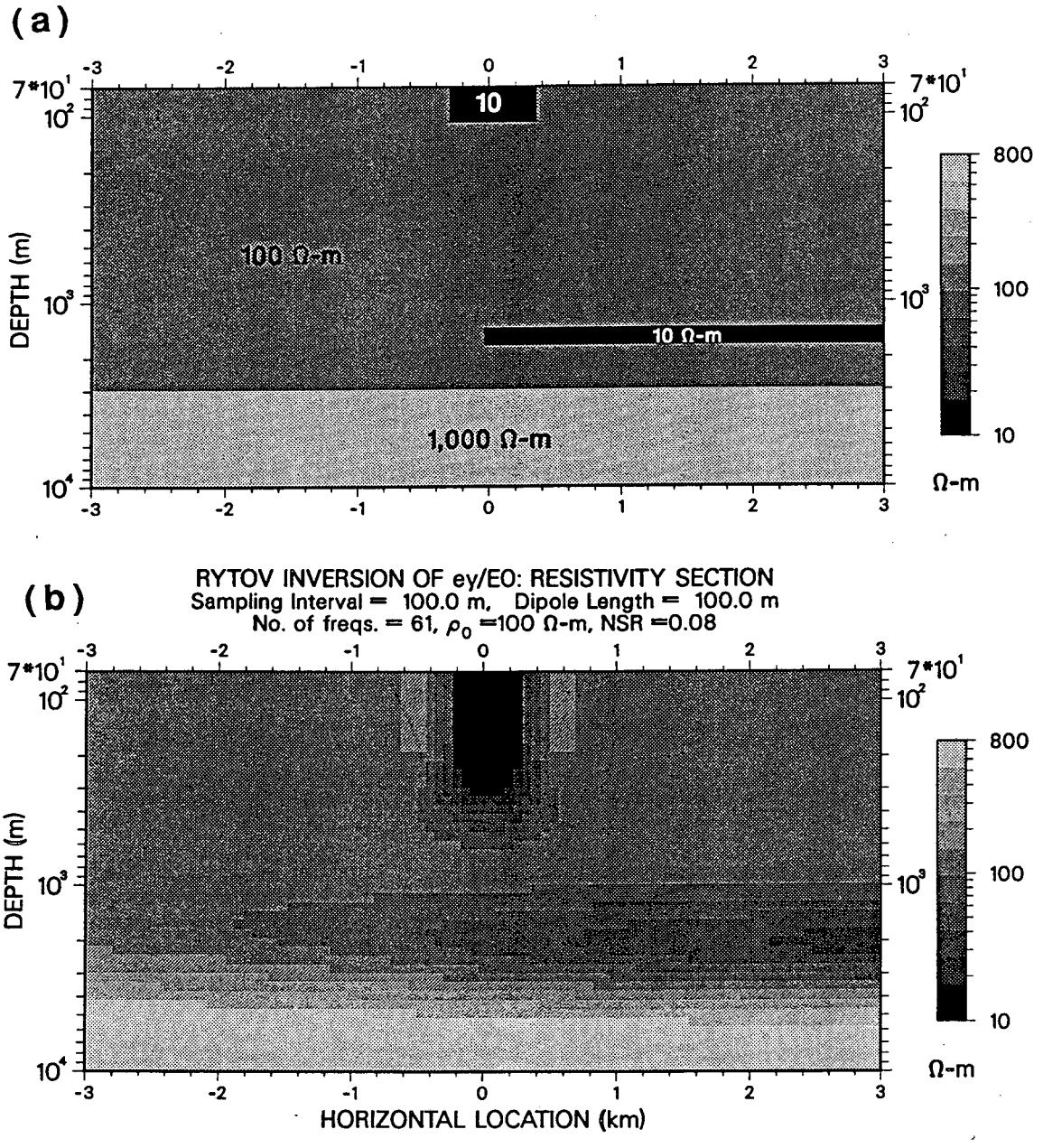

Figure 4-22. A semiinfinite buried slab and a surface inhomogeneity. **(a)** is the resistivity section across strike, and **(b)** is the resistivity section inverted from the TE electric field data (cf. Figure 4-27b). A total of 61 stations and 61 frequencies were used in the inversion. Stations were spaced at 100 m intervals, and the assumed noise-to-signal ratio was 0.08.

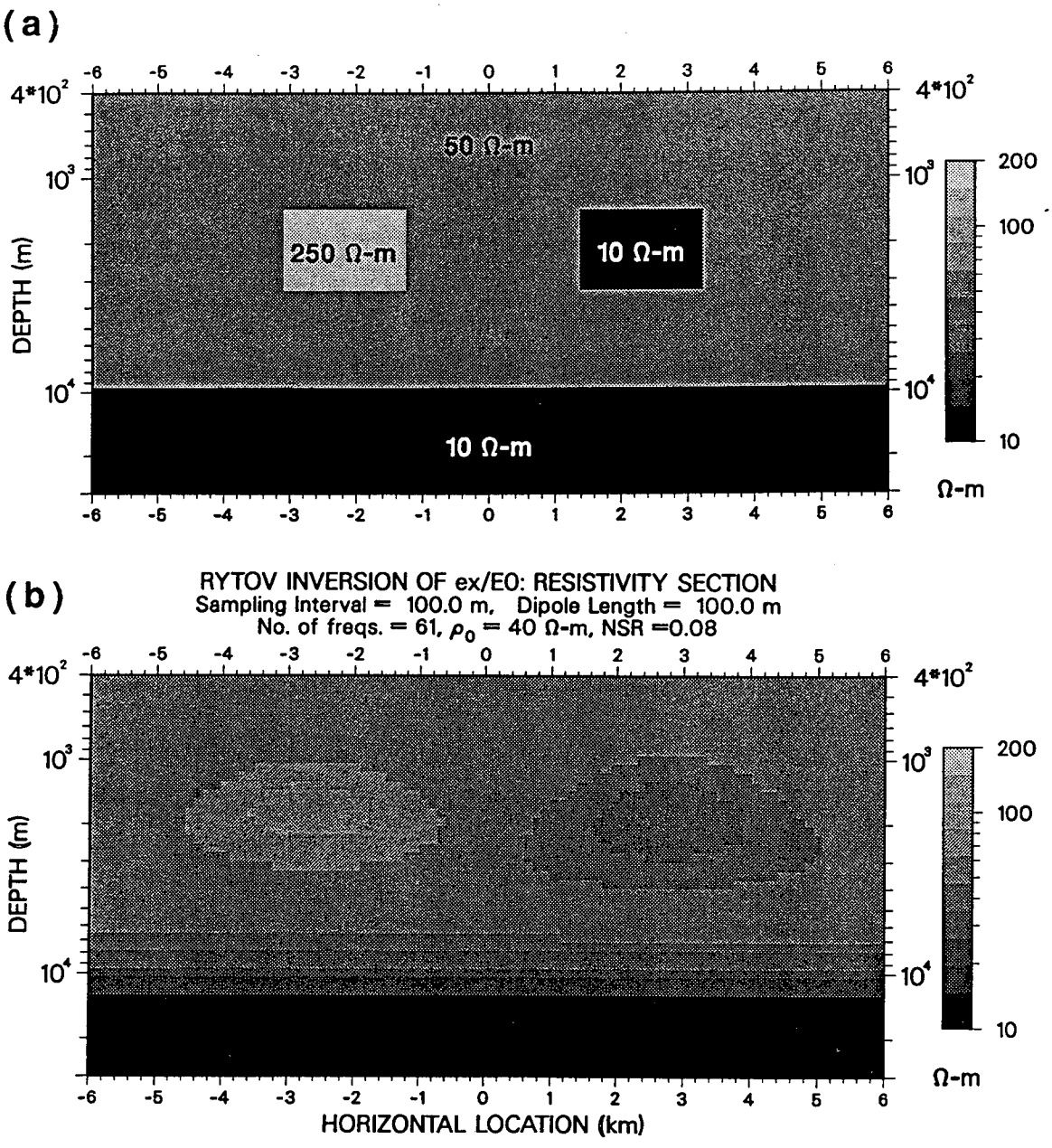

Figure 4-23. Symmetric conductive and resistive blocks. (a) is the resistivity section across strike, and (b) is the resistivity section inverted from the TM electric field data. A total of 121 stations and 61 frequencies were used in the inversion. Both station separation and dipole length were made constant and equal to 100 m. The assumed noise-to-signal ratio was 0.08.

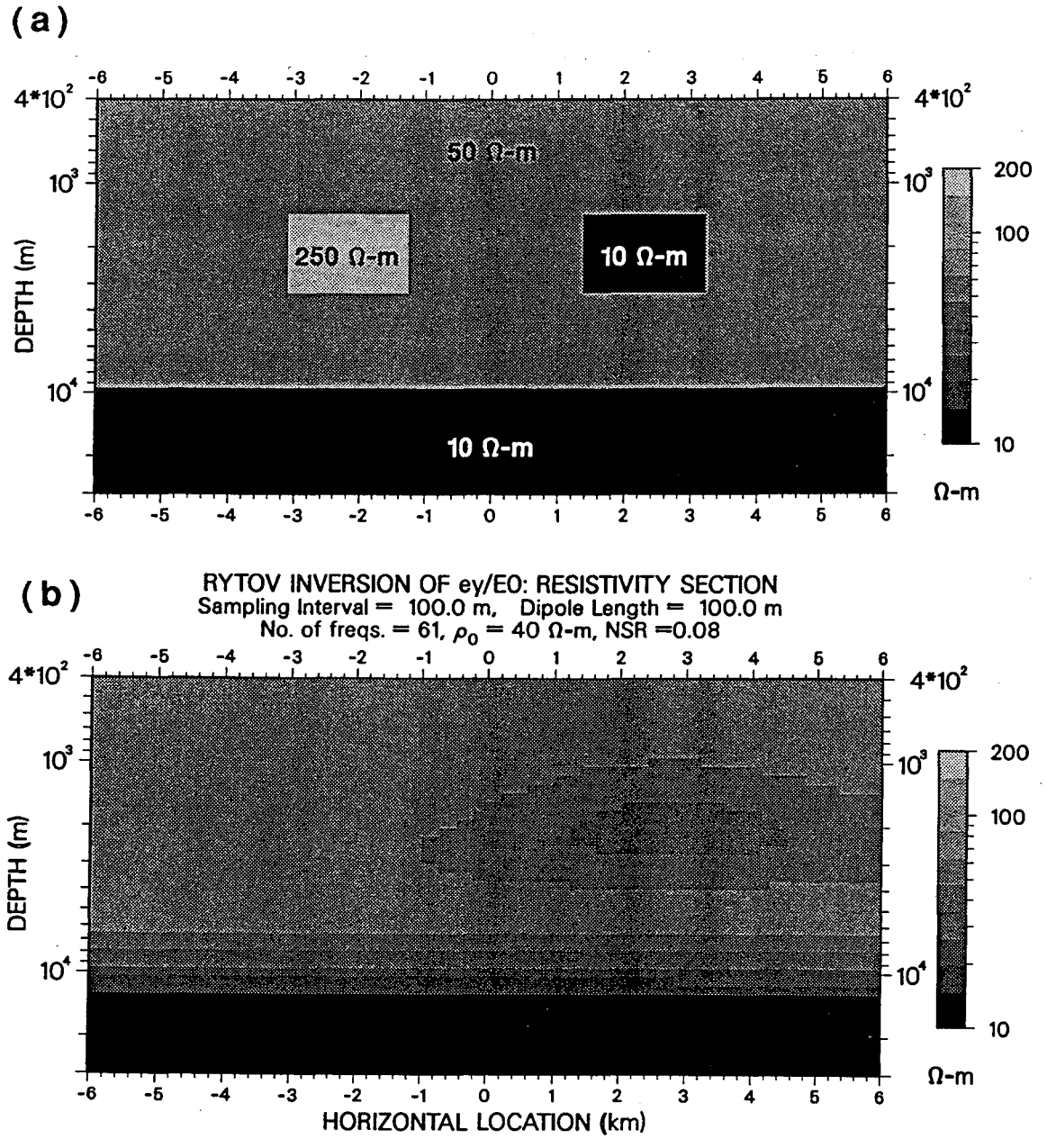

Figure 4-24. Symmetric conductive and resistive blocks. (a) is the resistivity section across strike, and (b) is the resistivity section inverted from the TE electric field data (cf. Figure 4-27b). A total of 121 stations and 61 frequencies were used in the inversion. Stations were spaced at 100 m intervals, and the assumed noise-to-signal ratio was 0.08.

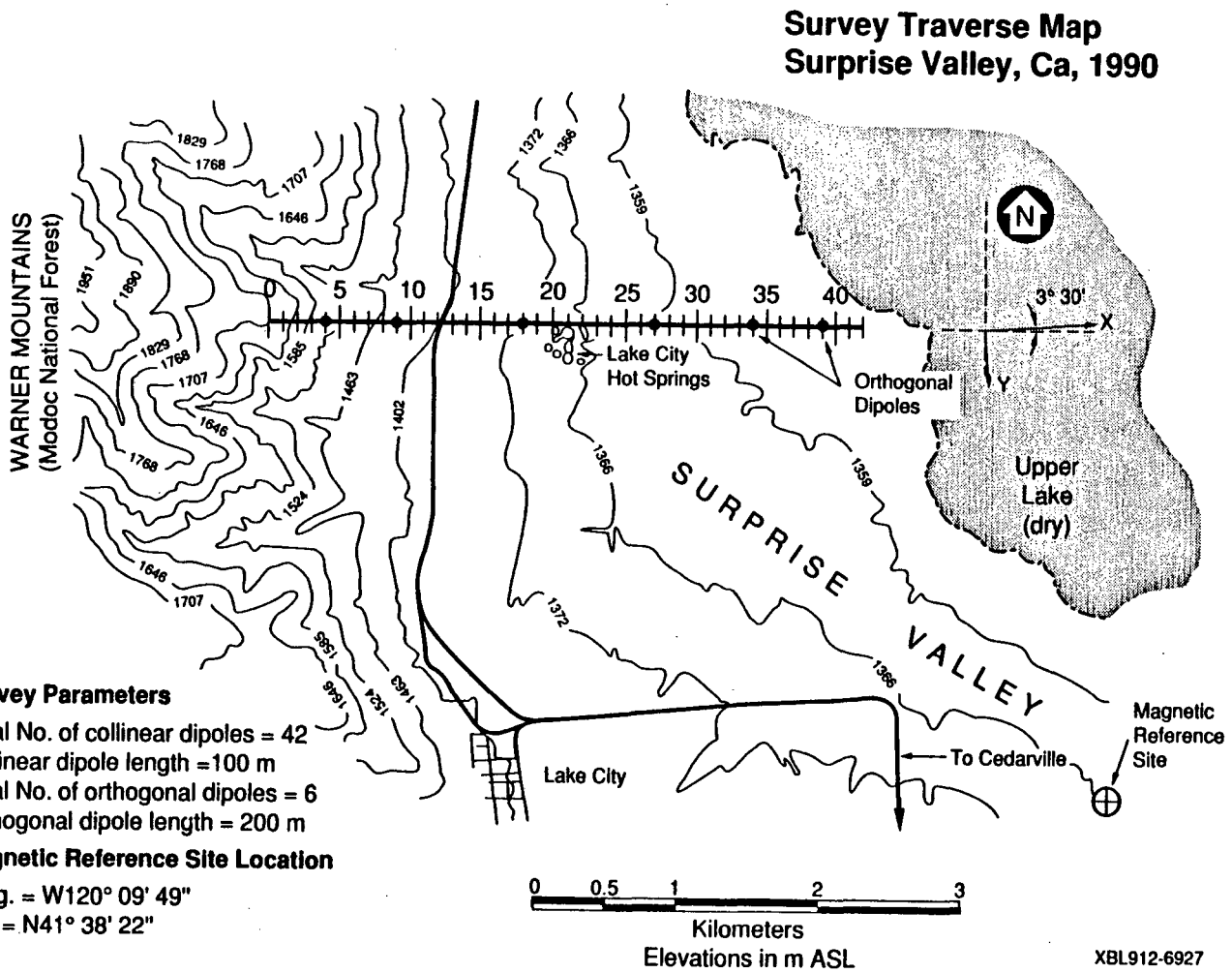

Figure 4-25. Location map of the Surprise Valley test survey. The traverse included 43 contiguous electric dipoles (spans) with a common length of 100 m. Orthogonal electric dipoles and pairs of induction coils were deployed at regular intervals along the traverse as well. The magnetic base station is shown in the lower right-hand corner of the map. Data were collected at 45 different frequencies, evenly distributed logarithmically in the band from 0.003 to 100 Hz.

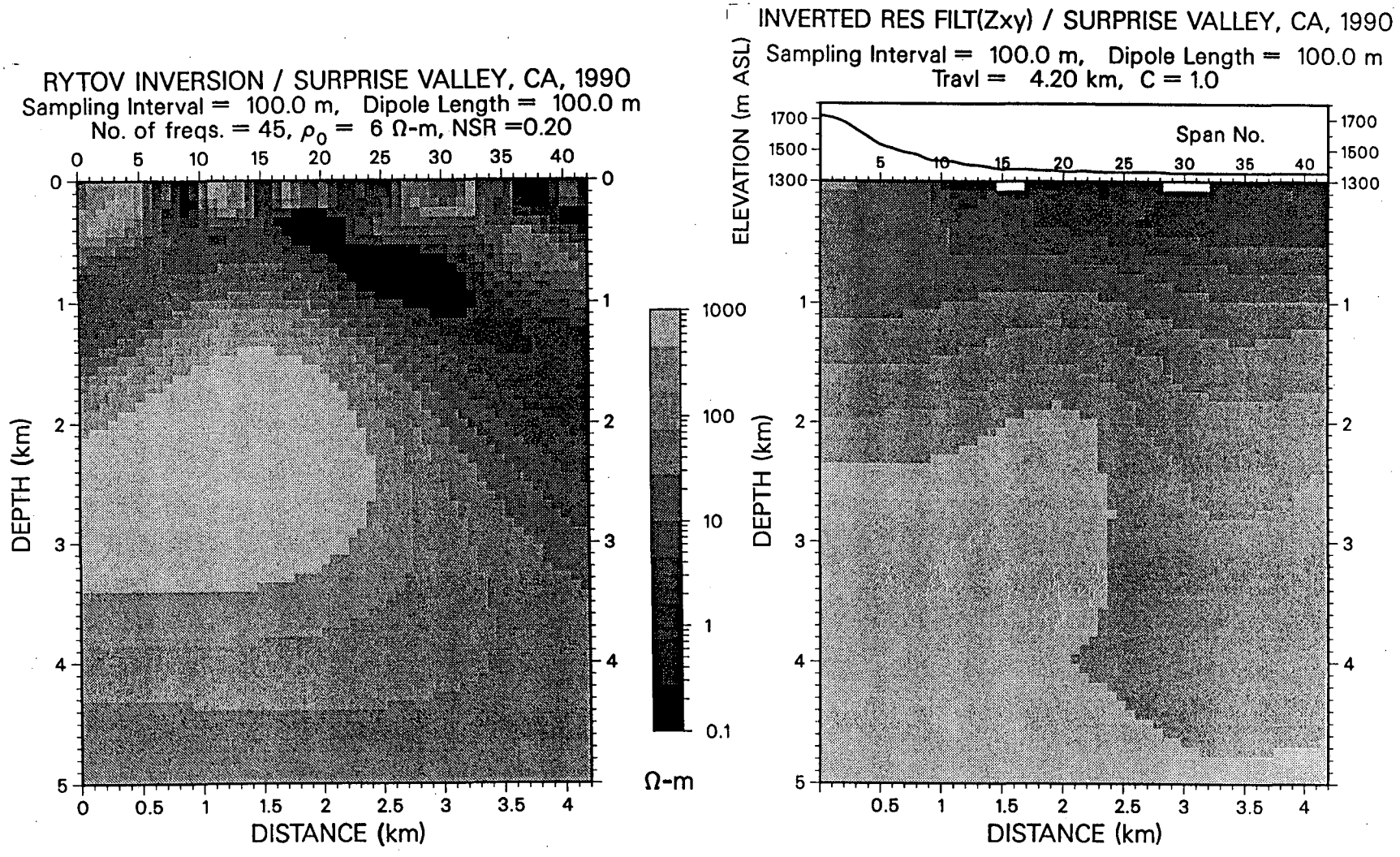

Figure 4-26. (a) Resistivity cross-section inverted with the linearized wavenumber procedure and the Rytov representation of the tangential electric field data along the Surprise Valley transect. Topographic variations were not accounted for. (b) Resistivity cross-section inverted by adaptive spatial filtering and subsequent Bostick (1977) inversion of the Surprise Valley tangential base impedances. Topographic variations were accounted for.

CHAPTER V

ELECTROMAGNETIC ARRAY PROFILING (EMAP)

Electromagnetic Array Profiling (EMAP) was conceived by Prof. Francis X. Bostick following extensive field, experimental, and theoretical MT research work carried out prior to 1980 by the Electromagnetics Research Laboratory (ERL) of The University of Texas at Austin. The first and earliest accounts of the technique can be traced back to various ERL internal reports (circa 1981) which, to the regret of the MT community, were never disclosed in the form of refereed publications. Prof. Bostick also described the seminal ideas about EMAP at a dozen or so informal talks presented to industrial and academic research groups in the USA. Some of the projects, and lecture discussions from the stimulating period of time during which EMAP underwent its initial phases of development have also been recorded by Dr. Bostick's graduate students in the form of Master's and Ph.D. theses. For instance, in dealing with lateral distortion effects due to 2- and 3-D thin sheets, Robertson (1983) tested the concept of spatial filtering on his numerically simulated data. A more general discussion of the subject of spatial filtering was presented by Torres-Verdín (1985) with a study of the Born approximation solutions for the surface MT fields, the mathematical expressions for which rest as the theoretical foundations of EMAP. More recently, Williams (1988) described the results of a test survey in the overthrust geological province of Wind River, Wyoming, and Booker (1988) advanced a practical method to quantify the effect that noisy electric and magnetic data have on the estimation of spatially filtered impedances. Bostick (1986) himself gave the first conference presentation on EMAP.

The topics presented in this chapter summarize some of the research contributions that, in close collaboration with Prof. Francis Bostick, the author has made to the use and understanding of EMAP. The presentation is centered on basic principles and ideas which are tested and expanded in light of 2-D models of subsurface resistivity, particularly with regards to the practical implementation of spatial filtering, a subject already introduced in Chapter IV. In addition, field data examples are presented that show both the feasibility and advantage of of using a continuous line of electric field measurements to sense the MT response of the subsurface. Analysis of procedures for the sounding of 2-D media with

oblique survey traverses, as well as the testing of EMAP over 3-D environments is left as main subjects of research in Chapter VI.

5.1 Introduction

EMAP is an adaptation of magnetotellurics in which a novel field procedure was designed to accomplish two objectives: (1) to overcome spatial aliasing effects associated with the sampling of the surface electric field, and (2) to deploy electric dipoles in such way that the recorded electric field data could be subject to an extended version of the spatial filtering exercised by an individual dipole.

In consideration to common 2- and 3-D electric static distortion, the first objective of EMAP is crucial to insure a successful geoelectric interpretation of the subsurface regardless of how the data are subsequently inverted into a cross-section of subsurface resistivity. Fulfillment of the second design objective of EMAP, however, immediately renders the collected data amenable to a method of interpretation whereby the static component of the surface electric response is separated from its inductive complement prior to inversion. This separation is achieved by progressive lengthening of the distance along which the electric field is spatially averaged at decreasing values of frequency. With the static component conveniently reduced, the filtered electric field data can be inverted into a cross-section of subsurface resistivity with relatively simple, efficient, and stable procedures similar to those used to invert 1-D or 2-D TE electric field data.

The developments presented in Chapter IV show that spatial filtering, or prewhitening, of surface electric field data is a definite element, explicit or implicit, in any procedure that is used to invert TM electric field data into a cross-section of subsurface resistivity. With this notion in mind, it becomes readily apparent that the closer the spacing between adjacent sampling locations the better the way in which the implicit low-pass filtering step will be performed by the inversion method.

However, the need for spatial low-pass filtering of the surface TM data is not as easy to detect and understand in the numerical labyrinths that arise with a nonlinear parametric method of inversion. This kind of inversion is attractive to the MT interpreter mainly because it does not place requirements on the way the data have to be sampled (either with respect to frequency or spatially) to estimate a cross-section of subsurface resistivity. The criterion that drives such methods is the production of a model that reproduces the measured data within an acceptable misfit error. Clearly, when one

considers all of the effects that an unrecognized electric static distortion may have on the inferred depths and resistivities, the satisfaction of a prescribed data misfit error becomes a moot criterion to judge the inversion of poorly sampled electric field data.

At first, it might appear that the EMAP spatial filtering process exacerbates the severe loss of lateral detail that is already present in the data because of the diffusive nature of the surface MT response. This is a valid argument only in the absence of static effects. As shown graphically in section 1.3, even though lateral channeling of the conduction current may sometimes provide a very wide lateral wavenumber content at frequencies for which the depth of penetration is consistent with the region of current flow, the same wavenumber harmonics persist at lower frequencies, and hence are no longer representative of current flow taking place deeper in the earth. *The aim of spatial filtering is simply to remove the wavenumber harmonics associated with conduction current at depths shallower than the effective depth of penetration at a particular frequency.* Since the surface response of the depth-sensitive induction component is already governed by a low-pass filtering process, spatial filtering of the surface electric field will be harmless if the cutoff wavenumber of the applied filter is kept outside the operational band of the induction component. The critical step of spatial filtering is to ascertain this cutoff wavenumber from direct inspection of the data

With the declared objective of employing spatial filtering for the interpretation of EMAP electric field data, this chapter begins with a description of the elements and operational characteristics of the technique. A central part of the exposition is the introduction of a data-adaptive spatial filtering technique whereby the cutoff wavenumber of the applied filter is varied along the survey path in response to changes in both local average resistivity and frequency. Application of this filtering technique shows encouraging results in the interpretation of data derived numerically from 2-D models possessing different degrees of structural complexity. Results are also shown for the application of EMAP at two different field locations. In the first example, a traverse of electric field data from the northern Basin and Range geological province of Nevada are visibly affected by frequency dependent static distortion. The second example describes a survey traverse for the geothermal evaluation of Surprise Valley, California where, even though surface static effects offered no serious difficulty, the continuous sampling of electric field data proved indispensable to detect important lateral variations in the electrical properties of the subsurface.

5.2 Sampling distance and the electric dipole as an alias protection filter

Consider a field procedure in which the potential difference measurements are uniformly separated along a straight line path and where the same separation, L, is used between the two electrodes at each measurement location. Assume that this path extends in the x direction with the electrodes in contact with the ground at the locations $x_j \pm L/2$ ($1 \le j \le M$), and that the connecting wires follow the straight line paths between the electrodes. The configuration for such an electric field array is shown in Figure 5-1.

Under the assumed conditions, the potential difference, V_j, measured at the j-th electric dipole along the electric field array can be written as

$$V_j = \int_{x_j - L/2}^{x_j + L/2} E_x(x)\, dx.$$

Thus, an estimate, $\overline{E}_{xj}$, of the electric field in the neighborhood of the sounding location, x_j, is readily obtained with the ratio

$$\overline{E}_{xj} = \frac{V_j}{L},$$

or, alternatively, from

$$\overline{E}_{xj} = \int_{-\infty}^{+\infty} g(x-x_j)\, E_x(x)\, dx,$$

where g(x) is the so-called "box-car" or rectangular function, defined as

$$g(x) = \begin{cases} \frac{1}{L}, & |x| \le \frac{L}{2} \\ 0, & |x| > \frac{L}{2} \end{cases}.$$

The electric field estimates, $\overline{E}_{xj}$, above are discrete and uniformly spaced samples of the continuous function $\overline{E}_x(x)$ described by

$$\overline{E}_x(x) = \int_{-\infty}^{+\infty} g(x_0-x)\, E_x(x_0)\, dx_0,$$

or, in compact notation, by

$$\overline{E}_x(x) = E_x(x) * g(x), \qquad (5.1)$$

where the symbol "$*$" indicates convolution. With the spatial Fourier transform of $E_x(x)$ defined as

$$E_x(\xi) = \mathcal{F}\{E_x(x)\} = \int_{-\infty}^{+\infty} E_x(x)\, e^{+i\xi x}\, dx,$$

equation (5.1) can be written in the wavenumber domain as

$$\overline{E}_x(\xi) = E_x(\xi)Sa(\xi), \tag{5.2}$$

where

$$\overline{E}_x(\xi) = \mathcal{F}\{\overline{E}_x(x)\}, \text{ and}$$

$Sa(\xi)$, the sampling function, is a low-pass filter with its first crossover at $\xi=\pm 2\pi/L$, and is determined from the expression

$$Sa(\xi) = \mathcal{F}\{g(x)\} = \int_{-\infty}^{+\infty} g(x)\, e^{+i\xi x}\, dx = \frac{\sin(\frac{\xi L}{2})}{\frac{\xi L}{2}}.$$

As evidenced by equation (5.2), the sampling function plays the role of an alias protection filter in the measurement process whereby samples, $\overline{E}_{xj}$, of the function $\overline{E}_x(x)$ are obtained at different locations along the electric field array. Since the $\overline{E}_{xj}$ series of estimates consists of direct samples of the function $\overline{E}_x(x)$, the only control on the degree of alias protection in the measurement process is through adjustments of the spacing, L, between measurement electrodes, and of the sampling interval, x_j-x_{j-1}, between adjacent sounding sites. The smaller the sampling interval the higher is the Nyquist wavenumber; the larger the value of L the lower the cutoff wavenumber of the sampling function. Although a lower cutoff wavenumber for the sampling function goes with better alias protection, it was shown in section 1.2 that this also may cause a loss of lateral resolution at high frequencies where the objective is to sense geoelectric features smaller than a dipole length. A standard dipole length should be comparable with the shallowest depth of penetration at the highest frequency. The electric field array, on the other hand, should be long enough to allow the suppression of static effects due to geoelectric structure of size comparable to the depth of penetration at the lowest frequency. Economic conditions are usually a key factor in determining both the length of the dipole and the distance covered by the electric field array. The practicalities involved in the gathering of electric and magnetic field data along and about the electric field array are discussed below.

5.3 EMAP field procedure

Estimating a profile of subsurface resistivity beneath a line of surface measurements may require closely spaced electric and magnetic field sampling locations, not only along the profile but also laterally away from it. When the survey path coincides with the x-axis, for instance, the frequency domain relationship between the tangential electric field, E_x, and the horizontal magnetic field components, H_x and H_y, measured at the same point along the path is

$$E_x(x,\omega) = Z_{xx}(x,\omega)\, H_x(x,\omega) + Z_{xy}(x,\omega)\, H_y(x,\omega), \qquad (5.3)$$

where ω is the radian frequency, x is the coordinate of the observation point, and the Z_{xx} and Z_{xy} terms are downward looking conventional MT impedances. These impedances are functions of the 3-D subsurface resistivity distribution and are time invariant.

As emphasized earlier, the modification of equation (5.3) related to EMAP allows one to perform spatial filtering of the tangential electric field component, E_x, along the survey path. Also, in contrast to conventional magnetotellurics, with the EMAP field procedure electric field measurements are not referred to the local magnetic field, but rather to the primary plane-wave magnetic field within the survey area. The latter is estimated by spatial areal averaging of the magnetic field measurements taken along and about the survey line (see section 2.6).

The first constraint imposed by a field procedure that requires processing and interpretation of MT fields rather than of impedances is that, because of their random source mechanisms, all electric and magnetic field signals have to be synchronously acquired. When the survey line consists of a great many sampling locations, the requirement of synchronization among all of the field measurements may place excessive demands even on the most powerful MT data acquisition systems. A procedure to overcome this practical limitation consists in recording the magnetic signals at a fixed base station during the same times signals are recorded at any of the field measurement locations.

In the frequency domain, the relationship between the magnetic field components, H_x and H_y, measured at a base site located at (x_B,y_B), and the E_x field component measured along the survey path can be written with the linear relation

$$E_x(x,\omega) = \hat{Z}_{xx}(x,\omega)\, H_x(x_B,y_B,\omega) + \hat{Z}_{xy}(x,\omega)\, H_y(x_B,y_B,\omega), \qquad (5.4)$$

where the terms $\hat{Z}_{xx}$ and $\hat{Z}_{xy}$ in this last equation, henceforth referred to as **base impedances** are not conventional MT impedances, but do exhibit the same time invariance property. In similar fashion, the relationship between the magnetic field components H_x and H_y measured at a survey point, (x,y), and the magnetic field components measured at the base site is expressed by the set of linear equations

$$H_x(x,\omega) = T_{xx}(x,y,\omega)\, H_x(x_B,y_B,\omega) + T_{xy}(x,y,\omega)\, H_y(x_B,y_B,\omega), \text{ and} \qquad (5.5)$$

$$H_y(x,\omega) = T_{yx}(x,y,\omega)\, H_x(x_B,y_B,\omega) + T_{yy}(x,y,\omega)\, H_y(x_B,y_B,\omega), \qquad (5.6)$$

where the terms T_{xx}, T_{xy}, T_{yx}, and T_{yy} are time invariant magnetic transfer functions.

With the use of equations (5.4) through (5.6), basic operations on the electric and magnetic fields such as spatial filtering and areal averaging can be performed on the estimated base impedances and magnetic transfer functions. The procedure suggested for the practical synchronization of field measurements embodied in equations (5.4) through (5.6) is essentially a generalization of the method described in section 4.11 as an intermediate step for the computation of secondary electric and magnetic field variations.

Finally, the EMAP modification of equation (5.3) relates the estimated primary magnetic field components, $\overline{H}_x$, and $\overline{H}_y$, with the measurements of E_x made along the survey path, and is written as

$$E_x(x,\omega) = \tilde{Z}_{xx}(x,\omega)\, \overline{H}_x(\omega) + \tilde{Z}_{xy}(x,\omega)\, \overline{H}_y(\omega). \qquad (5.7)$$

Because of their relation to the EMAP field procedure, the impedances $\tilde{Z}_{xx}$ and $\tilde{Z}_{xy}$ in equation (5.7) are henceforth referred to as the **EMAP impedances.** It is remarked that $\tilde{Z}_{xx}$ and $\tilde{Z}_{xy}$ can have different properties than the conventional and base impedances defined in equations (5.3) and (5.4), respectively, especially when the surface magnetic field exhibits appreciable local amplitude variations either along the survey path or at the base station.

Figure 5-2 depicts the characteristics of the EMAP field procedure. A simple modification of the field configuration shown in that figure would involve the measurement of the orthogonal electric field component, E_y, at selected locations along the survey path. If available, these measurements may be used to estimate, for instance, the dimensionality of the underlying resistivity distribution with standard procedures (Vozoff, Ed., 1986). However, the use of a single dipole perpendicular to the electric field array may prove

insufficient either to overcome aliasing effects or to reduce static distortion that can significantly bias the estimated parameters of dimensionality. Additionally, vertical magnetic field measurements can be acquired at selected locations along the survey path to ascertain the sensitivity of the electric field array to induction processes in the subsurface taking place laterally away from the path. These two options are discussed in more detail in Chapter VI. A procedure to carry out spatial filtering of the tangential electric field measurements made along the survey path is discussed next.

5.4 A data-adaptive spatial filtering procedure

Individual dipole responses measured along the electric field array may be combined to produce a wavenumber filtered output. A first choice for a low-pass spatial filter that can be synthesized from the electric field array is a Hanning window or "cosine bell." For one thing, the Hanning window has better roll-off characteristics in the wavenumber domain than the box-car function related to an individual dipole response. Moreover, because of its spatial symmetry the Hanning window has a purely real wavenumber response.

A Hanning window, h(x), of width W and centered about the origin is described by the formula

$$h(x) = \begin{cases} \frac{1}{W}\left(1 + \cos\frac{2\pi x}{W}\right), & |x| \le \frac{W}{2} \\ 0, & |x| > \frac{W}{2} \end{cases} , \qquad (5.8)$$

or, in the wavenumber domain, by

$$H(\xi) = \frac{\sin\left(\frac{W\xi}{2}\right)}{\frac{W\xi}{2}}\left[\,1 - 0.5\,\frac{\frac{W\xi}{2}}{\frac{W\xi}{2} + \pi} - 0.5\,\frac{\frac{W\xi}{2}}{\frac{W\xi}{2} - \pi}\,\right] . \qquad (5.9)$$

From this last expression it can be easily shown that the roll-off of $H(\xi)$ falls as $1/(W\xi)^3$ for large values of ξ, and that its 3dB amplitude cutoff point is approximately located at $\xi=4.52/W$. However, given the discrete characteristics of the electric field array, the continuous Hanning window given by equation (5.8) may at best be approximated as a "staircase" representation. This idea is graphically illustrated in Figure 5-3.

Assuming that the electric field array is deployed along a straight line, and that the electric dipoles have all the same length, the discrete Hanning window, $\hat{h}(x,x_k)$, synthesized from the electric field array about the point $x=x_k$ may be written as

$$\hat{h}(x,x_k) = \sum_{j=1}^{M} \beta_j \, g(x_j-x) \qquad k = 1, ..., M, \tag{5.10}$$

where M is the total number of dipoles in the array[1] .

The coefficients β_j in equation (5.10) describe the way in which dipole responses adjacent to the sounding site $x=x_k$ are weighed to emulate the shape of a Hanning window. For a given window width, W, and center point, x_k, these weights can be adjusted so that the difference between the continuous Hanning window, $h(x-x_k)$, and the synthesized version of it, $\hat{h}(x,x_k)$, is minimized in a least-squares sense. The difference, ψ, between these two windows is a function of position along the array, and is written as

$$\psi_k(\beta_j,\alpha) = \int_{-\infty}^{+\infty} \left[h(x-x_k) - \hat{h}(x,x_k)\right]^2 dx + \alpha \left(\int_{-\infty}^{+\infty} \hat{h}(x,x_k)\, dx - 1\right), \tag{5.11}$$

where the Lagrange multiplier, α, is introduced to enforce the unimodularity of $\hat{h}(x,x_k)$ in the minimization of ψ_k.

To minimize the functional ψ_k defined by equation (5.11), substitute equation (5.10) into equation (5.11) and differentiate with respect to α and all β_j's. The resulting set of normal equations has the simple solutions

$$\beta_j = \int_{x_j - L/2}^{x_j + L/2} h(x-x_k)\, dx \qquad \left(\sum_{j=1}^{M} \beta_j = 1\right), \tag{5.12}$$

It then follows that, for given window width, W, the coefficients β_j given by equation (5.12) will be zero whenever

$$x_j \le x_k - \frac{W}{2} - \frac{L}{2}, \text{ or} \tag{5.13}$$

$$x_j \ge x_k + \frac{W}{2} + \frac{L}{2}. \tag{5.14}$$

---

[1] Consideration of both curvilinear paths and variable dipole lengths entails only slight modifications to the developments presented in this section.

This implies that the actual minimum and maximum indexes for the summations in equations (5.11) and (5.12) are the largest and smallest values of j that satisfy the inequalities (5.13) and (5.14), respectively. Equations (5.10) an (5.12) provide a useful treatment for the special situation in which the center point, x_k, of $\hat{h}(x,x_k)$ is close to, or coincident with, an end of the survey traverse.

Even though a window width value is presupposed above for the derivation of the β_j coefficients, the selection of this parameter is critical to the filtering operation. The value of W can be adjusted if a cutoff wavenumber is specified beforehand. A useful choice of cutoff wavenumber, ξ_c, for the low-pass filter is the one for which, at a particular frequency, the amplitude of the electric induction component no longer dominates over the amplitude of the static component. For a subsurface resistivity distribution described by small lateral and vertical resistivity variations about an average value, this cutoff wavenumber is frequency dependent and inversely proportional to the Bostick (1977) depth of penetration, z_B, i.e.,

$$\xi_c(x_k,\omega) \approx \frac{1}{z_B(x_k,\omega)} \tag{5.15}$$

(see section 2.7). At a given frequency, ω, the Bostick depth of penetration is an estimate of the depth down to which the inductive response from the subsurface develops a maximum effect on the measured surface electric field. Over 1-D geoelectric media this depth of response can be estimated directly from the apparent resistivity curve (Bostick, 1977). However, in the presence of static effects the estimation of z_B from apparent resistivity data may suffer an appreciable bias. To reduce this bias, prior to computing z_B, the EMAP wave impedance $\tilde{Z}_{xy}$ defined in equation (5.7) may be low-pass filtered with a bootstrapping value of window width[2]. Subsequently, a Bostick depth of penetration is computed for the filtered impedance with the formula

$$z_B(x_k,\omega) = \frac{1}{\omega\mu}\left|\bar{Z}_{xy}(x_k,\omega)\right| \tag{5.16}$$

(Bostick, 1977), where

---

[2] When the only sample of the magnetic field is acquired at the base station, the base impedance, $\hat{Z}_{xy}$, can be used in place of $\tilde{Z}_{xy}$ to perform spatial filtering.

$$\overline{Z}_{xy}(x_k,\omega) = \sum_{j=1}^{M} \beta_j \widetilde{Z}_{xy}(x_k,\omega), \qquad (5.17)$$

and the β_j coefficients are computed from equation (5.12).

The important fact about equation (5.16) is that different widths, W, for the discrete Hanning window change the value of the depth of penetration, z_B. To clarify this important point by way of an example, consider the 2-D model shown in Figure 5-4, redrawn from Figure 1-1 to include the location of an extra sounding location. In the new figure, Site No. 1 is centered within the surface conductor, whereas Site No. 2 is located over the resistor and 250 m away from Site No. 1. The filtered TM apparent resistivity and impedance phase curves associated with Site No. 1 are shown in Figure 5-5. Both of these curves are plotted as functions of the Hanning-window width for a symmetric and discrete window centered about the sounding location and synthesized from 100-m dipole responses at three different frequencies, namely, 0.01, 1, and 100 Hz. For comparison, the apparent resistivity panel in Figure 5-5 also shows 1-D apparent resistivity values (constant with respect to window width) at the same three frequencies assuming that the outcropping conductor in Figure 5-4 is a layer rather than a block.

As evidenced from Figure 5-5, the magnitude of the filtered electric field at Site No. 1 can vary considerably with the width of Hanning window used to perform the spatial averaging (i.e., with the cutoff wavenumber of the applied filter). At 0.01 Hz, for instance, immediately after the window is wide enough to encompass electric field variations outside the conductor, the filtered apparent resistivity develops an asymptotic behavior toward the 1-D response value at the same frequency. Within the conductor, the filtered apparent resistivity is only slightly sensitive to the window width used in the averaging. At the highest frequency, however, excessively large values of W take the apparent resistivity curve far away from the 1-D response curve at the same frequency, hence causing oversmoothing of the electric response.

A criterion to choose a window width value that is consistent with the wavenumber content of the electric induction component stems from equation (5.15). This inequality can be made an equality in the following way:

$$\xi_c(x_k,\omega) = \frac{1}{c\, z_B(x_k,\omega)},$$

where c is an arbitrary real constant (see also section 2.7). The cutoff wavenumber, ξ_c, above is inversely proportional to the window width, W, so that one can write

$$W(x_k,\omega) = c\, z_B(x_k,\omega). \qquad (5.18)$$

To find the appropriate window width, W, that satisfies equation (5.18) for a prescribed value of c, one tracks amplitude response curves similar to those shown in Figure 5-5 along the window-width axis until the equality is satisfied within an acceptable tolerance level. This search can be done numerically in a number of ways, none of which entails significant computer times. In fact, a repeated sequence of window-width adaptations for as many dipoles and frequencies there are along the electric field array may take no more than a few seconds. A procedure that has proved very efficient for the adaptation of W along the electric field array is a simple fixed-point iteration of equation (5.18).

Several other points concerning the solution of equation (5.18) deserve special mention. First, the real constant, c, in that equation plays the role of a window-width expansion factor that must be input to the filter adaptation process to control the roll-off characteristics of the applied Hanning window. In adjusting c, it should be remembered that lateral detail in the $\widetilde{Z}_{xy}$ impedance function is lost when W increases very rapidly. This means that the smallest acceptable value for c is the most desirable. Experience shows that in most practical cases $1 \leq c \leq 4$ is an appropriate range. Second, the reason why only the $\widetilde{Z}_{xy}$ impedance is used in driving the filter adaptation process is that, even though the cross-coupling wave impedance, $\widetilde{Z}_{xx}$, may sometimes undergo large amplitude variations, this term is insensitive to the zero wavenumber harmonic of the lateral variations of subsurface resistivity (section 2.5), meaning that spatial filtering of $\widetilde{Z}_{xx}$ will consistently approach zero for increasing values of W. However, when the survey traverse is not a straight line both wave impedances, $\widetilde{Z}_{xx}$ and $\widetilde{Z}_{xy}$ must be filtered prior to rotation in the direction perpendicular to the effective direction of the electric field array. This point will be further clarified in Chapter VI. Finally, when the values of $\widetilde{Z}_{xy}$ are obtained from noisy electric and magnetic field data, the weights of the discrete Hanning window might include an additional factor inversely proportional to the standard deviation of the weighted impedances. Even though noise considerations are important in the analysis of the filter adaptation process described herein, further discussion of this aspect of the problem is deliberately omitted to concentrate on the general concept of spatial filtering.

5.5 Stability of the adaptive filtering process

The adaptation process described in the previous section does not enforce an explicit relation between window width values adapted at consecutive values of frequency. Unfortunately, this may sometimes lead to abrupt changes in window width from one frequency to another and hence reflect similar changes in the amplitude of the filtered impedance. Commonly, one encounters this situation when, as for the case of Site No. 1 in Figure 5-4, the Hanning window is centered within a surface conductor. In such cases, as shown in Figure 5-5, so long as the window is contained within the conductor, a change of W produces no appreciable change in the estimated depth of penetration. In fact, depending on the width of the surface conductor, the depth of penetration may remain smaller than a dipole length at a number of the highest frequencies. Both the shallower than usual depth of penetration and the insensitivity of the filtered impedance to a change in window width are due to the lateral current channeling imposed by the surface conductor. Only when the frequency is low enough to force the Hanning window outside of the conductor does the filtered impedance develop a significant change.

To understand this situation, Figures 5-6a and 5-6b show the apparent resistivity and impedance phase curves, plotted with respect to frequency, of the TM (Z_{xy}) impedances filtered at Site No. 1 and Site No. 2, respectively, of Figure 5-4. These curves were obtained with the adaptive filtering procedure described in the previous section assuming a 3 km-long traverse, laid out normal to strike and with contiguous dipoles deployed at 100 m intervals. The value of filter constant, c, used in the adaptation was 2. In Figure 5-6a, the discontinuity of the filtered apparent resistivity curve at about 4 Hz is due to a sudden expansion of the window once the depth of penetration is large enough to force the Hanning window outside of the conductor. By contrast, at Site No. 2, Figure 5-6b displays continuous filtered apparent resistivity and impedance phase curves obtained with exactly the same field parameters used in the derivation of the curves at Site No. 1. The discontinuous character of the apparent resistivity curve at Site No.1 is further clarified with the aid of Figure 5-7, wherein the values of Hanning window width adapted at both sites are plotted against frequency. This figure shows that above 40 Hz the window width adapted at Site No. 1 remains constant and equal to a dipole length, whereas at Site No. 2 the adapted window width exhibits a firm monotonic increase with decreasing values of frequency. At 40 Hz, the window-width curve at Site No. 1 finally reaches the critical point where the depth of penetration exceeds its stagnated value of 100 m, and slowly -almost linearly- increases to about 300 m at 4 Hz. It is at this point where the change in depth of

penetration is so drastic that the new window increases by a factor of 4, giving the discontinuity in the apparent resistivity curve shown in Figure 5-6a.

A way to control the rate of increase of window width, W, with decreasing frequency, ω, is as follows: starting with equation (5.18) together with substitution from equation (5.16), one can show that the rate of increase of logarithmic window width with a logarithmic decrement in frequency is given by

$$\frac{\partial \ln W(x,\omega)}{\partial \ln \omega} = \frac{\partial \ln \left| \bar{Z}_{xy}(x,\omega) \right|}{\partial \ln \omega} - 1 . \qquad (5.19)$$

This last equation places a bound on the decay rate of ln(W), such that

$$-1 \leq \frac{\partial \ln W(x,\omega)}{\partial \ln \omega} \leq 0 .$$

In particular, over a homogeneous half-space the decay rate of ln(W) with respect to $\ln(\omega)$ is constant and equal to -1/2 [3]. The only case that prevents the decay of ln(W) with increasing frequency is the one in which $\bar{Z}_{xy}$ responds to a perfect conductor, otherwise ln(W) cannot remain constant with respect to frequency. Hence, equation (5.19) may be used to impose bounds on the rate of decay of ln(W) as frequency increases to improve the performance of the filter adaptation process governed by equation (5.18).

A second and more specialized method that gives good results in most cases consists in first running an unconstrained window adaptation for all frequencies at a given site. The curve of ln(W) vs. $\ln(\omega)$ that results from this adaptation is then examined to check for a discontinuity. If the check is positive then the discontinuity is corrected for by linearly increasing the ln(W) values with respect to $-\ln(\omega)$ starting with the highest frequency until intersecting the unconstrained window-width curve. Yet another method exists which, although only applicable to strictly 2-D data, is quite interesting because of its physical implications. This consists of adapting the window width on the TE impedances (which incidentally are not affected by adaptive spatial filtering applied as proposed by equation 5.18). The values of W adapted this way are in the final step used to filter the TM impedances.

Figure 5-8 shows the variations of window width with respect to frequency that describe the performance of the constrained adaptive filtering procedure at Site No. 1 and at

[3] This result is consistent with the properties of the TM prewhitening filter defined in section 4.9.

Site No. 2. Both curves are smooth and compare reasonably well with each other. The respective filtered apparent resistivity and impedance phase curves, shown in Figures 5-9a and 5-9b, are also smooth and continuous. In fact, the plots in Figures 5-6b and 5-9b reveal no change in the filtered impedance at Site No. 2 once the window growth constraint has been included in the adaptive filtering process. The difference between the plots in Figures 5-6a and 5-9a, however, is remarkable, with the new apparent resistivity curve showing a much closer agreement with both TE and 1-D curves. Notice also that the filtered apparent resistivity curve at Site No. 2 is actually in better agreement with the 1-D curve than with the TE curve. An important observation is that in all cases the impedance phase curve is only slightly modified by the filtering process.

Assuming adequate electric field sampling conditions, the adaptive filtering procedure described above can in most cases be adjusted to render a smooth 2-D filtered apparent resistivity curve. Over 3-D media, however, deflection and turn-around of the conduction current (see section 2.5) can sometimes lead to abrupt variations in depth of penetration whereby, regardless of the way in which the window width is allowed to grow, the filtered apparent resistivity will develop irregular frequency variations. This situation should not handicap the subsequent estimation of depths and resistivities, because, after all, the filtered apparent resistivity and impedance phase curves as shown, for instance, in Figures 5-9a and 5-9b are not MT impedances in the strict sense of the word.

5.6 The nature of the filtered impedances

That the filtered impedances are not "real" MT impedances can be shown by simple inspection of the filtered apparent resistivity and phase curves shown in Figures 5-9a and 5-9b. In spite of the fact that these curves were derived by linear combination of 2-D TM impedances, certainly the resulting apparent resistivity and impedance phase do not relate to each other by the otherwise minimum-phase property that in the frequency domain is characteristic of 2-D TM impedances.

This apparently conflicting situation originates from the use of different filtering lengths at different frequencies. Had the filtering length being kept constant at all frequencies, no doubt the curves in Figures 5-9a and 5-9b would have exhibited minimum-phase characteristics, just as 2-D TM impedances are naturally minimum-phase when either simulated or acquired in the field with a fixed dipole length. Over 3-D media, however, the minimum-phase property cannot be taken for granted, especially in the presence of deflection and turn-around conduction current effects. Rather than being interpreted as MT

impedances with standard properties, each filtered impedance should be thought of as a set of as many filtered impedances as there are frequency samples in the Fourier analysis. Each member of this set of impedances is characterized by: (1) the window width (or length), W, with which it has been filtered, and (2) the frequency, ω, at which W was adapted. For the purposes of a display of filtered impedances vs. frequency (such as the ones shown in Figures 5-9a and 5-9b), however, each member of the impedance set is sampled only at the frequency, ω, for which it is identified. Below, the spatial filtering and subsequent inversion of 2-D TM impedances is tested over more complex synthetic models of subsurface resistivity.

5.7 Synthetic examples

The basic computations for the spatial filtering procedure described in the previous sections are complete when the filtered impedances, $\overline{Z}_{xy}$, have been obtained for the complete set of frequencies. These impedances may then be used to estimate a profile of the subsurface resistivity distribution beneath the survey path with techniques designed for the inversion of the inductive part of the surface electric field response (section 2.7), such as those used in the interpretation of 1-D or 2-D TE electric field data.

To test the performance of spatial adaptive filtering in the simplified inversion of surface electric field data, three synthetic 2-D models have been chosen. An actual 3-D MT response bears a great deal of similarity with the TM response of a 2-D earth (Swift, 1967, Wannamaker et al., 1984, and sections 2.3 and 2.4 of this thesis), meaning that applying the principles of spatial filtering to TM electric field data gathered over 2-D geoelectric media should be indicative of its performance over 3-D environments.

When a 2-D earth is excited by a vertically incident plane wave with TM polarization, the surface horizontal magnetic field is spatially constant (d'Erceville and Kunetz, 1962). Thus, if the EMAP traverse is laid out normal to strike the TM impedances are equivalent to any of the conventional, base, or EMAP impedances, Z_{xy}, $\hat{Z}_{xy}$, and $\tilde{Z}_{xy}$, respectively, defined in section 5.3, and hence amenable to spatial filtering of the surface electric field without modification. In addition, for the examples below these impedances are computed from electric dipole responses simulated by direct integration of the surface electric field. The frequency range of the simulated measurements is from 0.001 to 1,000 Hz and the sampling rate is 5 frequencies per decade. Finally, the survey traverse is kept at

a constant length of 4 km and includes 40 contiguous electric dipoles spaced at 100 m intervals.

5.7.1 Geologic Noise

The first model is shown in Figure 5-10a. It corresponds to a two-layer sequence in which the upper layer has a resistivity of 80 Ω•m, and the lower layer is a 5 Ω•m half-space 4 km below the surface. Geologic noise is introduced in the upper layer with a sequence of 20 equal-width (200 m) contiguous blocks of variable thickness. The resistivity of the overburden blocks varies from 2 to 400 Ω•m, and their thickness varies from 4 to 50 m. Both resistivity and thickness for each block were chosen with a Gaussian random number generator. Last but not least, a 1 Ω•m conductive block is buried within the upper layer at a depth of 400 m, and with lateral and vertical dimensions of 2000 and 700 m, respectively.

Figures 5-10b and 5-10c are the TM apparent resistivity and phase pseudosections, respectively, numerically simulated for the described model. The wide range of values included in the apparent resistivity pseudosection in Figure 5-10b evidences a surface electric field whose amplitude is dominated by the amplitude response of the overburden at nearly all frequencies. By contrast, lateral and frequency variations of impedance phase are only slightly affected by the overburden, and the phase pseudosection in a rough way reveals the various features contained in Figure 5-10a.

A suite of inverted resistivity sections derived by adaptive spatial filtering of the simulated TM impedances are shown in Figures 5-11a, 5-11b, and 5-11c, for filter constant values, c, of 2,3, and 4, respectively. The filtered impedances were transformed into resistivity vs. depth profiles via the Bostick pseudoinverse (Bostick, 1977). Accordingly, the variable nature of the near-surface values in the resistivity sections reflect the lateral variations at the shallowest depth of penetration (inverted at the highest frequency) along the profile. Comparison of the three inverted resistivity sections reveals that, even though increasing the value of filter constant, c, translates to better control of the electric static effects, excessively large values cause a loss of lateral detail in the inverted resistivity section. For what appears to be an optimal value for the filter constant, c=3, the associated apparent resistivity pseudosection is shown in Figure 5-12. This pseudosection offers a much different view of the surface electric response than the apparent resistivity pseudosection in Figure 5-10b. The computation time required for the spatial filtering and inversion steps involved in the derivation of the sections in Figure 5-11 was approximately 9 seconds in a Sun Spark 1^+ workstation.

Finally, to appreciate the effect that the electric response from the overburden has in the detection of both the conductive block and the basement, Figure 5-13a displays an inverted resistivity section obtained by spatial low-pass filtering (filter constant, c, of value 3) and subsequent Bostick inversion of the TM impedances generated from the model in Figure 5-10a without the random surface overburden. This resistivity section defines within acceptable tolerance margins the geometrical characteristics of the conductive block, and the inverted depths and resistivities compare well with the actual values displayed in Figure 5-10a.

The result of a last filtering and inversion exercise for this model is shown in Figure 5-13b. This resistivity section was derived from TM impedances simulated for the model of Figure 5-10a except that the resistivity of the overburden was made constant and equal to 10 Ω•m while its thickness remained variable. As for the case of Figures 5-11b and 5-13a, the value of filter constant, c, used in the derivation of the section in Figure 5-13b is 3. This is an interesting situation because, given that the surface conductor is wider than the buried rectangular block, one might think that suppressing the static effects in the former would entail such a filtering length that oversmoothing of the inductive signature from the block would be at risk. However, results are satisfactory and compare well with the model section shown in Figure 5-10a.

5.7.2 Topographic distortion and elevation correction

The second test model is shown in Figure 5-14a together with its simulated TM apparent resistivity and phase pseudosections displayed in Figures 5-14b and 5-14c, respectively. In this model, electric static distortion is introduced by way of abrupt topographic relief modelled as a quasi-periodic triangular interface between the air and a 200 Ω•m stratum. Each of the triangles that conform the surface relief has a base length of 400 m and a slope of 30°. Also, a 10 Ω•m semiinfinite slab with thickness of 3.6 km is buried at a depth of 400 m to simulate a subsurface fault. The model is terminated below the fault with a 1 Ω•m half-space buried at a depth of 4 km. Finally, notice that since the dipoles are laid out tangentially to the air-earth interface, some of them are actually longer than the otherwise standard horizontal length of 100 m.

Electric static effects due to topography are inferred by the strong vertical banding in the apparent resistivity pseudosection (Figure 5-14b), which in turn obscures the electric response of the remaining features in the model. The impedance phase pseudosection, on the other hand, shows no similar banding and does give an indication of both the fault and

the conductive basement. Adaptive spatial filtering with a filter constant, c, of value 3, and subsequent Bostick inversion of the simulated TM impedances produces the resistivity section shown in Figure 5-16a. Because in Figure 5-14a depths are measured with respect to an elevation datum placed at z=0, the depths of penetration displayed in the resistivity section have been corrected for the vertical offset of each station along the profile.

A more efficient and physically intuitive elevation correction than the simple compensation of dipole elevations is proposed in Figure 5-15. For this correction, an effective elevation for each dipole along the profile is computed by averaging the local and adjacent site elevations with exactly the same discrete Hanning window used to filter the EMAP impedances. Since the width of the window is a function of frequency and so is the depth of penetration, it becomes clear that the elevation correction will be frequency dependent as well. Figure 5-16b shows the inverted resistivity section obtained using this correction procedure. As a result, the vertical irregularities with which the upper boundary of the subsurface fault was inverted in Figure 5-16a have been almost completely eliminated.

The inverted resistivity section shown in Figure 5-16b exemplifies an important aspect of the buried contact problem whereby the recovered fault boundary has a progressive loss of high lateral wavenumber components with increasing depth. This situation is in agreement with the lateral wavenumber bounds for the Born inversion process discussed in Chapter IV.

5.7.3 Unaccounted adjustment distance

A third and last synthetic model is shown in Figure 5-17a. The 1-D background for this model consists of a 100 Ω•m upper layer and a 1,000 Ω•m basement buried 3 km below the surface. Features of 2-D nature are introduced by way of two 1 Ω•m semiinfinite rectangular slabs located within the upper layer of the 1-D background. Buried at depth of 900 m, the first slab has a thickness of 400 m and extends to the right of the section. The second slab has a thickness of 100 m and outcrops on the left-hand side of the section. No horizontal overlap exists between the two slabs and their respective terminations are 500 m apart. The unconfined nature of both 2-D features make this model a particularly interesting case of analysis

Figures 5-17b and 5-17c are the simulated TM apparent resistivity and impedance phase pseudosections, respectively. The values of apparent resistivity on the left-hand side

of Figure 5-17b are dominated by the electric static response of the outcropping slab. On the right-hand side of the pseudosection, however, electric static distortion comes into play only below 0.1 Hz and once the depth of penetration has surpassed the depth of the buried slab. This distortion somewhat dominates the inductive amplitude response of the resistive basement. By contrast, the different response components of the geoelectric model are grossly visible in the impedance phase pseudosection shown in Figure 5-17c.

Figure 5-18 displays the resistivity section derived by adaptive spatial filtering and subsequent Bostick inversion of the TM impedances using a filter constant, c, of value 1.5. In contrast with the previous two examples, a low value of c is here more appropriate given the absence of surface static effects on the right-hand side of the section. The inverted resistivity section shows with some clarity the various structural features in the model. However, close examination of the inferred resistivities reveals a slightly overestimated value for the basement. Overestimated resistivity values at depth come as a consequence of using a maximum filter length that has fallen short to account for the adjustment distances of the surface electric distortion introduced by the semiinfinite slabs (Ranganayaki and Madden, 1980).

5.8 White Pine County field example

During the Summer of 1984, the Geomagnetics Research Laboratory of the University at Texas at Austin conducted an EMAP field study in White Pine County, Nevada, approximately 20 miles southeast from the city of Eureka. The location map is shown in Figure 5-19.

The White Pine CO. survey consisted of 84 electric dipoles, each 244 m (800') long, and deployed end-to-end continuously along a 20.25 km-long traverse oriented approximately parallel to the azimuth N149°10'S. The traverse was laid out transversely to the Pancake Range, bordering on its northwest end with the Little Smoky Valley and with the Railroad Valley on its southeast end. The objective of the experiment was to test the EMAP field and interpretation procedures over a complicated geological setting. A single magnetic base station was deployed and data were collected at 37 different frequencies in the interval from 0.0015 to 488 Hz. Simultaneous measurements of electric field signals were made at 6 contiguous dipole locations on a daily basis.

Figure 5-20a is the apparent resistivity pseudosection of the Z_{xy} base impedances measured along the traverse. For reference, the topographic profile is shown in the upper

panel with elevations measured in meters above the sea level (m ASL). The presence of various local electric static effects is quite evident along the traverse, and except for a persistent resistive zone between 0.01 and 10 Hz, the apparent resistivity pseudosection shows little clue to the electric response of other geoelectric features in the subsurface. An important observation is that the most resistive stripe at spans 71 and 72 coincides with outcropping dacites (references for the local and regional geology are Nolan et al., 1974, Stewart, 1978 and 1980, and, Hamilton, 1988, among others.) The phase impedance pseudosection shown in Figure 5-20b, on the other hand, grossly reveals a wide intermediate resistive zone, a conductive basement, and other less prominent local features. Finally, adaptive spatial filtering (filter constant, c, equal to 3) and subsequent Bostick inversion of the Z_{xy} base impedances produce the resistivity section shown in Figure 5-21. The depths of penetration in this section are referred to an elevation datum placed at 1700 m ASL. It is remarked that even though the White Pine CO. traverse is not precisely straight, the departures from such condition do not cause an appreciable change in the results shown in Figure 5-21.

The inverted resistivity section in Figure 5-21 shows two separate resistive features, very likely of intrusive nature. One of these features, on the right-hand side of the section, actually outcrops between the dipole spans 71 and 72, and extends down to a depth of approximately 7 km. The second resistive feature, on the left-hand side of the section, does not outcrop and is buried at a depth of approximately 1 km. Both of these features are embedded in what is suggested as the geoelectric expression of the complex sedimentary sequence typical of the area, for which a conductive basement becomes visible at approximately 30 km below the datum. Given the fact that the survey traverse did not include enough ground, laterally, of the two sedimentary sequences bordering the area of study, the depth and resistivity values inverted for the conductive basement may not be properly resolved in Figure 5-21. In spite of this, however, both numbers appear to be in agreement with values reported from other sources of investigation in the northern Basin and Range area (see, for instance, Wannamaker, 1983.) Without additional geophysical and geological data along the section, more detailed comments on the geological consistency of Figure 5-21 are not ventured here. Sensitivity analysis via numerical simulation seems an attractive procedure to quantify both lateral and vertical resolution bounds with which the various geoelectric features in the inverted resistivity section can be resolved from the measured Z_{xy} base impedances.

The White Pine CO. survey shows with striking clarity that only when electric field data have been gathered in continuous form does one come to understand the adverse effects that long distances between sampling locations may have on the estimation of a cross-section of subsurface resistivity.

5.9 Surprise Valley field example

Details of this field example have been presented in Chapter IV. The objective here is to reexamine the resolution characteristics of the data with the adaptive spatial filtering procedure discussed in sections 5.4 through 5.6. A map describing the location of the survey line is replotted in Figure 5-22. The Surprise Valley survey was carried out with the participation of students and faculty of the Engineering Geoscience Group of the University of California, Berkeley, and staff of Lawrence Berkeley Laboratory. Funding was provided by both Trans-Pacific Geothermal Co. and the Department of Energy. The intent of the experiment was to ascertain the geoelectric structure of a region with extensive history of surface geothermal activity.

Surprise Valley, California, is located exactly on the western boundary of the Basin and Range geological province of the western USA. Structurally, the valley is an extended N-S graben limited to the west by the Warner Mountain Range and to the right by Hays Canyon Range. The Warner Mountain Range lies within the well-studied Warner Plateau, and originated from the continuous accumulation of lava flows of basaltic composition. Subsequently its strata were subjected to compressional forces that resulted in a westward tilt of 15° to 20°. The normal faulting processes that gave rise to Surprise Valley are the result of episodic crustal extension effects that continue to this day in the western Basin and Range province. Tertiary volcanics are the main components of the sedimentary sequence in Surprise Valley, although a conspicuous accumulation of quaternary conglomerates reaches a maximum thickness of approximately 4 km toward the center of the valley.

For the MT evaluation of Surprise Valley, a survey line was oriented perpendicularly to the predominant geologic strike (approximately in the W-E direction.) A total of 43 contiguous and collinear dipoles were deployed along the line at a constant interval of 100 m. In addition, 200 m orthogonal dipoles and pairs of induction coils were disposed at regular intervals to aid in the estimation of dimensionality of the underlying subsurface resistivity distribution. All electric and magnetic field signals measured along the survey line were referred to a fixed magnetic base station whose location is indicated in the lower right-hand corner of Figure 5-22. Even though apparent resistivity and

impedance phase curves for the orthogonal dipoles are not shown here, these revealed no significant lateral response variations except in the proximity of the Warner Range. Likewise, the recorded magnetic field variations along the line compared remarkably well with the magnetic variations recorded at the base station, and from this observation it was concluded that former could be neglected for all practical purposes. Finally, the geoelectric strike estimated at the orthogonal dipole locations confirmed that the line was in effect aligned almost perpendicularly to the dominant regional strike.

Electric and magnetic field data were collected at 45 frequencies, uniformly distributed at a rate of 10 samples per decade within the interval from 0.003 to 100 Hz. Apparent resistivity and phase pseudosections describing the Surprise Valley Z_{xy} base impedances are displayed in Figures 5-23a and 5-23b, respectively. The longer than usual vertical axis in these plots was chosen so that the inverted resistivity sections could be described with a 1:1 horizontal to vertical length scale. Both pseudosections reveal negligible surface static distortion on the Z_{xy} impedances, especially when compared against the level of surface distortion effects exhibited by the White Pine CO. field impedances. However, enough lateral response variations are exposed in the pseudosections to call for a continuous reconnaissance of the surface electric response.

Figures 5-24a, 5-24b, and 5-25a show the inverted resistivity sections obtained by adaptive spatial filtering and subsequent Bostick inversion of the Z_{xy} base impedances using filter constant values of 1, 1.5, and 0.5, respectively. The linear axis representation for depth used in these plots is not intended to reflect the true vertical resolution characteristics of the field data, and is simply used to facilitate the geological interpretation of the results. For this same reason both horizontal and vertical axes are displayed with the same scale. In fact, an upper bound of 5 km for the depth scale is consistent with the depth range expected to optimally describe the lateral variations of subsurface resistivity considering that the survey traverse is only 4.2 km long. Finally, the estimated depths shown in Figures 5-24a, 5-24b, and 5-25a are measured below the 1300 m ASL elevation datum, which, incidentally, coincides with the lower limit of the elevation panel displayed in those figures.

The filtering exercise with different filter constants, c, illustrates in a practical way how the optimal selection of this parameter is crucial to understanding the lateral resolution bounds with which the data can be interpreted. First of all, the values of the filter constant, c, used for the Surprise Valley traverse are smaller than those used with the White Pine CO. traverse because of the comparatively smaller surface static effects in the former. One

can see that for a filter constant value of 1.5, lateral detail in the inverted resistivity section has been practically eliminated, whereas for a value of filter constant below 0.5, electric static effects persist in the inverted resistivity section. To further clarify this last situation, Figure 5-25b shows the resistivity section derived by direct 1-D Bostick inversion of the unfiltered base impedances. This figure illustrates the extreme case wherein electric static effects are completely unaccounted for in the estimation of a cross-section of subsurface resistivity.

Exhaustive tests with different filter constants indicate that for the Surprise Valley data the critical region of c lies somewhere within 0.8 and 1. An optimal selection of filter constant in this range would require either additional geophysical and geological information or extensive numerical simulation work, or both. A criterion to be met when selecting c is that the inverted resistivity section be in qualitative agreement with the lateral and vertical variations of impedance phase. More specifically, the impedance phase pseudosection in Figure 5-23b indicates that the resistor on the left-hand side of the section has a limited vertical extent and that a conductive basement lies at the bottom of the section. Both of these features are adequately represented in the inverted resistivity section obtained with a filter constant of value 1 (Figure 5-24b), although the conductive basement becomes visible only when the depth axis is extended down to at least 10 km below the datum. For this purpose, a complementary resistivity section is displayed in Figure 5-26, wherein depths are measured with a logarithmic axis and down to 20 km. The depth and resistivity values shown in Figure 5-26 for this conductor are only approximate estimates in light of the fact that the estimated depth has already superseded the length of the traverse.

On purely geologic grounds, the resistive feature visible on the left-hand side of the inverted resistivity section (Figure 5-24b) is consistent with the geometrical characteristics of the well-studied upper block of the Hot Springs Fault. Both surface geology and gravity data indicate that the latter is a normal fault and that it has an estimated vertical displacement of approximately 4 km (Hedel, 1981). The geoelectric imprint of a second normal fault is recognized between dipole locations 8 and 10. This corresponds to the Front-Range Fault, which delineates the geological boundary between the Warner Mountain Range (or more globally the Warner Plateau) and the Surprise Valley graben (Tsvi Meidav, Trans-Pacific Geothermal Co., personal communication). Both the Hot Springs Fault and the Front-Range Fault are the principal members of a general stair-step fault pattern that best describes the structural boundary of the Surprise Valley graben. The Hot Springs Fault appears to be the ascending conduit for the thermal fluids which feed the hot springs

located between dipole locations 20 and 22. Although the subsurface heating mechanism is not clearly understood, the water source for those fluids is most probably the Warner Mountain Range itself.

This brief geologic outline of the Surprise Valley region appears to be in qualitative agreement with the geoelectric features represented in Figure 5-24b. In particular, the sloping character of the resistive block on the left-hand side of this figure lends credence to normal nature of the Surprise Valley fault system. Also, the westward tilt exhibited by the Warner Mountain Range appears properly represented over the same portion of the inverted geoelectric section. From the basis of these results, the Surprise Valley field example shows that even in the absence of significant surface static effects, continuous sampling of the electric field extracts the maximum amount of lateral information from the subsurface resistivity distribution.

5.10 Discussion and concluding remarks

The synthetic and field data examples described in the previous show the importance of using contiguous electric dipoles for sampling the electric response from the subsurface. Both field examples indicate the need for much closer spacings between electric field sampling locations that has been used conventionally. In addition, the studies in this chapter indicate when electric field data have been acquired continuously along the survey line, spatial filtering of the tangential electric field component proves an efficient means to reduce the static component of the response. Further, a simple inversion of the inductive component that remains after spatial filtering provides a relatively accurate cross-section of subsurface resistivity.

In connection with the prewhitening operator described in section 4.9, adaptive spatial filtering can be understood as a method to continuously update, laterally and vertically, the variations of local background resistivity along the traverse. The lower the sounding frequency, the larger the depth of penetration and the longer the distance along which the subsurface resistivity is averaged. Needless to say, the nature of these averages is intimately related to the diffusive mode in which the MT fields propagate in the subsurface.

The crucial step of spatial filtering is to determine whether, at a given frequency, the induction component no longer dominates over the static component. Over low-contrast subsurface resistivity models, this occurs when the cutoff wavenumber of the low-pass

filter is inversely proportional to the Bostick depth of penetration in the homogeneous background (section 2.7). This is the nominal cutoff wavenumber. However, because the Bostick depth of penetration can be biased by static effects, spatial filtering has to be tried with different cutoff wavenumbers until one is found which is in effect inversely proportional to the depth of penetration of the filtered impedance. The suppression of stronger than usual static distortion necessitates of a cutoff wavenumber even smaller than the reciprocal of the Bostick depth of penetration. This criterion remains consistent with the wavenumber bounds derived in Chapter IV for the maximum wavenumber that can be recovered from the subsurface resistivity distribution for a given frequency (or depth of penetration).

The factor by which the nominal cutoff wavenumber of the low-pass filter is further reduced has been referred here to as the filter constant. Normally, the selection of an optimal filter constant requires the trial of several of them until, from inspection of the inverted resistivity sections, it is judged that all static effects have been properly accounted for. In the presence of frequency-dependent static effects, a low value of the filter constant may be appropriate for shallow depths of penetration, whereas for the inversion of deeper subsurface resistivity variations the required filter constant may be progressively increased to its maximum value. A limit to the lateral extent of this filtering process is set by the length of the traverse: even if data have been acquired at frequencies for which the depth of penetration may be larger than the traverse length, there will be no certainty that the inverted depths and resistivities have not suffered from a bias effect due to unaccounted for static distortion.

Although the filter used in the synthetic and field examples above was parameterized as a discrete Hanning window, it appears that so long as both the cutoff wavenumber and the roll-off of the filter are carefully adjusted, different discrete filters may be designed to perform the spatial filtering of the electric field data. The Hanning window is attractive because it is symmetric and has simple properties. Filters with more sophisticated and even asymmetrical shapes may introduce bias of their own on the filtered sections unless they are chosen to deal with specific characteristics of the data. Sasaki (1989), following a seemingly independent study of the sensitivity of dipole and Hanning window responses for the suppression of static effects advocated the use of a simple Hanning window.

Also, in spite of the fact shown in Chapter IV that filtering (prewhitening) of electric field data can be done in the wavenumber domain, filtering in the space domain

offers much greater flexibility. An important advantage of space-domain filtering over wavenumber-domain filtering is that it is much easier to compensate for edge effects with the former. For instance, the Wiener filtering procedure introduced in section 5.4 for the discretization of a Hanning window, takes into account edge effects in a most natural way. Moreover, wavenumber-domain filtering is only appropriate when the characteristics of the filter remain the same for all the sites along the electric field array, otherwise repeated Fourier transformations will be necessary to perform filtering for as many variations of filter characteristics there are along the electric field array.

Jones et al. (1989) have reported a study based on their interpretation of the "conventional" EMAP filtering. They mistakenly assumed that in the EMAP spatial filtering procedure the width of the Hanning window is determined as the inverse of a depth of penetration value estimated from the unfiltered impedances. Because of this, they showed the EMAP spatial filtering may, in the presence of static effects, lead to oversmoothing of valuable information in the electric field data. To "avoid" this situation, they proposed instead to perform the filtering step in the wavenumber domain such that the frequency-wavenumber properties of the filter could be tailored not to oversmooth valuable response characteristics that are known a priori from the subsurface. With so many flawed assumptions about the EMAP spatial filtering procedure in Jones et al.'s (1989) study, any explanatory note here is probably unnecessary. The only comment that seems pertinent, though, is that with an appropriate choice of filter constant, the adaptive spatial filtering process described in section 5.4 can be made to respect specific portions of the wavenumber-frequency spectrum of the unfiltered data, and thus minimize undesired smoothing.

An important note regarding the way in which the filtered impedances can be inverted into a cross-section of subsurface resistivity is that, even though a simple 1-D Bostick inversion may yield relatively accurate results, this is neither the only nor the optimal procedure available. Indeed, more sophisticated procedures of 1-D inversion may be used with each one of the filtered EMAP impedances. In so doing, however, it must be remembered that the standard curves of filtered apparent resistivity and impedance phase (such as those shown, for instance, in Figures 5-6 and 5-9) do not obey the basic properties of conventional MT impedances (see section 5.6). Because of this, the use of a nonlinear procedure to carry out the 1-D inversions becomes much more elaborate than the use of a straightforward frequency-by-frequency method such as the Bostick pseudoinverse.

At a given point along the electric field array, the modified 1-D inverse of the filtered impedance would be done more or less in the following way. First, at the highest frequency a window width is adapted with the aid of equation (5.18), such that all remaining frequency samples are filtered with the same window. An exact 1-D inverse is then applied to the impedance filtered this way, and only that portion of the inverted resistivity profile is retained for which the depth is shallower or comparable to the product cW, where c is the filter constant and W is the window width. Second, the same spatial filtering is performed except that now the window width is increased to its next higher value. The new filtered impedance is then 1-D inverted such that, once again, only that portion of the inverted resistivity profile is retained for which the depth of penetration is comparable to the new cW product. Furthermore, the retained portion of the inverted resistivity profile should not overlap with the portion derived in the previous filtering-inversion step. This sequence of steps are repeated until all remaining values of W have been processed. Clearly, an inversion method with these characteristics exacts a much greater toll in computer time than the Bostick pseudoinverse. However, it can be used at only certain points along the survey traverse (for instance, in the neighborhood of well-logging locations) and even some window-width values can be omitted from the analysis to simplify the computations.

A next step of sophistication in carrying out the inversion of EMAP impedances consists in performing nonlinear iterative 2-D TM inversions where the simulated data are spatially filtered at each iteration and then contrasted against the filtered field impedances until an appropriate match is attained. Both, 1-D and 2-D nonlinear procedures for the inversion of EMAP impedances remain as challenging tasks for future developments in the interpretation of continuously acquired MT data.

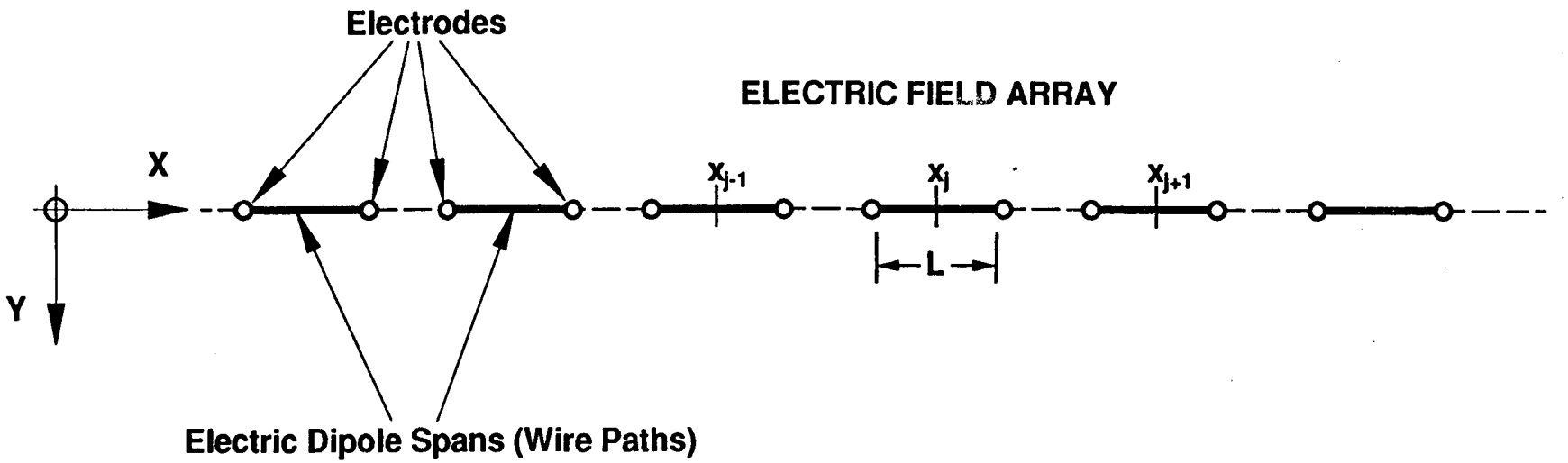

Figure 5-1. Graphical description of an electric field array composed of uniform and evenly spaced electric dipoles.

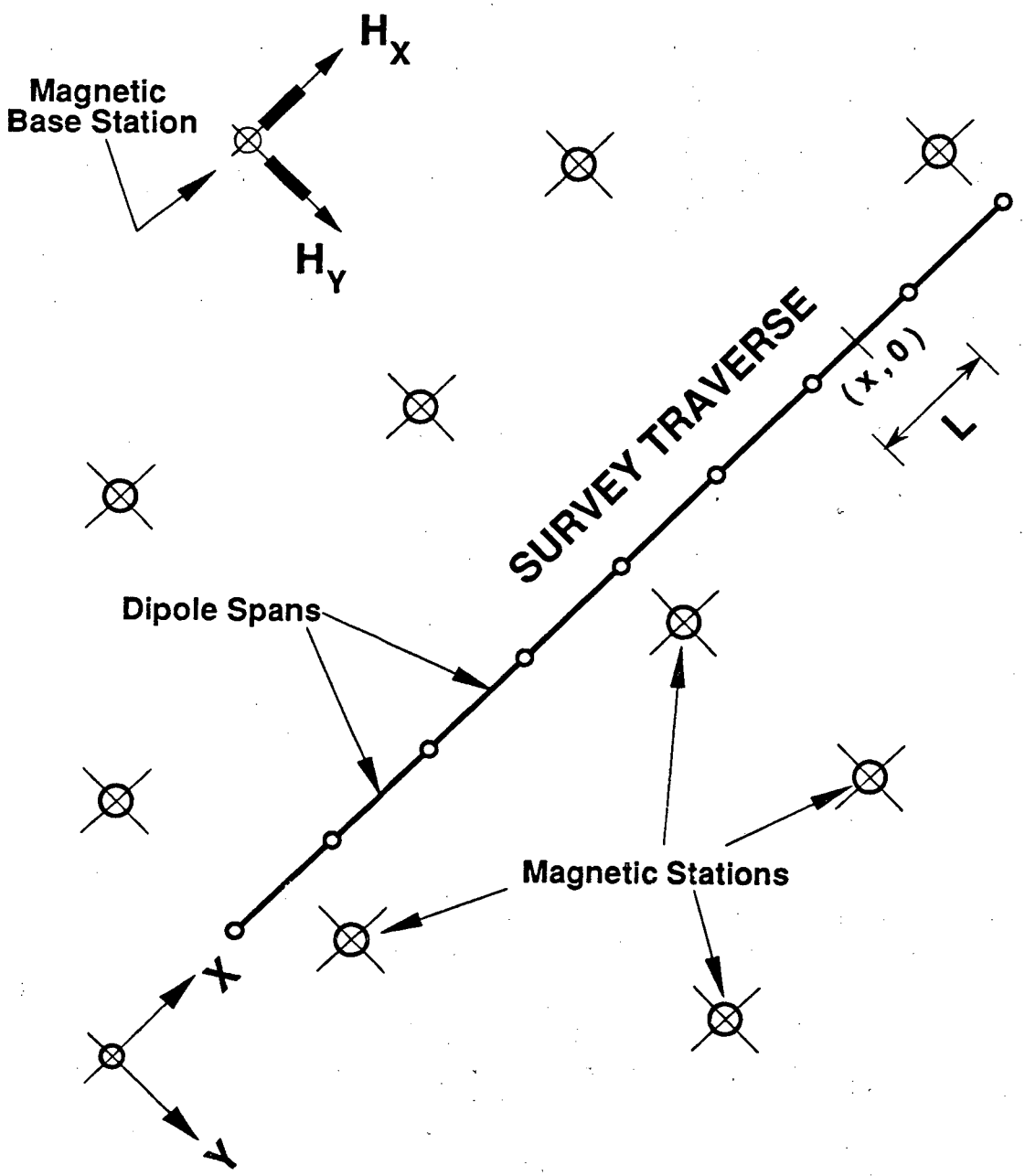

Figure 5-2. Graphical description of the EMAP field procedure.

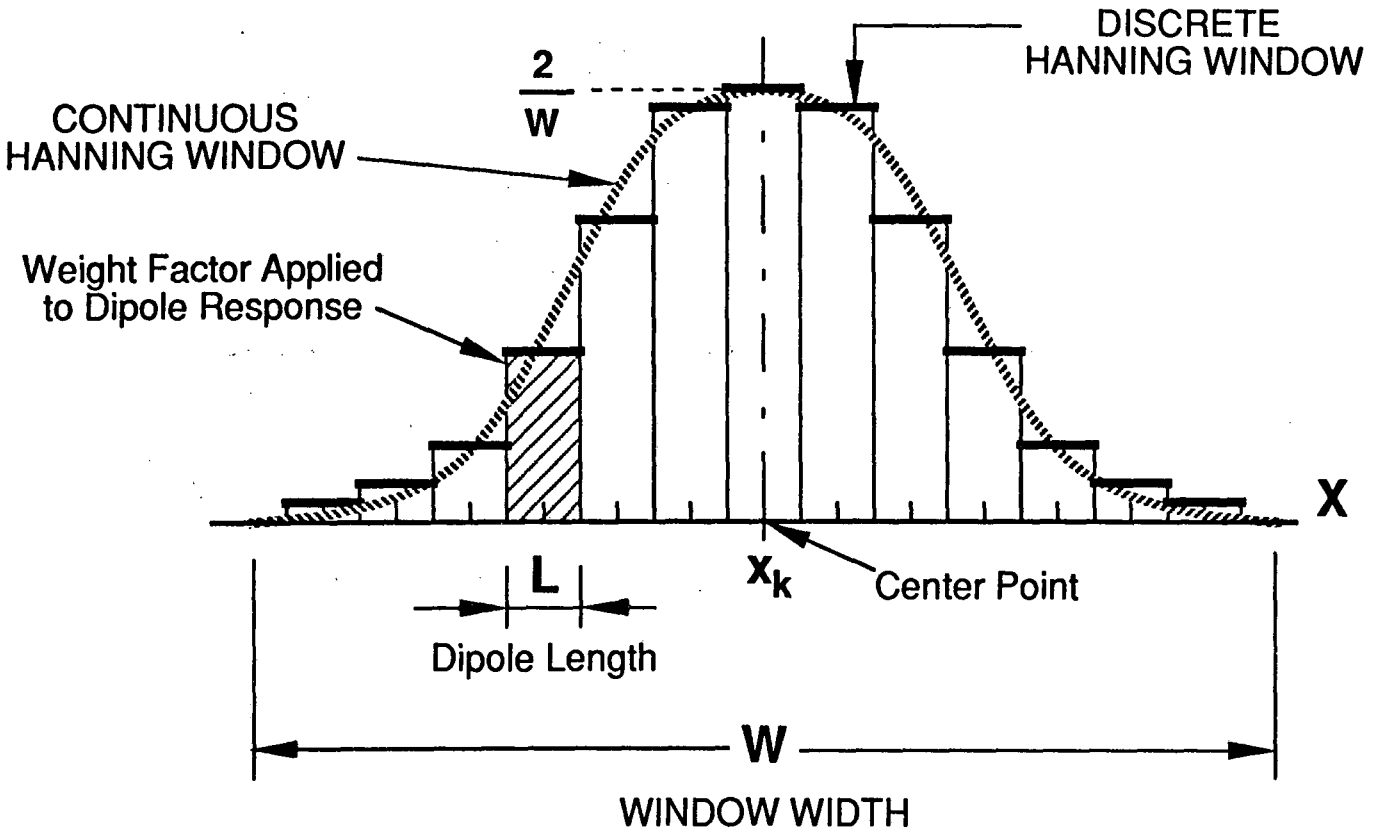

Figure 5-3. Continuous and discrete Hanning windows. The discrete Hanning window is synthesized from the rectangular functions that describe each one of the dipole responses along the electric field array.

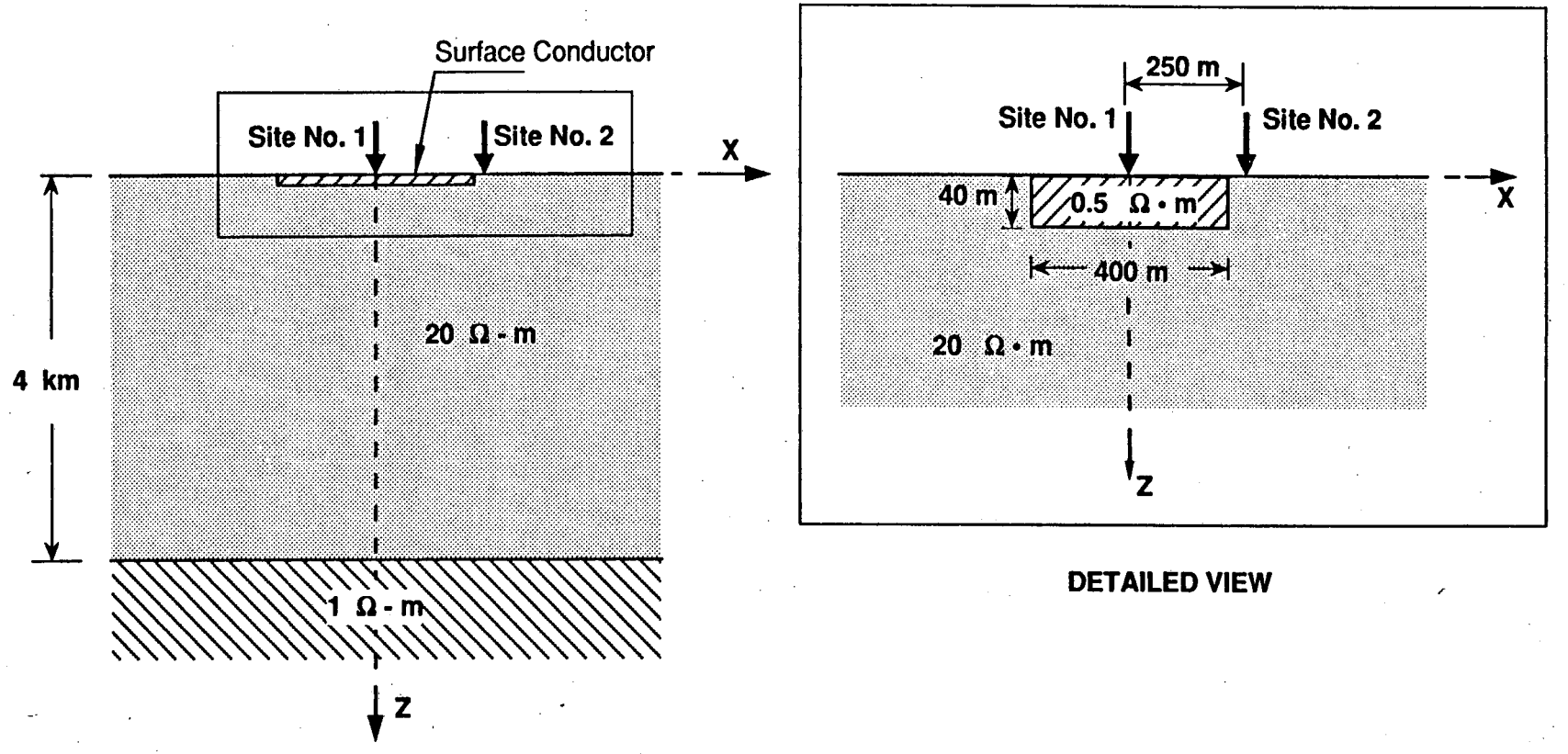

Figure 5-4. Cross-section perpendicular to strike of a 2-D surface conductor embedded in an otherwise 1-D medium. Locations for two test MT stations are shown as well.

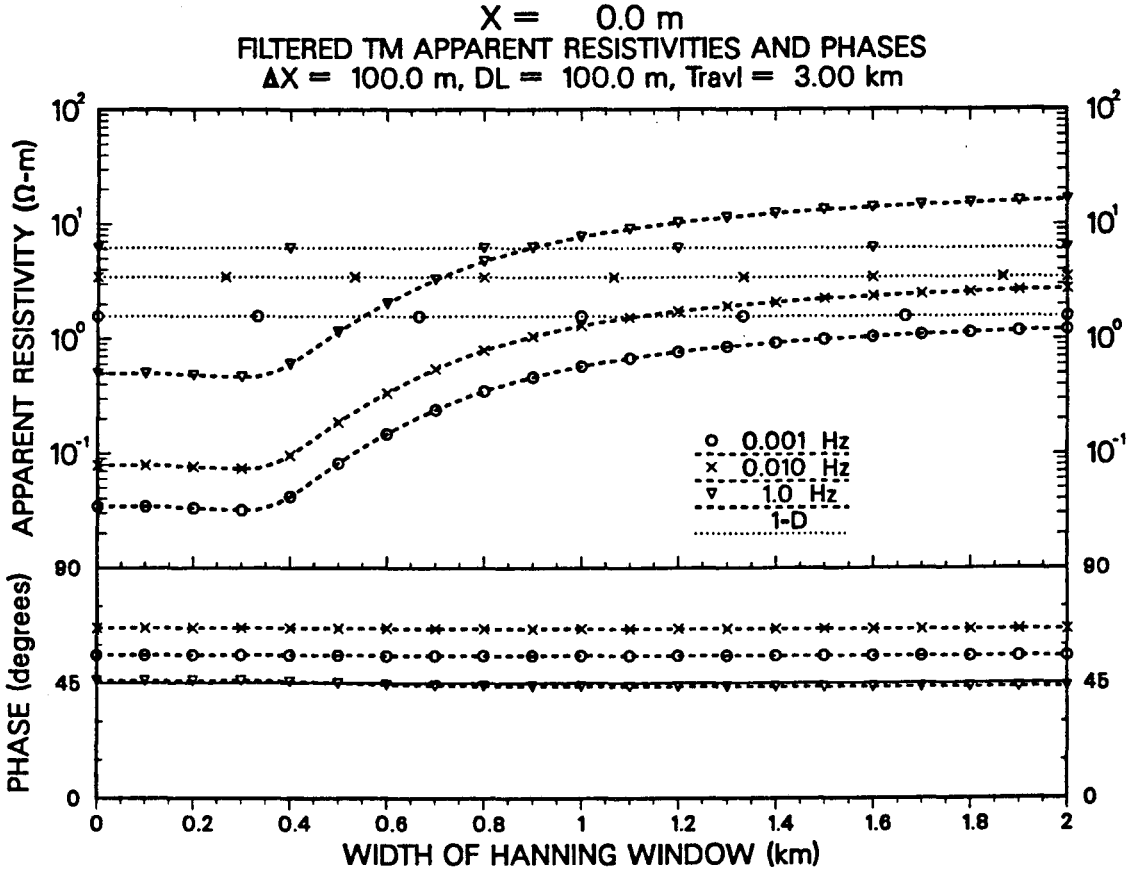

Figure 5-5. Apparent resistivity and impedance phase curves describing the variations of the spatially filtered TM impedance at Site No 1 (Figure 5-4) with respect to the width of Hanning window used to perform the filtering. Curves are shown for three different frequencies, namely, 0.01, 1, and 100 Hz. For comparison, constant apparent resistivity lines are shown at the same frequencies describing the 1-D response of a medium in which the surface conductor of Figure 5-4 has infinite lateral extent.

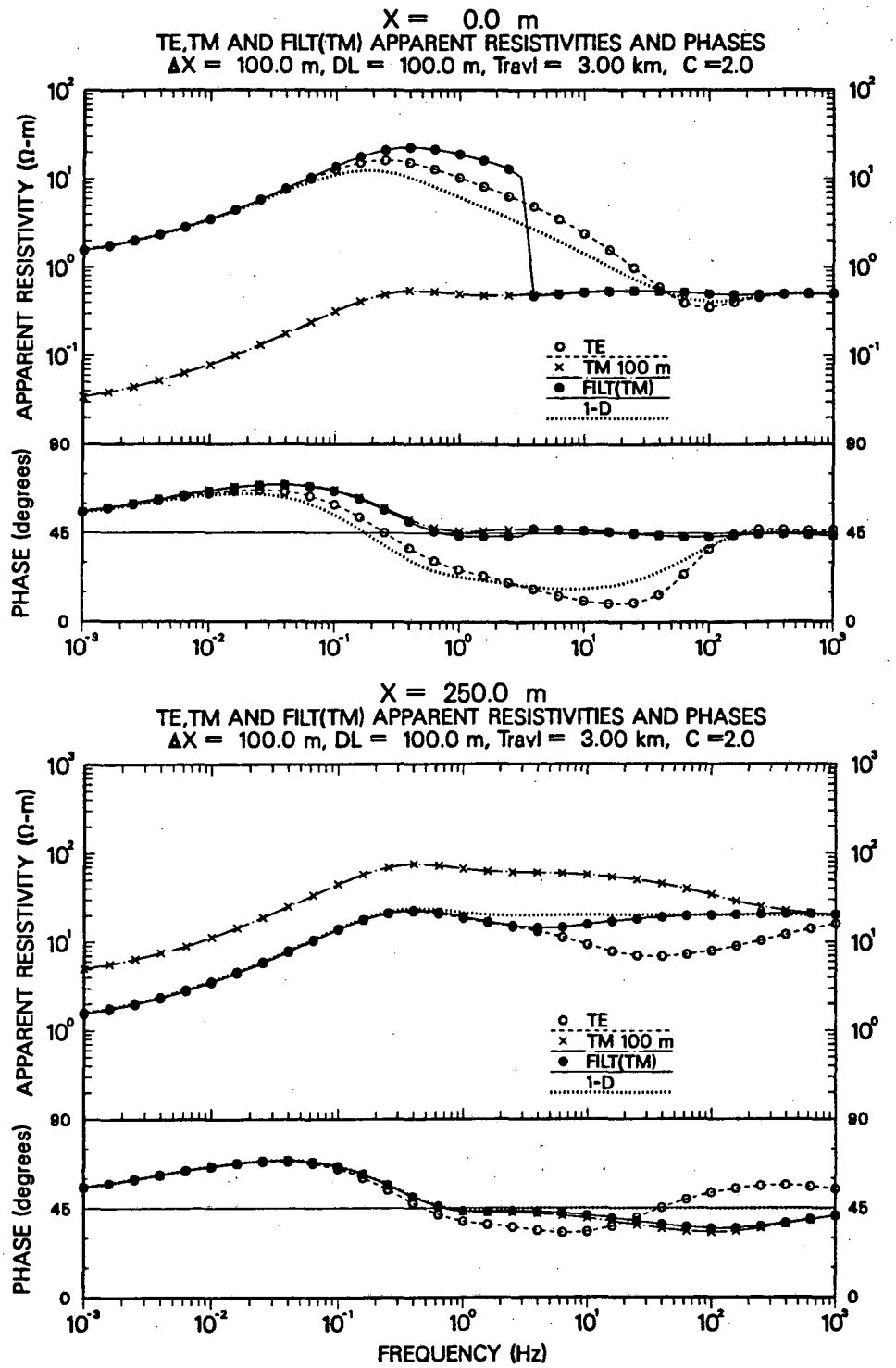

Figure 5-6. Apparent resistivity and impedance phase curves of the spatially filtered TM impedance at Site No. 1 (**a**) and Site No. 2 (**b**) (Figure 5-4) obtained using an unconstrained adaptive filter. Spatial filtering was carried out assuming a 3 km long traverse composed of uniform and contiguous 100 m electric dipoles. A filter constant, c, of value 2 was used to produce the results shown. Also, plots of the TE, TM (100 m dipole length) and 1-D responses are displayed for comparison. The 1-D curves describe the response of a medium in which for (**a**) the surface conductor of Figure 5-4 has infinite lateral extent, whereas for (**b**) the surface conductor is not included.

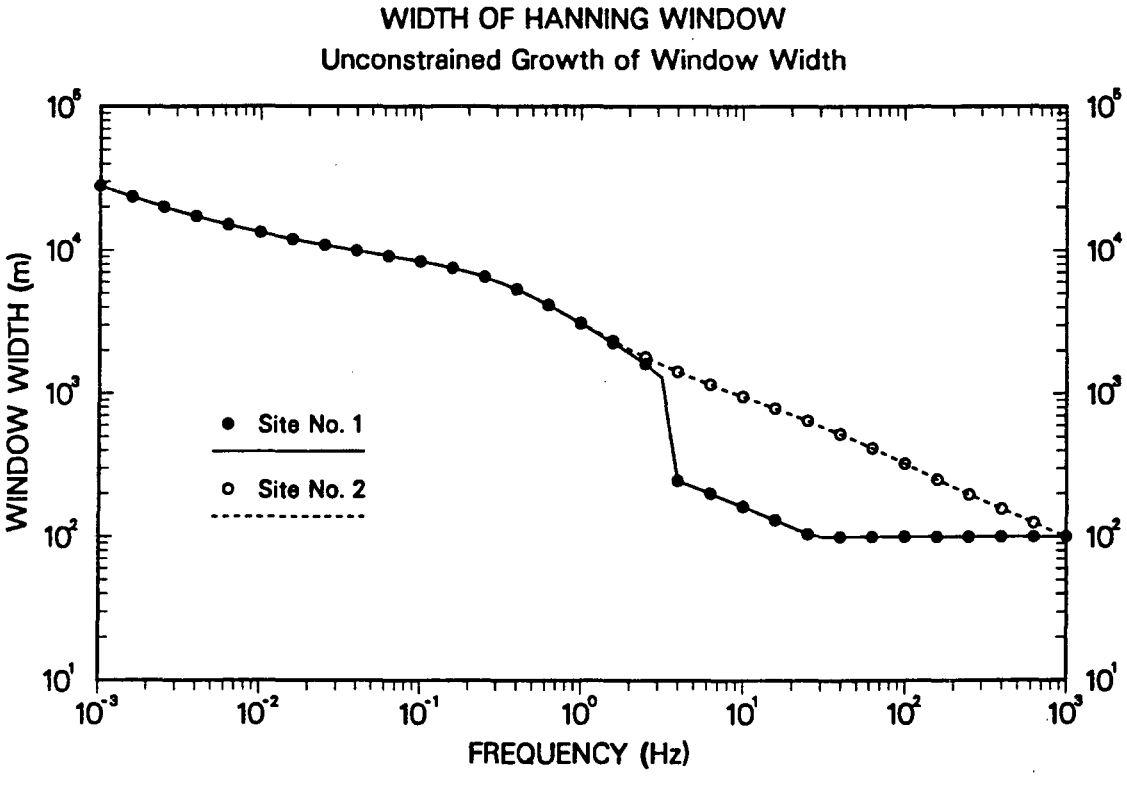

Figure 5-7. Curves of Hanning-window width adapted with the unconstrained spatial filtering procedure at Site No. 1 and Site No. 2. The values of window width shown were used to produce the apparent resistivity and impedance phase curves of Figure 5-6.

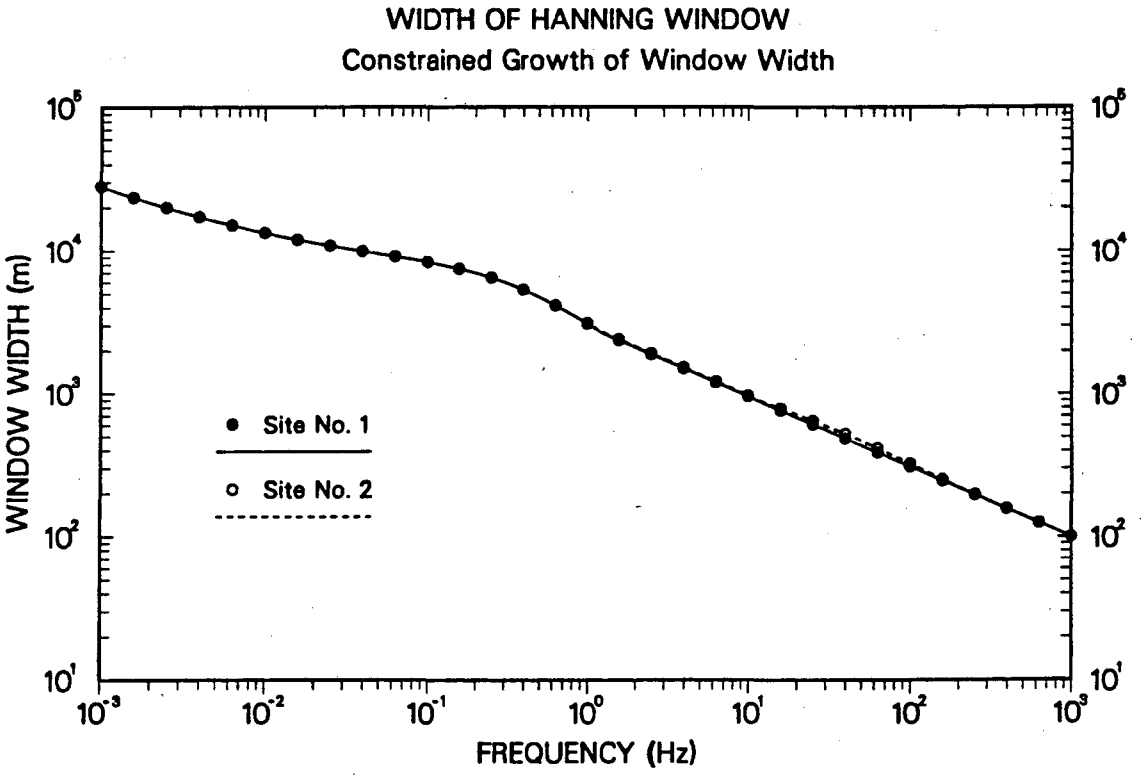

Figure 5-8. Curves of Hanning-window width adapted with the constrained spatial filtering procedure at Site No. 1 and Site No. 2. The values of window width shown were used to produce the apparent resistivity and impedance phase curves of Figure 5-9.

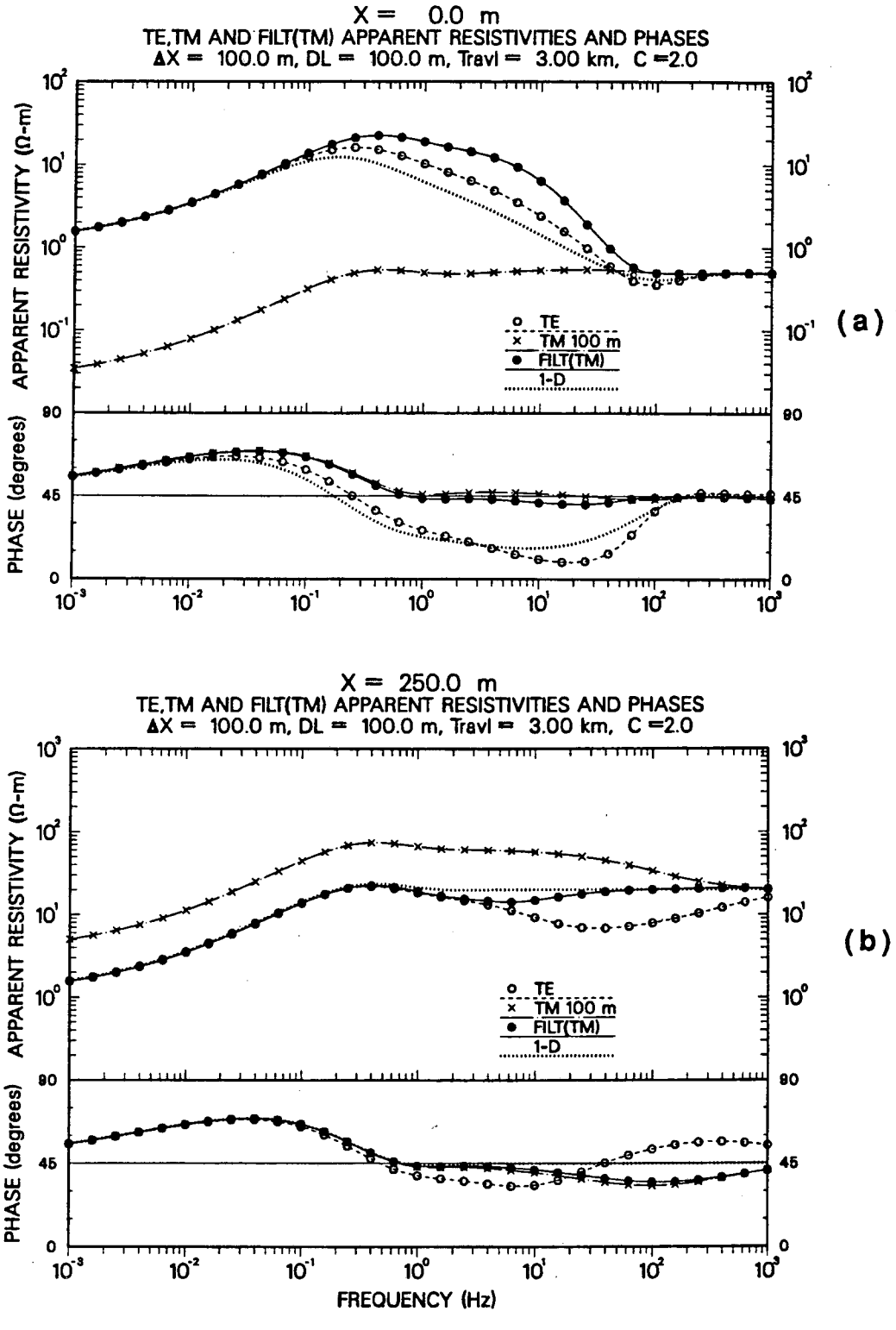

Figure 5-9. Apparent resistivity and impedance phase curves of the spatially filtered TM impedance at Site No. 1 (**a**), and Site No. 2 (**b**) (Figure 5-4) obtained using a constrained adaptive filter (cf. Figure 5-6).

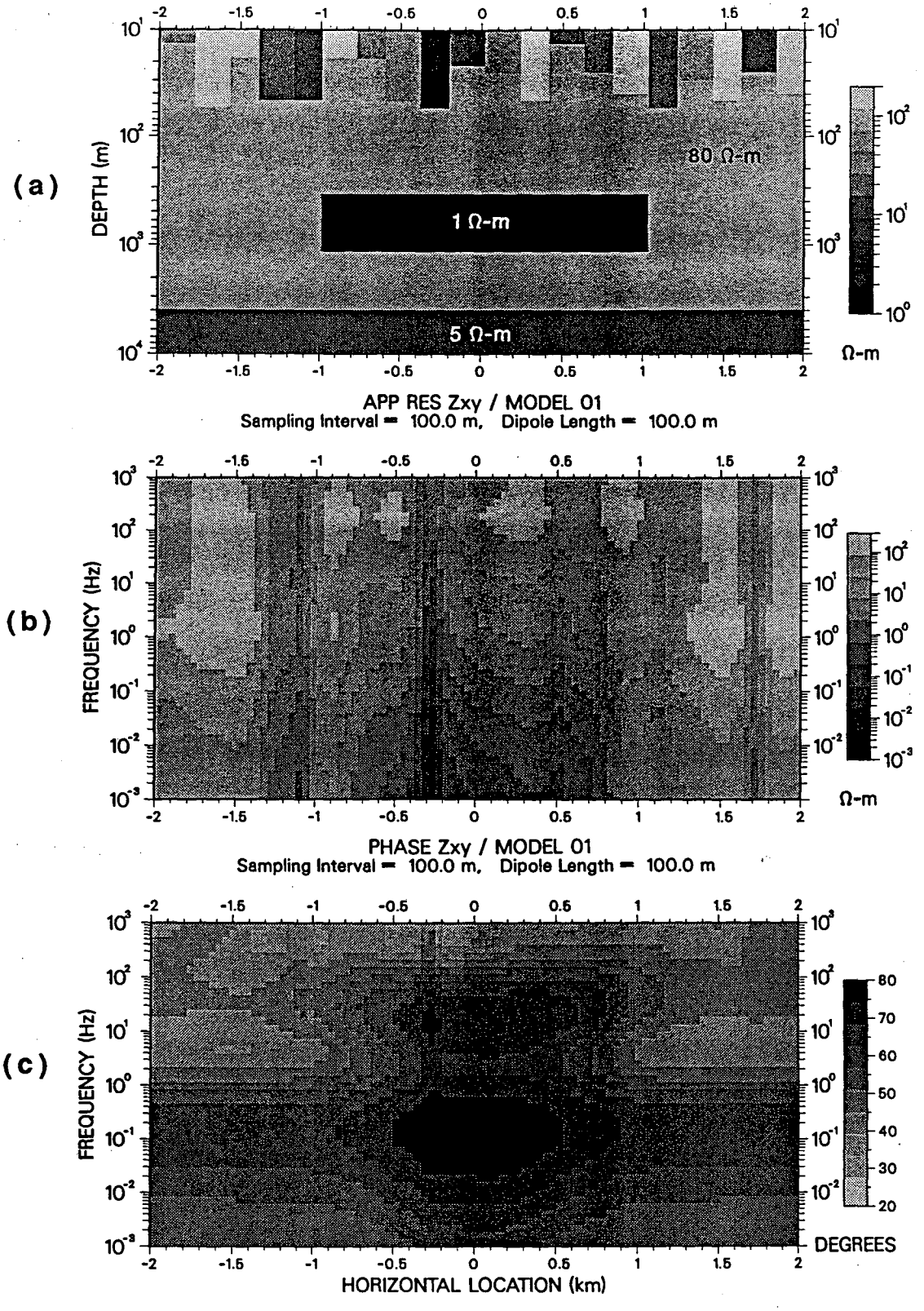

Figure 5-10. Geologic noise model. (a) is the model plot, and (b) and (c) are the simulated TM apparent resistivity and phase pseudosections, respectively.

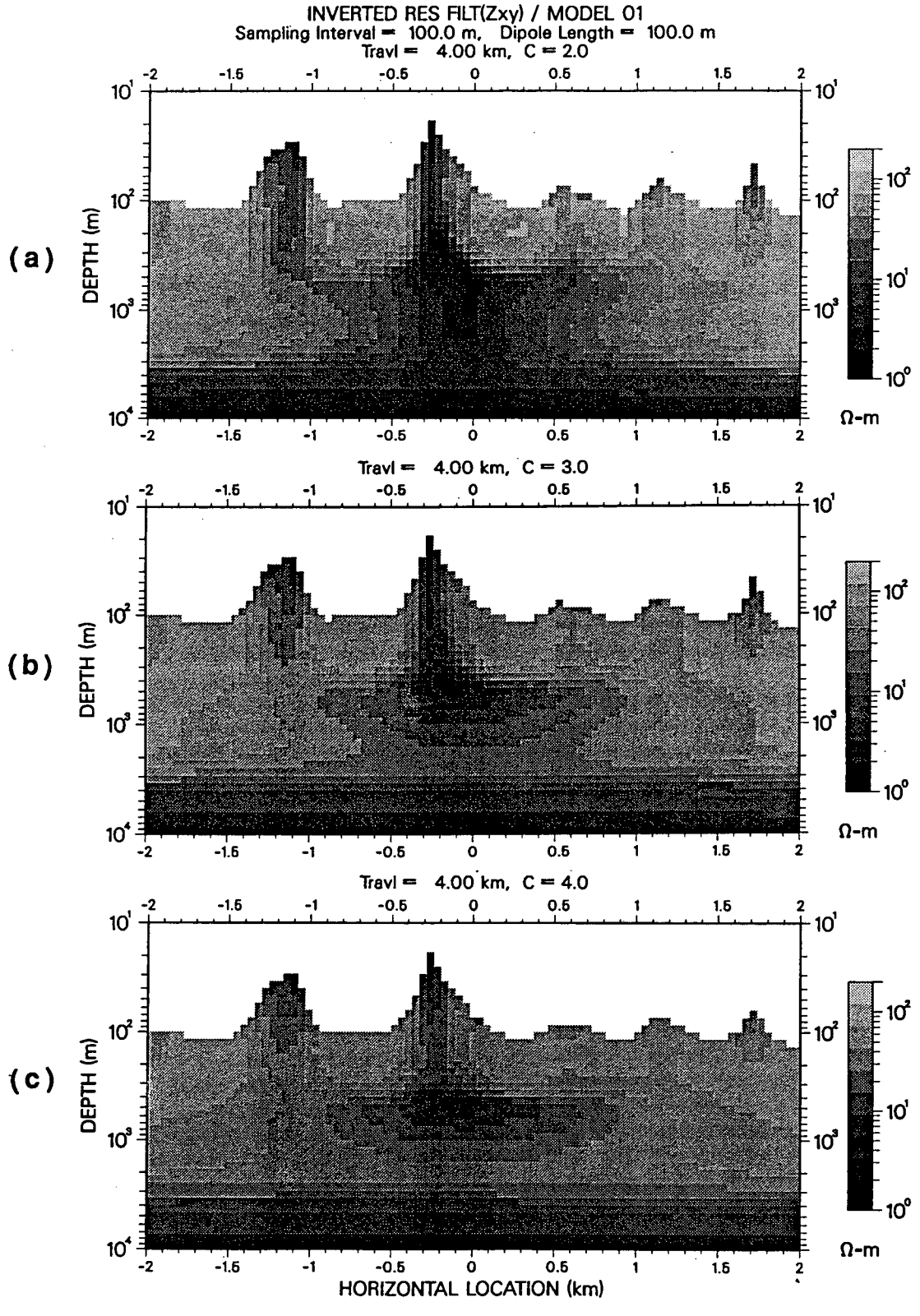

Figure 5-11. Geoelectric sections derived by spatial low-pass filtering and subsequent Bostick inversion of the TM impedances described in Figures 5-10b and 5-10c. The **(a)**, **(b)**, and (c) sections correspond to filter constants, c, of values 2, 3, and 4, respectively..

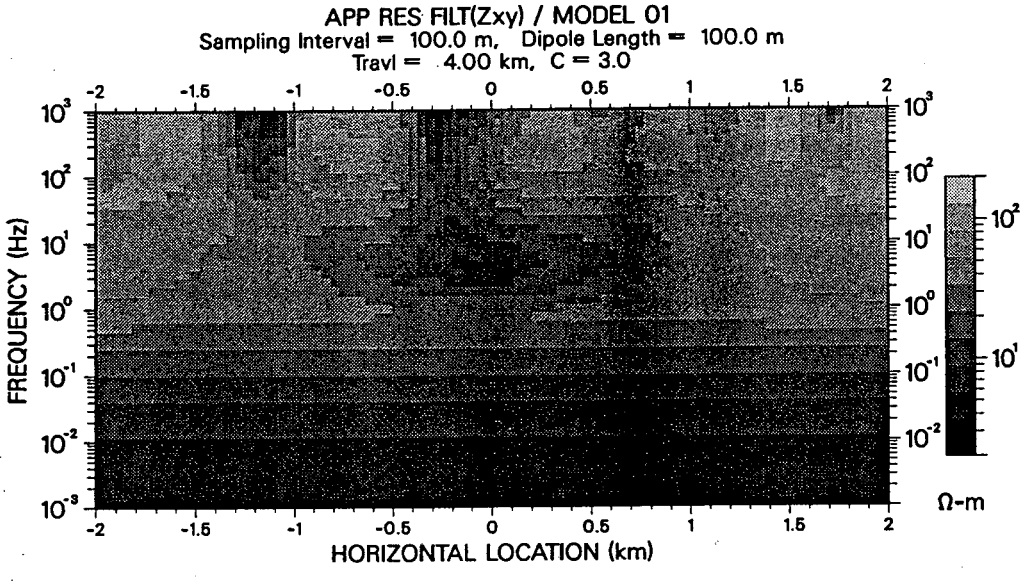

Figure 5-12. Apparent resistivity pseudosection of the spatially filtered TM impedance for the geologic noise model described in Figure 5-10a. A filter constant, c, of value 3 was used to produce the pseudosection.

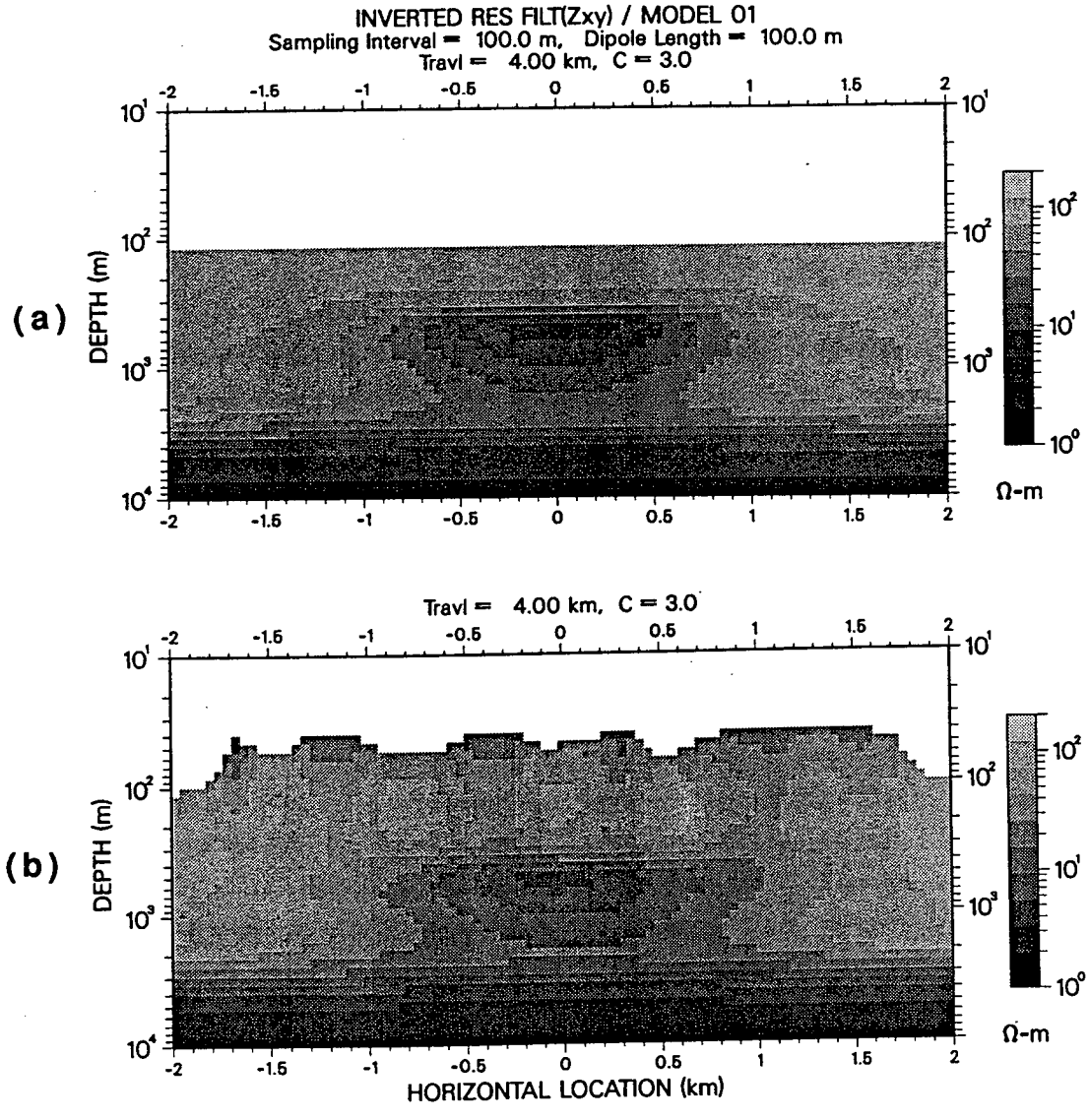

Figure 5-13. Geoelectric sections derived by spatial low-pass filtering and subsequent Bostick inversion of the TM impedances simulated for the model described in Figure 5-10a, except that in (a) no surface overburden was present, and in (b) the overburden was set to have the same thickness variations as in Figure 5-10a and a constant resistivity of 10 Ω•m. Both sections were obtained with the use of a filter constant, c, of value 3 (cf. to Figure 5-11b).

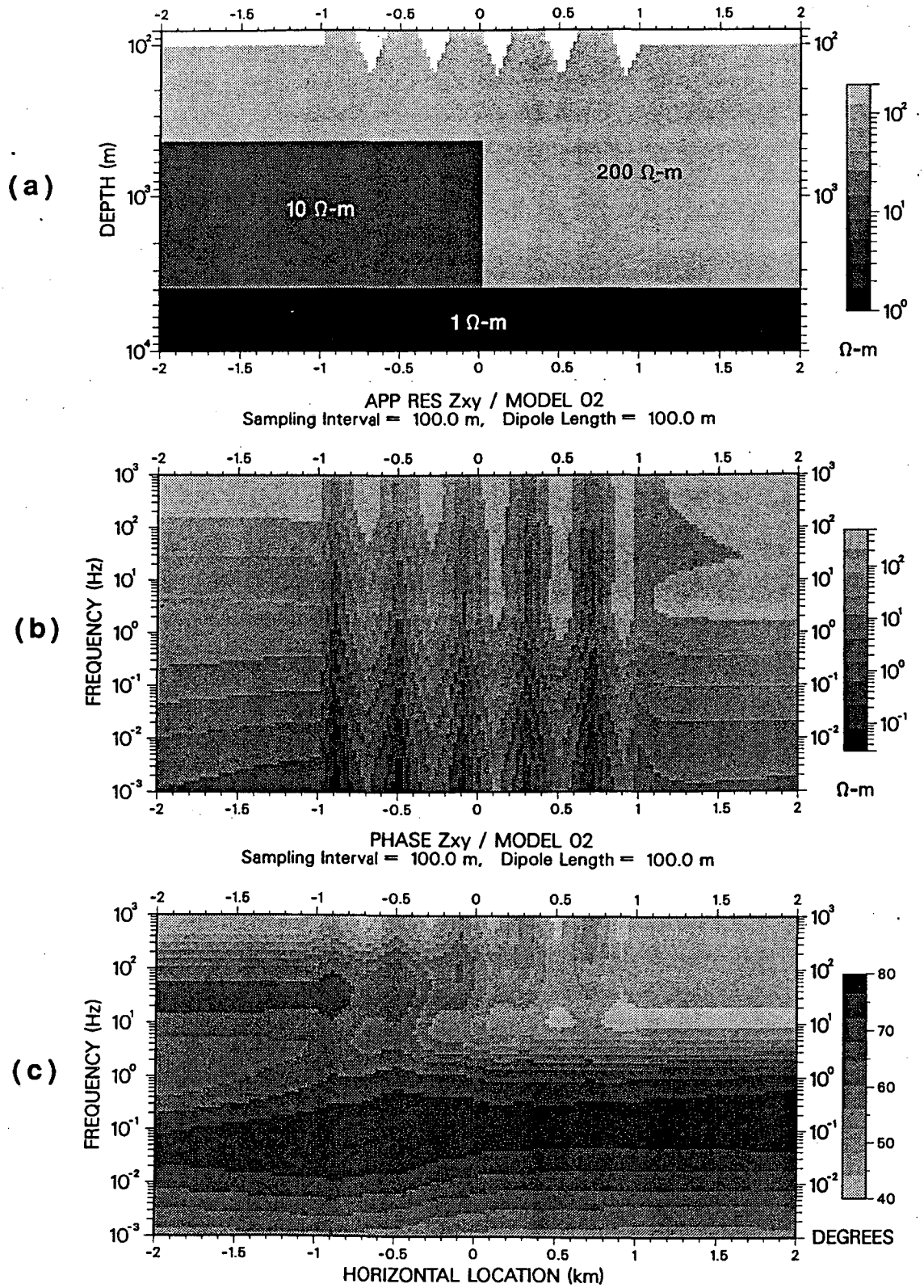

Figure 5-14. Topographic distortion model. (a) is the model plot, and (b) and (c) are the simulated TM apparent resistivity and phase pseudosections, respectively.

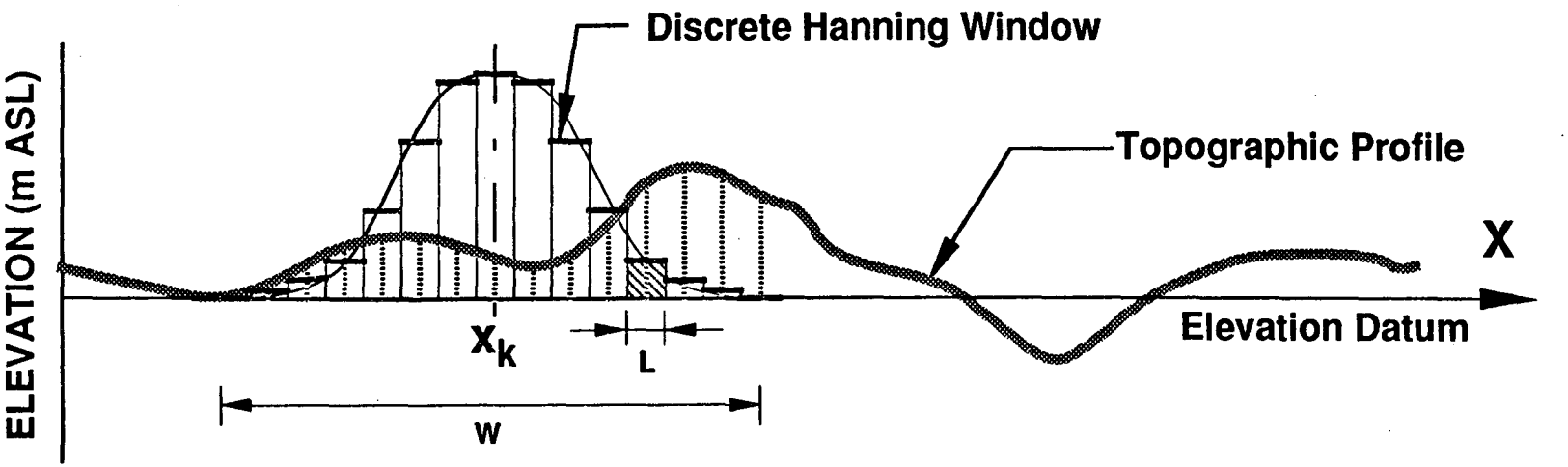

Figure 5-15. Diagram showing the use of spatial filtering for the estimation of an elevation correction: the topographic profile is filtered laterally with the same Hanning window that was used in the spatial filtering of the base impedances at a given value of frequency. The average elevation obtained with this procedure is then compensated from the depth of penetration inferred at the same frequency.

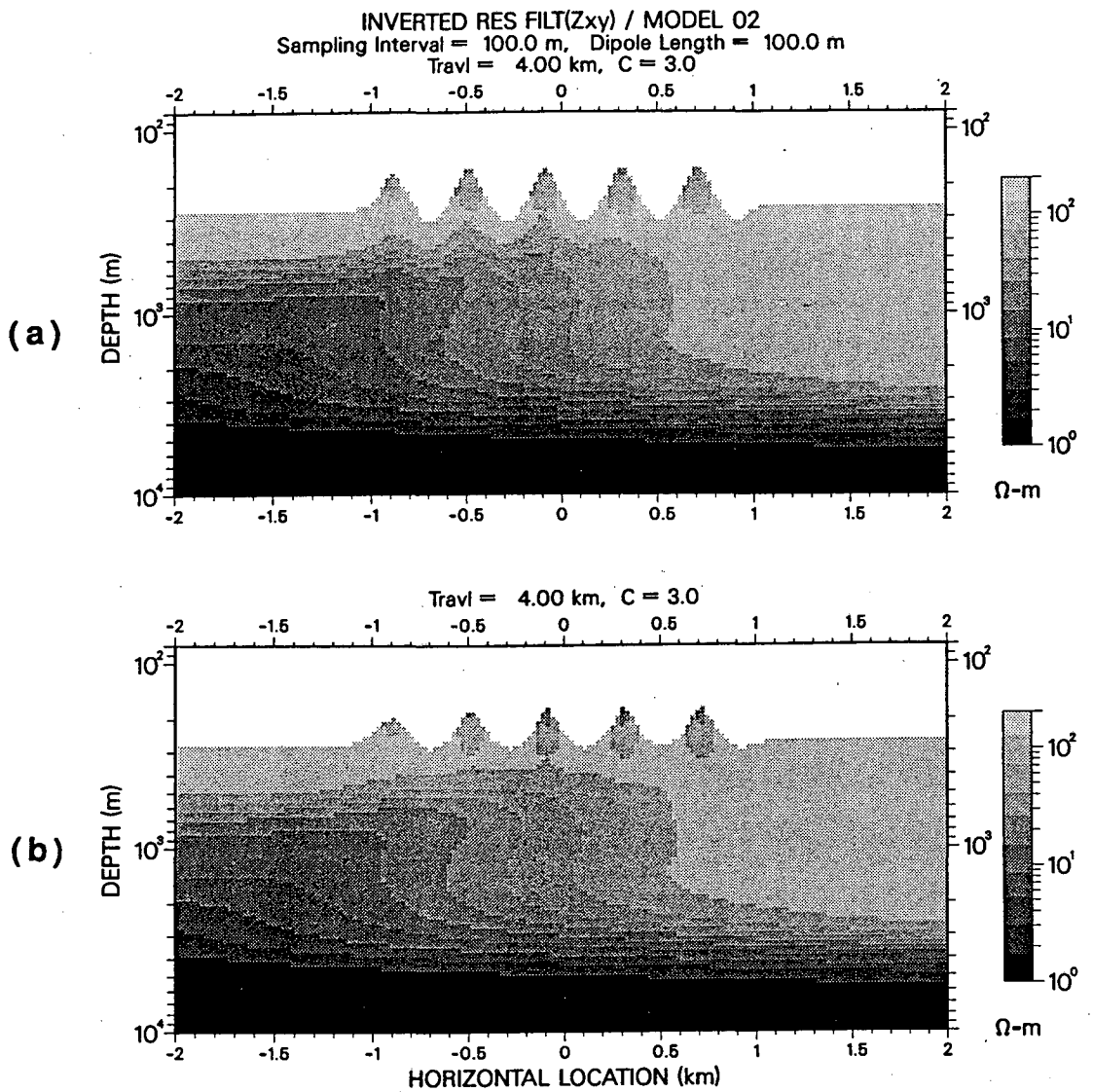

Figure 5-16. Geoelectric sections derived by spatial low-pass filtering and subsequent Bostick inversion of the TM impedances described in Figures 5-14b and 5-14c. Both sections were obtained with the use of a filter constant, c, of value 3. However, in (a) an elevation correction was applied by direct compensation of the dipole elevations, whereas in (b) the dipole elevations were compensated with use of the spatial filtering procedure described in Figure 5-15.

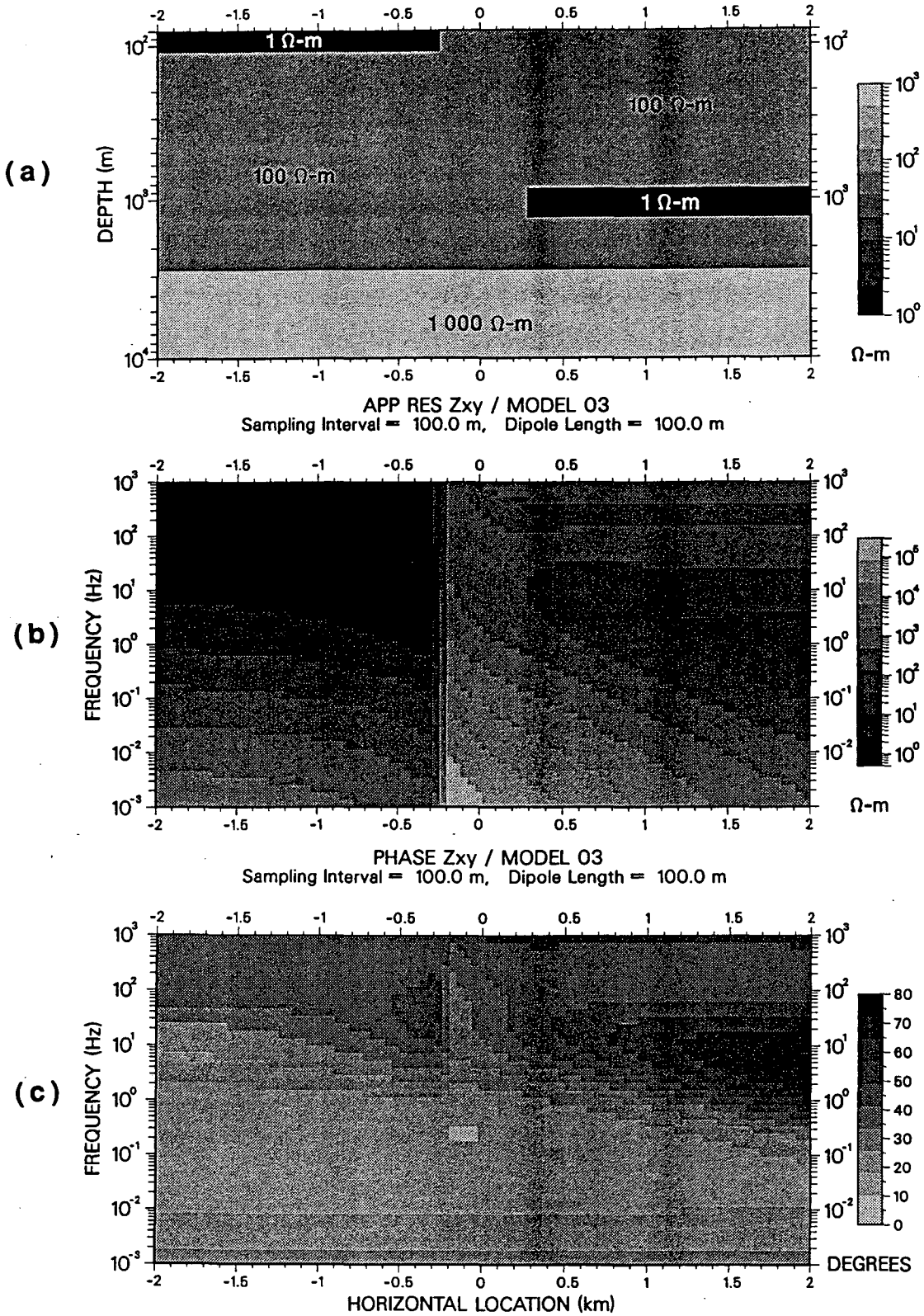

Figure 5-17. Model for the study of adjustment distance effects. **(a)** is the model plot, and **(b)** and **(c)** are the simulated TM apparent resistivity and phase pseudosections, respectively.

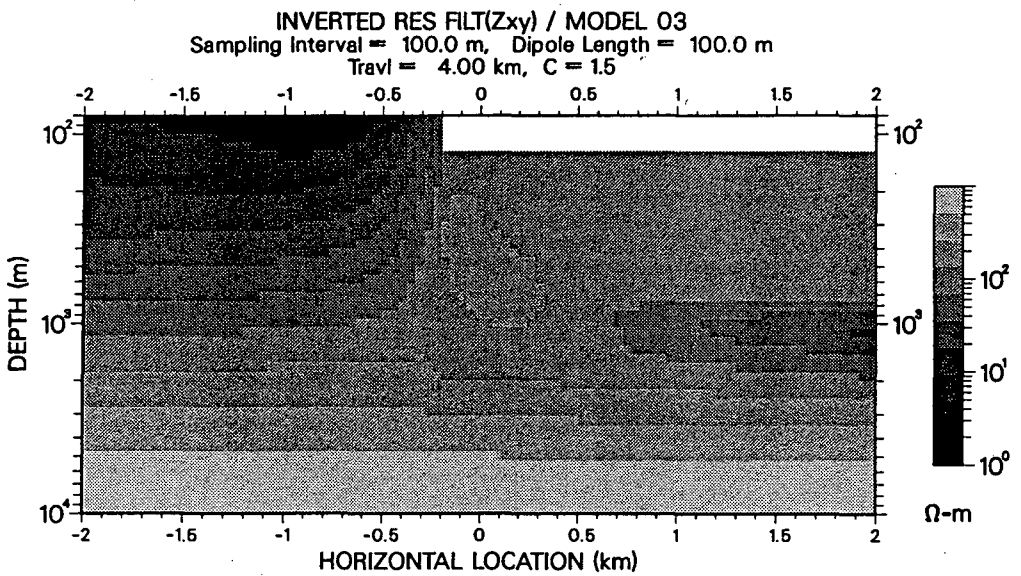

Figure 5-18. Geoelectric section derived by spatial low-pass filtering and subsequent Bostick inversion of the TM impedances described in Figures 5-17b and 5-17c. The section was obtained with the use of a filter constant, c, of value 1.5.

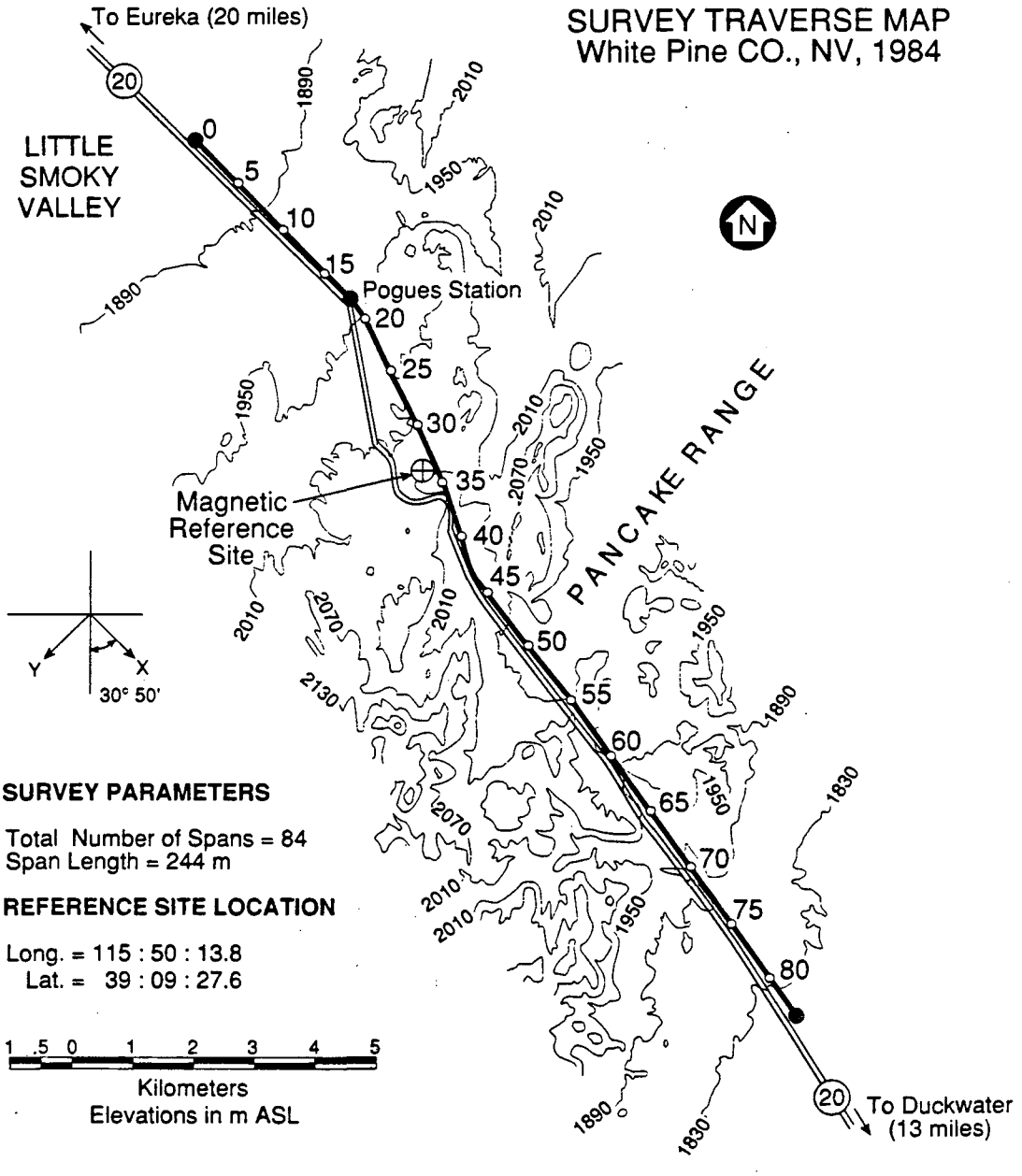

Figure 5-19. Location map of the White Pine CO. test survey. The traverse included 84 contiguous electric dipoles (spans) with a common length of 244 m (800'). A single magnetic base station was deployed and data were collected at 37 different frequencies, evenly distributed logarithmically in the band from 0.0015 to 488 Hz.

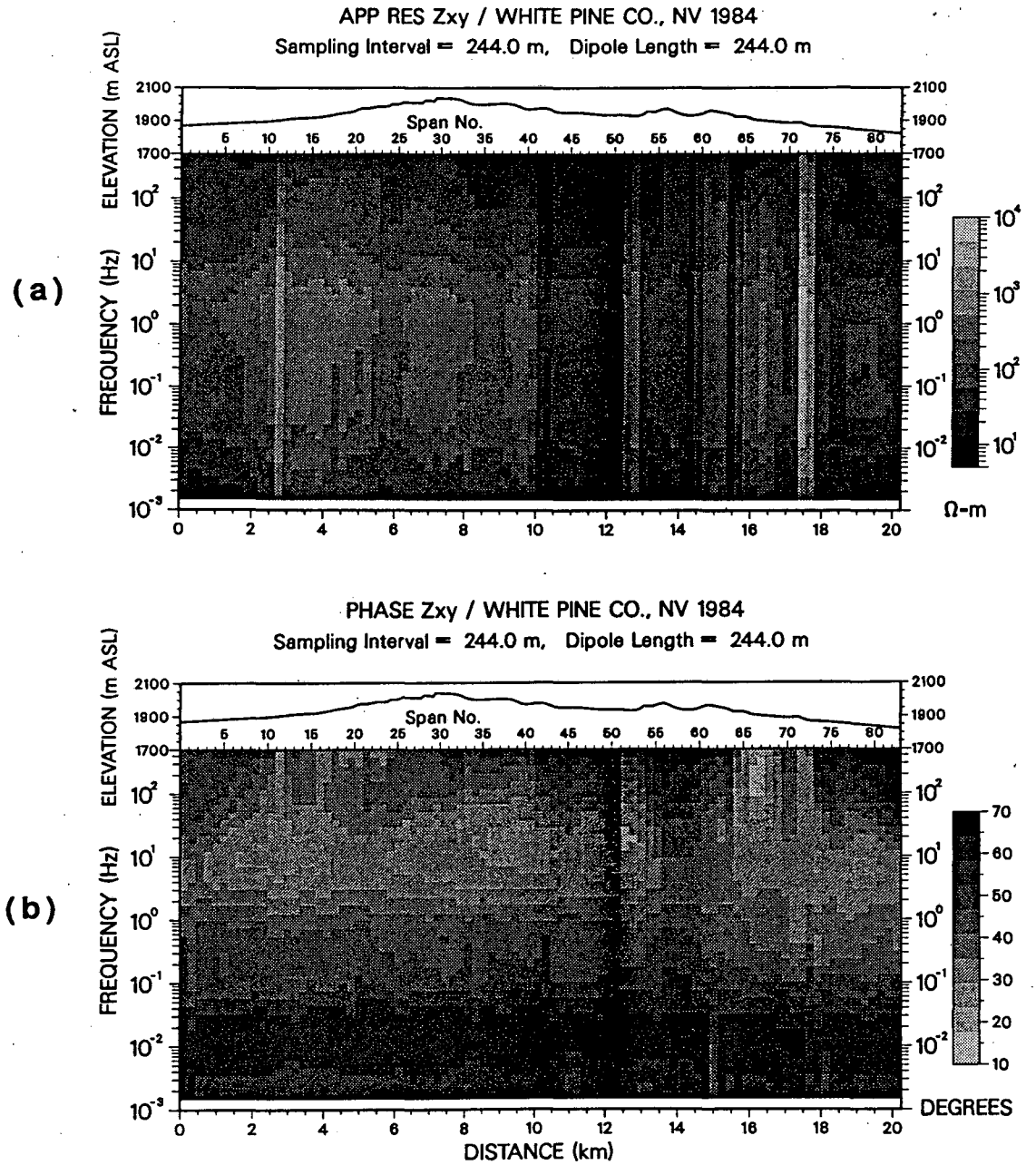

Figure 5-20. Apparent resistivity and phase pseudosections, **(a)**, and **(b)**, respectively, of the Z_{xy} base impedances measured along the White Pine CO. traverse. For reference, the topographic profile is shown in the upper panel with elevations given in meters above the sea level (m ASL).

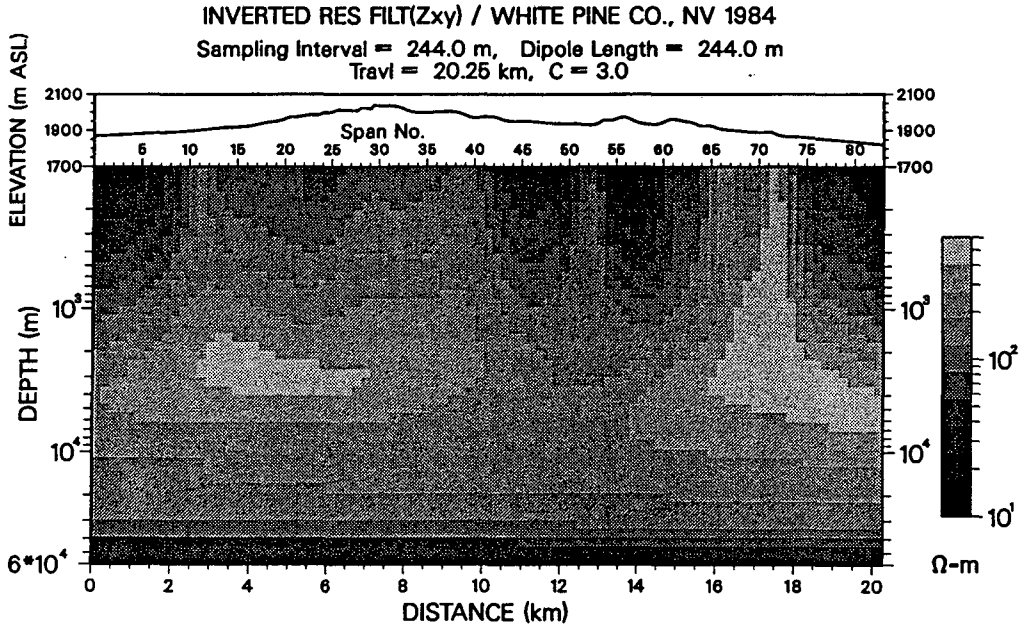

Figure 5-21. Geoelectric section derived by spatial low-pass filtering and subsequent Bostick inversion of the Z_{xy} base impedances measured along the White Pine CO. traverse. The section was obtained with the use of a filter constant, c, of value 3. Depths are measured in meters below an elevation datum placed at 1700 m ASL.

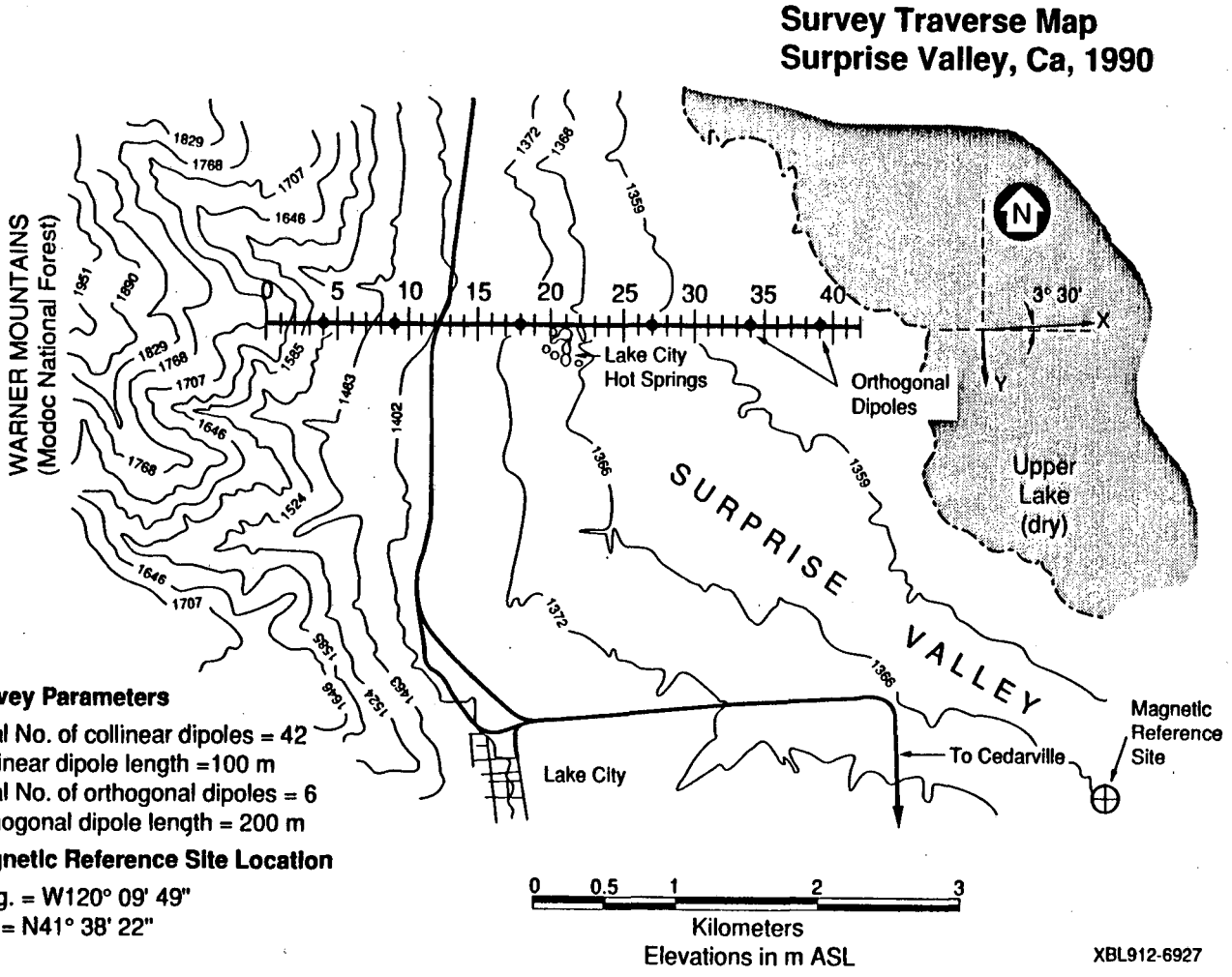

Figure 5-22. Location map of the Surprise Valley test survey. The traverse included 43 contiguous electric dipoles (spans) with a common length of 100 m. Orthogonal electric dipoles and pairs of induction coils were deployed at regular intervals along the traverse as well. The magnetic base station is shown in the lower right-hand corner of the map. Data were collected at 45 different frequencies, evenly distributed logarithmically in the band from 0.003 to 100 Hz.

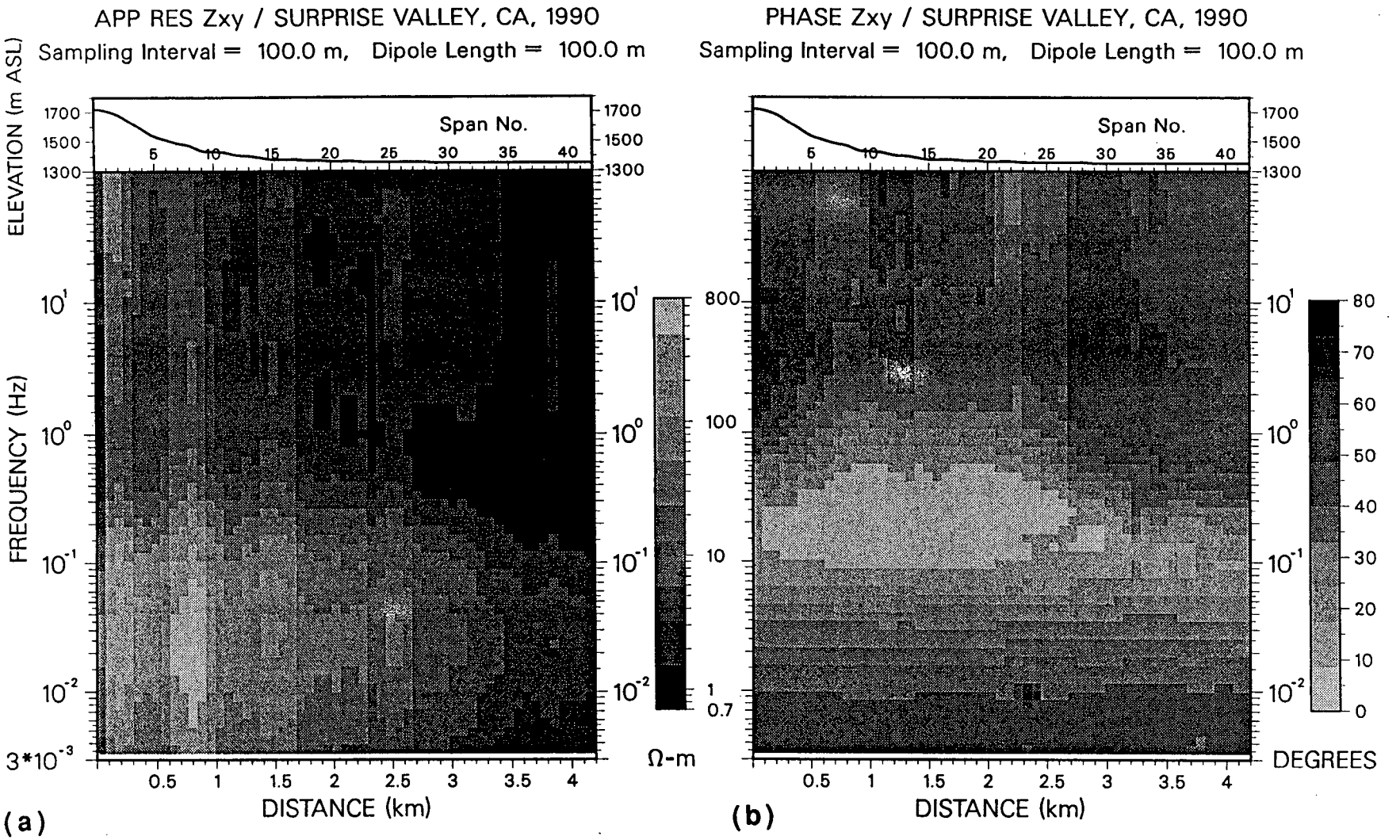

Figure 5-23. Apparent resistivity and phase pseudosections, **(a)**, and **(b)**, respectively, of the Z_{xy} base impedances measured along the Surprise Valley traverse. For reference, the topographic profile is shown in the upper panel with elevations given in meters above the sea level (m ASL).

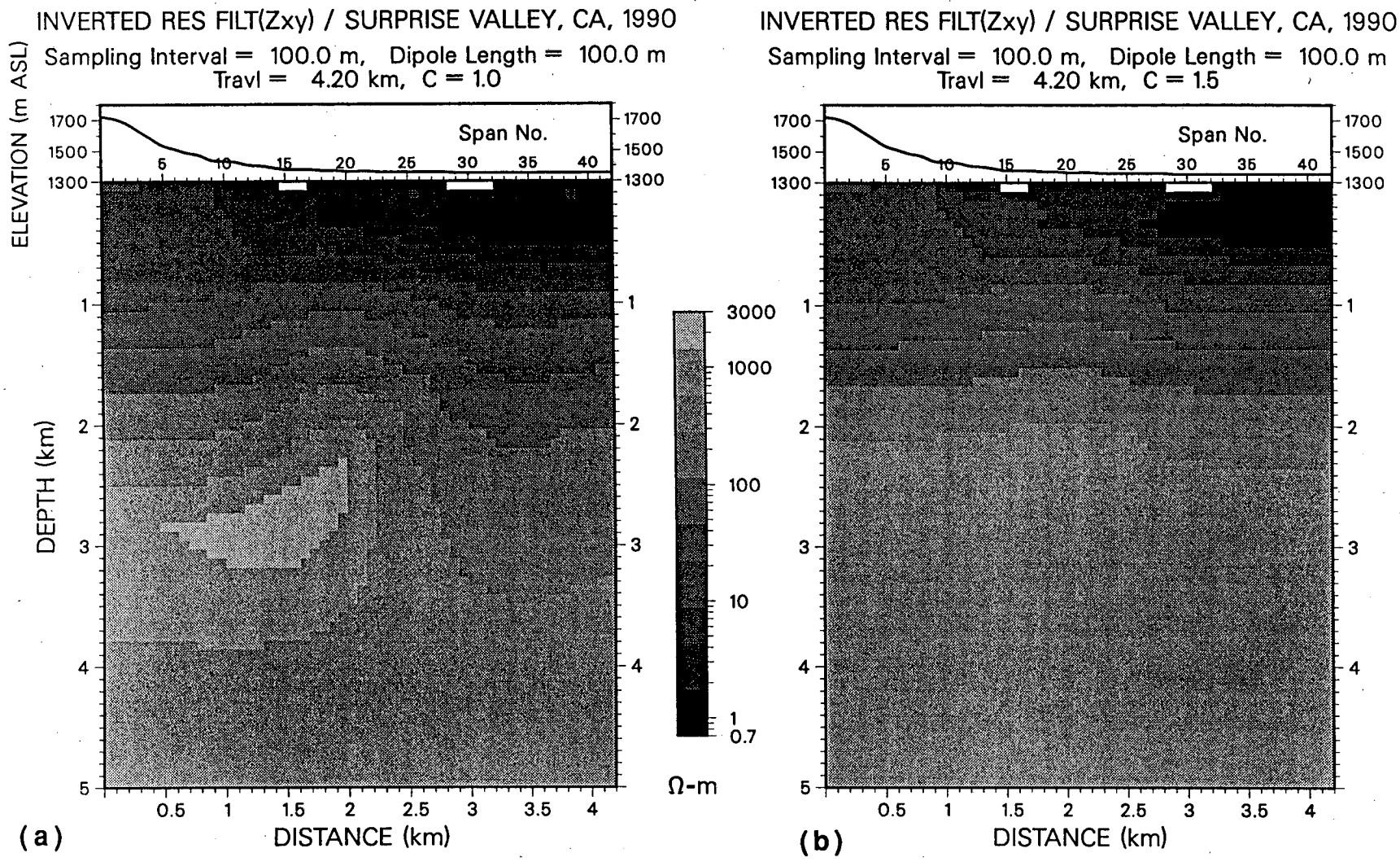

Figure 5-24. Geoelectric sections derived by spatial low-pass filtering and subsequent Bostick inversion of the Z_{xy} base impedances measured along the Surprise Valley traverse. **(a)** is the section obtained with a filter constant, c, of value 1, whereas **(b)** was obtained with a value of c equal to 1.5. Depths are measured in meters below an elevation datum placed at 1300 m ASL.

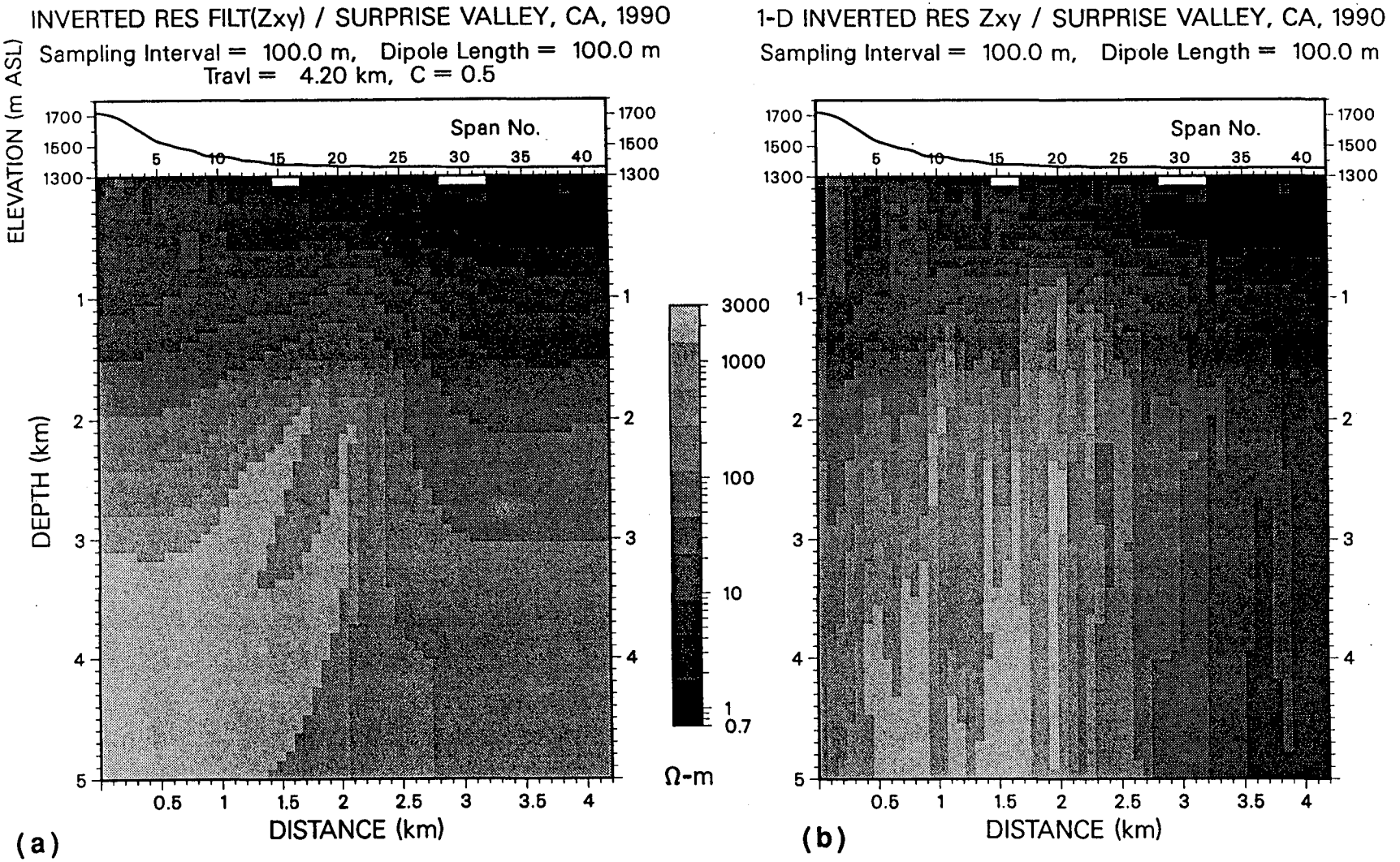

Figure 5-25. Geoelectric sections derived by spatial low-pass filtering and subsequent Bostick inversion of the Z_{xy} base impedances measured along the Surprise Valley traverse. **(a)** is the section obtained with a filter constant, c, of value 0.5, whereas **(b)** was obtained with a value of c equal to 0, that is to say, without spatial filtering. Depths are measured in meters below an elevation datum placed at 1300 m ASL.

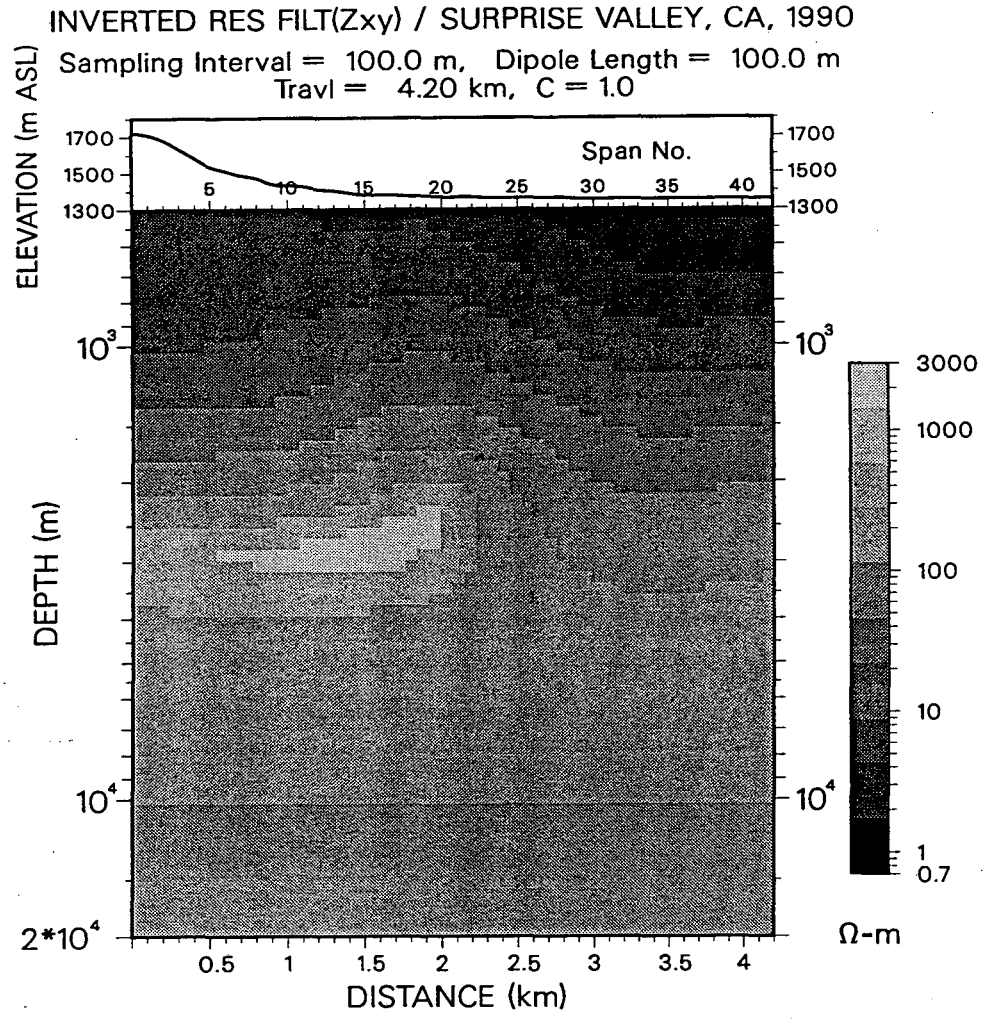

Figure 5-26. Geoelectric section derived by spatial low-pass filtering and subsequent Bostick inversion of the Z_{xy} base impedances measured along the Surprise Valley traverse. The section was obtained with a filter constant, c, of value 1. Depths are displayed with a logarithmic axis from 500 to 20,000 m below the elevation datum placed at 1300 m ASL.

CHAPTER VI

PROPERTIES OF EMAP IN 2- AND 3-D ENVIRONMENTS

6.1 Introduction

In Chapter V, methods used for the acquisition, spatial filtering, and subsequent inversion of EMAP impedances were tested on 2-D synthetic models assuming a line of measurements taken normal to strike. This chapter considers a more complicated field situation for the same methods, including both the case of a survey traverse oblique to strike and the presence of confined 3-D scatterers. Specifically, over 2-D media, it is shown that both TE and TM impedances can be approximated from the base impedances, $\hat{Z}_{xx}$ and $\hat{Z}_{xy}$, when the survey traverse is laid out at an angle with respect to strike. Estimation of the geoelectric strike direction requires only one additional orthogonal electric dipole. However, with the occurrence of local 3-D static distortion, estimation of the regional strike, if any, is best done with an orthogonal line of contiguous electric field measurements.

Over 3-D media, the synthetic EMAP model study presented here is aimed at evaluating the performance of spatial filtering over buried and surface scatterers; attention is paid to the cases where the line of measurements is either perpendicular or oblique with respect to the principal geometrical axis of the scatterer. A critical point of this task is the study of EMAP responses when the survey traverse is offset from the 3-D scatterers. For instance, it is shown that measurements of the vertical magnetic field could be used to recognize the presence of lateral induction effects on the in-line electric field. However, the suppression of electric static effects by way of spatial filtering is primarily controlled by the adjustment distance of the 3-D scatterer regardless of how the latter is transected by the line of measurements.

This chapter also includes a case history based on a three-line EMAP survey carried out over the Sengan geothermal prospect in Japan. Tangential electric field data gathered along the three lines reveal a highly 3-D subsurface resistivity distribution. The objective here is to use the electric response measured at the intersection points between pairs of lines to estimate the geoelectric strike as a function of frequency. In so doing, spatial filtering is applied to the electric field measurements along each intersecting survey line to suppress

3-D static effects prior to the rotation of conventional MT impedances. It is shown that unsuppressed static effects may cause a significant bias not only on the induction strike but also on other MT parameters of dimensionality. As corollary to these studies, a simple technique is proposed for the acquisition of conventional MT impedances that can be used to minimize electric static effects in the estimation of induction and dimensionality parameters.

6.2 Properties of EMAP in 2-D environments

In an effort to improve the exploration potential of EMAP over 2- and 3-D geoelectric media, Sigal (1989) recently advanced a similar field procedure wherein, as shown in Figure 6-1, the contiguous electric dipoles are deployed in a "zig-zag" pattern; he did so seeking to obtain continuous estimates of all tensor impedance components along the line of measurements. Particularly, Sigal (1989) remarks that because EMAP measures only one electric field component, the standard field procedure (Figure 5-2) cannot yield estimates of the TE and TM impedances when the survey is performed in 2-D environments. The developments below, however, demonstrate that so long as the line of measurements is oblique with respect to strike, both TE and TM impedances can be estimated from measurements of the tangential electric field components without having to "zig-zag" the survey path.

For simplicity, assume that the EMAP traverse coincides with the x-Cartesian axis (Figure 6-2). In the frequency domain, the relationships between the electric and magnetic field components measured along the survey line with the magnetic fields measured at the magnetic base station may be written as

$$E_x = \hat{Z}_{xx} H_x^B + \hat{Z}_{xy} H_y^B, \tag{6.1}$$

$$H_x = T_{xx} H_x^B + T_{xy} H_y^B, \text{ and} \tag{6.2}$$

$$H_y = T_{yx} H_x^B + T_{yy} H_y^B, \tag{6.3}$$

where H_x^B and H_y^B are the x and y magnetic field components, respectively, measured at the base station, E_x is the tangential electric field, and H_x and H_y are the local magnetic fields. The notation $\hat{Z}_{xx}$ and $\hat{Z}_{xy}$ is used to designate **base impedances** (equation 5.4), and the terms T_{xx}, T_{xy}, T_{yx}, and T_{yy} are magnetic transfer functions (equations 5.5 and 5.6).

The standard definition of MT impedance components, Z_{xx} and Z_{xy}, on the other hand, follows from the linear relationship

$$E_x = Z_{xx}H_x + Z_{xy}H_y. \tag{6.4}$$

It is pointed out that in the EMAP field procedure the magnetic field needs not be measured at as many locations as the electric field. Typically, the lateral magnetic field variations are not as significant as the lateral variations of the electric field, and thus one can rely on much longer sampling distances to intercalate the pointwise variations of magnetic field along the survey traverse. With an interpolation scheme of this nature, local magnetic transfer functions can in turn be computed in the form suggested by equations (6.2) and (6.3) from the base magnetic fields. In this respect, substitution of equations (6.2) and (6.3) into equation (6.1) together with comparison with equation (6.4) yields explicit relations between the base and conventional impedances, namely,

$$Z_{xx} = \frac{1}{h^2}(T_{yy}\hat{Z}_{xx} - T_{yx}\hat{Z}_{xy}), \text{ and}$$

$$Z_{xy} = \frac{1}{h^2}(T_{xx}\hat{Z}_{xy} - T_{xy}\hat{Z}_{xx}),$$

where

$$h^2 = T_{xx}T_{yy} - T_{xy}T_{yx}.$$

Formulas relating EMAP (equation 5.7) and conventional impedances can be derived in similar fashion. The remaining elements of the impedance tensor, namely, Z_{yx}, and Z_{yy}, can only be calculated if the orthogonal electric field component, E_y, is measured as well. However, if at any given point along the line of measurements only one dipole is used to measure E_y there will be no guarantee that this measurement will not be spatially aliased. Sigal's (1989) zig-zag electric field path does yield continuous estimates of E_y, but, as intuitively seen from Figure 6-1, once the spatial filtering length required to suppress static effects is a few times longer than a dipole length, the effective direction for filtering will no longer be the y-axis. In fact, the longer the filtering distance the more parallel to the x-axis the effective direction for filtering becomes. On the other hand, rotation of the electric field measurements into mutually orthogonal directions prior to performing spatial filtering may project existing 3-D static effects in a rather adverse way (see sections 6.2.1 and 6.5 below).

Suppose for the moment that the subsurface consists of only 2-D variations of resistivity. For this situation, Figure 6-2 illustrates both a line of measurements laid out at an angle, θ, with respect to strike, and a Cartesian coordinate frame with its x'- and y'-axes in the directions parallel and perpendicular to strike, respectively. In the x'-y' coordinate frame, the E'_x and E'_y electric field components are described by the uncoupled linear equations

$$E'_x = Z_{TM}H'_y, \text{ and}$$

$$E'_y = -Z_{TE}H'_x,$$

where the complex variables Z_{TE} and Z_{TM} are the TE and TM impedances, respectively, that characterize the geoelectric properties of the underlying 2-D medium. By counterclockwise rotation of the electric and magnetic field components E'_x, H'_x, and H'_y, respectively, into the x-y Cartesian coordinate frame, one obtains the expressions

$$Z_{xx} = (Z_{TE} - Z_{TM})\sin\theta\cos\theta, \text{ and} \quad (6.5)$$

$$Z_{xy} = Z_{TE}\sin^2\theta - Z_{TM}\cos^2\theta \quad (6.6)$$

relating the TE and TM impedances with the Z_{xx} and Z_{xy} tensor impedance components measured with the x-y Cartesian coordinate frame. These expressions can only be implemented in practice when θ is known.

Equations (6.5) and (6.6) above indicate that whenever θ is neither 0° nor 90° one can solve for both TE and TM impedances from measurements of Z_{xx} and Z_{xy} acquired along the oblique traverse. If θ=0° then Z_{xx}=0 and Z_{xy}=Z_{TM}; if θ=90° then Z_{xx}=0 and Z_{xy}=Z_{TE}. Explicit relations for both Z_{TE} and Z_{TM} in terms of the Z_{xx} and Z_{xy} impedances are

$$Z_{TE} = Z_{xx}\cot\theta + Z_{xy}, \text{ and} \quad (6.7)$$

$$Z_{TM} = -Z_{xx}\tan\theta + Z_{xy}. \quad (6.8)$$

For the common situation in which the magnetic field is sampled at only the base site, the TE impedances estimated via equation (6.7) will reflect only the lateral variations of TE electric field. Likewise, if the TE impedances are estimated from the $\tilde{Z}_{xx}$ and $\tilde{Z}_{xy}$ EMAP impedances, these will reflect variations of the ratio between the electric field $-E'_y$, and the primary magnetic field, H'_{0x}. On the other hand, usage of either local, base, or

primary magnetic field components does not modify the nature of the TM impedances.The mixture of both TE- and TM-like electric field responses that explains in general the Z_{xy} (either base or EMAP) traverse impedances proves useful to understand how spatial filtering works when the line of measurements is oblique with respect to strike.

By way of example, consider the geoelectric cross-section shown in Figure 6-3a. This corresponds to a 2-D vertical fault model projected at a 45° angle with respect to strike (the projection angle, θ, defined as illustrated in Figure 6-2). The vertical fault separates rectangular blocks with resistivities of 100 and 1,000 Ω•m on the left- and right-hand sides of the section, respectively, and is terminated on the surface with a 10,000 Ω•m symmetric block (vertical and lateral dimensions of 100 and 500 m, respectively). At depth, the fault is underlain by a 10 Ω•m half-space buried 3 km below the surface. Figures 6-3b and 6-3c are the cross-sections of subsurface resistivity derived by Bostick inversion of the TE and spatially filtered (filter constant, c, equal to 3) TM impedances, respectively. Both TE and TM impedances were estimated from the $\widetilde{Z}_{xy}$ EMAP impedances using the formulas (6.7) and (6.8) and assuming primary magnetic field components instead of a laterally varying surface magnetic field. In turn, $\widetilde{Z}_{xy}$ EMAP impedances along the survey traverse were simulated from the responses of 100 m-long contiguous electric dipoles. Because of the 45° angle projection in the model section (Figure 6-3a), the traverse length used for spatial filtering was made 2 km longer than the standard normal-to-strike length of 4 km. The numerical simulations were performed in the frequency band from 0.001 to 1,000 Hz, at a rate of 5 samples per decade. Resistivity cross-sections derived directly from the $\widetilde{Z}_{xy}$ EMAP impedances via spatial filtering and subsequent Bostick inversion are shown in Figures 6-4b and 6-4c in association to filter constant values, c, of 2 and 3, respectively.

The lateral resolution characteristics described in Chapter IV for both TE and TM impedance are well exemplified in Figures 6-3b and 6-3c. For instance, the progressive loss of high wavenumber harmonics with respect to depth is evidenced by the smoothness with which the vertical fault boundary has been recovered in each case. This loss of wavenumber harmonics is much more pronounced for the TE electric field than for the TM electric field. However, the TE electric field response exhibits better vertical resolution characteristics (the conductive basement is better resolved in this case) than the TM electric field. In contrast, the sections derived from the $\widetilde{Z}_{xy}$ impedances are somewhat smoother laterally than the section derived from the estimated TM impedances, but do show a flatter basement. The difference in lateral behavior between the $\widetilde{Z}_{xy}$ and TM resistivity sections is due to the superposition of TE electric field variations in the $\widetilde{Z}_{xy}$ impedances, which even

though has acted in detriment of the high wavenumber harmonics, it has improved the vertical resolution characteristics of the section (increasing the value of filter constant, c, smooths the $\widetilde{Z}_{xy}$ section laterally, but does not translate to a more severe loss of vertical resolution.)

A second model example is shown in Figure 6-5a; this is a projected version of the geologic noise model studied in section 5.7.1. The survey traverse is laid out at a 45° angle with respect to strike, and consists of 100 m-long contiguous electric dipoles deployed along a total distance of 6 km. From these dipoles, $\widetilde{Z}_{xy}$ impedances were simulated in the same frequency range and with the same sampling interval as in the previous example. Resistivity cross-sections derived by spatial filtering and subsequent Bostick inversion of the TM and $\widetilde{Z}_{xy}$ impedances are shown in Figures 6-5b and 6-5c, respectively. In both cases, the spatial filter was adapted with a filter constant, c, of value 3. Barring the difference in traverse length (the effective length normal to strike is about the same), the inverted TM resistivity section compares well with the resistivity section shown in Figure 5-11b, and which was derived directly from the simulated TM impedances measured perpendicularly to the strike. On the other hand, even though the $\widetilde{Z}_{xy}$ impedances have yielded a laterally smoother resistivity section than the estimated TM impedances, the former have been superior in resolving the conductive basement. Likewise, the vertical gap between the most conductive block of the surface overburden and the buried rectangular block is better resolved in the $\widetilde{Z}_{xy}$ section than in the TM section. Finally, as a parenthetical note, Figures 6-6b and 6-6c show the apparent resistivity and phase pseudosections, respectively, of the $\widetilde{Z}_{xx}$ cross-coupling impedances. As evidenced by these figures, even though both amplitude and phase may attain large values at some points, the pseudosections reveal a somewhat randomly distributed electric field response. In fact, this randomness helps explain why spatial filtering of the cross-coupling component consistently approaches zero for progressively longer averaging distances (see section 2.5), and thus why only the $\widetilde{Z}_{xy}$ impedance is used to drive the adaptive spatial filtering procedure described in section 5.4.

Because adaptive spatial filtering is relatively harmless to the TE (purely inductive) electric field response, filtering performed on the $\widetilde{Z}_{xy}$ impedances will suppress only the static component of the TM electric field response. In this regard, equation (6.6) shows that the influence of TE electric field effects on the filtered $\widetilde{Z}_{xy}$ impedances will increase with increasing values of the angle, θ, between the survey traverse and the normal-to-strike

direction. Values of θ over 45° cause the $\tilde{Z}_{xy}$ impedances to contain a larger proportion of the TE impedances than of the TM impedances. Conversely, values of θ lower than 45° cause just the opposite effect. Thus, spatial filtering and subsequent inversion of the $\tilde{Z}_{xy}$ impedances may be thought of as a joint inversion of both TE and TM impedances when the survey traverse is laid out at an angle with respect to strike. A 45° traverse is the break even point where both TE and TM impedances are equally weighed in the inversion process. The tradeoff incurred on with the use of an oblique traverse, however, is an increase in survey length, the latter proportional to $\tan(\theta)$. A field procedure that can be implemented for the estimation of θ is discussed below.

6.2.1 Estimation of the strike angle

The preceding analyses show that estimation of both TE and TM impedances from the $\tilde{Z}_{xx}$ and $\tilde{Z}_{xy}$ traverse impedances can only be accomplished if the strike angle, θ, is known beforehand. This estimation requires measurements of the electric field orthogonal to the line of measurements. In 2-D environments, only one orthogonal dipole is needed to calculate θ (Figure 6-2). Orthogonal and tangential electric field data acquired at the same control point can be assembled into a standard MT tensor, which in turn can be analyzed with standard techniques to yield an estimate of strike angle (see, for instance, Vozoff, 1972). In addition, vertical magnetic field data may be acquired at the same point to properly discriminate between the strike and normal-to-strike directions.

Even though a number of practical situations exist where the bulk MT response of the subsurface can be considered 2-D in a regional scale, often near-surface resistivity anomalies cause enough electric static distortion to severely bias the estimation of the regional strike angle by conventional techniques (see Groom and Bailey, 1989, for an excellent analysis of this topic) To circumvent this difficulty on the interpretation of conventional MT impedances, Groom and Bailey (1989) propose an ad-hoc matrix factorization for the 2x2 impedance tensor that can unravel regional strike directions in the presence of 3-D electric static distortion. However, because of the short electric field sampling distances that are normally used to acquire conventional MT impedances, Groom and Bailey's (1989) matrix factorization method is of limited use precisely where it would be most valuable.

The procedure suggested here for the estimation of a regional 2-D strike angle under 3-D electric static distortion is illustrated in Figure 6-7. This consists of the deployment of

an additional line of electric dipoles (a mini-EMAP line) perpendicular to the main line of measurements. Data acquired from these dipoles are amenable to the spatial filtering procedures described in Chapter V for the suppression of static distortion; the longer the orthogonal traverse the more efficiently the static distortion can be suppressed over a wider frequency range. However, when economic conditions severely constrain the deployment of a string of electric dipoles, one can be opt for the deployment of a single but longer dipole at regular spacings along the traverse (see the Surprise Valley field example in section 5.9). The disadvantage of a single longer dipole over a string of them is that the former may sometimes miss valuable information about the inductive response at the highest frequencies.

Upon applying spatial filtering both along the mini-EMAP line and along the main survey traverse, the regional geoelectric strike angle, θ, can be estimated at the intersection point (or points), and the TE and TM impedances computed from equations (6.7) and (6.8) at the remaining points along the line of measurements. In principle, spatial filtering along the mini-EMAP line should yield a depth of penetration comparable to that obtained with spatial filtering performed along the main survey traverse at the same frequency. This specialized form of spatial filtering along orthogonal directions is tested with a field example in section 6.5.

The location for the orthogonal mini-EMAP traverse (or long orthogonal dipole) should not be arbitrary, especially when the influence of 2-D geoelectric features is confined to only some portions of the survey traverse. For best results, the orthogonal mini-EMAP line should be deployed at a point (or points) where lateral induction effects are most conspicuous. Such points can be determined by inspection of the $\widetilde{Z}_{xx}$ cross-coupling impedance. Barring the presence of 3-D electric static distortion, large lateral variations of $\widetilde{Z}_{xx}$ are indicative of induction current oriented at an angle with respect to the survey traverse. It is at points where this occurs that the location of the mini-EMAP line (or longer orthogonal dipole) is most appropriate.

6.3 EMAP simulation in 3-D environments

Use of EMAP for the sounding of 3-D geoelectric media involves a few practical considerations, some of which are simple extensions of the ideas discussed above in reference to the sampling of 2-D surface electric field responses. In contrast, however, depending on their relative dimensions and depth of burial, confined 3-D scatterers often provide a weaker inductive MT response than 2-D scatterers with the same cross-section.

Moreover, over 3-D media there is always the possibility not only of transecting confined 3-D scatterers at an arbitrary angle but also of sensing their static and inductive electric responses without having transected them at all. The simulation study presented in this section is aimed primarily at examining the performance of EMAP in these last two situations. To this end, surface electric and magnetic field data were synthesized with the 3-D integral equation code of Wannamaker (1990) which, among other things, allows for outcropping scatterers. The standard frequency range from 0.001 to 1,000 Hz is considered, and includes 5 frequency samples per decade. Only straight survey traverses are studied and the convention adopted is that the x-axis coincides with the survey traverse and that the z-axis points downward into the earth. In all cases, $\widetilde{Z}_{xy}$ EMAP impedances are computed from the responses of 100 m dipoles (simulated by numerical integration of the tangential electric fields) deployed end-to-end along the traverses. The model examples consist of (1) a simple buried 3-D scatterer and, (2) a combination of both surface and buried 3-D scatterers.

6.3.1 A simple 3-D scatterer in a 1-D background

Both a plan view and a cross-section of the first model example are shown in Figure 6-8. The 1-D background of this model is composed of a 250 Ω•m upper layer and a 1 Ω•m basement, the latter buried 4 km below the surface. A single 3-D scatterer is introduced in the form of a 1 Ω•m rectangular block buried at a depth of 100 m and with lateral dimensions of 700 m x 700 m and thickness of 300 m. The two survey traverses considered for the EMAP simulation are described in the plan view of Figure 6-8: Line 1 transects the 3-D scatterer directly above it, and Line 2 is offset 200 m away from it. Both lines have a common length of 3 km.

Apparent resistivity and phase pseudosections describing the simulated $\widetilde{Z}_{xy}$ impedances along Line 1 are shown in Figures 6-9b and 6-9c, respectively. In Figure 6-9b, the static effect introduced by the buried 3-D scatterer on the inductive 1-D background response is evident in the central portion of the pseudosection. Along Line 2, the corresponding apparent resistivity and phase pseudosections of the $\widetilde{Z}_{xy}$ impedances are displayed in Figures 6-10b and 6-10c, respectively. Even though the model cross-section along Line 2 does not transect the 3-D scatterer, the $\widetilde{Z}_{xy}$ apparent resistivity pseudosection in Figure 6-10b shows electric static effects superimposed on the inductive signature of the conductive basement. In contrast, the impedance phase pseudosection along the same line

shows significant lateral variations only at the highest frequencies, which can only be explained by the offset 3-D scatterer.

Resistivity cross-sections derived by spatial filtering and subsequent Bostick inversion of the simulated $\tilde{Z}_{xy}$ impedances along Line 1 and Line 2 are shown in Figures 6-11b and 6-11c, respectively. Both sections were obtained with the use of a filter constant, c, of value 2. In Figure 6-11b, the lateral variations of the shallowest depth of penetration are determined by the underlying resistivity profiles, and this is why even at the highest frequency (shallowest depth of penetration) the buried 3-D scatterer gives the impression of a surface feature. In general, however, the section compares well with the adjoining model cross-section (Figure 6-11a). Along Line 2, spatial filtering proved successful in suppressing the electric static effect from the buried 3-D block and superimposed on the inductive signature of the conductive basement. However, even after spatial filtering has been performed, the relative proximity of the buried 3-D scatterer has left a clear imprint on the inverted resistivity section shown in Figure 6-11b. Because the inductive signature of the 3-D scatterer is also visible in the impedance phase pseudosection, it is impossible to ascertain whether the scatterer is offset from the survey traverse without additional in-line field measurements. Deployment of an orthogonal dipole may be helpful in resolving this situation, but as emphasized in section 6.2 above, it may also be dangerous under complex static distortion if precautions are not taken to minimize spatial aliasing. A more viable alternative consists of making measurements of the vertical magnetic field at regular intervals along the survey traverse, as described below.

The magnetic field measurements, H_z, made along the survey traverse can be written in terms of the primary magnetic field components, H_{0x} and H_{0y}, with the linear relation

$$H_z = \tilde{K}_{zx}H_{0x} + \tilde{K}_{zy}H_{0y}, \qquad (6.9)$$

where the terms $\tilde{K}_{zx}$ and $\tilde{K}_{zy}$ are modified tipper transfer functions[1]. The functions $\tilde{K}_{zy}$ and $\tilde{K}_{zx}$ are mostly governed by inductive effects from conduction current parallel and perpendicular to the line of measurements, respectively. The combined lateral and frequency behavior of both tipper transfer functions provides indication of subsurface induction current either oriented at an angle with respect to the traverse or offset from it. For instance, along Line 2 of Figure 6-8, Figures 6-12b and 6-12c show the

[1] Vozoff (1972) has presented a similar linear expression with tipper components that relate the local horizontal and vertical magnetic fields.

pseudosections of the real part of the tipper transfer functions $\widetilde{K}_{zy}$ and $\widetilde{K}_{zx}$, respectively. Even though both pseudosections exemplify lower than practical tipper values, the prevalent positive response of the real component of $\widetilde{K}_{zy}$ together with the negligible response values of the real part of $\widetilde{K}_{zx}$ are indicative of an inductive scatterer located to the left side of the traverse, as is in fact the case.

As stressed in in section 2.6, the secondary magnetic fields measured on the surface are much less sensitive to near-surface scatterers than the secondary electric fields are, and for this reason the gathering of vertical magnetic field data becomes an attractive procedure to ascertain induction effects that cannot be evaluated from tangential electric field measurements alone. However, in the presence of multiple scatterers, both laterally and at depth, care must be exercised to interpret the tipper measurements. In the most difficult cases the deployment of an additional line of measurements cannot be avoided.

6.3.2 Surface and buried 3-D scatterers in a 1-D background

A slightly different version of the previous example is described in Figures 6-13 and 6-14. Several degrees of complexity can be recognized in this new model regarding both the subsurface resistivity structure and the way in which the survey traverse is laid out with respect to the predominant current channeling paths in the 3-D scatterers.

The 1-D model background consists of a two-layer sequence in which the upper layer has a resistivity of 80 Ω•m and the lower layer is a 1,000 Ω•m half-space buried at a depth of 3.5 km. Surface resistivity anomalies are introduced in the model by way of three elongated rectangular blocks, two of which have a resistivity of 5 Ω•m, lateral dimensions of 800 m x 200 m and thickness of 50 m. The third surface block has a resistivity of 500 Ω•m, lateral dimensions of 500 m x 2 km, thickness of 250 m and, most importantly, is oriented perpendicularly to the remaining surface blocks. A single buried 3-D rectangular scatterer is located in the upper layer of the 1-D background at a depth of 700 m. This last block has lateral dimensions of 2 km x 1 km and thickness of 1km. The three survey traverses considered for the simulation study have a common length of 4 km.

A cross-section of subsurface resistivity along Line 1 is shown in Figure 6-15a. The corresponding apparent resistivity and phase pseudosections describing the simulated $\widetilde{Z}_{xy}$ impedances along the same line are shown in Figures 6-15b and 6-15c, respectively. Similarly, model sections and impedance pseudosections for Line 2 and Line 3 are shown in Figures 6-16 and 6-17, respectively. This set of plots reveals rather interesting electric

static distortion effects. In particular, lateral deflection patterns in the distribution of surface conduction current are evidenced in the apparent resistivity pseudosections for Line 2 and Line 3. In contrast, the corresponding impedance phase pseudosections exhibit the same effects only at the highest frequencies. Also, static distortion effects caused by surface scatterers adjacent but not intersected by the survey traverse are visible in the apparent resistivity pseudosections simulated along Line 1 and Line 2.

Resistivity sections derived by spatial filtering and subsequent Bostick inversion of the $\widetilde{Z}_{xy}$ impedances over Line 1, Line 2, and Line 3 are shown in Figures 6-18, 6-19, and 6-20, respectively. For comparison, each of these figures includes also a resistivity section derived from $\widetilde{Z}_{xy}$ impedances simulated without near-surface scatterers. The values of filter constant, c, used in the filtering step were adjusted to minimize lateral smoothing of the inductive signature derived from the buried rectangular block. Because of this, in some of the sections the filter constant is larger with the presence of near-surface static effects than without them (either 2 or 1, respectively).

Even though along Line 1 the inverted resistivity section (Figures 6-18b) provides good indication to the lateral extent of the buried conductive block, its vertical boundaries are somewhat obscured by the resistive block directly above it. Also, the surface conductive slabs have caused a slight vertical distortion in the section, but the most interesting effect is located at their end points, where the lateral deflection of surface current (lateral current channeling) has produced the impression of a resistive feature. Without near-surface static effects (Figure 6-18c), the buried block is well determined both laterally and vertically, except that the resistivity recovered for this feature is approximately 10 times higher than its actual value. This discrepancy seems excessive especially when compared, for instance, against the resistivity value one would recover under similar circumstances for the case of a 2-D scatterer with the same cross-section. However, because in fact the induction response of a confined 3-D scatterer can be several times smaller than the response of a 2-D body with the same cross-section (the controlling parameters are depth of burial and strike length of the 3-D scatterer), the vertical resolution characteristics are not the same in both cases. An approximate 1-D inversion technique such as the Bostick (1977) pseudoinverse is particularly sensitive to this situation.

The inverted resistivity section for Line 2 (Figures 6-19b) shows lateral induction effects introduced by both resistive and conductive surface slabs at the shallowest depths, but still provides good indication of the buried rectangular block across the section.

However, as in the case of Line 1, the resistivity inferred for this feature is about 10 times higher than its actual value. Also, because of the fact that the scattering section of the buried block along Line 2 is smaller than its scattering section along Line 1, the same block appears slightly smoother laterally in Figure 6-19b than in Figure 6-18b. This situation is even clearer in the resistivity section inverted without the presence of surface static distortion (Figure 6-19c).

Along Line 3, the inverted resistivity section (Figure 6-20b) shows at the shallowest depths the presence of both the surface resistive block and an unexpected resistive anomaly. The latter anomaly is spurious and originates from the lateral deflection of conduction current that exists in the vicinity of the conductive slab. In effect, on the surface most of the conduction current is being channeled along the principal geometrical axis of the slab so that, slightly away from it, the absence of conduction current is equivalent to the presence of a resistive feature at the same point, thus the spurious anomaly. Another important feature of the resistivity section shown in Figure 6-20b is the excessive lateral smoothness with which the buried block has been recovered (especially when compared against the profiles that for the same block were recovered along Line 1 and Line 2.) This situation is somewhat analogous to the 2-D test cases of section 6.2, where it was found that if the traverse is laid out oblique to strike then a proportion of the TE electric field response is automatically absorbed by the $\widetilde{Z}_{xy}$ impedances. In similar fashion, in addition to the predominant TM-like induction component measured along Line 1 and Line 2, along Line 3 the $\widetilde{Z}_{xy}$ impedances bear a significant proportion of the TE-like induction component due to induction current parallel to the principal geometrical axis of the buried block. Because of the inherent lateral smoothness of this TE-like inductive response, the resistivity section derived from the $\widetilde{Z}_{xy}$ impedances along Line 3 develops what is termed "lateral conductive leakage" at depth (see also Figure 6-20c). However, exactly as described in section 6.2 above, with approximate knowledge of the main geometrical axis of the causative scatterer, this smoothness may be somewhat reduced by decoupling the TM-like response in the $\widetilde{Z}_{xy}$ impedances prior to spatial filtering.

6.4 Discussion of simulation results

The 2- and 3-D synthetic model examples analyzed above indicate that spatial filtering of the surface electric field is an efficient procedure for the suppression of static effects even when the traverse is laid out at an angle with respect to the predominant geoelectric strike. Over 3-D media, spatial filtering is also adequate for reducing electric

static effects due to resistivity anomalies offset from the survey traverse. That the latter conclusion is correct can be intuitively demonstrated with the aid of Figure 6-21. In this figure, a closed contour of integration, Γ, for the line integral

$$\oint_{\Gamma} \mathbf{E} \cdot d\ell$$

that describes spatial filtering applied to the electric field, **E**, is laid out over a surface 3-D scatterer responsible for static distortion. The contour Γ is closed below the surface with a semicircle of infinite radius such that the contribution from this segment portion of the contour becomes negligible for all practical purposes. In the DC limit, regardless of the way in which the contour is drawn on the surface (even in curvilinear fashion), Faraday's law shows that the electric field integral will vanish provided that the integration path has its end points outside the area of secondary field distortion. This simple physical construct indicates that suppression of 3-D electric static effects by way of spatial filtering does not require that the traverse be laid out directly over the causative body. The most important requirement, though, is that the traverse be long enough to include the spatial region of secondary electric static distortion.

It was also seen from the synthetic model examples above that inversion of the electric induction component remaining after spatial filtering yields a relatively accurate cross-section of subsurface resistivity. However, several points should be made clear regarding this procedure of inversion. It was found that spatial filtering and subsequent inversion of the $\widetilde{Z}_{xy}$ traverse impedances may sometimes lead to appreciable lateral smoothing ("lateral conductive leakage") of the resistivity section when the traverse is laid out at an angle with respect to the predominant geoelectric strike. This situation, far from expressing a detrimental characteristic of spatial filtering, is related to the obliqueness of the traverse. More specifically, an oblique traverse introduces some amount of TE-like induction response on the $\widetilde{Z}_{xy}$ impedances calculated from the tangential electric fields. Because the TE-like electric response varies more smoothly, laterally, than the TM-like response measured along a transect perpendicular to a principal strike direction, the induction component of $\widetilde{Z}_{xy}$ remaining from spatial filtering will lead to a laterally smooth resistivity cross-section. Moreover, it should be recalled that the induction response of a buried 3-D scatterer with finite strike length is not as prominent as the induction response of a buried 2-D scatterer with the same cross-section. For this reason, the vertical resolution characteristics of the electric induction component are in general superior in 2-D media.

Lastly, inasmuch as spatial filtering is insensitive to the electric induction component, the spatially filtered impedances may retain the induction response of 3-D scatterers located laterally away from the survey traverse. Recognizing such lateral induction effects can be accomplished in various ways. It was stressed here that because the vertical magnetic field is affected by DC current channeling only in very pathological situations, measurements of this component may be interpreted to diagnose those situations. Pursuing similar objectives with the use of orthogonal dipoles, or sequence of orthogonal dipoles is explored below with a field example.

6.5 Sengan field example

The Sengan exploration project was one of the most promising targets of a large research and development effort undertaken by the government of Japan to assess the geothermal potential of that country. The area of study is located in the border between the Akita and Iwate Prefectures of Honshu Island, as indicated in the location map shown in Figure 6-22. Previous reconnaissance studies in this region suggested an active geothermal zone at a depth of approximately 2 km; geological and geophysical studies almost immediately followed (see, for instance, Uchida et al., 1987, and Uchida, 1990). Use of seismic methods turned out to be impractical because of access problems, abrupt topographic relief and complicated surface geology. Thus, initially, MT and DC resistivity soundings were acquired at scattered locations in the area to understand basic properties of the andesite-rhyolite volcanic sediments underlying the quaternary surface deposits (mainly breccias and volcanic agglomerates) that exist in the proximity of the Hachimantai volcano. However, the subsequent interpretation of those data yielded inconclusive results mainly because of complicated 3-D response effects.

It was at this point that in early 1988 the New Energy and Industrial Technology Development Organization (NEDO) of Japan, decided to finance the exploration of the Sengan geothermal project with the EMAP technique. This decision was partly made with the intent to ascertain whether EMAP was a viable technique for the exploration of other similarly complicated geothermal targets in Japan. The survey was contracted to the Japanese exploration company Marc-Rand Co., which in turn deferred the field data acquisition portion of the project to the now defunct US company Advanced Energy Technology.

The Sengan EMAP project consisted of three survey traverses, hereafter referred to as Line A, Line B, and Line C, laterally extending over the most significant portion of the

geothermal reservoir as it was known from geological and geophysical data. A description of the survey parameters involved in the exploration of each line can be found in the table insert of Figure 6-22. Because of severe topography (Line A and Line B actually transect the Hachimantai volcano) and technical problems with the mobilization of equipment, a variable dipole was used along each line and, as can be seen from Figure 6-22, the electric field lines could not be laid out in straight lines. Locations of the magnetic base station and additional MT sites are indicated in Figure 6-22 as well. Tangential electric field data along Line B and Line C were gathered in the frequency band from 0.01 to 250 Hz at a rate of 7 samples per decade. Along Line A, the frequency range of the measurements extended only from 0.06 to 250 Hz. Because of the curvilinear nature of the EMAP lines in the Sengan project, the procedures described in Chapter V for the spatial filtering of the $\hat{Z}_{xy}$ traverse impedances require of some additional processing steps. These are summarized in the following lines.

In the frequency domain, the relationship between the tangential electric field, E_t, measured at a given point along the electric field array, and the magnetic field components, H_x^B and H_y^B, measured at the base station is expressed by the linear equation

$$E_t = Z_{tx}H_x^B + Z_{ty}H_y^B,$$

where the terms Z_{tx} and Z_{ty} are in-line impedances. In this last equation, the orientation of electric field component, E_t, in general does not coincide with the orientation of either of the magnetic field components H_x^B and H_y^B. The relation between the base impedances, $\hat{Z}_{xx}$, and $\hat{Z}_{xy}$, and the in-line impedances, Z_{tx} and Z_{ty}, can be obtained by projecting the magnetic field components H_x^B and H_y^B in directions parallel and perpendicular to each dipole along the electric field array. This procedure is illustrated in Figure 6-23, where the Cartesian coordinate frame x'-y' is used to describe the local orientation of each dipole (with the x'-axis parallel to the dipole direction), and the x-y coordinate frame is used to describe the magnetic field measurements acquired at the base station. With the rotation angle, ϕ, between the two coordinate frames defined positive in the azimuthal direction (clockwise rotation), the relationship between the two sets of impedances is given by

$$\hat{Z}_{xx} = Z_{tx}\cos\phi + Z_{ty}\sin\phi, \text{ and} \qquad (6.9)$$

$$\hat{Z}_{xy} = -Z_{tx}\sin\phi + Z_{ty}\cos\phi. \qquad (6.10)$$

Apparent resistivity and phase pseudosections of the Sengan base impedances, $\hat{Z}_{xy}$, computed with equations (6.9) and (6.10) are shown in Figures 6-24, 6-25, and 6-26 along Line A, Line B, and Line C, respectively. A separate upper panel in these figures describes the corresponding topographic profile with elevations given in meters above the sea level (m ASL). The presence of significant static distortion is evidenced by localized vertical banding in the three apparent resistivity pseudosections.

In carrying out spatial filtering and inversion of the $\hat{Z}_{xy}$ base impedances, however, the latter should be computed from equations (6.9) and (6.10) only after spatial filtering of the in-line impedances has been performed. Spatial filtering is done using a slightly modified version of the adaptive spatial filtering procedure described in section 5.4. Accordingly, along the curvilinear traverse both in-line impedances, Z_{tx} and Z_{ty} are first filtered (here the main difference with the procedure described in section 5.4 is that both in-line impedances are filtered instead of simply the principal impedance component along a straight traverse) with a bootstrapping in-line filtering length, W. Upon filtering, an equivalent straight direction for the curvilinear electric field average (the integral $\int \mathbf{E} \cdot d\boldsymbol{\ell}$) is estimated with a weighed average of the individual dipole responses included in the filtering length, W. This direction yields the rotation angle, ϕ, that is needed to compute the effective impedances, $\hat{Z}_{xx}$ and $\hat{Z}_{xy}$, with the use of equations (6.9) and (6.10). An effective Bostick depth of penetration, z_B, computed from the impedance $\hat{Z}_{xy}$ is then multiplied by the filter constant, c, and the resulting product compared against the filtering length, W. This filtering length is then varied until a match with the product cz_B is found within the prescribed tolerance. The procedure is repeated at as many array locations and frequencies there are along each EMAP line.

Figure 6-27 through 6-29 show the inverted resistivity sections derived by spatial filtering and subsequent Bostick inversion of the $\hat{Z}_{xy}$ impedances along each line of the Sengan project. These impedances were obtained with the aforementioned spatial filtering and rotation procedure using a filter constant, c, of value 2. The resistivity sections compare well at their intersection points in spite of the fact that spatial filtering was performed independently along each one of them. An interesting feature shown in the three resistivity sections is a resistive uplift buried at a depth of approximately 1 km below the elevation datum (placed at 700 m ASL). Previous studies in the area have identified this resistive feature with a granitic intrusion. On the other hand, the prominent shallow

conductor in the three sections corresponds to the geoelectric expression of welded rhyolitic tuff and to a less extent of breccias and volcanic agglomerates, and on plan view correlates well with the limits of the Hachimantai volcano.

Even though a detailed geoelectric interpretation of the Sengan EMAP data goes beyond the scope of this thesis, pseudosections and resistivity sections along the three lines show a complicated 3-D subsurface resistivity distribution. Attention is focused instead on whether spatial filtering can aid in determining unbiased MT parameters of geometrical dimensionality in the presence of electric static distortion at the intersection points between lines. To this end, a comparison is made below between MT induction strike angles estimated with and without the use of spatial filtering at the intersection points between Line A and Line B, and between Line A and Line C.

Simulation studies aimed at understanding the effect of electric static distortion on the estimation of dimensionality parameters have been reported before. For instance, Groom and Bailey (1989) simulated 3-D static distortion with an anomalous surface hemisphere embedded in a 2-D background medium. Park and Livelybrooks (1989), on the other hand, showed that the use of the popular impedance tensor determinant, although rotationally invariant, could be highly sensitive to 3-D static effects and thus lead to erroneous interpretations of the subsurface. However, field data studies dealing with the same problems have been scant or at best inconclusive because of insufficient control on the geoelectric characteristics of the underlying subsurface structure. The resistivity sections derived for the Sengan project do provide enough knowledge of the underlying resistivity structure to make this an attractive study.

Figures 6-30a and 6-30b show the estimated strike direction at the Line A-Line B (AB) and Line A-Line C (AC) intersection points, respectively. In each figure, separate plots describe the frequency variations of the estimated rotation angle before and after adaptive spatial filtering of the in-line impedances along each intersecting line. Strike directions in these plots are measured with their true North azimuth. The full 2x2 MT tensors at the AB and AC points were assembled with the electric field components measured at the same points and the magnetic fields measured at the base station. In so doing, the measured electric fields were first projected to the x-y Cartesian coordinate frame at the base station. With this MT tensor, the strike angle was determined as the rotation direction which minimized the sum of the squares of the off-diagonal entries, Z_{xy} and Z_{yx} (Stodt, 1981). For the case of the filtered results, adaptive spatial filtering was performed

prior to rotation of the electric field measurements to avoid "leakage" of static effects in the projected components.

The estimated strike angles shown in Figures 6-30a and 6-30b all lie within the second quadrant (or fourth quadrant, depending on the measuring convention), and both filtered and unfiltered curves exhibit differences of at most 30°. At the AC intersection point, the difference between the two curves is largest at the highest frequencies. However, the most remarkable difference between the filtered and unfiltered curves appears at the lowest frequencies, where the estimated strike angles for the unfiltered curves at the AB and AC points smoothly asymptote 150°. In fact both of these curves overlap at frequencies below 10 Hz. On the other hand, even though the filtered curves seem both to asymptote 120° instead of 150° at the lowest frequencies, they do not overlap. As a matter of fact, both of the filtered curves suggest that the underlying resistivity distribution has no predominant strike direction. In contrast, without additional knowledge of the underlying resistivity structure, simple inspection of the unfiltered curves would lead one to believe that the ground is essentially 2-D below 10 Hz, an inconsistent result considering the 3-D character of the subsurface revealed by the three electric field lines.

This simple example averts the potential danger of estimating MT parameters of induction from single-dipole measurements where conditions are not created to minimize spatial aliasing and suppress static effects.

6.6 Conclusions and recommendations

The 2- and 3-D evaluation studies presented in this chapter demonstrate that the EMAP field procedure is suitable for the exploration of complicated geoelectric environments. However, because the study of 3-D structures demands, in general, the profiling of MT fields in more than one direction, precautions should be taken to recognize 3-D induction effects in the tangential electric fields acquired along a single traverse. Additional field components should be measured along the traverse whenever possible. For instance, it was shown that the acquisition of vertical magnetic field data helps ascertain the presence of induction processes taking place laterally away from the traverse. Also, the deployment of orthogonal dipoles at certain locations allows one to estimate parameters of dimensionality that might, among other things, shed light to induction current flowing at an angle with respect to the line of measurements. However, because the acquisition of electric field data requires closely spaced sampling locations both to avert and suppress static effects, deployment of orthogonal dipoles with the required sampling conditions at all

locations may not be practical from an economic point of view. The studies presented in this chapter suggest that the orthogonal electric field could instead be sampled at a few points along the survey line either with a long electric dipole, or better, with a string of them. A mini-traverse of orthogonal dipoles not only minimizes spatial aliasing problems, but also lends itself to the use of adaptive spatial filtering to suppress static effects without excessive smoothing of the induction component at the highest frequencies.

Under very special circumstances, when only one MT station is all that is needed for reconnaissance purposes rather than for detailed exploration work, the developments presented in this chapter suggest that the deployment of a "cross" of electric dipoles may be an adequate field procedure; this is shown in Figure 6-31. The number of dipoles positioned along each line of the cross will be determined by the channel capabilities of the data acquisition system in use, excluding two channels that are necessary to measure the horizontal magnetic field. If desired, an additional channel could be used to measure the vertical magnetic component. This field configuration allows one to recognize and suppress static effects to at least a depth of penetration comparable with the length of each line of the cross. It may also be used to calibrate the survey parameters (for instance, dipole length, traverse length and frequency range) that are needed to study the underlying resistivity structure prior to embarking upon detailed work along a continuous survey line .

Regarding the length of the survey traverse, it was emphasized above that (1) it should be comparable with the depth of penetration at the lowest frequency to allow adequate suppression of static effects, and (2) it should be consistent with the adjustment distance of the 2- or/and 3-D scatterers (see sections 5.7.3 and 6.4). In connection with this second requirement, there have been important studies to assess distortion effects caused by large-scale induction current processes. Among these studies, Mackie et al. (1989), and more recently, Madden and Mackie (1990) have shown, for instance, that coast effects may cause a significant low-frequency induction bias even at points located tens of kilometers away from the ocean-continent boundary (vertical anisotropy of the crust). The same studies indicate that, within sedimentary basins, so long as the sounding frequency is low enough to cause the depth of penetration to be larger that the lateral and vertical dimensions of the basin, local induction effects fall-off and crustal anisotropy becomes a dominant factor in the inductive response from the subsurface. Both of these studies recommend that 2- or/and 3-D numerical simulation be used to assess regional distortion effects in the measured data and hopefully to correct for them before engaging into detailed interpretation tasks. To this end, they recommend that all available geological and geophysical

information be compiled and fed into a preliminary synthetic model. A similar conclusion has been recently advanced by Singer (1991).

Recognizing regional distortion effects in the measured data is critical to the success of EMAP for crustal and in general for deep sounding studies. Long survey traverses are necessary for the suppression of static effects at frequencies for which the zone of inductive response is tens of kilometers deep. In addition, lateral distortion effects of dimensions comparable with the length of the traverse (for instance, ocean-continent boundary effects, and the exotic channeling of currents flowing around sedimentary basins) should be evaluated either with complementary electric and magnetic field measurements (for instance, with the use of long electric dipole "crosses" such as those described in Figure 6-31) or with 2- and 3-D numerical simulation studies or with both. It should be emphasized, however, that because in most cases numerical simulation cannot reproduce all of the features that are needed to accurately evaluate regional distortion effects, the results obtained this way should be examined with great care. They will be, at best, a first-order approximation to the intricate regional distribution of subsurface resistivity. The lack of adequately sampled MT data cannot be replaced in any endeavor to understand the geoelectrical properties of the earth's crust.

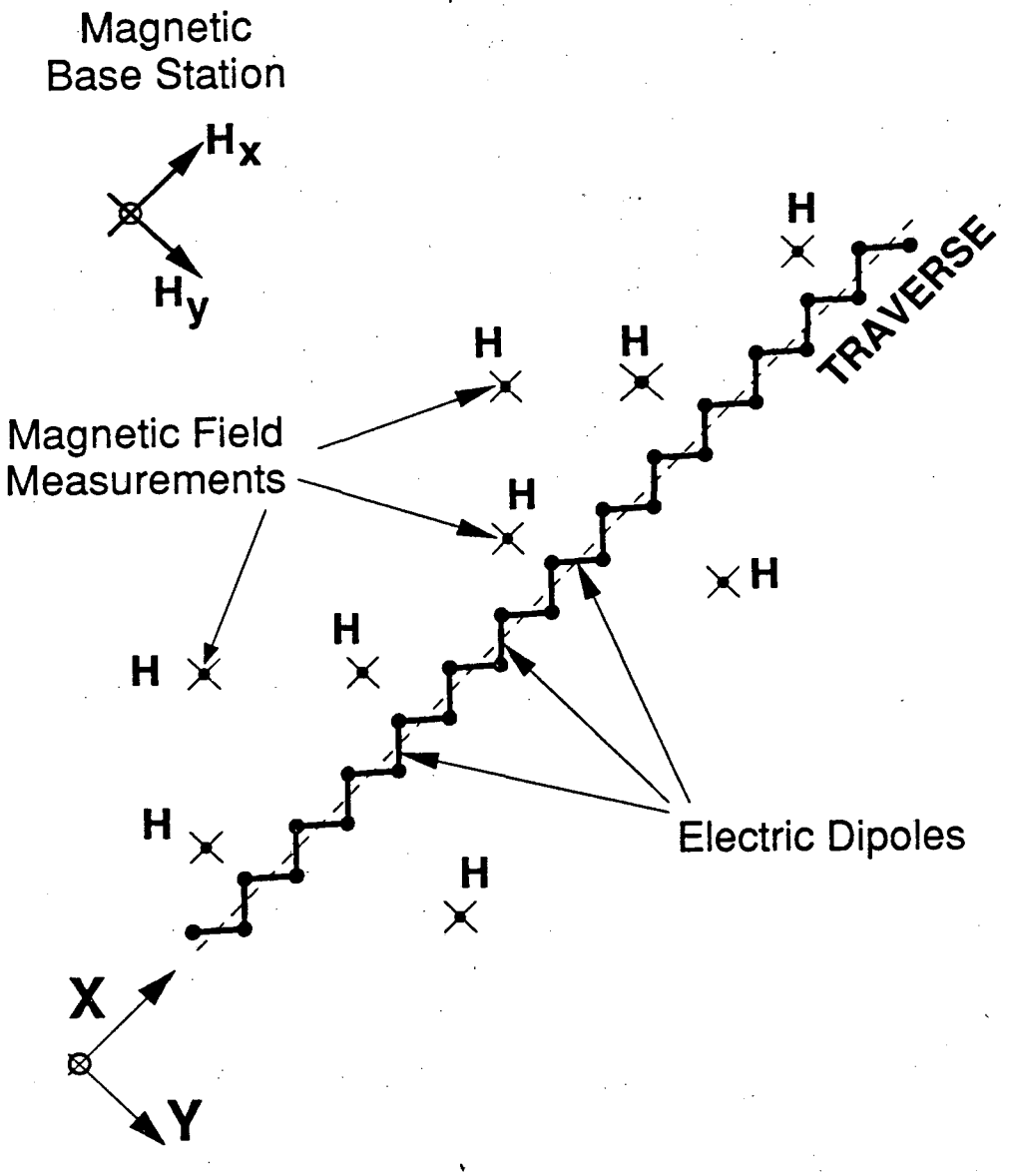

Figure 6-1. Graphical description of Sigal's (1989) modification of the EMAP field procedure.

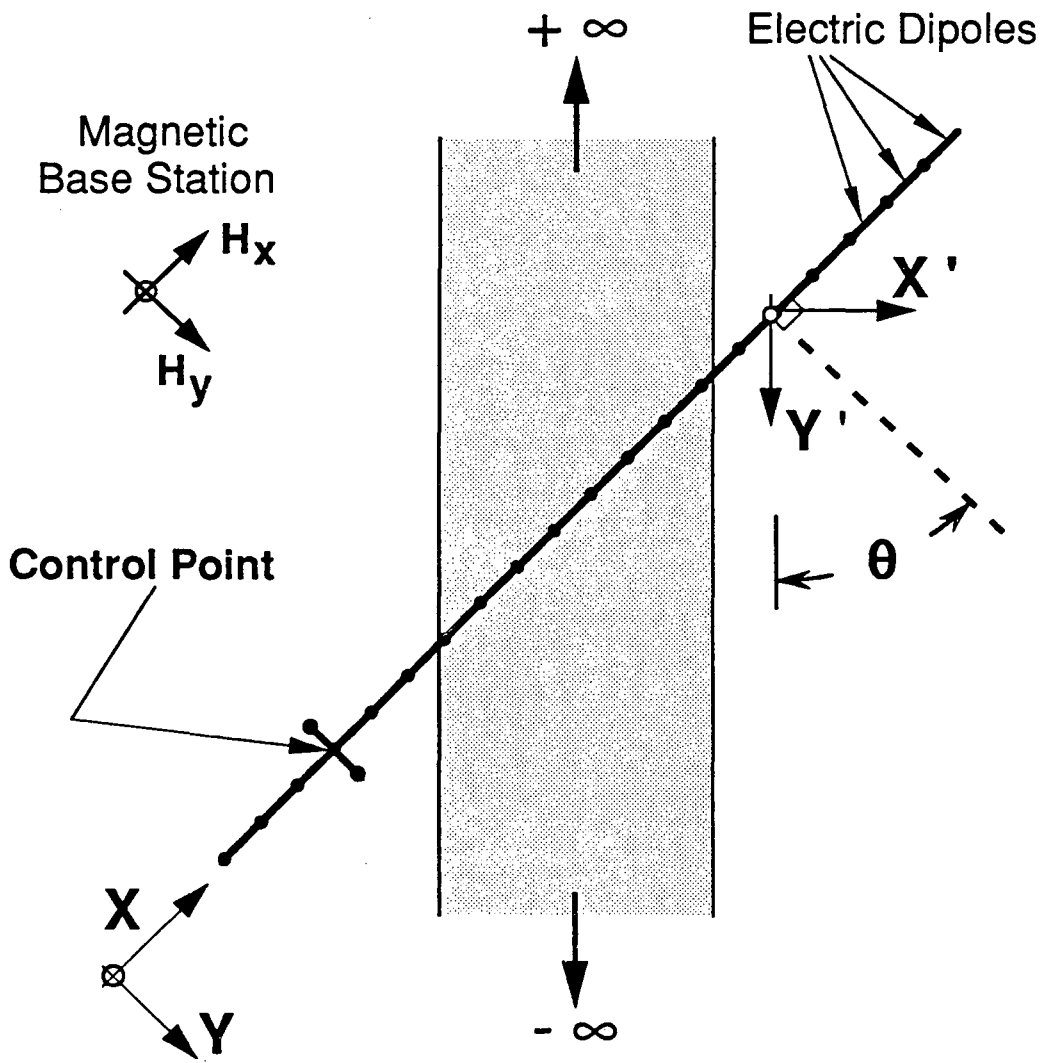

Figure 6-2. EMAP survey traverse laid out over 2-D ground at an angle, θ, with respect to strike. A single orthogonal dipole is used for the estimation of θ.

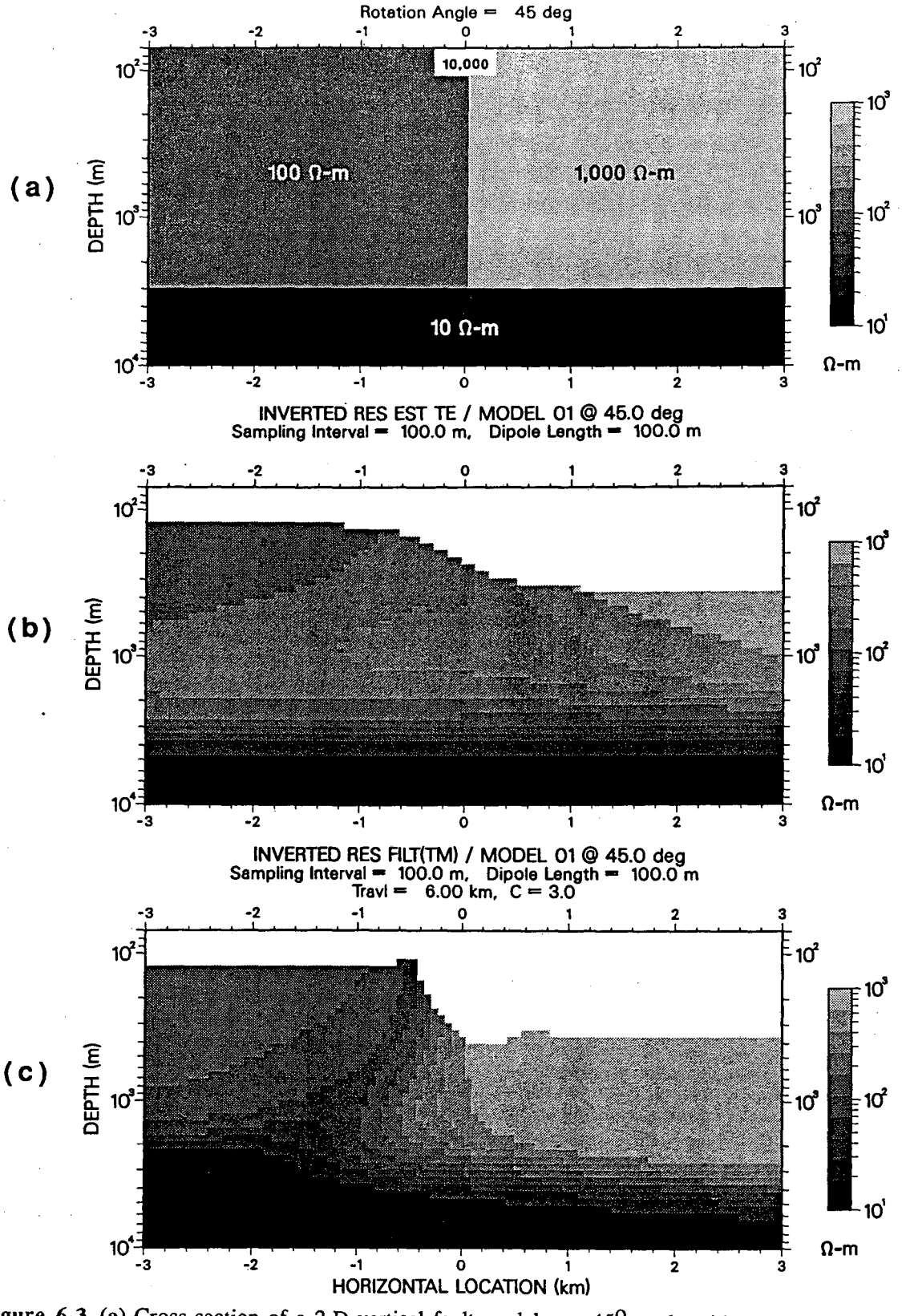

Figure 6-3. (a) Cross-section of a 2-D vertical fault model at a 45^{o} angle with respect to strike. (b) Geoelectric section derived by Bostick inversion of the estimated TE impedances. (c) Geoelectric section derived by spatial filtering (filter constant, c, equal to 3) and subsequent Bostick inversion of the estimated TM impedances.

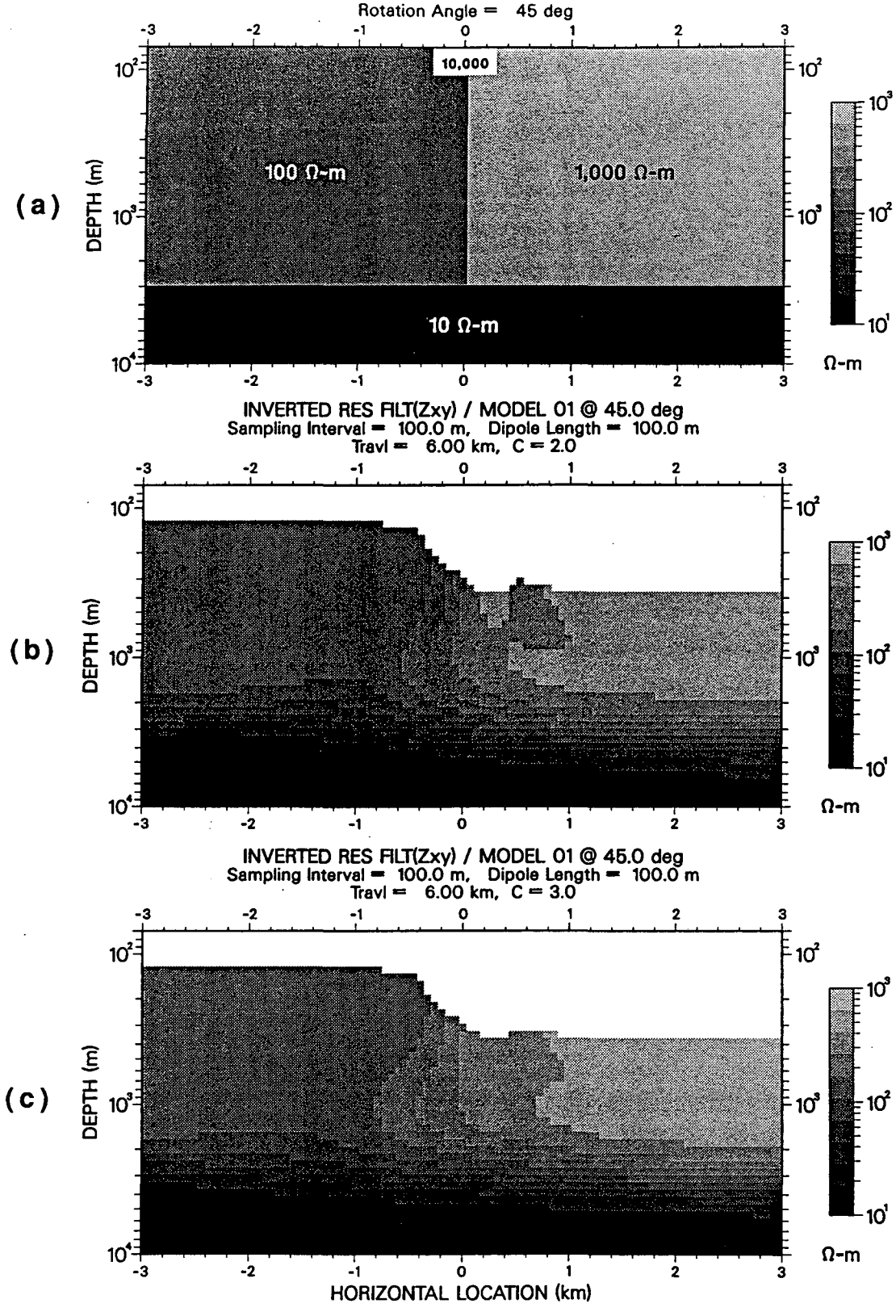

Figure 6-4. (a) Cross-section of a 2-D vertical fault model at a 45^{o} angle with respect to strike (Figure 6-3a). (b) and (c) are the geoelectric sections derived by spatial filtering and subsequent Bostick inversion of the Z_{xy} EMAP impedances using filter constant values of 2 and 3, respectively.

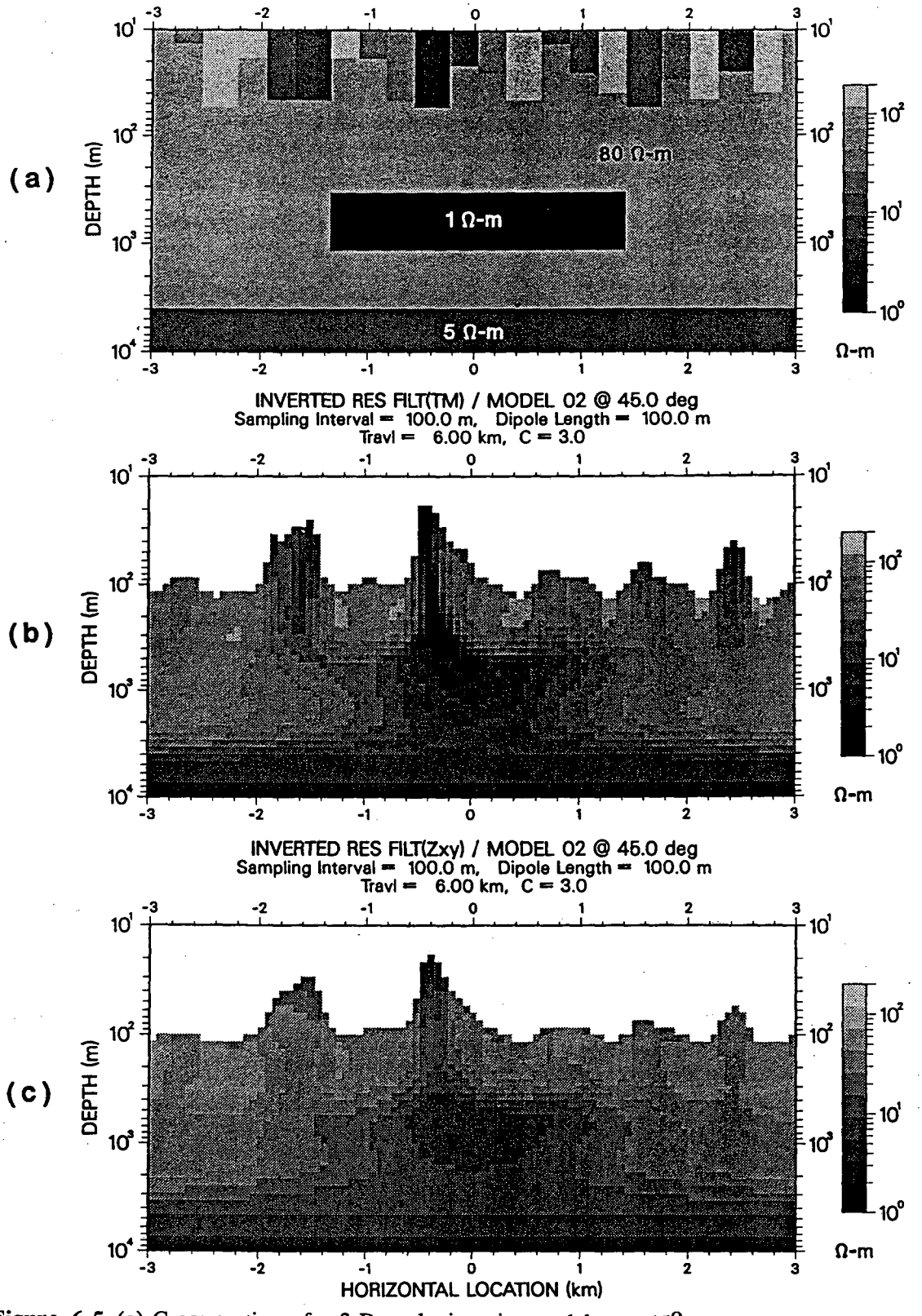

Figure 6-5. (a) Cross-section of a 2-D geologic noise model at a 45^{o} angle with respect to strike (cf. Figure 5-10a). (b) Geoelectric section derived by spatial filtering and subsequent Bostick inversion of the estimated TM impedances (cf. Figure 5-11b). (c) Geoelectric section derived by spatial filtering and subsequent Bostick inversion of the Z_{xy} EMAP impedances simulated along the oblique traverse. A filter constant, c, of value 3 was used to obtain both resistivity sections.

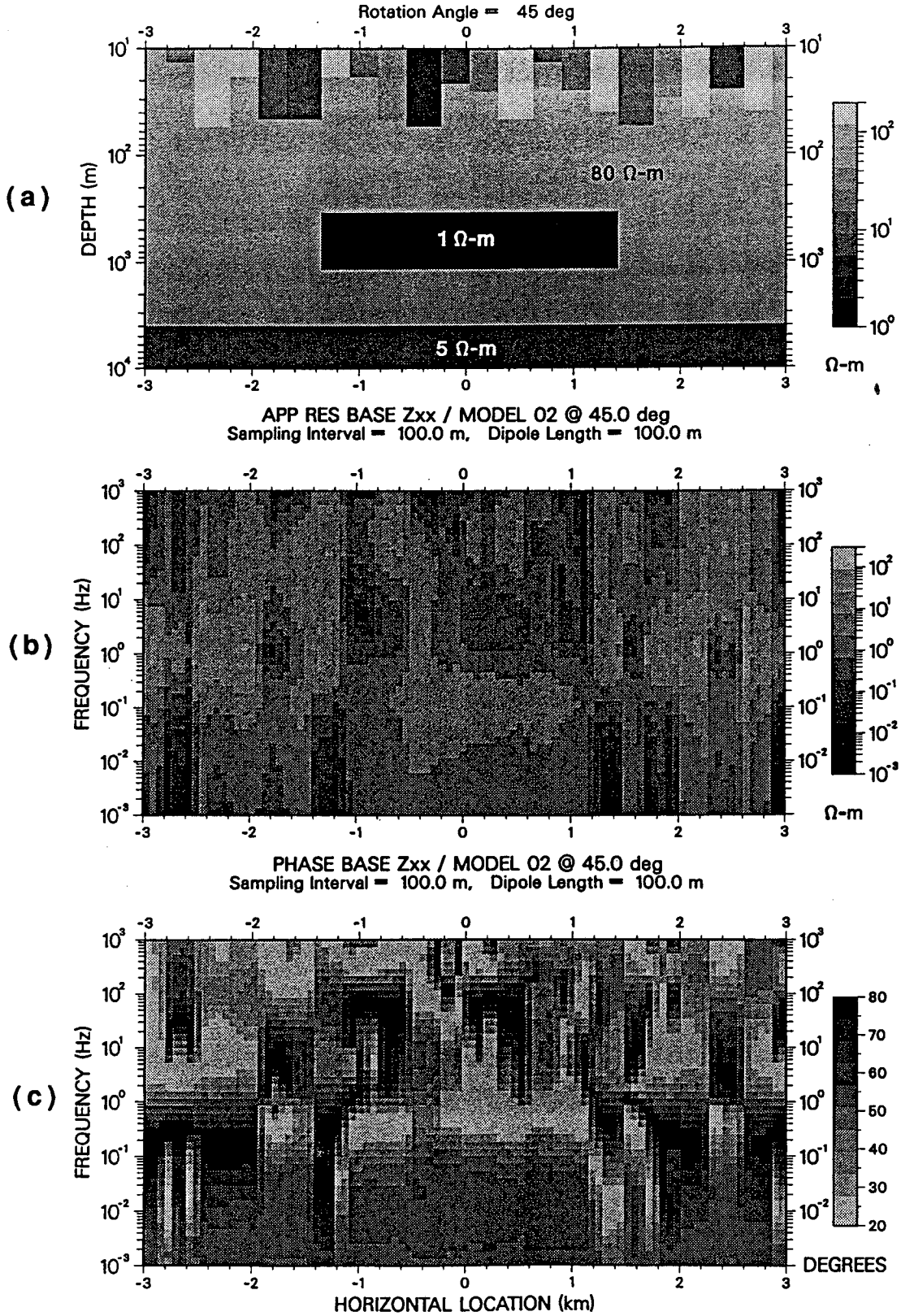

Figure 6-6. (a) Cross-section of a 2-D geologic noise model at a 45^{o} angle with respect to strike (Figure 6-5a). (b) and (c) are the apparent resistivity and phase pseudosections of the Z_{xx} cross-coupling EMAP impedances.

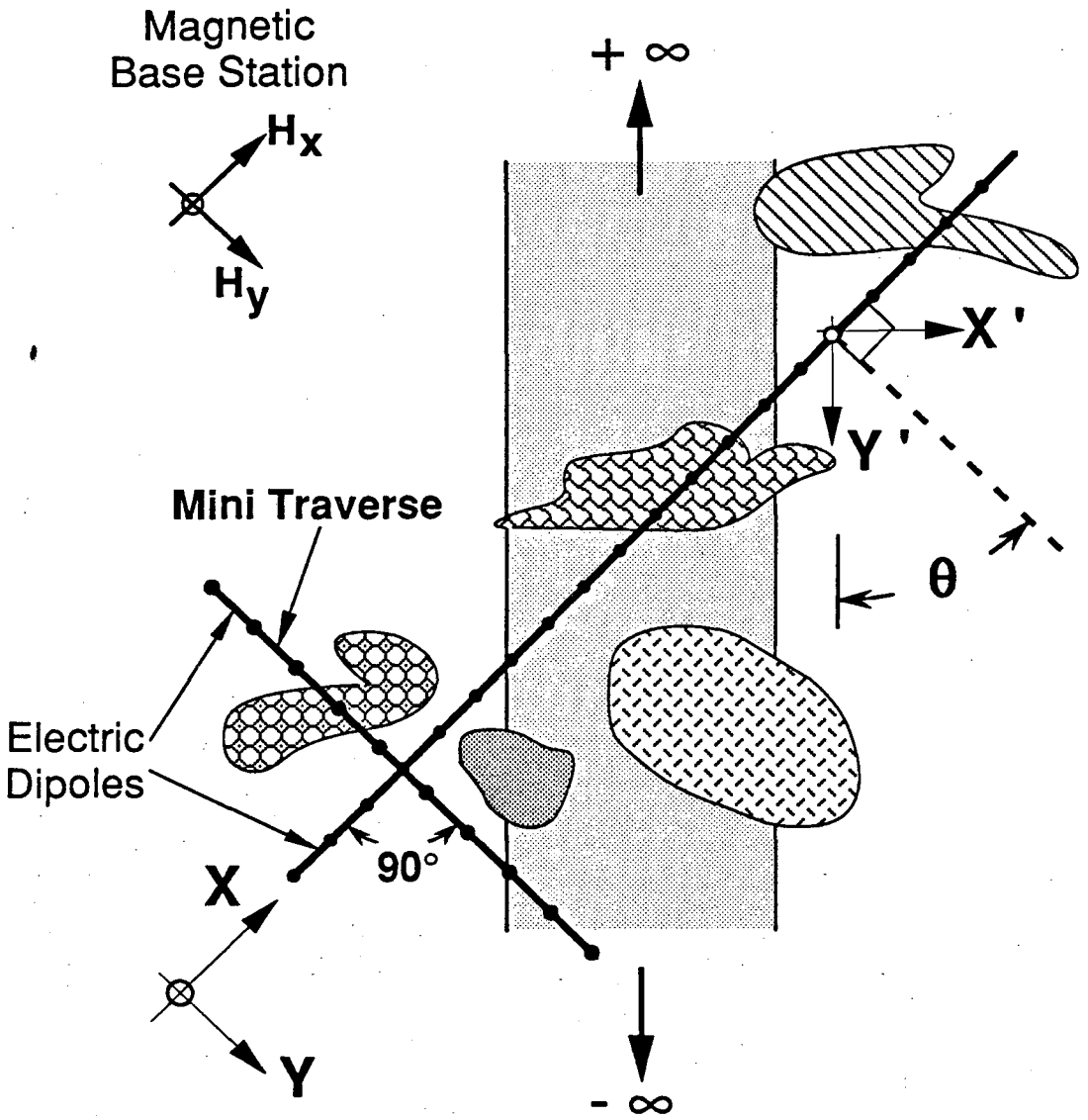

Figure 6-7. Graphical description of the suggested field procedure for the estimation of a regional 2-D strike angle, θ, under 3-D electric static distortion.

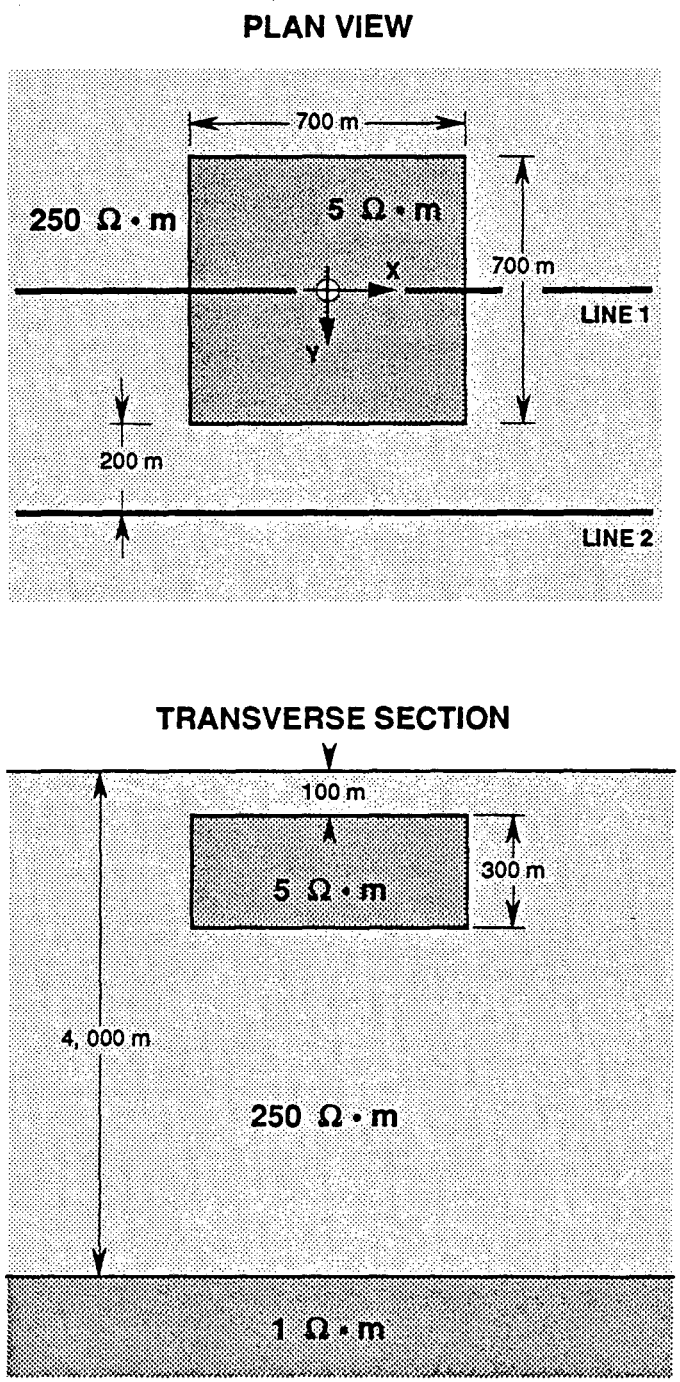

Figure 6-8. Plan view and transverse section of a simple 3-D scatterer buried in a 1-D background (3-D model No. 1). Line 1 and Line 2 are EMAP survey traverses. The vertical scale has been slightly distorted.

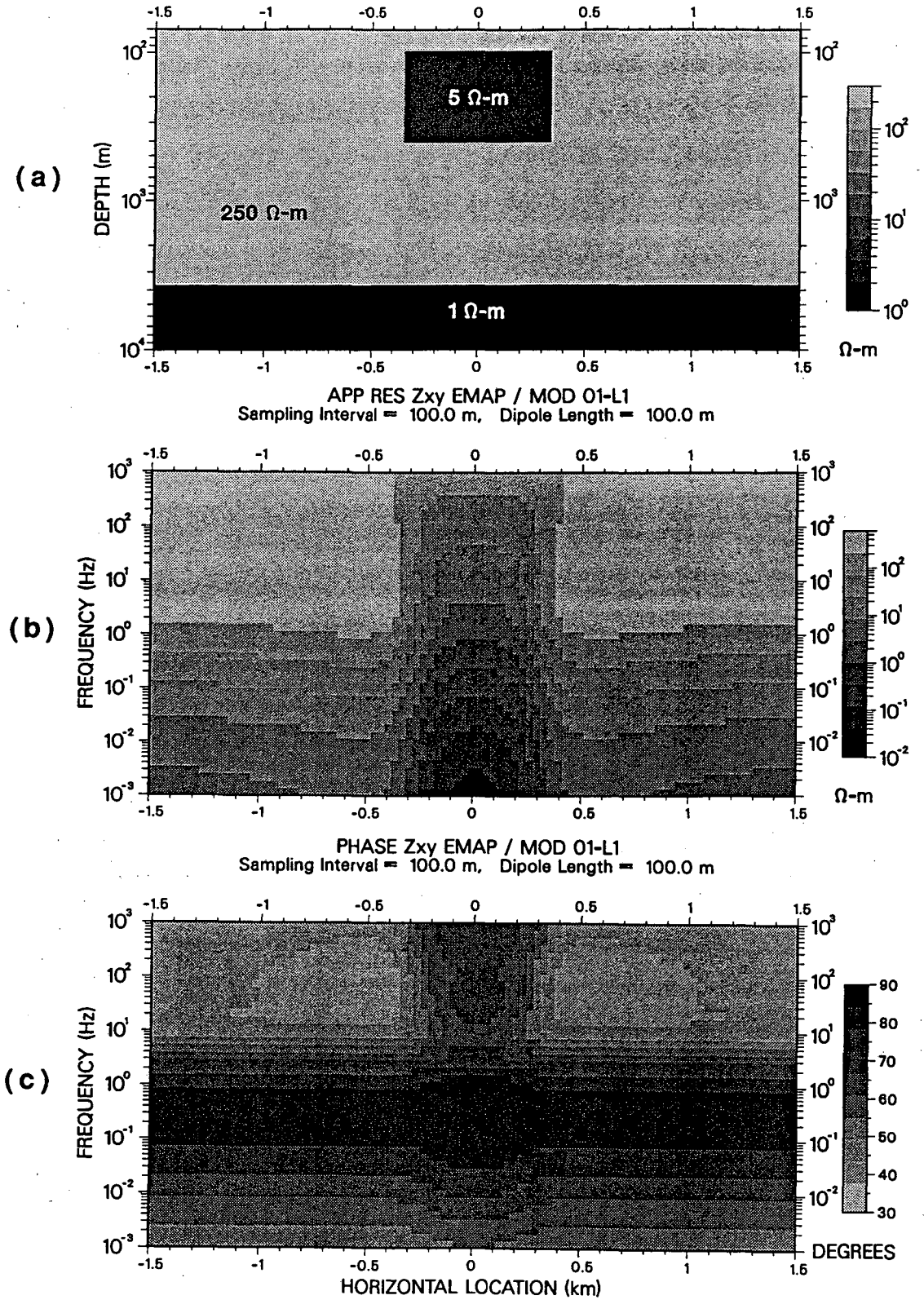

Figure 6-9. (a) Cross-section of 3-D model No. 1 (Figure 6-8) along Line 1. (b) and (c) are the apparent resistivity and phase pseudosections, respectively, of the Z_{xy} EMAP impedances.

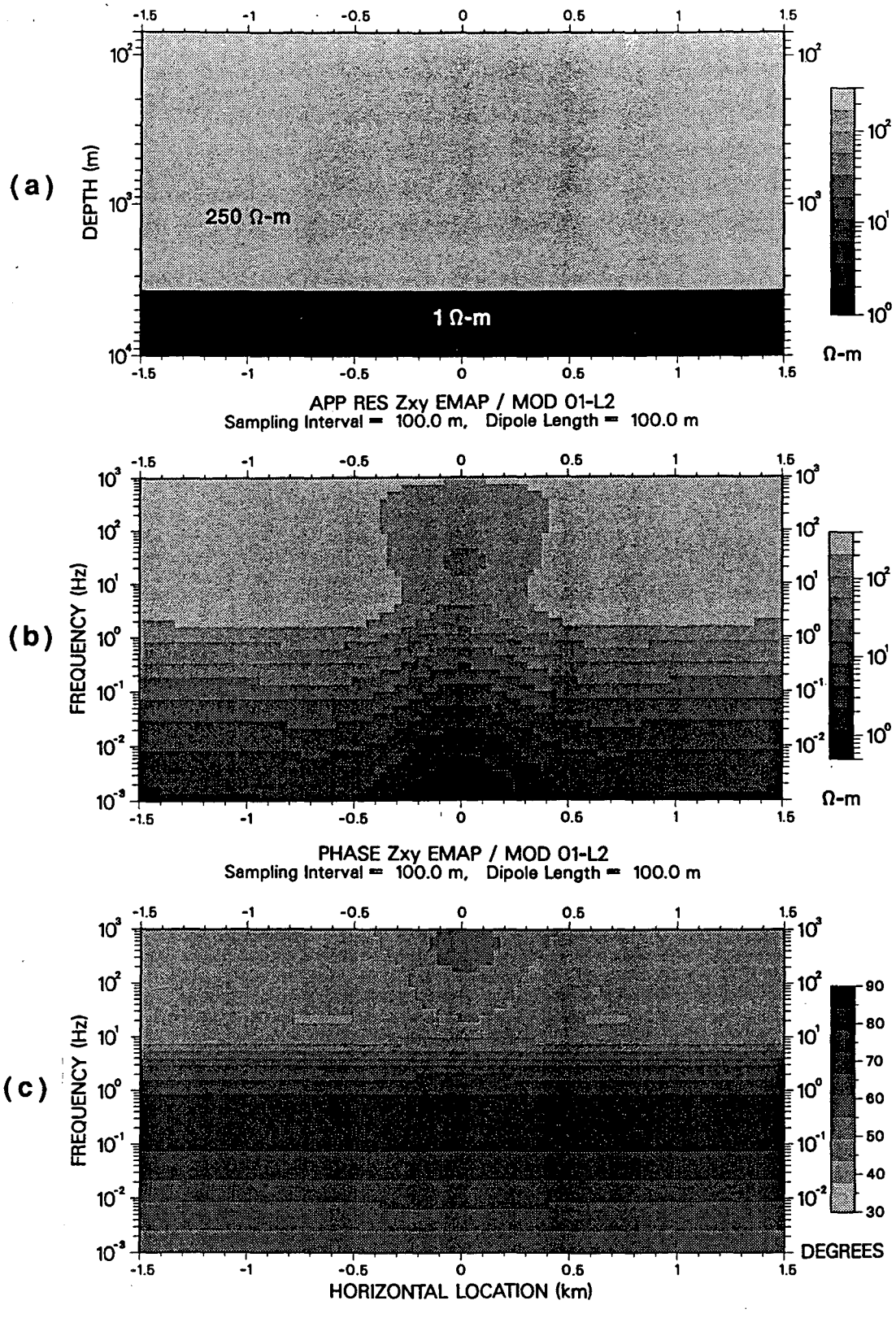

Figure 6-10. (a) Cross-section of 3-D model No. 1 (Figure 6-8) along Line 2. (b) and (c) are the apparent resistivity and phase pseudosections, respectively, of the Z_{xy} EMAP impedances.

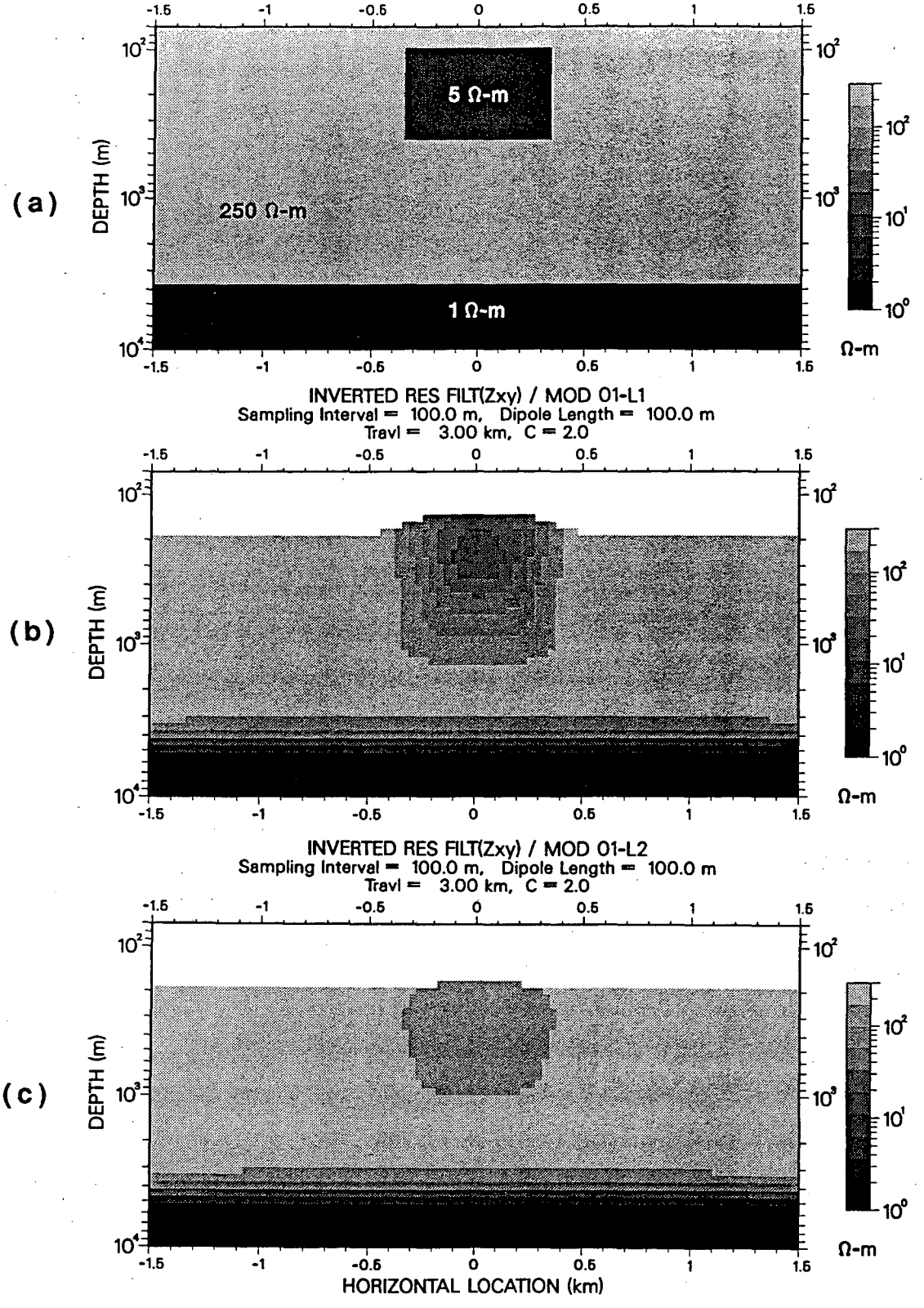

Figure 6-11. (b) and (c) are geoelectric sections derived by spatial filtering and subsequent Bostick inversion of the simulated Z_{xy} EMAP impedances along Line 1 (Figure 6-9) and Line 2 (Figure 6-10), respectively. The model cross-section along Line 1 is shown for comparison in (a). A filter constant, c, of value 2 was used to obtain both inverted resistivity sections.

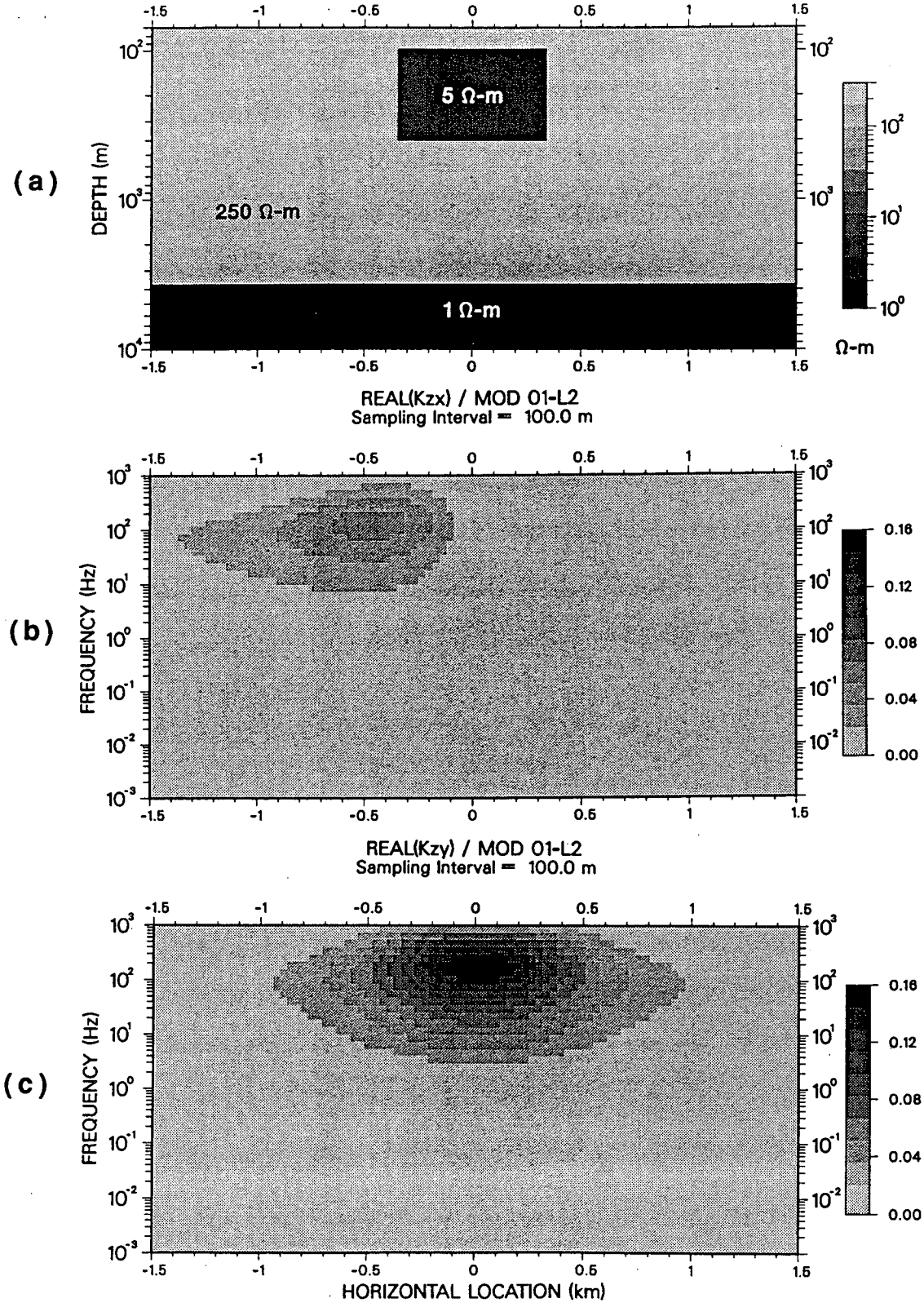

Figure 6-12. **(b)** and **(c)** are pseudosections of the real part of the K_{zx} and K_{zy} tipper transfer functions, respectively, along Line 2 of Figure 6-10. The model cross-section along Line 1 is shown for comparison in **(a)**.

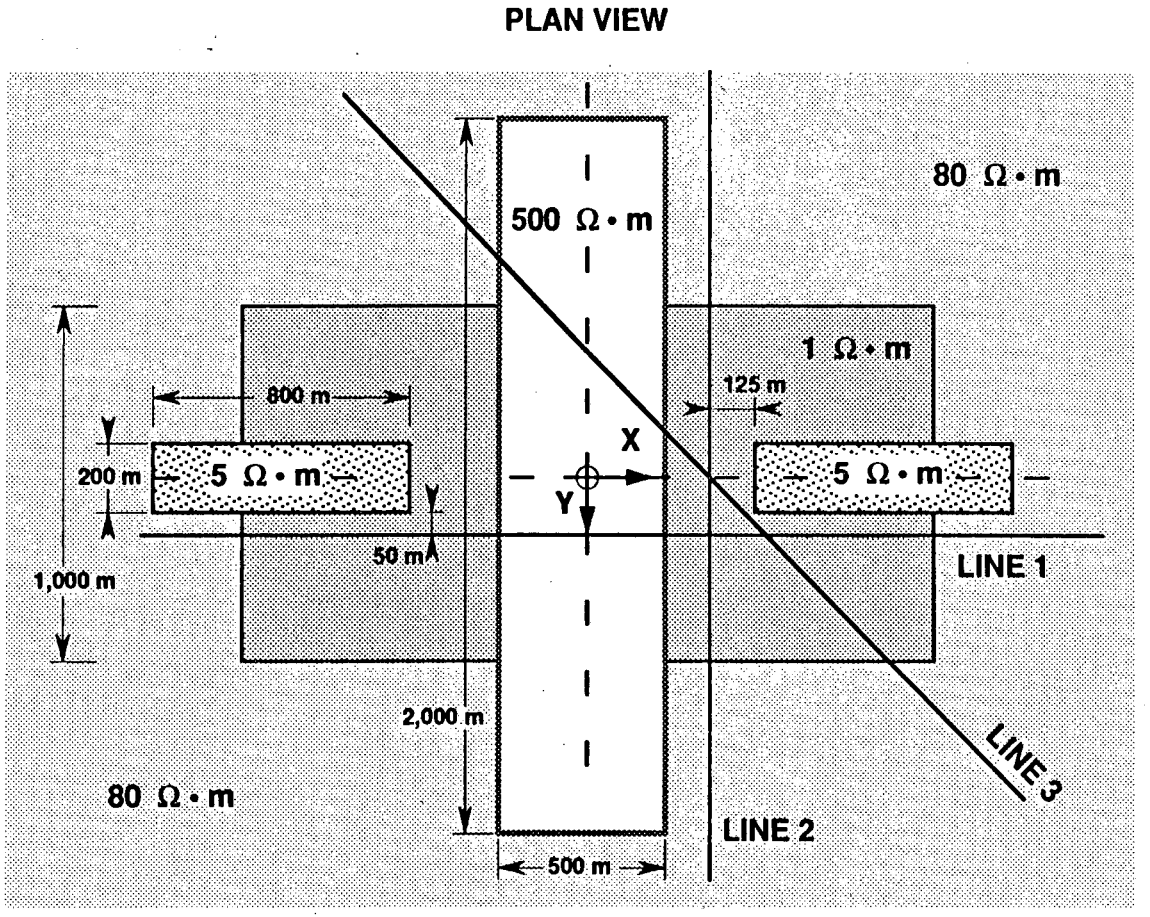

Figure 6-13. Plan view of a geoelectric model with surface and buried 3-D scatterers embedded in a 1-D background (3-D model No. 2). The accompanying transverse section is shown in Figure 6-14. Line 1, Line 2, and Line 3 are EMAP survey traverses.

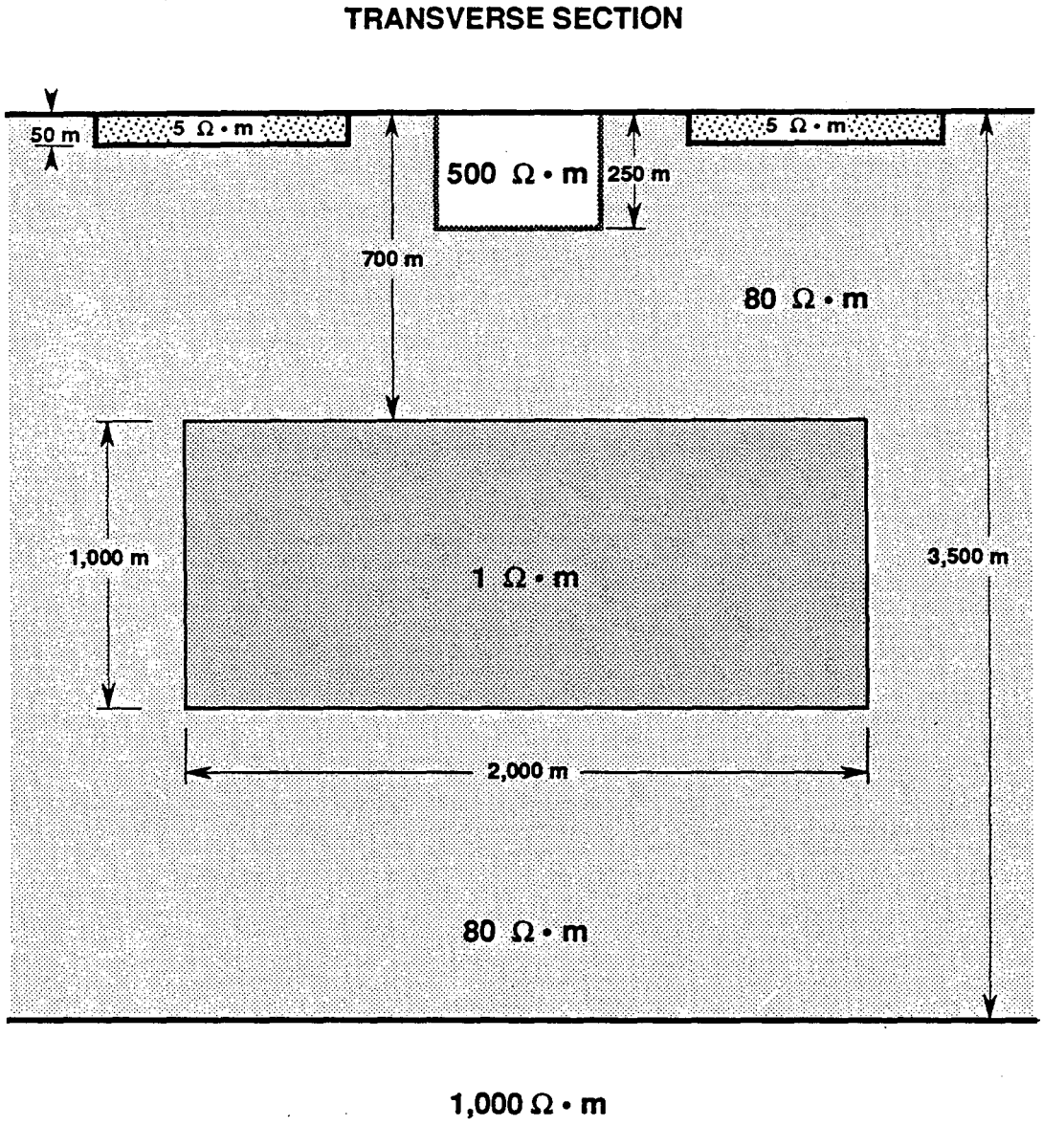

Figure 6-14. Generalized transverse section of 3-D model No.2 (Figure 6-13). The vertical scale has been slightly distorted.

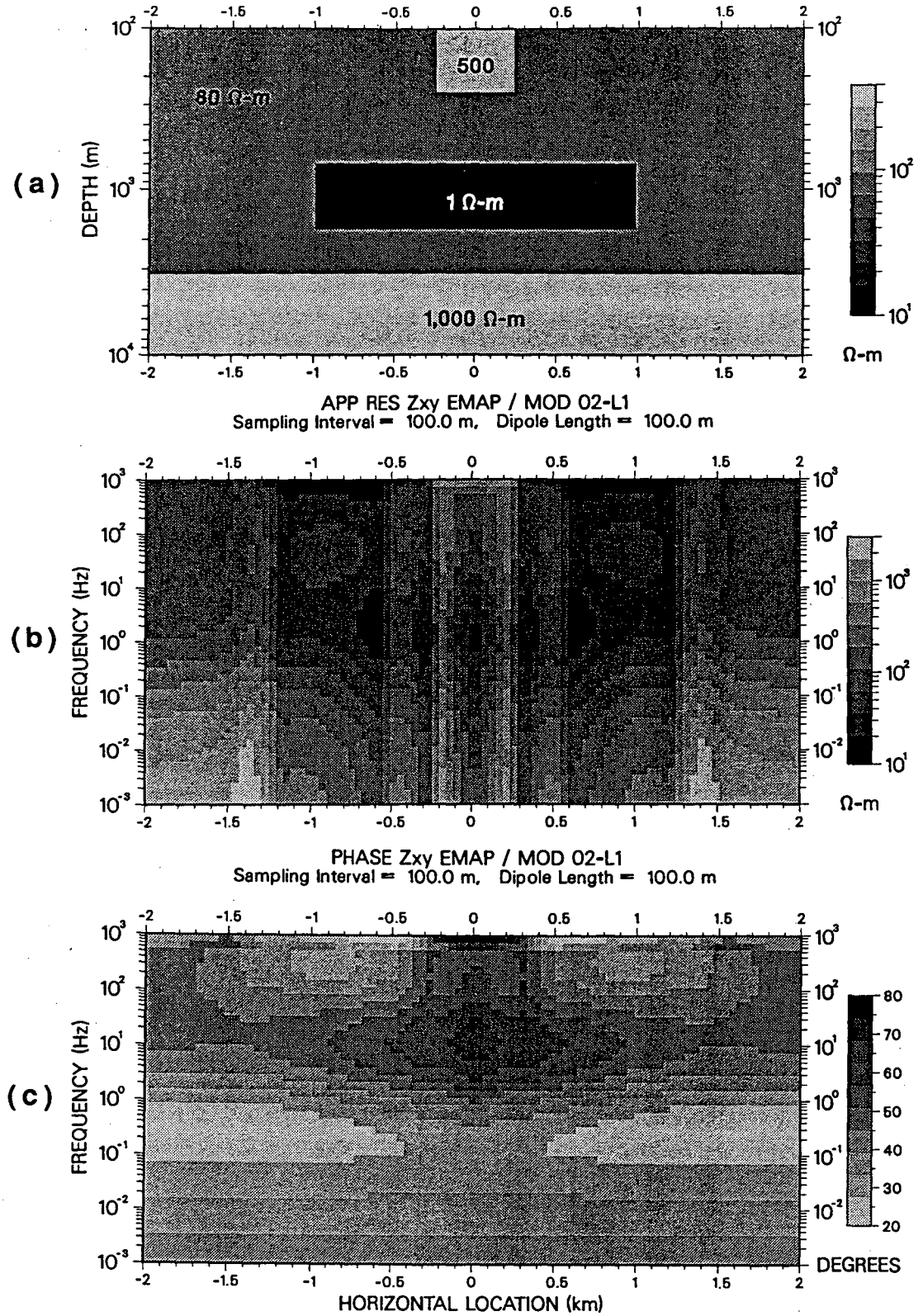

Figure 6-15. (a) Cross-section of 3-D model No.2 (Figure 6-13) along Line 1. (b) and (c) are the apparent resistivity and phase pseudosections, respectively, of the Z_{xy} EMAP impedances.

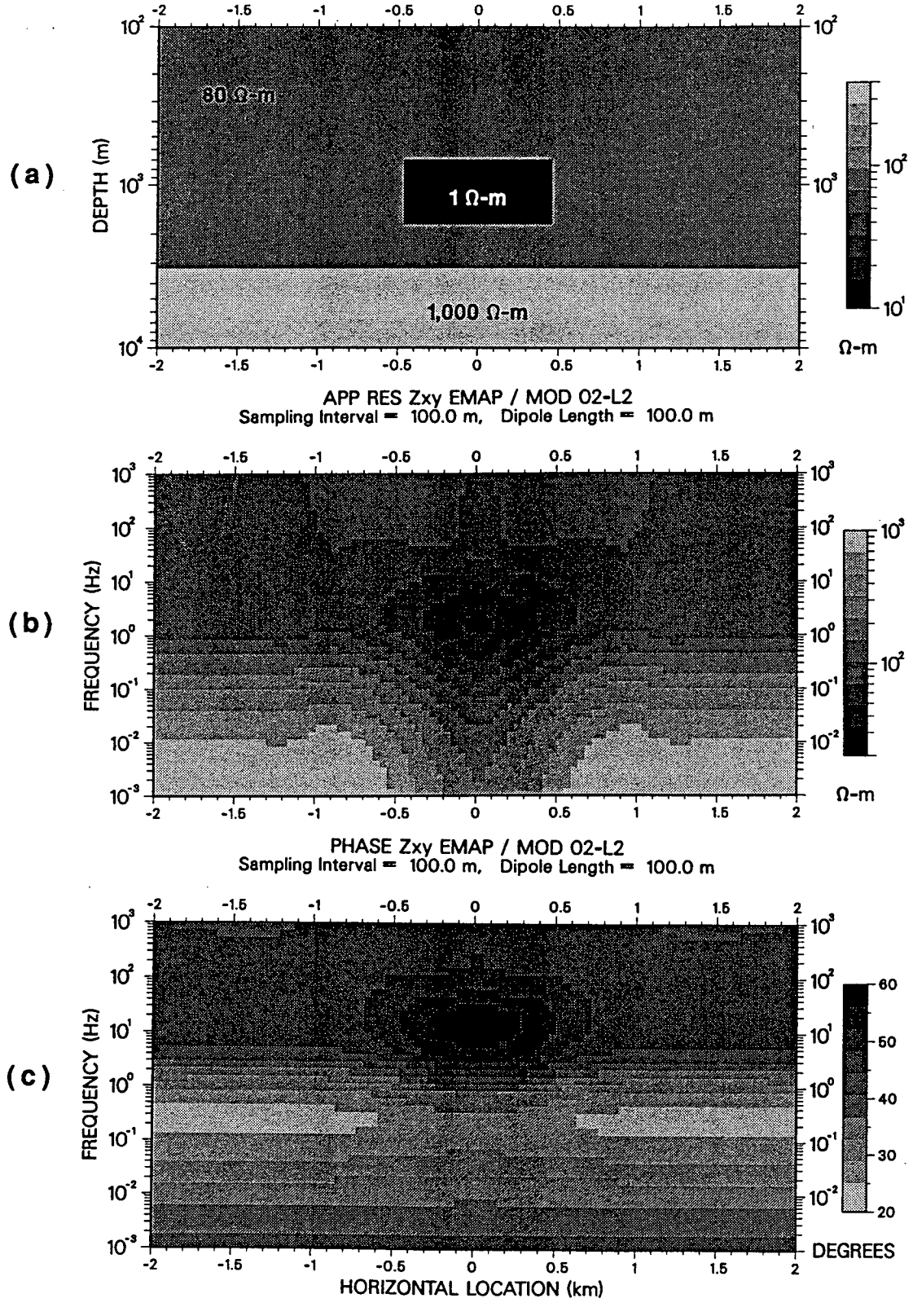

Figure 6-16. (a) Cross-section of 3-D model No.2 (Figure 6-13) along Line 2. (b) and (c) are the apparent resistivity and phase pseudosections, respectively, of the Z_{xy} EMAP impedances.

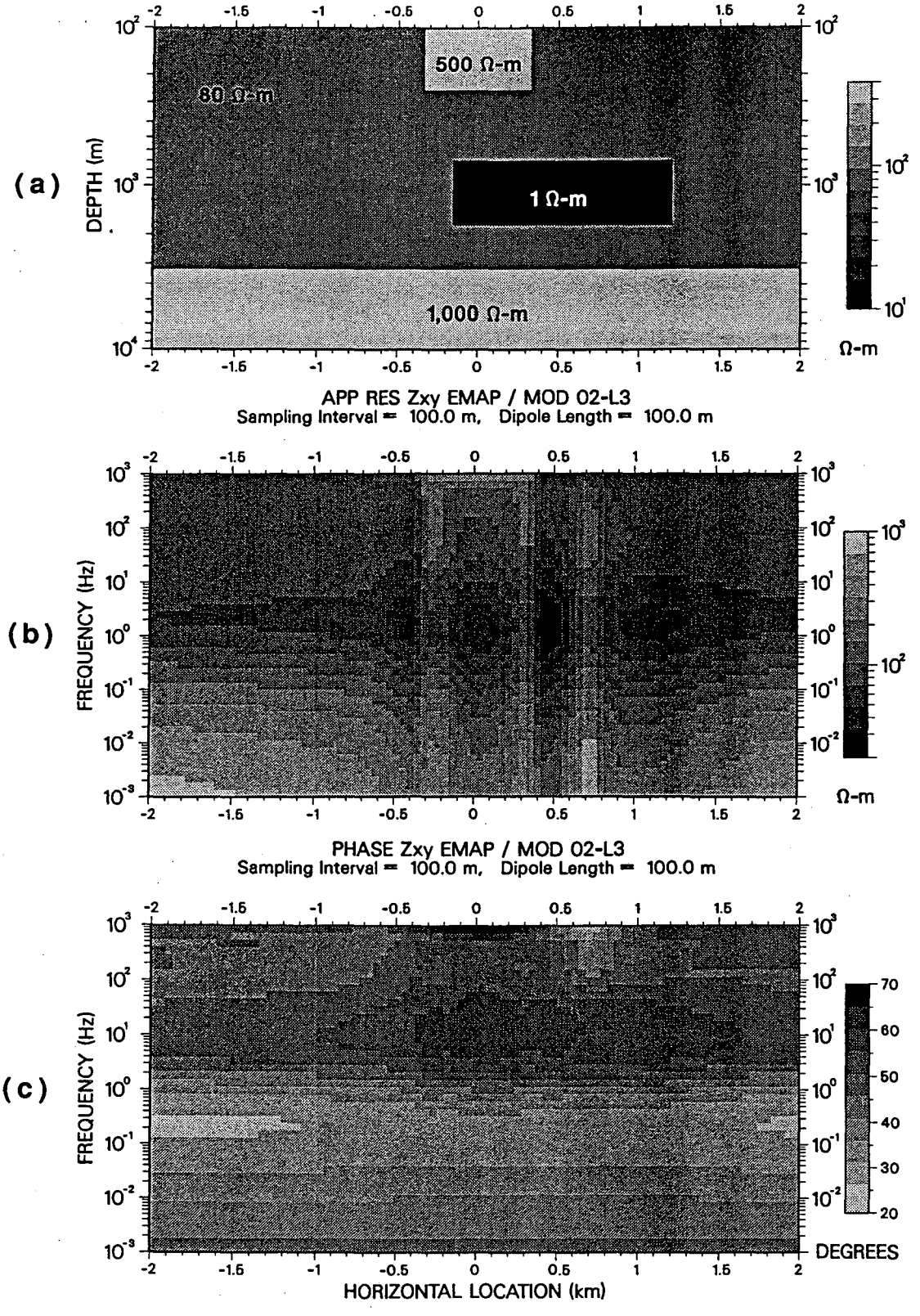

Figure 6-17. (a) Cross-section of 3-D model No.2 (Figure 6-13) along Line 3. (b) and (c) are the apparent resistivity and phase pseudosections, respectively, of the Z_{xy} EMAP impedances.

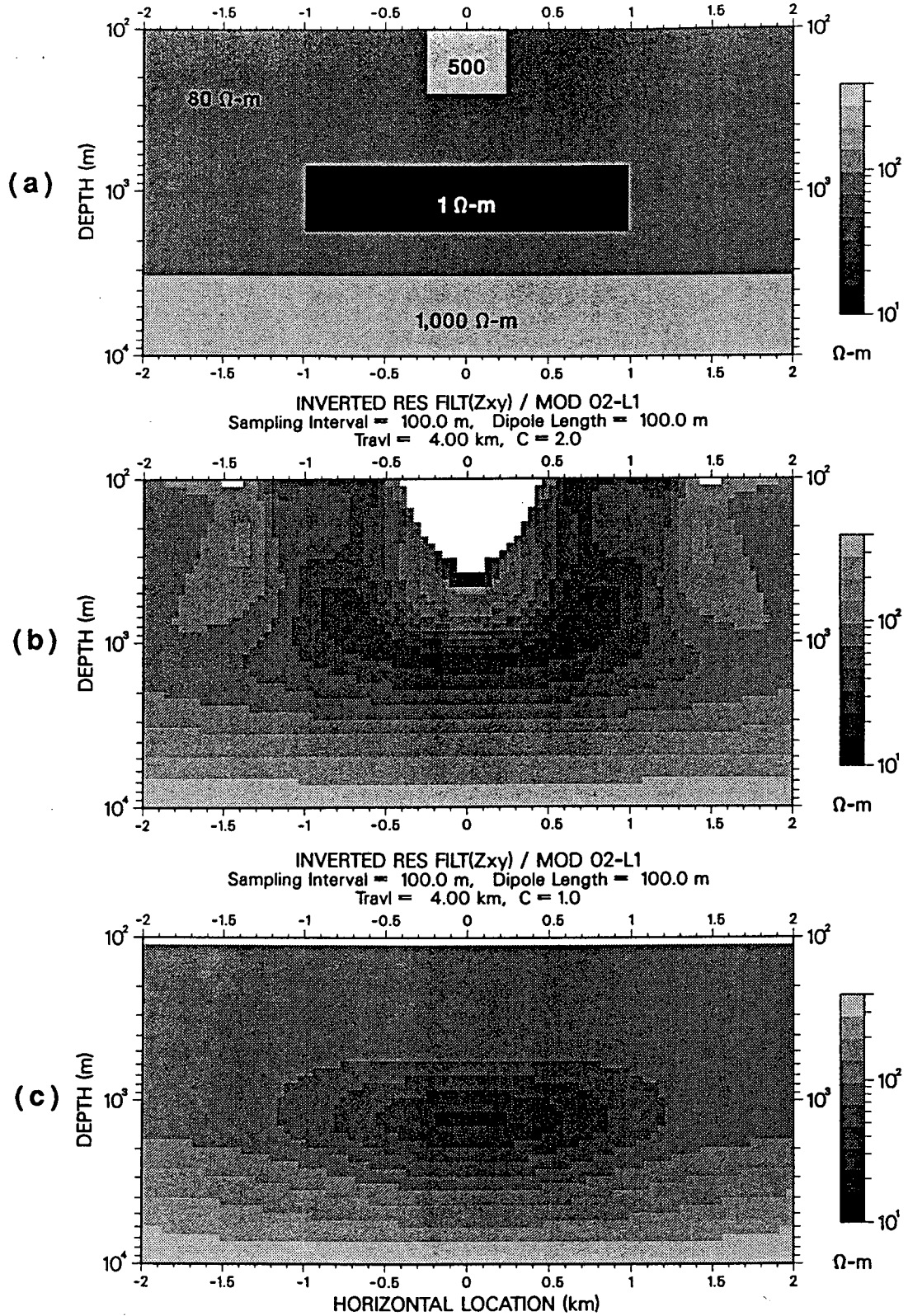

Figure 6-18. Geoelectric sections derived by spatial filtering and subsequent Bostick inversion of the simulated Z_{xy} EMAP impedances along Line 1 of 3-D model No. 2 (Figure 6-14). (b) and (c) are the inverted resistivity resistivity sections with and without surface 3-D scatterers, respectively. The model cross-section along Line 1 is shown for comparison in (a). Filter constants, c, of value 2 and 1 were used to obtain the resistivity sections in (b) and (c), respectively.

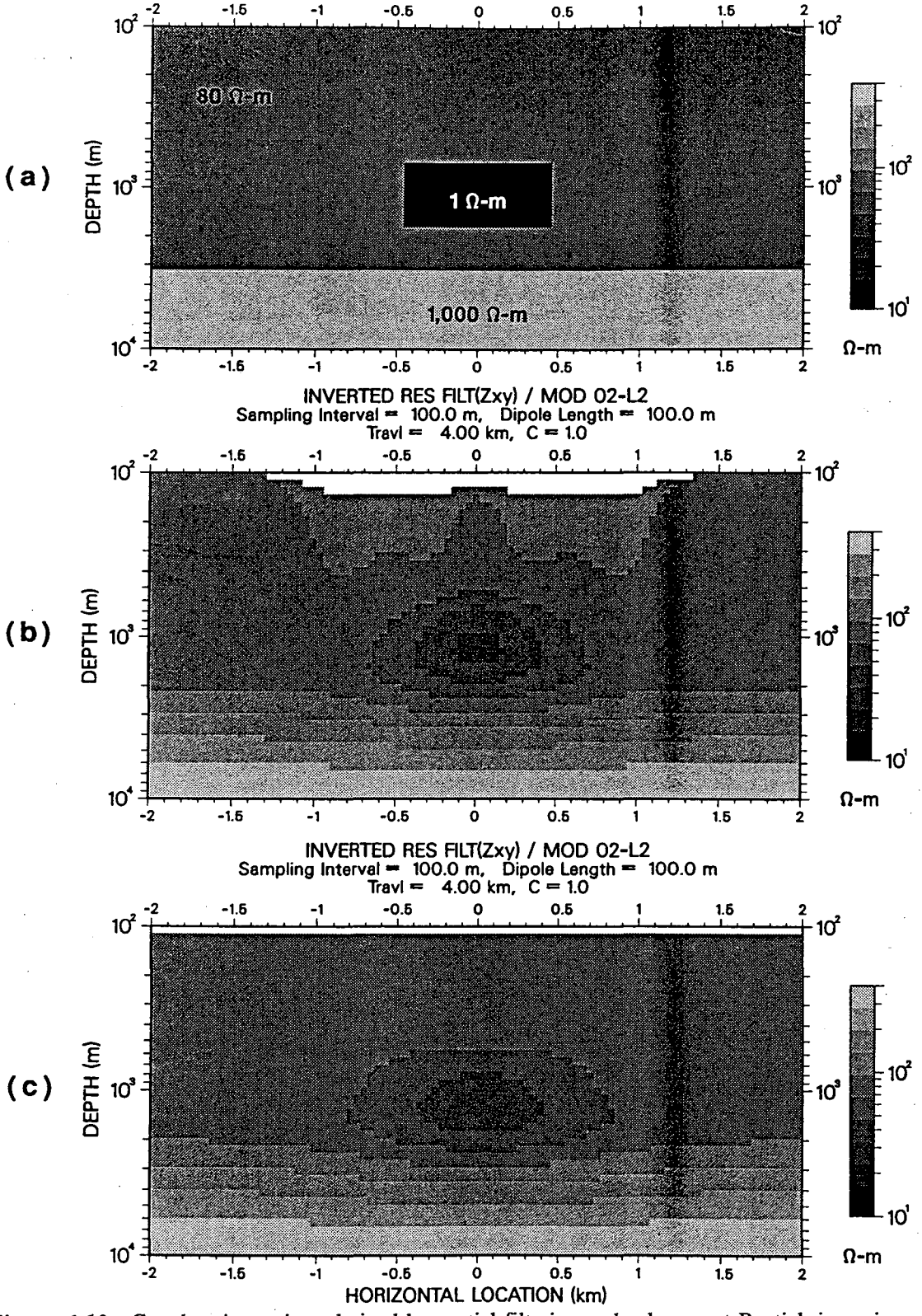

Figure 6-19. Geoelectric sections derived by spatial filtering and subsequent Bostick inversion of the simulated Z_{xy} EMAP impedances along Line 2 of 3-D model No. 2 (Figure 6-15). (**b**) and (**c**) are the inverted resistivity resistivity sections with and without surface 3-D scatterers, respectively. The model cross-section along Line 2 is shown for comparison in (**a**). A filter constant, c, of value 1 was used to obtain both inverted resistivity sections.

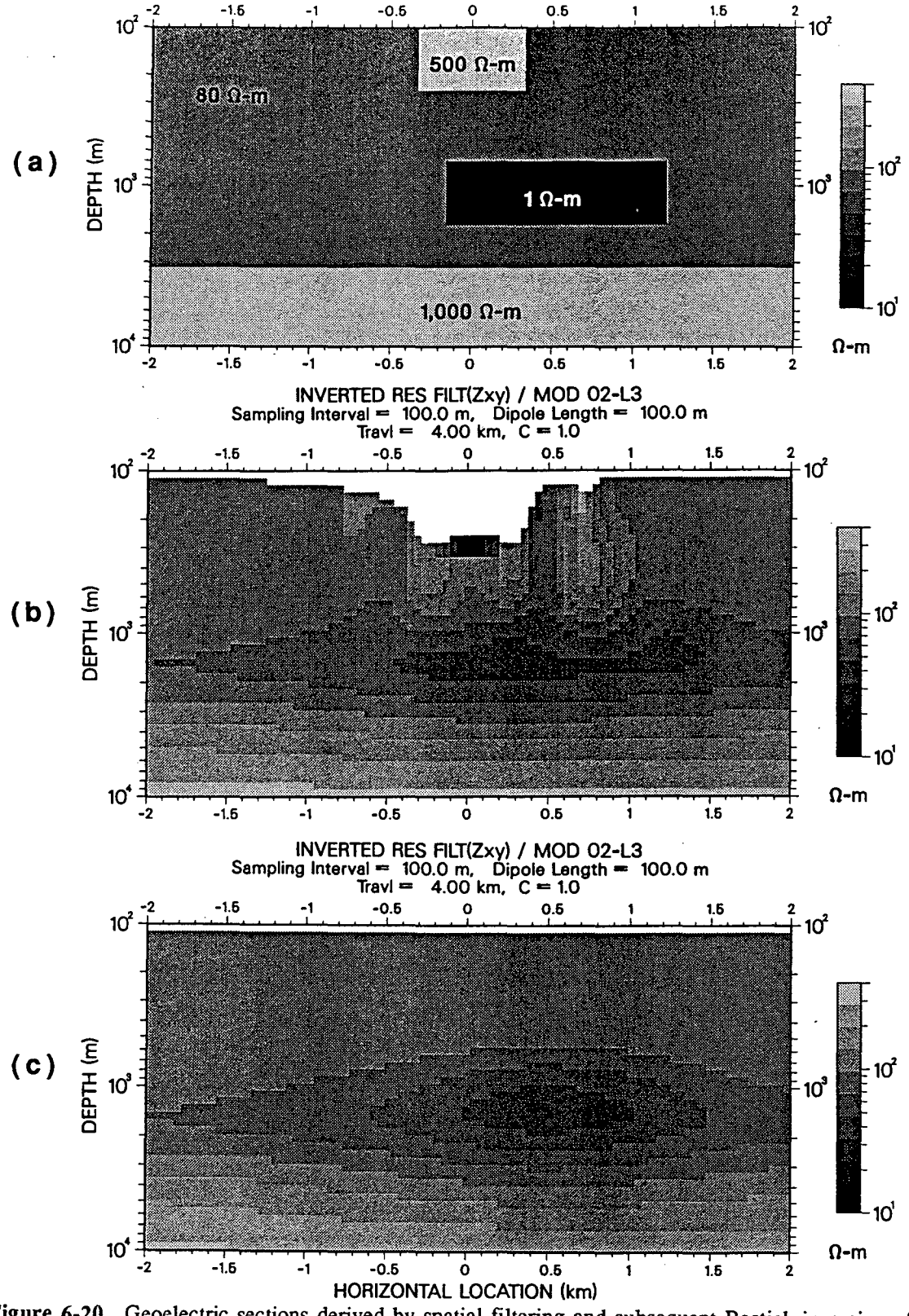

Figure 6-20. Geoelectric sections derived by spatial filtering and subsequent Bostick inversion of the simulated Z_{xy} EMAP impedances along Line 3 of 3-D model No. 2 (Figure 6-16). (b) and (c) are the inverted resistivity resistivity sections with and without surface 3-D scatterers, respectively. The model cross-section along Line 3 is shown for comparison in (a). A filter constant, c, of value 1 was used to obtain both inverted resistivity sections.

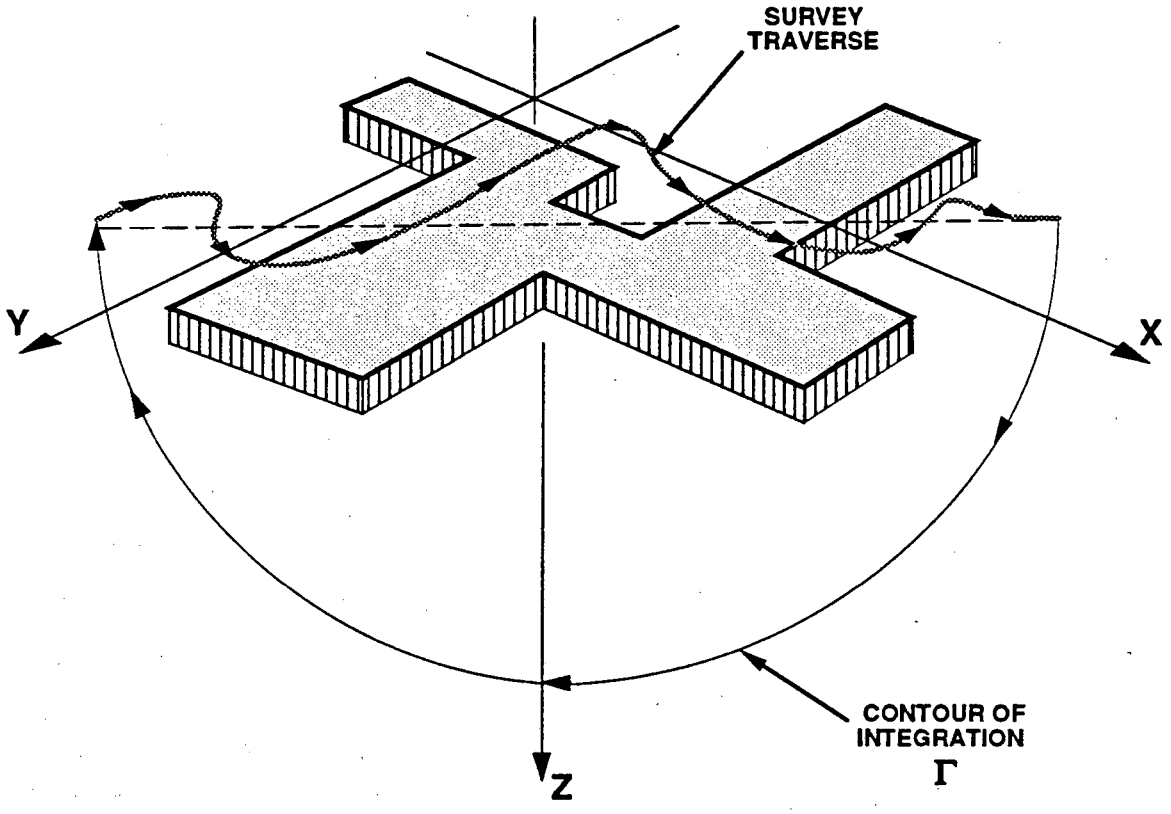

Figure 6-21. Diagram describing the way in which the closed-line integral $\int E \cdot d\ell$ is evaluated over the surface (the survey traverse), and along a semicircle of infinite radius, to suppress static effects. In the DC limit, regardless of the integration path the surface integral will vanish if its end points coincide with locations where the secondary electric field distortion is negligible.

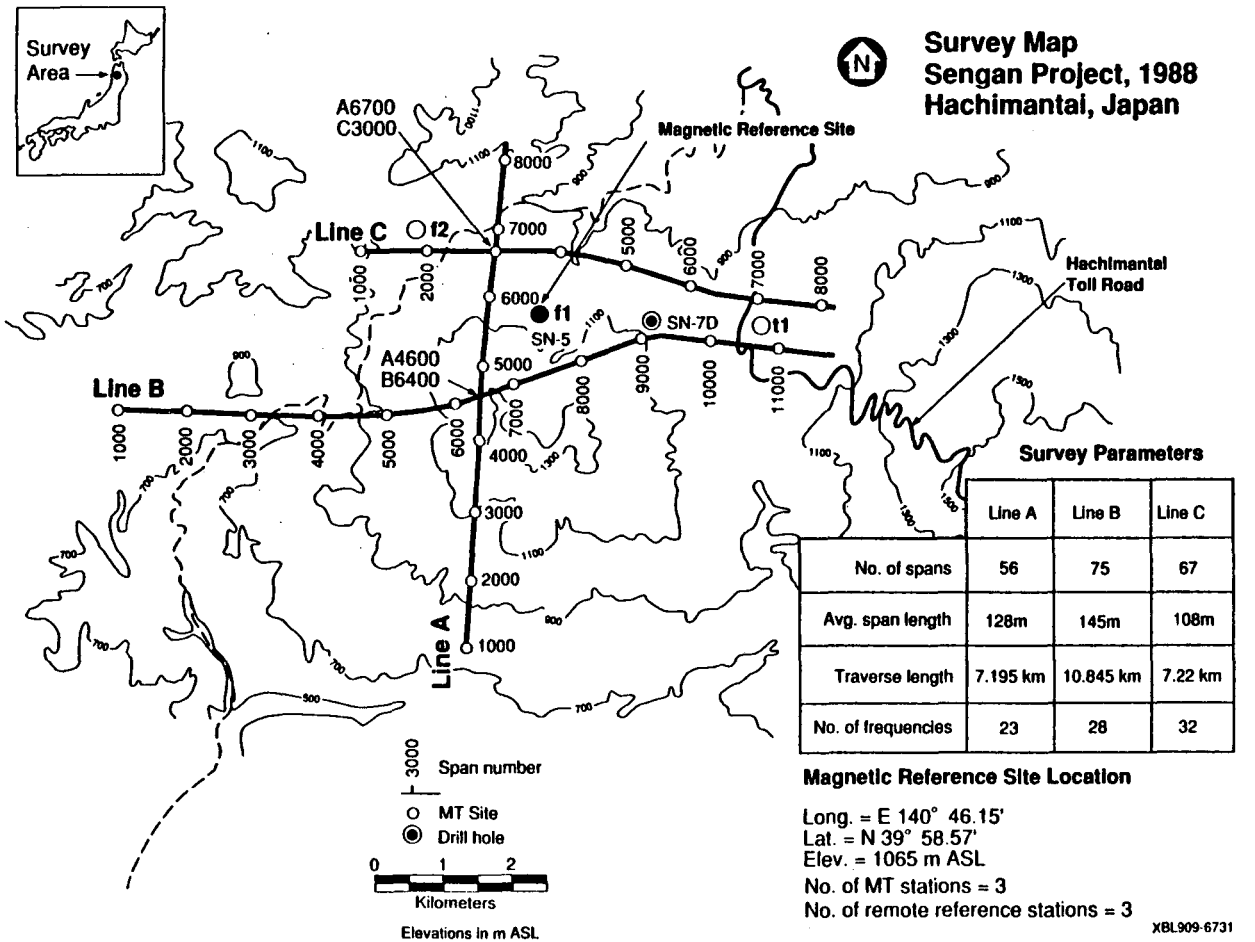

Figure 6-22. Location map of the Sengan EMAP project. Lines A, B, and C are the survey traverses. Field parameters along each line are detailed in the table insert. Also, locations are shown for the magnetic base station, conventional MT sites, and drill-holes.

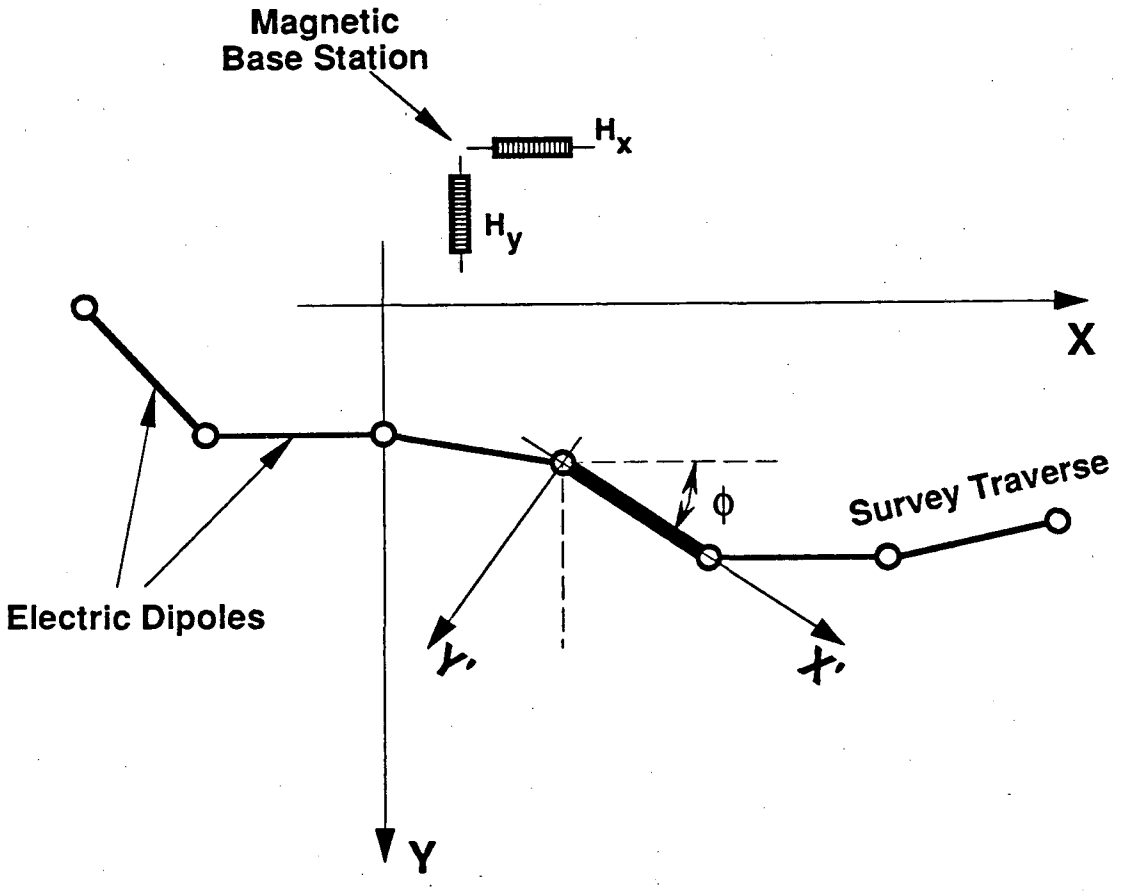

Figure 6-23. Graphical description of the procedure that is used to transform the measured in-line impedances into base impedances along a curvilinear EMAP traverse: the magnetic fields measured at the base site are rotated in the directions parallel and perpendicular to each one of the electric dipoles.

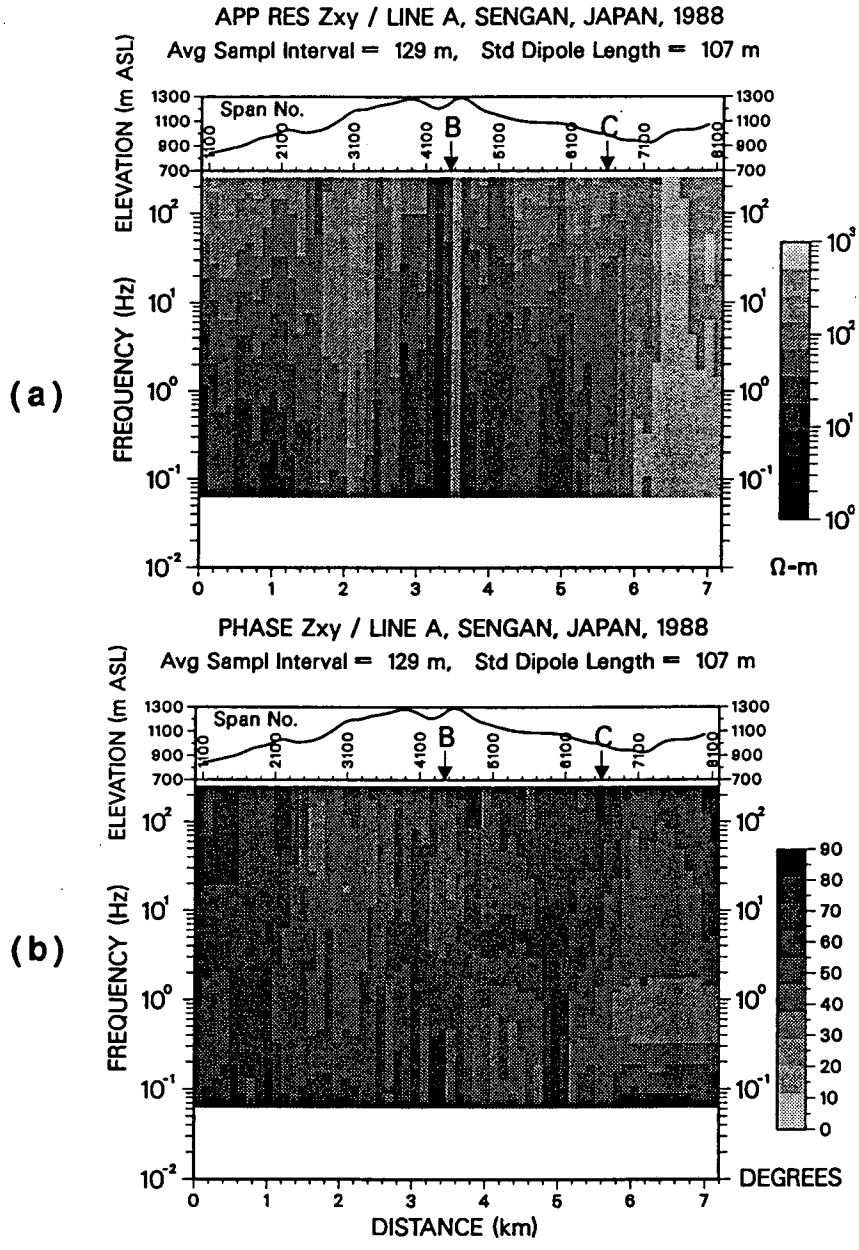

Figure 6-24. Apparent resistivity and phase pseudosections, (a), and (b), respectively, of the Z_{xy} base impedances measured along Line A of the Sengan EMAP project (Figure 6-20). For reference, the topographic profile is shown in the upper panel of both pseudosections with elevations given in meters above the sea level (m ASL).

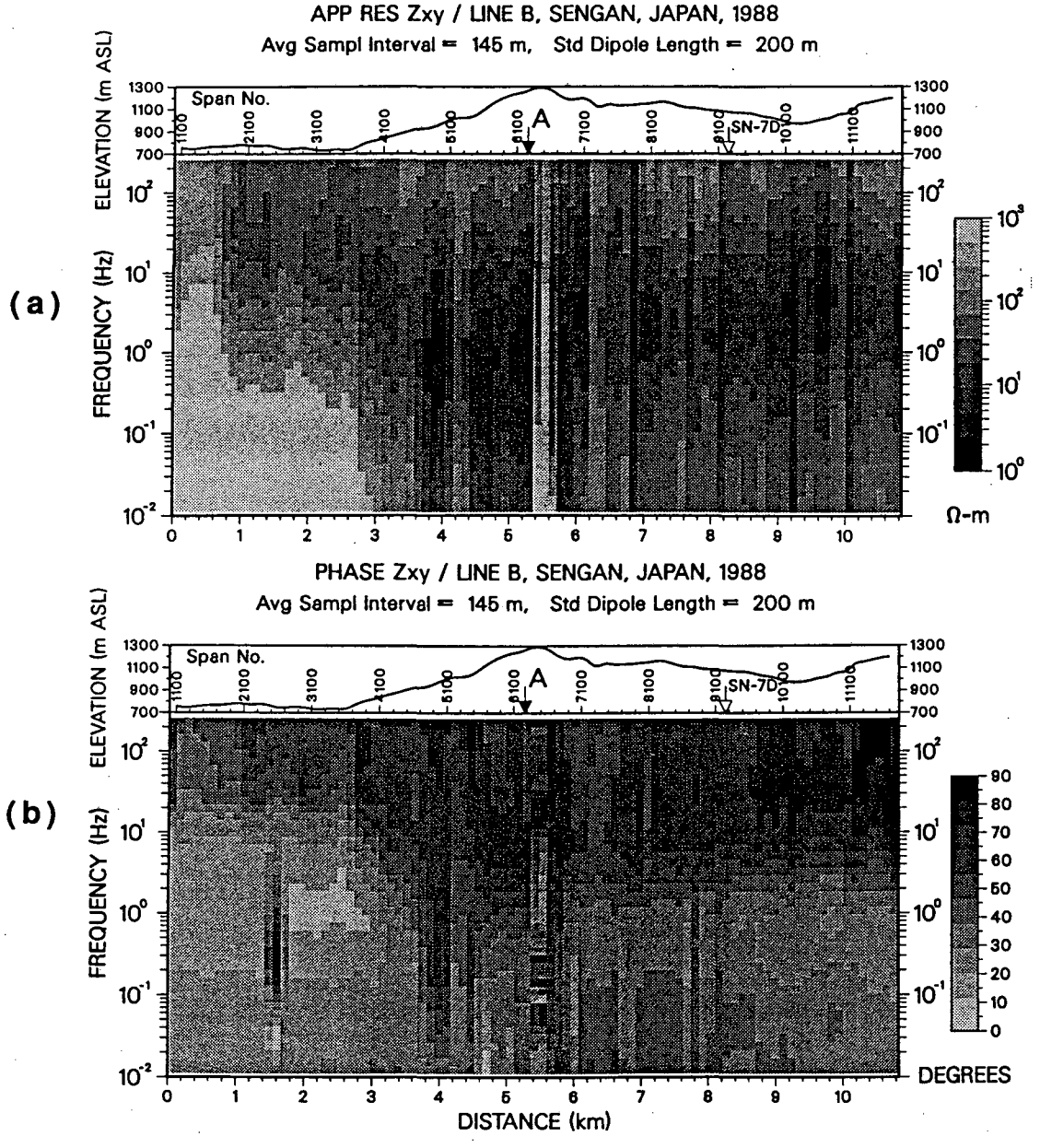

Figure 6-25. Apparent resistivity and phase pseudosections, (a), and (b), respectively, of the Z_{xy} base impedances measured along Line B of the Sengan EMAP project (Figure 6-20). For reference, the topographic profile is shown in the upper panel of both pseudosections with elevations given in meters above the sea level (m ASL).

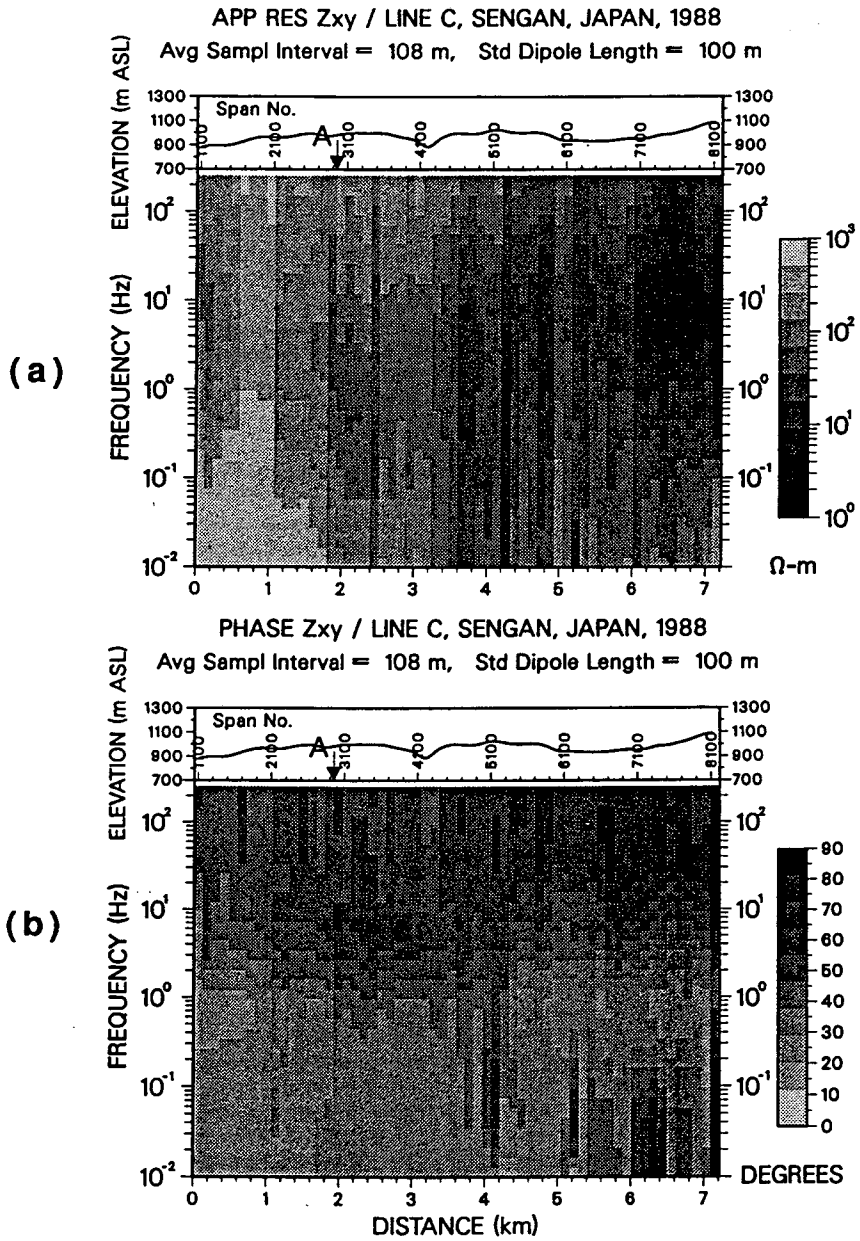

Figure 6-26. Apparent resistivity and phase pseudosections, (a), and (b), respectively, of the Z_{xy} base impedances measured along Line C of the Sengan EMAP project (Figure 6-20). For reference, the topographic profile is shown in the upper panel of both pseudosections with elevations given in meters above the sea level (m ASL).

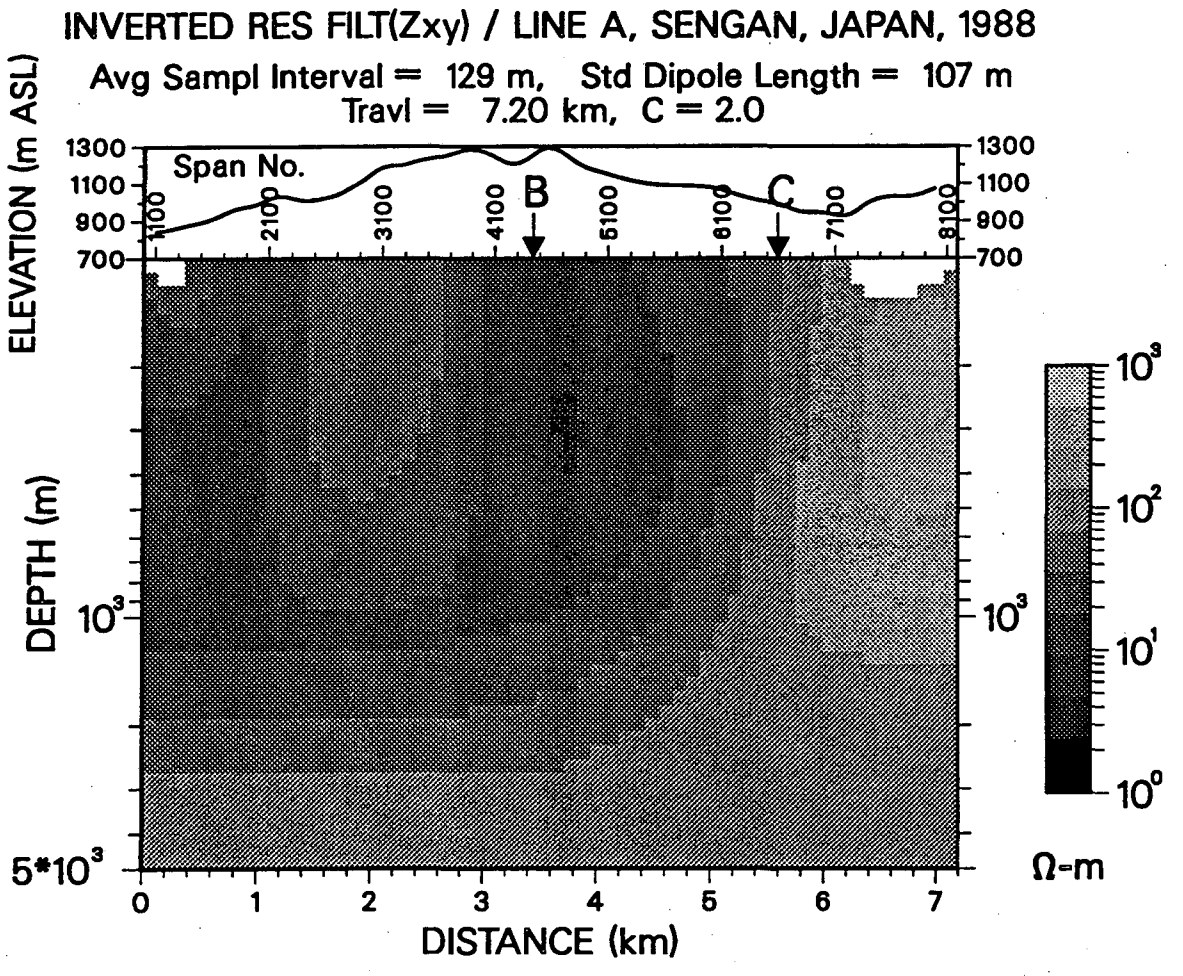

Figure 6-27. Geoelectric section derived by spatial filtering and subsequent Bostick inversion of the Z_{xy} base impedances measured along Line A of the Sengan EMAP project (Figure 6-20). The section was obtained with the use of a filter constant, c, of value 2. Depths are measured in meters below an elevation datum placed at 700 m ASL.

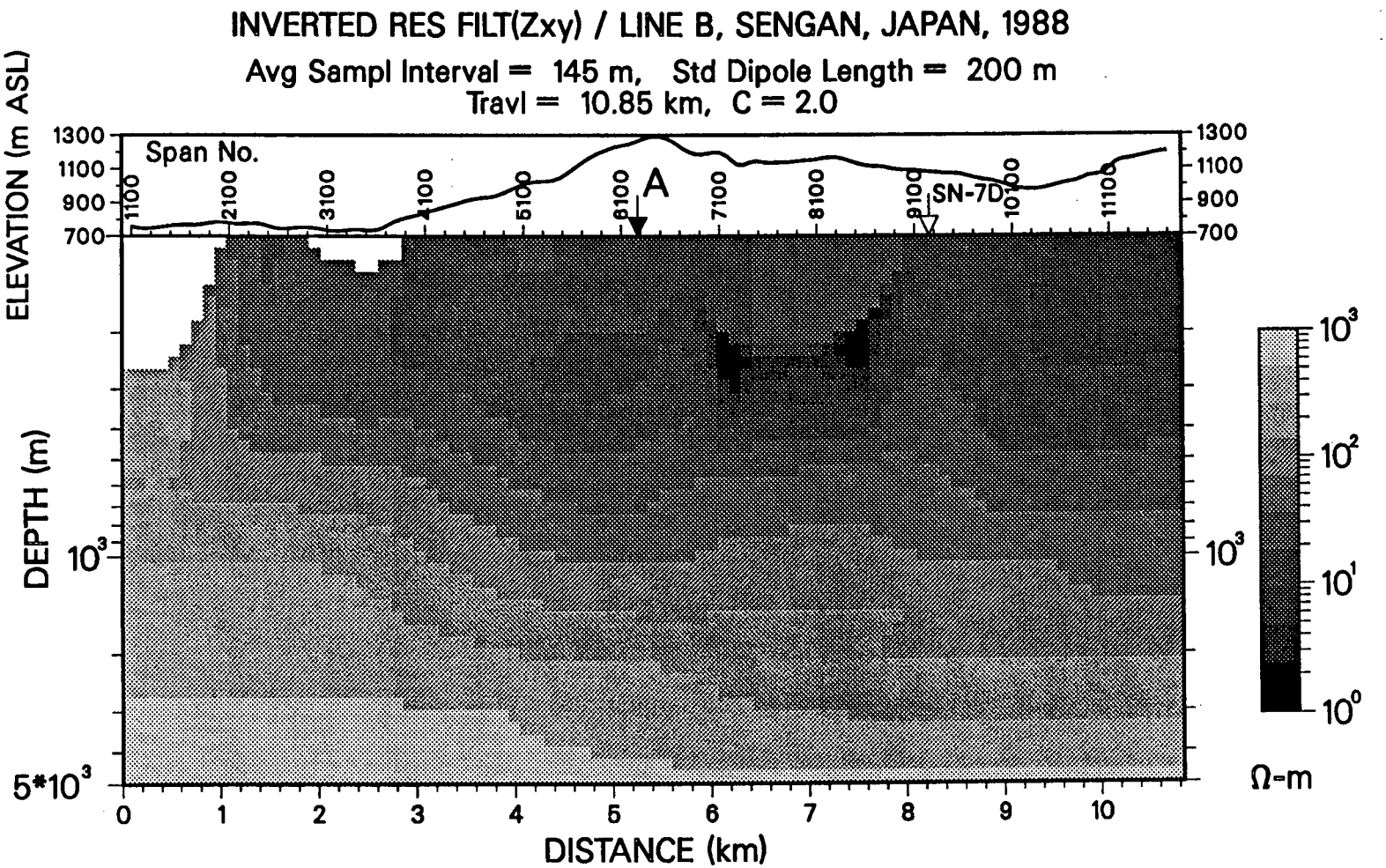

Figure 6-28. Geoelectric section derived by spatial low-pass filtering and subsequent Bostick inversion of the Z_{xy} base impedances measured along Line B of the Sengan EMAP project (Figure 6-21). The section was obtained with the use of a filter constant, c, of value 2. Depths are measured in meters below an elevation datum placed at 700 m ASL.

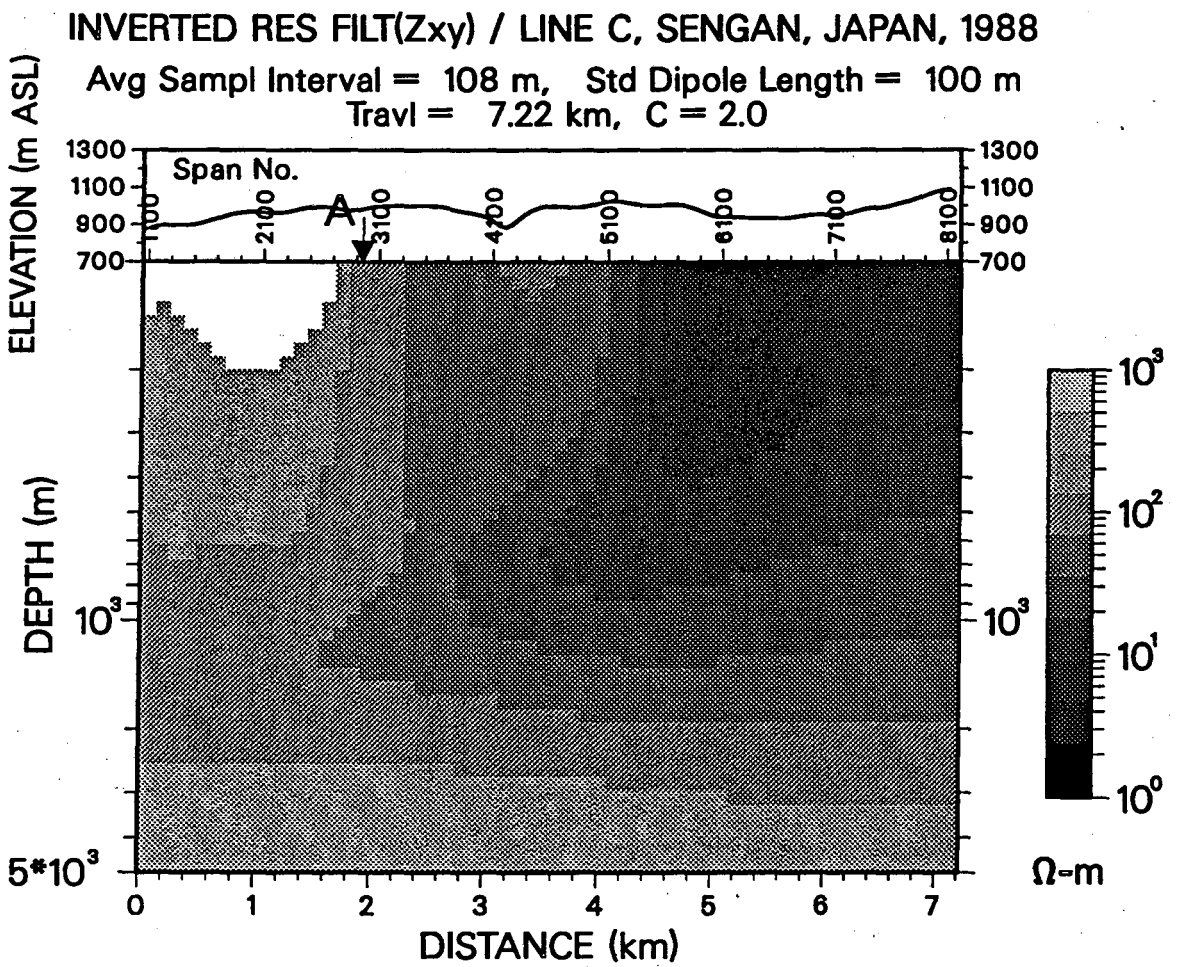

Figure 6-29. Geoelectric section derived by spatial low-pass filtering and subsequent Bostick inversion of the Z_{xy} base impedances measured along Line C of the Sengan EMAP project (Figure 6-22). The section was obtained with the use of a filter constant, c, of value 2. Depths are measured in meters below an elevation datum placed at 700 m ASL.

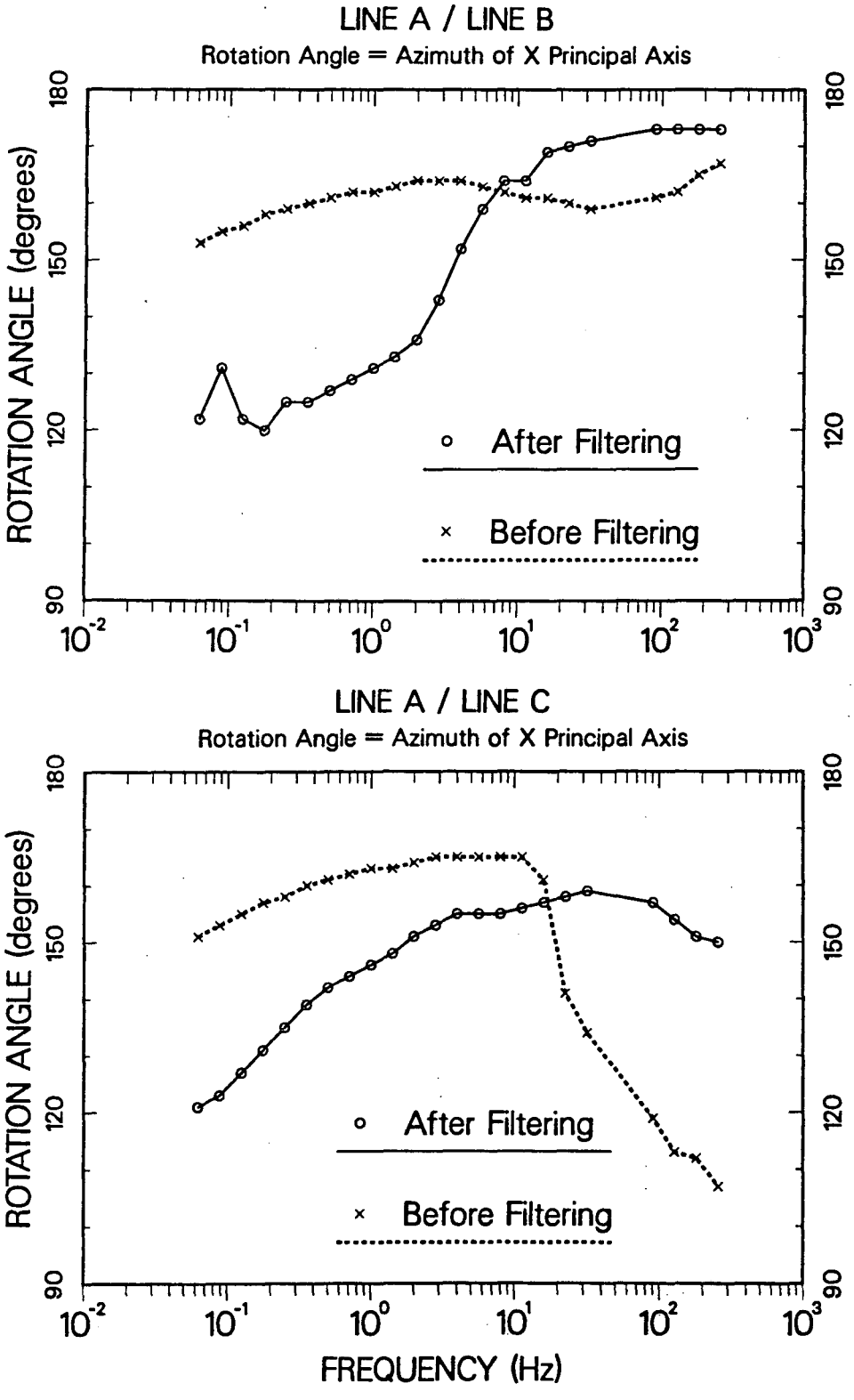

Figure 6-30. Induction strike angles, θ, estimated from MT impedance tensors assembled at the two line intersections of the Sengan EMAP project (Figure 6-20). (a) and (b) are plots of strike angle (measured as true North azimuths) with respect to frequency estimated at the Line A-Line B and Line A-Line C intersections, respectively, with and without spatial filtering along each intersecting line.

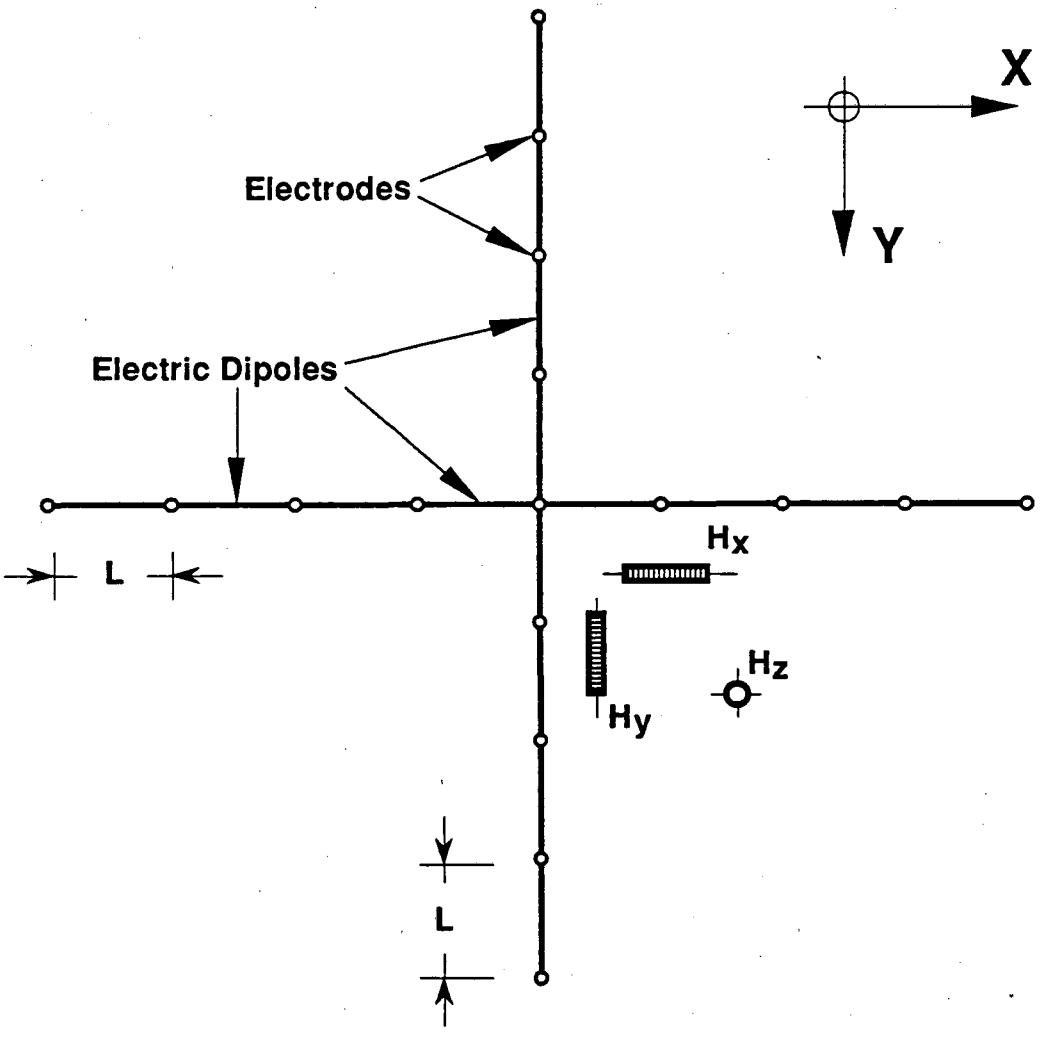

Figure 6-31. Diagram showing the suggested field procedure for the estimation of conventional MT impedances in the presence of electric static distortion: a "cross" of electric dipoles is used to reduce spatial aliasing and ultimately to suppress static effects by increasing the length of the electric field average with decreasing values of frequency. All electric dipole measurements are referred to a common magnetic station, which may also include a vertical magnetic field sensor.

CHAPTER VII

SUMMARY

Se miente más de la cuenta por falta de fantasía
También la verdad se inventa
Antonio Machado

The acquisition of MT data should be approached from the perspective of the well established sampling theorem. In essence, the recovery of lateral resistivity variations in the subsurface requires the sampling distance to be in accord with the spatial characteristics of the signal, that is to say of the electric of magnetic surface field response. It has been shown in practical applications of magnetotellurics that lateral electric field variations can be substantial along relatively short distances; in fact, lateral discontinuities in the surface electric field are not uncommon. Conversely, the lateral magnetic field variations are never discontinuous and in general are characterized by smooth and small oscillations about the primary magnetic field. These properties indicate that inference of lateral variations in the subsurface resistivity distribution requires much shorter sampling distances for electric than for magnetic fields. Unfortunately, magnetic field variations alone are not sufficient to uniquely determine the lateral and vertical characteristics of the subsurface resistivity distribution. The measurement of electric field variations cannot be avoided if one is interested in recovering specific values of depth and resistivity for the geoelectric features whose MT response can be discerned on the surface. Thus, a natural question to ask is, how short should the sampling distance be to guarantee optimal recovery of the lateral resistivity variations both laterally and at depth? The answer to this question lies precisely in the well known sampling theorem for signals, which states that the maximum lateral wavelength that can be truly recovered from the sampled signal is equal to one-half the sampling distance. Of course, when nothing is known a priori of the signal that is being sampled, it is appropriate to use as short as possible a constant sampling distance. With respect to frequency, and ultimately with respect to depth, the diffusive nature of the MT response dictates that the depth of response increases with decreasing values of the sounding frequency. This implies that, to guarantee the recovery of a laterally varying geoelectric feature in the subsurface, one needs to select a specific value of frequency or

range of frequencies for which the effective depth of response secures a measurable EM backscattering effect.

The major difficulty in sampling electric field signals is that their amplitude response can be significantly affected by shallow and spatially localized geoelectric features. In consequence, the measured electric field amplitude at decreasing values of frequency often does not bear a one-to-one relationship with geoelectric features buried at increasing depths of response. This unfortunate phenomenon has been referred to as the static effect in allusion to its DC nature. In contrast, barring the occurrence of certain complex 3-D current distortion effects, the electric phase response does reflect the EM backscattering of features buried at increasing depths when one lowers the sounding frequency. Because of this, the phase response is in effect purely inductive. However, in keeping with the principle of constant nastiness, the electric amplitude response is needed to determine lateral and vertical resistivity variations because the phase response does not define them uniquely. Thus, in summary, lateral measurements of the electric field response should be made in a way that guarantees both adequate sampling of the large amplitude variations and recognition of static effects. Strictly speaking, over structurally complex 3-D environments, the electric field sampling procedure required to satisfy the requirements of the sampling theorem entails the deployment of sounding stations not only along a survey line, but over a surface grid. However, without losing sight of the 3-D and tensor nature of the surface MT response, this thesis followed a practical historical progression of magnetotellurics and concentrated on the 1- and 2-D aspects of the problem.

In spite of the fact that a linear model for the MT response is incomplete for the accurate description of EM scattering in practical exploration situations, it allows one to perform a model-independent study of the vertical and lateral resolution characteristics of the technique, particularly in connection with the continuous profiling of MT fields.

Over 1-D media, a simple logarithmic parameterization of both frequency and depth of the linearized solutions yields a convolutional model response relationship between the vertical variations of subsurface resistivity and the measured electric field data. This suggests that the logarithmic depth scale is natural for the diffusive MT response, and that the logarithmic sampling that is normally used with respect to frequency is consistent with the resolving power. A Wiener estimation procedure to map frequency variations of the electric field into resistivity variations along the logarithmic depth scale reveals that the use of more than 8 frequency samples per decade is unnecessary considering the resolving power of noisy MT data. Numerical experiments with the 1-D linearized inverse suggest

that the Rytov (logarithmic) parameterization of the electric field data is superior to the Born (algebraic) parameterization. In general, it can be stated that the linear system equations hold not only when the resistivity contrasts are small, but also when, regardless of the magnitude of the resistivity contrast, when the frequency variations of the electric field response are small. Because numerical experiments with the linearized 1-D inverse produce reasonable results in cases where the assumption of linearity is not valid, one can conclude that the physical insights gained from this simplified method of solution are not too far from reality. The linearized inverse could be easily extended to a nonlinear method of inversion in which the inverted model is continually updated either by way of a Born series or by iterative checks between the data and the simulated results.

When the linearized MT forward problem is specialized for 2-D subsurface resistivity distributions, it becomes evident that the resolution with which one can estimate lateral and vertical variations of subsurface resistivity is determined by the particular electric or magnetic field quantity fed to the inversion process. Moreover, a wavenumber-domain formulation of the 2-D linear inverse problem shares a few of the characteristics of the 1-D linearized inverse, and for this reason the latter can be used as a benchmark in lateral resolution studies of 2-D MT data. An ad hoc factorization of the wavenumber-domain linear equations reveals that a vertical response kernel is common to all the TM and TE field components. This kernel exhibits an exponential loss of response to the lateral detail in the subsurface with increasing values of the product $\gamma=2\pi k z_B$, where k is the linear wavenumber, and z_B is the Bostick depth of penetration at a given frequency. The distinction among the various TM and TE field components is defined by a wavenumber prefilter which operates on the lateral variations of subsurface resistivity and whose cutoff characteristics are essentially controlled by the sounding frequency. For the TE magnetic field components, the prefilter produces a null in the surface response at the DC wavenumber. On the other hand, the prefilter is a low-pass filter for TE electric field data and a high-pass filter for TM electric field data. The high-pass filter nature of the TM electric prefilter is related to the way in which the static effect is impressed on the electric field component. In contrast, the TE electric field component is purely inductive and hence is devoid of static effects, thus the low-pass filter nature of its associated prefilter. A significant consequence of the high-pass filter nature of the TM prefilter is that stability in the inversion of TM electric field data can be naturally achieved by allowing the prefilter to operate on the data instead of on the lateral variations of subsurface resistivity. When this is done, the prefilter behaves as a stable low-pass filter of the measured TM electric fields. The resulting operation is thus equivalent to a data prewhitening step in which the cutoff

wavenumber of the prewhitening operator decreases with decreasing values of frequency. Compared to the TE prefilter, however, the TM prewhitening filter has a slightly wider wavenumber band, and it is for this reason that TM electric field data possess better lateral resolution characteristics than TE electric field data. With regard to the magnetic field data, the null of the magnetic prefilter at k=0 causes these components to be insensitive to the 1-D background of the subsurface resistivity distribution. Furthermore, the relationship between the TE electric and magnetic prefilters indicate that all surface TE field components are linearly related with respect to position.

The 2-D linearized inverse predicts that, below the Nyquist wavenumber dictated by the sampling distance, and at a 1% noise-to-signal ratio in the measured MT data, the maximum wavenumber that can be recovered from the lateral variations of subsurface resistivity distribution is approximately the inverse of the Bostick (1977) depth of penetration. This result permits one to perform simple approximate calculations to estimate the lateral resolution that can be expected from an MT survey aimed at determining the geometrical characteristics of a given target. Numerical experiments with the 2-D linearized inverse corroborate that the underlying physical principles hold even when the low-contrast assumption is violated, and are in agreement with the expected lateral and vertical resolution characteristics of both TM and TE electric field data. The inversion algorithm developed in this thesis consists of a sequence of pseudo 1-D inverses at each lateral wavenumber to estimate the real and imaginary wavenumber harmonics of the 2-D subsurface resistivity distribution. Inverse Fourier transformation is subsequently used to derive a model estimate in the space domain. A space-domain formulation can be the subject of future research efforts with special attention to the role of the TM prewhitening operator in the new domain. Likewise, an iterative Born inversion procedure could be used to continually update the lateral and vertical changes of the background resistivity which was assumed constant in the linearized inverse formulation.

Electromagnetic Array Profiling (EMAP) is one MT profiling technique where the requirements stipulated by the sampling theorem in the measurement of lateral electric field variations are satisfied. The EMAP field procedure consists of the deployment of electric dipoles end-to-end along the survey line. This configuration also enables one to perform spatial filtering on the measured electric field variations in a controlled fashion. In fact, the use of spatial filtering can be seen as a practical way to incorporate the role of the TM prewhitening filter over geoelectric media where the assumption of a constant background resistivity is simply out of the question. Moreover, analysis of the 3-D equations derived

under the assumption of a linear MT response elicits a similar prewhitening wavenumber filter to be used with electric field data collected on a grid. Such equations indicate that if spatial filtering is to be applied to suppress 3-D static effects, this has to be performed in a directional fashion. In plain physical terms, spatial filtering over 3-D geoelectric media reflects the action of the $\int \mathbf{E} \cdot d\ell$ integral inherent to the acquisition characteristics of an individual electric dipole. In so doing, frequency dependent static effects in the electric response are reduced and the remaining electric component may be interpreted with procedures suitable for a purely inductive MT response. The way in which spatial filtering of the tangential electric field is performed essentially consists of simultaneous lateral and vertical calibration of the cutoff characteristics of the prewhitening filter. This is done directly in the space domain via a nonlinear fixed-point iteration procedure wherein the width of the applied window is varied until the filtered electric field produces an estimate of the depth of response which is a multiple of the window width. The constant that linearly relates the width of the filtering window with the depth of penetration estimated from the filtered electric field can be judiciously chosen to control the degree of lateral smoothing inflicted upon the original data to reduce static effects. In fact, over homogeneous media, the adaptive calibration of the low-pass filter produces an identical filter response to that of the TM prewhitening filter derived from the 2-D linearized inverse. A possible avenue for future research in connection with the optimization of the prewhitening filter consists of a recursive double sequence of both spatial filtering and 1-D localized inversion. This thesis exploited a simplified view of such an inversion method by using a Bostick (1977) pseudoinverse to map the filtered results into depth and resistivity estimates along the line of measurements.

In practice, spatial filtering of the electric field requires that all the measurements be synchronously acquired. Knowing the random source characteristics of MT data, this is a rather strong demand on a field procedure that may potentially consist of tens or even hundreds of electric field dipoles. A way to circumvent such a difficulty consists in the deployment of a fixed base magnetic field station while electric and magnetic field measurements are acquired along the survey line. The in-line electric field measurements referred to the fixed magnetic base station yield stationary impedances that can be used in place of actual electric field values to carry out the spatial filtering step. A further refinement to this field procedure consists in performing an areal average of the magnetic field measurements acquired within the survey area to estimate the primary magnetic field. Because the magnetic field is insensitive to the 1-D background, its areal average will tend

to represent the constant primary magnetic field for a large enough number of magnetic field sensors adequately disposed along and about the survey line. The estimated primary magnetic field can then be used to normalize the in-line base impedances such that the latter exclusively reflect the lateral variations of the secondary electric field away from the 1-D background response.

A collection of 2-D simulation examples which includes strong surface static effects as well as highly nonlinear response characteristics, yields a very encouraging evaluation for the adaptive spatial filtering of electric field data. Further, the feasibility of EMAP is attested to by three field examples over geological environments where lateral variations in the geoelectric response simply cannot be discounted. These are prime examples of actual exploration situations where only after electric field data have been gathered in continuous fashion does one come to fully appreciate the extent to which unheeded static effects can bias the subsequent geoelectric interpretation when the sampling distance is of the order of kilometers. Needless to say, electric field data acquired in continuous fashion does not exclusively lead to a method of inversion where spatial filtering is enforced. Any of the parametric nonlinear inversion algorithms reported elsewhere in the EM geophysical literature may be used on these data.

Ever since EMAP came to light, much unnecessary emphasis has been placed on the limitations of the technique for imaging practical 3-D geoelectric media or even over 2-D media when the survey line might be oblique to strike. It was found here that, over 2-D media, the tangential electric field measurements can yield estimates of both TE and TM impedances provided that the survey line is oblique with respect to strike. To estimate these two impedances, it is necessary that the strike angle be known beforehand. This can be accomplished by deploying an orthogonal dipole at a single point along the survey line. Use of EMAP over geoelectric environments where there is a prevalent 2-D induction strike at depth but in which there are also 3-D surface scatterers, may call for a small-scale version of an EMAP line in the orthogonal direction in order to satisfy the requirements of the sampling theorem and to be able to suppress possible static effects. The suggestion made in this thesis is that instead of acquiring data with orthogonal electric dipoles at exactly the same locations where tangential electric field data are gathered, one can use either much longer dipoles or, better, strings of them, perpendicular to the main survey line with lateral spacings equal to a few times the sampling distance used to measure the tangential electric field. The collection of well sampled (here "well" means with satisfaction of the sampling theorem and with static effects previously suppressed) orthogonal electric

field data helps considerably in ascertaining whether the tangential electric fields measured along the survey line are affected by the induction response of either offset scatterers or geoelectric features whose principal geometrical axis is oblique to the survey line. Alternatively, because the vertical magnetic field is distorted by static effects only in very pathological situations, measurements of this component along the survey line can serve to indicate the presence of such induction effects at a much lower operational cost.

On the other hand, the use of spatial filtering (or data prewhitening) to suppress static effects on 3-D synthetic electric field data and also on 2-D electric field data sampled obliquely with respect to strike, yields very encouraging results. A simple Bostick inversion carried out on the induction electric component that remains after filtering yields a relatively accurate resistivity cross-section below the line of measurements. The only case that deserves special mention is the one in which the survey line crosses the principal geometrical axis of the inductive scatterer at an angle. In this case, the tangential electric field measurements are a "blend" of both TE-like and TM-like induction response components. Given that the lateral TE electric field response is much smoother than the TM electric field response, the degree of lateral smoothness in the inversion will depend on the proportion of the TE-like response that has "leaked" into the tangential electric field measurements. The larger the angle between the survey traverse and the principal geometrical axis of the scatterer, the larger the proportion of TE-like response, and therefore the smoother the inverted resistivity section. Because the TE and TM electric field responses often bear different pieces of information regarding the nature of the vertical and lateral variations of subsurface resistivity, it is recommended that, whenever applicable and possible, the two mode responses be separated and subsequently interpreted in independent ways. A joint interpretation of both mode responses may be pursued after individual inversions have been obtained.

Estimation of dimensionality parameters and regional strike angles can be biased by 3-D static effects. It was shown that, with the use of orthogonal lines of electric dipoles, static effects can be suppressed prior to performing estimation of MT parameters from tensor impedances. In fact when the use of a continuous line of electric field measurements is impossible because of economic limits, an option is to deploy a "cross" of electric dipoles with a maximum number of dipoles determined by the capabilities of the acquisition system. Alternatively, such a cross can be used to calibrate both the frequency range and the dipole length to be used along a continuous line of measurements before embarking upon the full-scale operation.

Clearly, in an EMAP survey the depth of penetration that can be achieved without bias due to static effects is proportional to the length of the traverse. This may seem a serious practical requirement if the technique is to be applied in crustal studies, where the desired depths of penetration are of the order of 50 km or more. Furthermore, as emphasized by Mackie at al. (1988), and Madden and Mackie (1990), at those depths of response one cannot discount current distortion effects of a regional scale such as ocean-continent boundaries, large sedimentary basins, and mountain ranges. In most of these situations, it would be extremely difficult to deploy a continuous electric field line, even when dipoles could be made as long as perhaps 1 km. It should be reiterated, however, that the need for closely spaced electric field measurements is not a whim but simply an effort to satisfy the requirements imposed by the sampling theorem, and this becomes more important when, in addition to recognizing anomalous conductive zones in the crust, one is interested in determining specific values of resistivity and depth of such features. A field procedure that seems a good compromise between deploying a very long line of electric dipoles (that perhaps has to cross cultural-noise areas, heavily trafficked roads, rivers and high mountain passes), or positioning a dozen or so single MT stations at 10 km intervals, consists of first carrying out a calibration survey with one or more continuous lines of dipoles from which somewhat accurate knowledge of the background crustal geoelectric structure could be obtained with some interpretation procedure that also minimizes static distortion effects (spatial filtering is but one of such procedures) and can ascertain 3-D induction effects along the line(s) of measurements. Subsequently, single MT stations or dipole-crosses of MT stations could be deployed at larger spacings and tied in with the measurements inferred from the calibration survey. In so doing, particular attention should be paid to the lateral variations of impedance phase, which are only in extreme cases subject to static distortion. With the lateral variations of impedance phase, and to some extent of apparent resistivity, referred to the calibrated resistivity section, one could "strip out" local distortion effects and derive approximate values for both resistivity and depth below the single MT site useful at a crustal sounding scale. Numerical simulation of somewhat well determined regional distortion effects, such as ocean-continent boundaries, could be done prior and after the survey to ascertain their influence on the measurements acquired both along the continuous calibration(s) line and also at isolated MT sites.

REFERENCES

Abramowitz, M., and Stegun, I. A., 1972, Handbook of mathematical functions with formulas, graphs, and mathematical tables: National Bureau of Standards, Applied Mathematics Series No. 55.

Aki, K., and Richards, P. G., 1980, Quantitative seismology, theory and methods, II: W. H. Freeman and Co.

Andrieux, P., and Wightman, W. E., 1984, The so-called static corrections in magnetotelluric measurements: 54th Ann. Internat. Mtg., Soc. Explor. Geophys., Expanded Abstracts, 43-44.

Backus, G. E., and Gilbert, J. F., 1967, Numerical application of a formalism for geophysical inverse problems: Geophys. J. Roy. Astr. Soc., **13**, 247-276.

Backus, G. E., and Gilbert, J. F., 1968, The resolving power of gross earth data: Geophys. J. Roy. Astr. Soc., **16**, 169-205.

Backus, G. E., and Gilbert, J. F., 1970, Uniqueness in the inversion of inaccurate gross earth data: Phil. Trans. Roy. Soc. London, A., **266**, 123-192.

Bahr, K., 1987, Interpretation of the magnetotelluric impedance tensor: Regional induction and local telluric distortion: J. Geophys., **62**, 1-9.

Bailey, R. C., 1970, Inversion of the geomagnetic induction problem: Proc. Roy. Soc. London, **315**, 185-194.

Bannister, P. R., and Hart, W. C., 1968, Quasi-static fields of dipole antennas below the earth's surface, *in* Quasi-static electromagnetic fields: Naval Underwater Systems Center, Department of the Navy.

Baños, A. Jr., 1966, Dipole radiation in the presence of a conducting half-space: Pergamon Press, Inc.

Barrodale, I., and Roberts, F. D. K., 1973, An improved algorithm for ℓ_1 approximation: SIAM J. Numer. Anal., **10**, 834-848.

Berdichevsky, M. N., Dmitriev, V. I., 1976, Basic principles of interpretation of magnetotelluric sounding curves, *in* Adam, A., Ed., Geoelectric and geothermal studies: KAPG Geophysical Monograph, Akademiai Kiado, Budapest, 165-221.

Berdichevsky, M. N., Vanyan, L. L., Kuznetsov, V. A., Levadny, V. T., Mandelbaum, M. N., Nechaeva, G. P., Okulessky, B. A., Shilosky, P. P., and Shpak, I. P., 1980, Geoelectric model of the Baikal region: Phys. Earth Planet. Inter., **22**, 1-11.

Berdichevsky, M. N., and Zhdanov, M. S., 1984, Advanced Theory of Deep Geomagnetic Sounding: Elsevier Science Publ. Co., Inc.

Bergland, G. D., and Dolan, M. T., 1979, Fast Fourier transform algorithms, *in* Programs for digital signal processing: IEEE Press.

Boehl, J. E., Bostick, F. X., Jr., and Smith, H. W., 1977, An application of the Hilbert transform to the magnetotelluric method: EGRL Technical Report, The University of Texas at Austin.

Booker, J. A., 1988, Statistical processing of magnetotelluric data, M.Sc. thesis, The University of Texas at Austin.

Bostick, F. X., Jr., 1977, A simple almost exact method of MT analysis, *in* Ward, S., Ed., Workshop on Electrical Methods in Geothermal Exploration, Univ. of Utah Res. Inst., U. S. Geol. Surv. Contract 14-08-0001-g-359, 174-183.

Bostick, F. X., Jr., 1986, Electromagnetic array profiling: 56th Ann. Internat. Mtg., Soc. Explor. Geophys., Expanded Abstracts, 60-61.

Bostick, F. X., Jr., Shoham, Y., and Smith, H. W., 1979, An optimal inverse for the linearized one-dimensional magnetotelluric problem: 49th Ann. Internat. Mtg., Soc. Explor. Geophys., Expanded Abstracts, *in* Geophysics, **45**, 554.

Bracewell, R. N., 1965, The Fourier transform and its applications: McGraw-Hill Book Co.

Cagniard, L., 1953, Basic theory of the magneto-telluric method of geophysical exploration: Geophysics, **18**, 605-635.

Claerbout, J. F., and Muir, F., 1973, Robust modeling with erratic data: Geophysics, **38**, 826-844.

Constable, S. C., Parker, R. L., and Constable, C. G., 1987, Occam's inversion: A practical algorithm for generating smooth models from electromagnetic sounding data: Geophysics, **52**, 289-300.

deGroot-Hedlin, C., and Constable, S., 1990, Occam's inversion to generate smooth, two-dimensional models from magnetotelluric data: Geophysics, **55**, 1613-1624.

d'Erceville, I., and Kunetz, G., 1962, The effect of a fault on the earth's natural electromagnetic field: Geophysics, **27**, 651-665.

Edwards, R. N., 1974, The magnetometric resistivity method and its application to the mapping of a fault: Can. J. Earth Sci., **11**, 1136-1156.

Franklin, J. N., 1970, Well-posed stochastic extensions of ill-posed linear problems, J. Math. Anal. Appl., **31**, 682-716.

Gill, P. E., Murray, W., and Wright, M. H., 1981, Practical optimization: Academic Press Inc.

Gómez-Treviño, E., 1987, Nonlinear integral equations for electromagnetic inverse problems: Geophysics, **52**, 1297-1302.

Goldstein, N. E., 1988, Subregional and detailed exploration for geothermal-hydrothermal resources: Geotherm. Sci. and Tech., **1**, 303-431.

Goldstein, M. A., and Strangway, D. W., 1975, Audio-frequency magnetotellurics with a grounded dipole source: Geophysics, **40**, 669-683.

Groom, R. W., and Bailey, R. C., 1989, Decomposition of magnetotelluric impedance tensors in the presence of local three-dimensional galvanic distortion: J. Geophys. Res., **94B2**, 1913-1925.

Habashy, T. M., and Mittra, R., 1987. On some inverse problems in electromagnetics: J. Electrom. Waves Appl., **1**, 25-58.

Hamilton, W.,1988, Tectonic setting and variations with depth of some cretaceous and cenozoic structural and magmatic systems of the western United States, *in* Ernst, W. G., Ed., Metamorphic and crustal evolution of the western United States: Prentice-Hall, Inc.

Harrington, R. F., 1961, Time-harmonic electromagnetic fields: McGraw-Hill Book Co.

Hedel, C., 1981, Map showing the geothermal resources of the Lake City-Surprise Valley area, Modoc County, California: USGS map MP-1299.

Honkura, Y., Niblett, B. R., and Kurtz, R. D., 1976, Changes in magnetic and telluric fields in a seismically active region of eastern Canada: Tectonophysics, **34**, 219-230.

Honkura, Y., 1978, On a relation between anomalies in the geomagnetic and telluric fields observed at Nakaizu and the Izu-Oshima-Kinhai earthquake of 1978: Bull. Earthquake Res. Inst., **53**, 931-937.

Hopper, M. J., 1979, HARWELL subroutine library, a catalog of subroutines: AERE, Harwell, Didcot, Oxon, OX11 ORA, England.

Jones, A. G., 1988, Static-shift of magnetotelluric data and its removal in a sedimentary basin environment: Geophysics, **53**, 967-978.

Jones, A. G., Boerner, D. E., Kurtz, R. D., Oldenburg, D., and Ellis, R. G., 1989, EMAP data processing in the wavenumber domain: 59th Ann. Internat. Mtg., Soc. Expl. Geophys., Expanded Abstracts, 172-174.

Jupp, D. L. B., and K. Vozoff, 1977, Two-dimensional magnetotelluric inversion: Geophys. J. R. Astr. Soc., **50**, 333-352.

Kaufman, A. A., and Keller, G. V., 1981, The magnetotelluric sounding method: Elsevier Science Publ. Co., Inc.

Kunetz, G., 1972, Processing and interpretation of magnetotelluric soundings: Geophysics, **37**, 1005-1021.

Lawson, C. L., and Hanson, R. J., 1974, Solving least squares problems: Prentice-Hall, Inc.

Lee, S., McMechan, G. A., and Aiken, C. L. V., 1987, Phase-field imaging: the electromagnetic equivalent of seismic migration: Geophysics, **52**,104-117.

Mackie, R. L., Bennett, B. R., and Madden, T. R., 1988, Long-period magnetotelluric measurements near the central California coast: a land-locked view of the conductivity structure under the Pacific Ocean, Geophys. J., **95**, 181-194.

Madden, T. R., and Mackie, R. L., 1989, Three-dimensional magnetotelluric modeling and inversion: Proc. IEEE, **77**, 318-333.

Madden, T., and Mackie, R. L., 1990, Enhancement of regional distortions of MT fields by anisotropy of high-contrast layers: 60th Ann. Internat. Mtg., Soc. Expl. Geophys., Expanded Abstracts, 510-511.

Mano, K., 1970, Interrelation between terms of the Born and Rytov expansions: Proc. IEEE, **58**, 1168-1169.

Marsden, J. E., 1973, Basic complex analysis: W. H. Freeman and Co.

Menke, W., 1984, Geophysical data analysis: Discrete inverse theory: Academic Press Inc.

Moore, R. K., and Blair, W. E., 1961, Dipole radiation in a conducting half-space: J. Res. Nat. Bureau Stand., **65D**, 547-563.

Morrison, H. F., Nichols, E. A., Torres-Verdín, C., Booker, J. R., and Constable, S. C., 1990, Comparison of magnetotelluric inversion techniques on a mineral prospect in Nevada: 60th Ann. Internat. Mtg., Soc. Expl. Geophys., Expanded Abstracts, 516-519.

Morse, P. W., and Feshbach, H., 1953, Methods of Theoretical Physics: McGraw-Hill Book Co., Inc.

Nolan, T. B., Merriam, C. W., and Blake, M. C., Jr., 1974, Geologic map of the Pinto Summit quadrangle, Eureka and White Pine Counties, Nevada: USGS map I-793.

Oldenburg, D. W., 1979, One-dimensional inversion of natural source magnetotelluric observations: Geophysics, **44**, 1218-1244.

Oldenburg, D. W., 1984, An introduction to linear inverse theory: IEEE Trans. Geosci. Remote Sensing, **GE-22**, 665-674.

Oldenburg, D. W., and Ellis, R. G., 1990, Inversion of geophysical data using an approximate inverse mapping: Internat. Symp. on Borehole Geophysics, University of Arizona, and Soc. Expl. Geophys., Expanded Abstracts.

Orange, A. S., 1989, Magnetotelluric exploration for hydrocarbons: Proc. IEEE, **77**, 287-317.

Papoulis, A., 1965, Probability, random variables, and stochastic processes: McGraw-Hill Book Co.

Park, S. K., and Livelybrooks, D. W., 1989, Quantitative interpretation of rotationally invariant parameters in magnetotellurics: Geophysics, **54**, 1483-1490.

Park, S. K., and Torres-Verdín, C., 1988, A systematic approach to the interpretation of magnetotelluric data in volcanic environments with applications to the quest of magma in Long Valley, California: J. Geophys. Res., **93B11**, 13265-13283.

Parker, R. L., 1977, Understanding inverse theory: Ann. Rev. Earth. planet. Sci., **5**, 35-64.

Parker, R. L., 1980, The inverse problem of electromagnetic induction: Existence and construction of solutions based on incomplete data: J. Geophys. Res., **85B8**, 4421-4428.

Parker, R. L., and Whaler, K. A., 1981, Numerical methods for establishing solutions to the inverse problem of electromagnetic induction: J. Geophys. Res., **86B10**, 9574-9584.

Pellerin, L., and Hohmann, G. W., 1990, Transient electromagnetic inversion: A remedy for magnetotelluric static shifts: Geophysics, **55**, 1242-1250.

Pelton, W. H., and Furgerson, B., 1989, High-density 3-D MT: Swath MT and grid MT: 59th Ann. Internat. Mtg., Soc. Expl. Geophys., Expanded Abstracts, 179-181.

Ranganayaki, R. P., and Madden, T. R., 1980, Generalized thin sheet analysis in magnetotellurics: An extension of Price's analysis: Geophys. J. R. Astr. Soc., **60**, 445-457.

Robertson, J. C., 1983, A study of magnetotelluric fields in laterally inhomogeneous earth models: Ph.D. thesis, The University of Texas at Austin.

Robinson, E. A., and Treitel, S., 1980, Geophysical signal analysis: Prentice Hall, Inc.

Rodi, W. L., Swanger, H. J., and Minster, J. B., 1984, ESP/MT: An interactive system for two-dimensional magnetotelluric interpretation: 54th Ann. Internat. Mtg., Soc. Expl. Geophys., Expanded Abstracts, *in* Geophysics, **49**, 611.

Sancer, M. I., and Varvatsis, A. D., 1970, A comparison of the Born and Rytov methods: Proc. IEEE, **58**, 140-141.

Sasaki, Y., 1989, Two-dimensional joint inversion of magnetotelluric and dipole-dipole resistivity data: Geophysics, **54**, 254-262.

Sasaki, Y., 1989, Sensitivity analysis of magnetotelluric measurements in relation to static effects: Geophys. Prosp., **37**, 395-406.

Shoemaker, C. L., Shoham, Y., and Hockey, R. L., 1989, Calibration study of natural source electromagnetic array data recorded over a well in Oregon: Proc. IEEE, **77**, 334-337.

Sigal, R. F., 1989, Method of magnetotelluric exploration with a zigzag array: U.S. Patent 4,862,089.

Singer, B. Sh., 1991, Allowance for static distortions in magnetotellurics, a review paper: Surveys in Geophys., submitted.

Smith, J. T., and Booker, J. R., 1988, Magnetotelluric inversion for minimum structure: Geophysics, **53**, 1565-1576.

Smith, J. T., and Booker, J. R., 1990, Rapid inversion of two- and three-dimensional magnetotelluric data: in press, J. Geophys. Res.

Spies, B. R., 1989, Depth of investigation in electromagnetic sounding methods: Geophysics, **54**, 872-888.

Sternberg, B. K., Washburne, J. C., and Pellerin, L., 1988, Correction for the static shift in magnetotellurics using transient electromagnetic soundings: Geophysics, **53**, 1459-1468.

Stewart, J. H., 1978, Basin and Range structure in western North America: a review, *in* Smith, R. B., and Eaton, G. P., Eds., Cenozoic tectonics and regional geophysics of the western cordillera: Geol. Soc. Am. Mem., 152, 1-31.

Stewart, J. H., 1980, Geology of Nevada: Nevada Bur. Min. Geol., Special Pub. 4.

Stodt, J., 1981, Algorithms for magnetotelluric calculations in the frequency domain: Phoenix Geosciences, internal report.

Swift, C. M., Jr., 1967, A magnetotelluric investigation of an electrical conductivity anomaly in the southwestern United States: Ph.D. thesis, Massachusetts Institute of Technology.

Takasugi, S., Kawakami, N., and Muramatsu, S., 1989, Development of a "high-accuracy MT" system and analysis of corresponding high-density MT measurements: 59th Ann. Internat. Mtg., Soc. Expl. Geophys., Expanded Abstracts, 175-178.

Taylor, H. L., Banks, S. C., and McCoy, J. F., 1979, Deconvolution with the ℓ_1 norm: Geophysics, **44**, 39-52.

Tikhonov, A. N., 1950, On determining electrical characteristics of the deep layers of the earth's crust, Dokl. Acad. Nauk, USSR, **73**, 295-297.

Torres-Verdín, C., 1985, Implications of the Born approximation for the magnetotelluric problem in three-dimensional environments: M.Sc. thesis, The University of Texas at Austin.

Torres-Verdín, C. and Bostick, F. X., Jr., 1990, Implications of the Born approximation for the magnetotelluric problem in three-dimensional environments: Geophysics, accepted for publication.

Torres-Verdín, C. and Bostick, F. X., Jr., 1990, Principles of spatial surface electric field filtering in magnetotellurics: Electromagnetic Array Profiling (EMAP): Geophysics, accepted for publication.

Torres-Verdín, C., and Bostick, F. X., Jr., 1990, Properties of EMAP in two-dimensional environments: 60th Ann. Internat. Mtg., Soc. Expl. Geophys., Expanded Abstracts, 520-523.

Torres-Verdín, C., and Pellerin, L., 1989, Simulation of EMAP responses in three-dimensional environments: 59th Ann. Internat. Mtg., Soc. Expl. Geophys., Expanded Abstracts, 168-171.

Treitel, S., and Lines, L. R., 1982, Linear inverse theory and deconvolution: Geophysics, **47**, 1153-1159.

Uchida, T., Ogawa, Y., and Kikuchi, T., 1987, Resistivity structure of the Sengan geothermal area, northeast Japan, as inferred from the two-dimensional interpretation of Schlumberger soundings: Rept. Geol. Surv. Jap., 266, 505-531.

Uchida, T., 1990, Reservoir structure of the Sengan geothermal field interpreted from the resistivity data: J. Geoth. Res. Soc. Jap., **12**, 1-21.

Vozoff, K., 1972, The magnetotelluric method in the exploration of sedimentary basins: Geophysics, **37**, 98-141.

Vozoff, K., Ed., 1986, Magnetotelluric Methods: Soc. Expl. Geophys., Geophysics Reprint Series No. 5.

Wait, J. R., 1961, The electromagnetic fields of a horizontal dipole in the presence of a conducting half-space: Can. J. Phys., **39**, 1017-1026.

Wannamaker, P. E.,1983, Resistivity structure of the northern Basin and Range, *in* The role of heat in the development of energy and mineral resources in the northern Basin and Range province: Geoth. Res. Counc. Special Rep. 13, 345-362.

Wannamaker, P. E., 1990, Modeling three-dimensional magnetotelluric responses using integral equations: U.S. Dept. of Energy rep. DOE/ID/12489-63, University of Utah Research Institute.

Wannamaker, P. E., Booker, J. R., Filloux, J. H., Jones, A. G., Jiracek, G. R., Chave, A. D., Tarits, P., Waff, H. S., Egbert, G. D., Young, C. T., Stodt, J. A., Martínez, M., Law, L. K., Yukutake, T., Segawa, J. S., White, A., and Green, A. W., Jr., 1989, Magnetotelluric observations across the Juan de Fuca subduction system in the EMSLAB project: J. Geophys. Res., **94B10**, 14111-14125.

Wannamaker, P. E., Booker, J. R., Jones, A. G., Chave, A. D., Filloux, J. H., Waff, H. S., and Law, K. L., 1989, Resistivity cross section through the Juan de Fuca subduction system and its tectonic implications: J. Geophys. Res., **94B10**, 14127-14144.

Wannamaker, P. E., Hohmann, G. W., and Ward, S. H., 1984, Magnetotelluric responses of three-dimensional bodies in layered earths: Geophysics, **44**, 1517-1533.

Wannamaker, P. E., Stodt, J. A., and Rijo, L., 1987, A stable finite element solution for two-dimensional magnetotelluric modeling: Geophys. J., R. Astron., Soc., **88**, 277-296.

Warren, R.K., and Srnka, L.J., 1990, EMAP exploration in the volcanics of the Columbia River Basin, Washington: 60th Ann. Internat. Mtg., Soc. Expl. Geophys., Expanded Abstracts, 524-527.

Weidelt, P., 1972, The inverse problem of geomagnetic induction: Geophys. J., **38**, 257-289.

Williams, J. B., 1988, An EMAP survey of the southern Wind River overthrust, Wyoming, M.Sc. thesis, The University of Texas at Austin.

Word, D. R., Goss, R., and Chambers, D. M., 1986, An EMAP case study: 56th Ann. Internat. Mtg., Soc. Expl. Geophys., Expanded Abstracts, 61-63.

Word, D. R., Smith, H. W., and Bostick, F. X., Jr., 1969, An investigation of the magnetotelluric tensor impedance method: EGRL Technical Report No. 82, The University of Texas at Austin.

Zhdanov, M. S., 1988, Integral transforms in geophysics: Springer-Verlag New York, Inc.

Zhdanov, M. S., and Frenkel, M. A., 1983, Solution of inverse problems by analytical continuation of a transient electromagnetic field in reversed time: J. Geomag. Geoelectr., **35**, 747-765.

Zonge, K. L., Ostrander, A. G., and Emer, D. F., 1986, Controlled-source audio-frequency magnetotelluric measurements, *in* Vozoff, K., Ed., Magnetotelluric Methods: Soc. Expl. Geophys., 749-763.

APPENDIX A

A PLANE-WAVE DECOMPOSITION FOR THE EM FIELDS EXCITED BY A BURIED ELECTRIC DIPOLE

A.1 Introduction

This appendix is divided into two mutually related sections. First, a plane-wave decomposition is obtained that describes the EM fields radiated by an electric dipole in an unbounded conductive medium. Second, the expressions for the homogeneous plane-wave expansion are generalized for the case in which the same dipole is buried within a homogeneous half-space and the observation point lies on the interface between the conductive half-space and perfectly insulating air. The latter problem has been dealt with by Wait, 1961, Moore and Blair, 1961, Baños, 1966, and Bannister and Hart, 1968, among others. However, in solving the same problem the approach presented here is best suited for the derivation of the MT transfer functions introduced in Chapter II.

A.2 Plane-wave decomposition of the electric dipole fields in a homogeneous medium

For convenience, the electric dipole is oriented in the x-direction and is centered at the origin; the z-axis points downward (Figure A-1) Two distinct media are considered in this problem: Medium 1 is above the x-y plane and medium 2 below; in both media the conductivity is constant and equal to σ_0.

The differential equation satisfied by the electric field is analogous to equation (2.9), and reads as

$$\nabla^2\mathbf{E}(\mathbf{r}) + \kappa^2\,\mathbf{E}(\mathbf{r}) = i\omega\mu\,\delta(\mathbf{r})\,\hat{\mathbf{i}}\,, \qquad \text{(A.1)}$$

where $\kappa^2 = -i\omega\mu\sigma_0$, and $\mathbf{r} = x\,\hat{\mathbf{i}} + y\,\hat{\mathbf{j}} + z\,\hat{\mathbf{k}}$.

A solution for the electric field **E** in equation (A.1) and its associated magnetic field, **H**, is now pursued via two transverse vector potentials following the principles of the L-M-N decomposition described by Morse and Feshbach (1953), namely, let

$$\mathbf{E}_j = \mathbf{E}_{jM} + \mathbf{E}_{jN}, \text{ and} \tag{A.2}$$

$$\mathbf{H}_j = \mathbf{H}_{jM} + \mathbf{H}_{jN}, \quad j = 1,2 \tag{A.3}$$

where the subscript j identifies the medium in which field observations are made, and the subscripts M and N denote transverse, or solenoidal (divergenceless) fields derived from a vector potential. The use of a longitudinal (curl-free) component in equations (A.2) and (A.3) is not required because both $\mathbf{E}_j$ and $\mathbf{H}_j$ are divergenceless and satisfy the homogeneous Helmholtz equation. Electric and magnetic fields related to the transverse vector potentials are constructed from the relations

$$\mathbf{E}_M = \nabla x \Psi \hat{\mathbf{k}}, \text{ and} \tag{A.4}$$

$$\mathbf{H}_N = \nabla x \Omega \hat{\mathbf{k}}, \tag{A.5}$$

where Ψ and Ω are scalar potentials satisfying the homogeneous Helmholtz equation,

$$\nabla^2(\Psi,\Omega) + \kappa^2(\Psi,\Omega) = 0.$$

The M and N electric and magnetic fields, $\mathbf{E}_M$ and $\mathbf{H}_N$, respectively, are coupled with their magnetic and electric field counterparts described by equations (A.4) and (A.5) via Maxwell's equations, i.e.,

$$\mathbf{E}_N = \frac{1}{\sigma_0} \nabla x \nabla x \Omega_N \hat{\mathbf{k}}, \text{ and} \tag{A.6}$$

$$\mathbf{H}_M = -\frac{1}{i\omega\mu} \nabla x \nabla x \Psi_M \hat{\mathbf{k}}. \tag{A.7}$$

Here, solutions for the potentials Ψ and Ω are chosen in the form of Cartesian scalar plane-wave functions, expressed as

$$\Psi_j = \Psi_{0j} e^{-i \boldsymbol{\kappa} \cdot \mathbf{r}}, \text{ and} \tag{A.8}$$

$$\Omega_j = \Omega_{0j} e^{-i \mathbf{k} \cdot \mathbf{r}}, \quad j = 1,2 \tag{A.9}$$

where Ψ_0 and Ω_0 are complex constants, and $\boldsymbol{\kappa} = \xi \hat{\mathbf{i}} + \eta \hat{\mathbf{j}} + \zeta \hat{\mathbf{k}}$ is the propagation vector, with

$$\xi^2 + \eta^2 + \zeta^2 = \kappa^2, \tag{A.10}$$

such that the wavenumber ζ is explicitly written as

$$\zeta = \pm\sqrt{\kappa^2 - \xi^2 - \eta^2} \ . \tag{A.11}$$

The sign opted for in equation (A.11) is the one that yields positive real and negative imaginary parts for ζ, so that both of the solutions (A.8) and (A.9) remain finite as the observation point, **r**, recedes away from the dipole.

A closed-form solution for the total electric field vector in equation (A.1) is written in terms of the Cartesian plane-wave vector components as

$$\mathbf{E}(\mathbf{r}) = \frac{1}{(2\pi)^2} \iint_{-\infty}^{+\infty} \mathbf{E}(\xi,\eta)\, e^{-i\boldsymbol{\kappa}\cdot\mathbf{r}}\, d\xi\, d\eta. \tag{A.12}$$

In similar fashion,

$$\mathbf{H}(\mathbf{r}) = \frac{1}{(2\pi)^2} \iint_{-\infty}^{+\infty} \mathbf{H}(\xi,\eta)\, e^{-i\boldsymbol{\kappa}\cdot\mathbf{r}}\, d\xi\, d\eta.$$

Thus, in solving for both $\mathbf{E}(\mathbf{r})$ and $\mathbf{H}(\mathbf{r})$, the derivations below are aimed at finding a solution for the plane-wave vector harmonics $\mathbf{E}(\xi,\eta)$ and $\mathbf{H}(\xi,\eta)$ contained in their integral representation form.

Substitution of equations (A.8) and (A.9) into equations (A.4) through (A.7) and finally into (A.2) and (A.3) yields the following expressions for the EM fields in media 1 and 2:

$$\mathbf{E}_1 = \left(-i\eta\Psi_1 + \frac{\xi\zeta}{\sigma_0}\Omega_1\right)\hat{\mathbf{i}} + \left(i\xi\Psi_1 + \frac{\eta\zeta}{\sigma_0}\Omega_1\right)\hat{\mathbf{j}} + \frac{\xi^2+\eta^2}{\sigma_0}\Omega_1\,\hat{\mathbf{k}}\ ,$$

$$\mathbf{H}_1 = \left(-i\eta\,\Omega_1 - \frac{\xi\zeta}{i\omega\mu}\Psi_1\right)\hat{\mathbf{i}} + \left(i\xi\,\Omega_1 - \frac{\eta\zeta}{i\omega\mu}\Psi_1\right)\hat{\mathbf{j}} - \frac{\xi^2+\eta^2}{i\omega\mu}\Psi_1\,\hat{\mathbf{k}}\ ,$$

$$\mathbf{E}_2 = \left(-i\eta\Psi_2 - \frac{\xi\zeta}{\sigma_0}\Omega_2\right)\hat{\mathbf{i}} + \left(i\xi\Psi_2 - \frac{\eta\zeta}{\sigma_0}\Omega_2\right)\hat{\mathbf{j}} + \frac{\xi^2+\eta^2}{\sigma_0}\Omega_2\,\hat{\mathbf{k}}\ , \text{ and}$$

$$\mathbf{H}_2 = \left(-i\eta\,\Omega_2 + \frac{\xi\zeta}{i\omega\mu}\Psi_2\right)\hat{\mathbf{i}} + \left(i\xi\,\Omega_2 + \frac{\eta\zeta}{i\omega\mu}\Psi_2\right)\hat{\mathbf{j}} - \frac{\xi^2+\eta^2}{i\omega\mu}\Psi_2\,\hat{\mathbf{k}}\ .$$

Finally, matching the required electric and magnetic field boundary conditions on the plane z=0, where the surface current density is expressed as $\mathbf{K}_s(\xi,\eta) = (1)\,\hat{\mathbf{i}}$, gives way to the following coefficients for the Cartesian plane-wave functions:

$$\Omega_{10} = -\Omega_{20} \equiv \Omega_0 = \frac{-i\xi}{2(\xi^2+\eta^2)}, \text{ and} \tag{A.13}$$

$$\Psi_{10} = \Psi_{20} \equiv \Psi_0 = \frac{-i\omega\mu\eta}{2\zeta(\xi^2+\eta^2)}. \tag{A.14}$$

Equations (A.13) and (A.14) substituted into equations (A.8) and (A.9) constitute the solution for the Cartesian vector wave functions describing the EM perturbation of an electric dipole in an unbounded conducting medium.

A.3 Plane-wave decomposition of the fields due to an electric dipole buried in a half-space

The electric dipole is now located at the point $(0,0,z_0)$, as indicated in Figure A-2. There are three separate vertical domains for this problem: medium 1 is the insulating half-space $z<0$, medium 2 is the region $0\le z\le z_0$ of the conductive half-space directly above the dipole, and medium 3 is the space, $z>z_0$, below the dipole. Boundary conditions on the half-space interface are accounted for by introducing both primary and reflected plane wave fields in media 1 and 2, as well as transmitted fields in medium 1. Let

$$\Psi_2 = \Psi_0\, e^{-i\zeta z_0}\, e^{-i\boldsymbol{\kappa}_2 \cdot \mathbf{r}}, \text{ and}$$
$$\Omega_2 = \Omega_0\, e^{-i\zeta z_0}\, e^{-i\boldsymbol{\kappa}_2 \cdot \mathbf{r}}$$

describe the Cartesian scalar wave potentials associated with the primary electric and magnetic fields in medium 2. Likewise, the scalar wave potentials associated with the plane-wave fields reflected downward from the air-earth interface can be written as

$$\Psi_2' = R_\Psi \Psi_0\, e^{-i\zeta z_0}\, e^{-i\mathbf{k}_2' \cdot \mathbf{r}}, \text{ and}$$
$$\Omega_2' = R_\Omega \Omega_0\, e^{-i\,\zeta z_0}\, e^{-i\boldsymbol{\kappa}_2' \cdot \mathbf{r}},$$

where R_Ψ and R_Ω are the Fresnel reflection coefficients of the air-earth interface, and the propagation vectors $\boldsymbol{\kappa}_2$ and $\boldsymbol{\kappa}_2'$ point upward and downward, respectively. The fields

transmitted into the insulating half-space, on the other hand, are derived from the scalar potentials

$$\Psi_1 = T_\Psi \Psi_0 \, e^{-i\zeta_1 z_0} \, e^{-i\,\mathbf{k}_1 \cdot \mathbf{r}}, \text{ and}$$
$$\Omega_1 = T_\Omega \Omega_0 \, e^{-i\zeta_1 z_0} \, e^{-i\mathbf{k}_1 \cdot \mathbf{r}},$$

where T_Ψ and T_Ω are the Fresnel transmission coefficients associated with the air-earth interface. The wavenumber ζ_1 in these last expressions satisfies the dispersion relation in the insulating half-space, namely, $\xi^2 + \eta^2 + \zeta_1^2 = 0$, in which case,

$$\zeta_1 = -i\sqrt{\xi^2 + \eta^2}\,,$$

where the negative sign is preferred to render both scalar wave functions Ψ_1 and Ω_1 finite as the observation point recedes away from the interface into the insulating half-space.

Substitution of the above scalar potentials into equations (A.2) through (A.7) yields the following solution for the Cartesian plane-wave vector functions in medium 2:

$$\mathbf{E}_2 = [-i\eta(1 + R_\Psi e^{-i2\zeta z})\Psi_2 + \frac{\xi\zeta}{\sigma_0}(1 - R_\Omega e^{-i2\zeta z})\Omega_2]\hat{\mathbf{i}} +$$
$$[i\xi(1 + R_\Psi\, e^{-i2\zeta z})\Psi_2 + \frac{\eta\zeta}{\sigma_0}(1 - R_\Omega e^{-i2\zeta z})\Omega_2]\hat{\mathbf{j}} +$$
$$\frac{\xi^2 + \eta^2}{\sigma_0}(1 + R_\Omega e^{-i2\zeta z})\Omega_2\,\hat{\mathbf{k}}\,, \text{ and}$$
$$\mathbf{H}_2 = [-\frac{\xi\zeta}{i\omega\mu}(1 - R_\Psi e^{-i2\zeta z})\Psi_2 - i\eta(1 + R_\Omega e^{-i2\zeta z})\Omega_2]\hat{\mathbf{i}} +$$
$$[-\frac{\eta\zeta}{i\omega\mu}(1 - R_\Psi e^{-i2\zeta z})\Psi_2 + i\xi\,(1 + R_\Omega e^{-i2\zeta z})\Omega_2]\hat{\mathbf{j}} -$$
$$\frac{\xi^2 + \eta^2}{i\omega\mu}(1 + R_\Psi e^{-i2\zeta z})\Psi_0\,\hat{\mathbf{k}}\,.$$

In medium 1, on the other hand, the plane-wave vector functions are given by

$$\mathbf{E}_1 = (-i\eta T_\Psi \Psi_2 + \frac{\xi\zeta_1}{\sigma_1} T_\Omega \Omega_2)\,\hat{\mathbf{i}} +$$
$$(i\xi T_\Psi \Psi_2 + \frac{\eta\zeta_1}{\sigma_1} T_\Omega \Omega_2)\,\hat{\mathbf{j}} + \frac{\xi^2 + \eta^2}{\sigma_1} T_\Omega \Omega_2\,\hat{\mathbf{k}}\,], \text{ and}$$
$$\mathbf{H}_1 = (-\frac{\xi\zeta_1}{i\omega\mu} T_\Psi \Psi_2 - i\eta T_\Omega \Omega_2)\,\hat{\mathbf{i}} +$$

$$\left(\frac{\eta\zeta_1}{i\omega\mu}T_\Psi\Psi_2 + i\xi T_\Omega\Omega_2\right)\hat{j} - \frac{\xi^2+\eta^2}{i\omega\mu}T_\Psi\Psi_2\,\hat{k}\,.$$

The required continuity of the tangential electric and magnetic fields on the half-space interface (z=0) decouples the field solutions related to each of the scalar potentials Ψ and Ω. Thence, solutions for the Fresnel reflection and transmission coefficients are

$$R_\Psi = \frac{\zeta - \zeta_1}{\zeta + \zeta_1} = \frac{\zeta + i\sqrt{\xi^2+\eta^2}}{\zeta - i\sqrt{\xi^2+\eta^2}}\,, \tag{A.15}$$

$$R_\Omega = -1\,, \tag{A.16}$$

$$T_\Psi = 1 + R_\Psi\,, \text{ and} \tag{A.17}$$

$$T_\Omega = 1 + R_\Omega = 0\,. \tag{A.18}$$

With these solutions, the Cartesian plane-wave vector components for the EM fields on the half-space boundary (z=0) are finally written as

$$E_x(\xi,\eta,\omega) = \left\{\frac{-i\omega\mu}{i\zeta}\left[\frac{\xi^2+\eta^2\left(\frac{1+R_\Psi}{2}\right)}{\xi^2+\eta^2}\right] - \frac{\xi^2}{i\zeta\sigma_0}\right\}e^{-i\zeta z_0}\,, \tag{A.19}$$

$$E_y(\xi,\eta,\omega) = \left\{\frac{-i\omega\mu}{i\zeta}\left[\frac{\xi\eta\left(\frac{1-R_\Psi}{2}\right)}{\xi^2+\eta^2}\right] - \frac{\xi\eta}{i\zeta\sigma_0}\right\}e^{-i\zeta z_0}, \tag{A.20}$$

$$E_z = 0\,, \tag{A.21}$$

$$H_x(\xi,\eta) = \frac{\xi\eta}{(\xi^2+\eta^2)}\left(\frac{1-R_\Psi}{2}\right)e^{-i\zeta z_0}, \tag{A.22}$$

$$H_y(\xi,\eta) = \frac{\eta^2}{(\xi^2+\eta^2)}\left(\frac{1-R_\Psi}{2}\right)e^{-i\zeta z_0}, \text{ and} \tag{A.23}$$

$$H_z(\xi,\eta) = \frac{\eta}{\zeta}\left(\frac{1+R_\Psi}{2}\right)e^{-i\zeta z_0}. \tag{A.24}$$

Equations (A.19) through (A.24) can be modified to describe plane-wave vector components in connection with an electric dipole shifted from the z-axis at the location

(x_0,y_0,z_0). The solution comes directly from the shifting property of the Fourier transform (A.12), namely,

$$\mathbf{E}(x,y/x_0,y_0) = \frac{1}{(2\pi)^2}\iint_{-\infty}^{+\infty} \mathbf{E}(\xi,\eta/0,0)\left(e^{-i\xi x_0}\, e^{-i\eta y_0}\right) e^{-i\,\xi x}\, e^{-i\,\eta y}\, d\xi d\eta, \qquad (A.25)$$

where the vector $\mathbf{E}(\xi,\eta/0,0)$ is the plane-wave vector component for the electric field of an electric dipole buried at a depth z_0 below the origin (equations A.19 through A.21). The vector $\mathbf{E}(x,y/x_0,y_0)$, on the other hand, is the total electric field related to the offset dipole. For an observation point (x,y) fixed at the origin, equation (A.25) also yields the Fourier transform, with respect to the source-point coordinates, x_0 and y_0, of the total electric field vector $\mathbf{E}(0,0/x_0,y_0)$, namely,

$$\mathcal{F}_{(x_0,y_0)}\{\mathbf{E}(0,0/x_0,y_0)\} = \mathbf{E}(-\xi,-\eta/0,0)\ .$$

In summary, when the observation point is fixed at the origin and the dipole is moved laterally, the Fourier transform that describes field response values with respect to dipole location can be obtained by reflection about the point $(\xi=0,\eta=0)$ of the expressions (A.19) through (A.24). The wavenumber expressions that result from this operation are the MT transfer functions introduced in Chapter II.

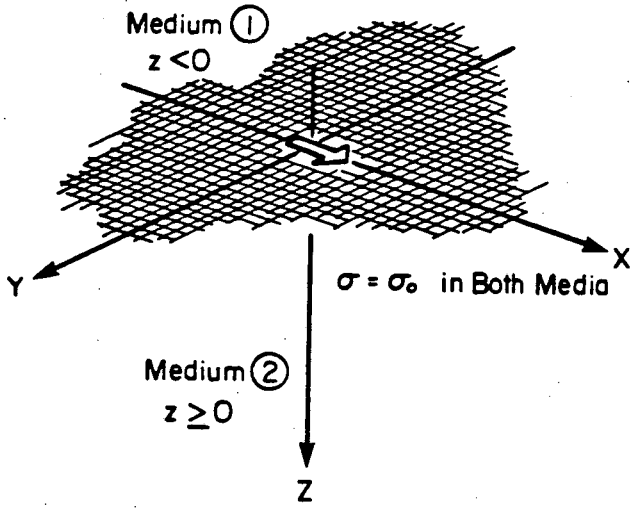

Figure A-1. First source configuration for the plane-wave expansion: an infinitesimal electric dipole is placed at the origin of an unbounded homogeneous conductive medium. The dipole is polarized in the x-direction.

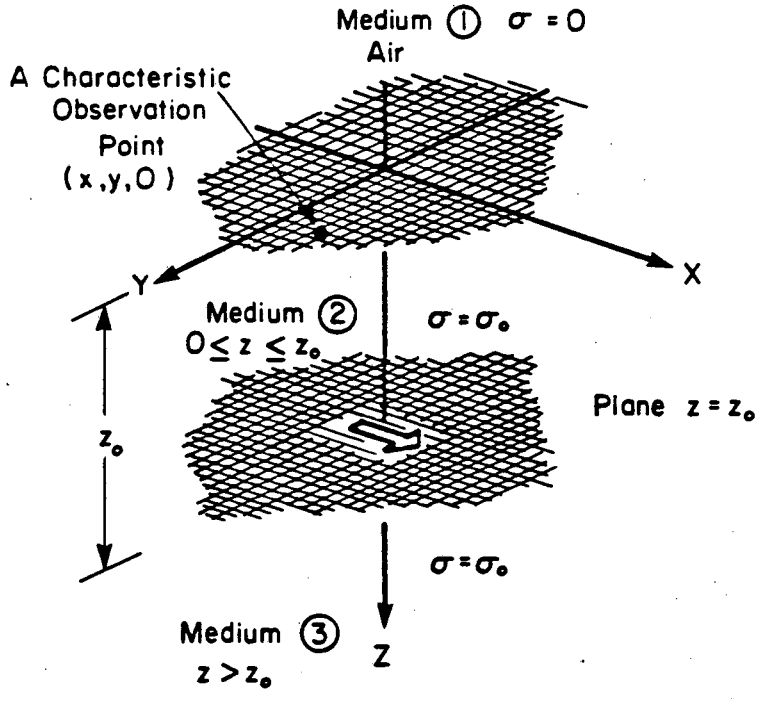

Figure A-2. Second source configuration for the plane-wave expansion: the electric dipole of Figure A-1 is now immersed in a conductive half-space at the location $(0,0,z_0)$.

APPENDIX B

ADDITIONAL EXAMPLES OF 1-D BORN INVERSION

B.1 Description

This appendix contains additional examples that illustrate the performance of the linearized 1-D inversion procedures studied in Chapter III. In all cases, data have been numerically simulated for 64 frequency samples, evenly distributed in logarithmic fashion and spanning the interval from 0.0005 to 1,000 Hz. The figures are self-explanatory, and their format follows all of the plotting conventions established in Chapter III.

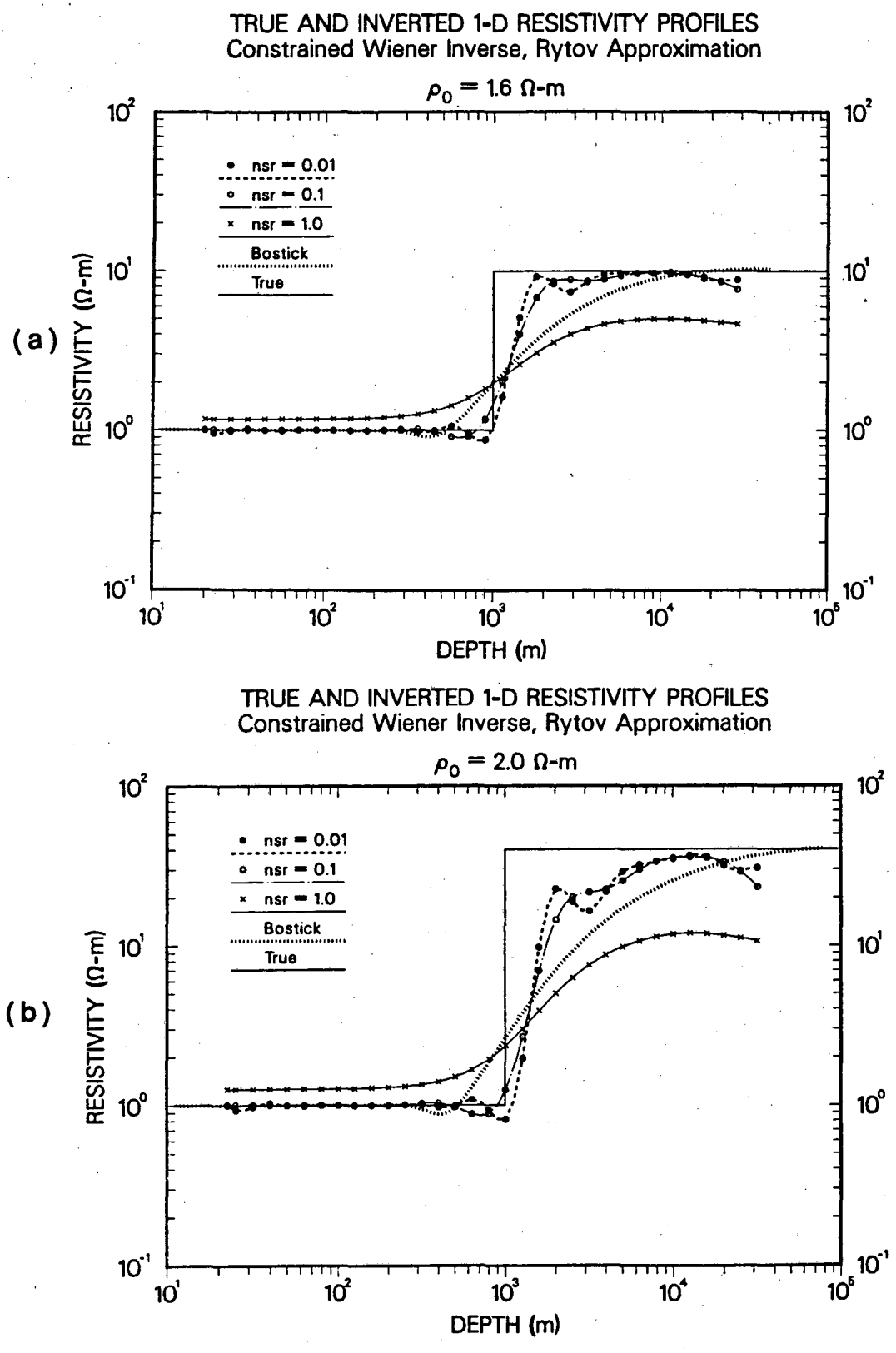

Figure B-1. A study of contrast effects over a resistive step: Rytov inversion.

(c)

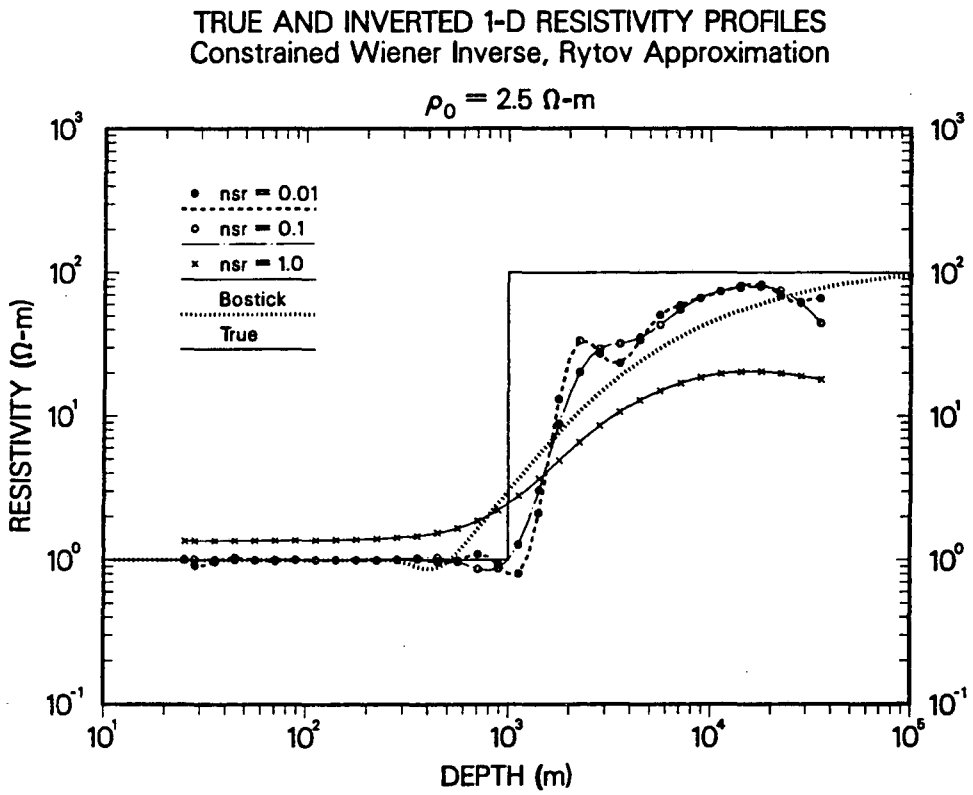

Figure B-1 (continued). A study of contrast effects over a resistive step: Rytov inversion.

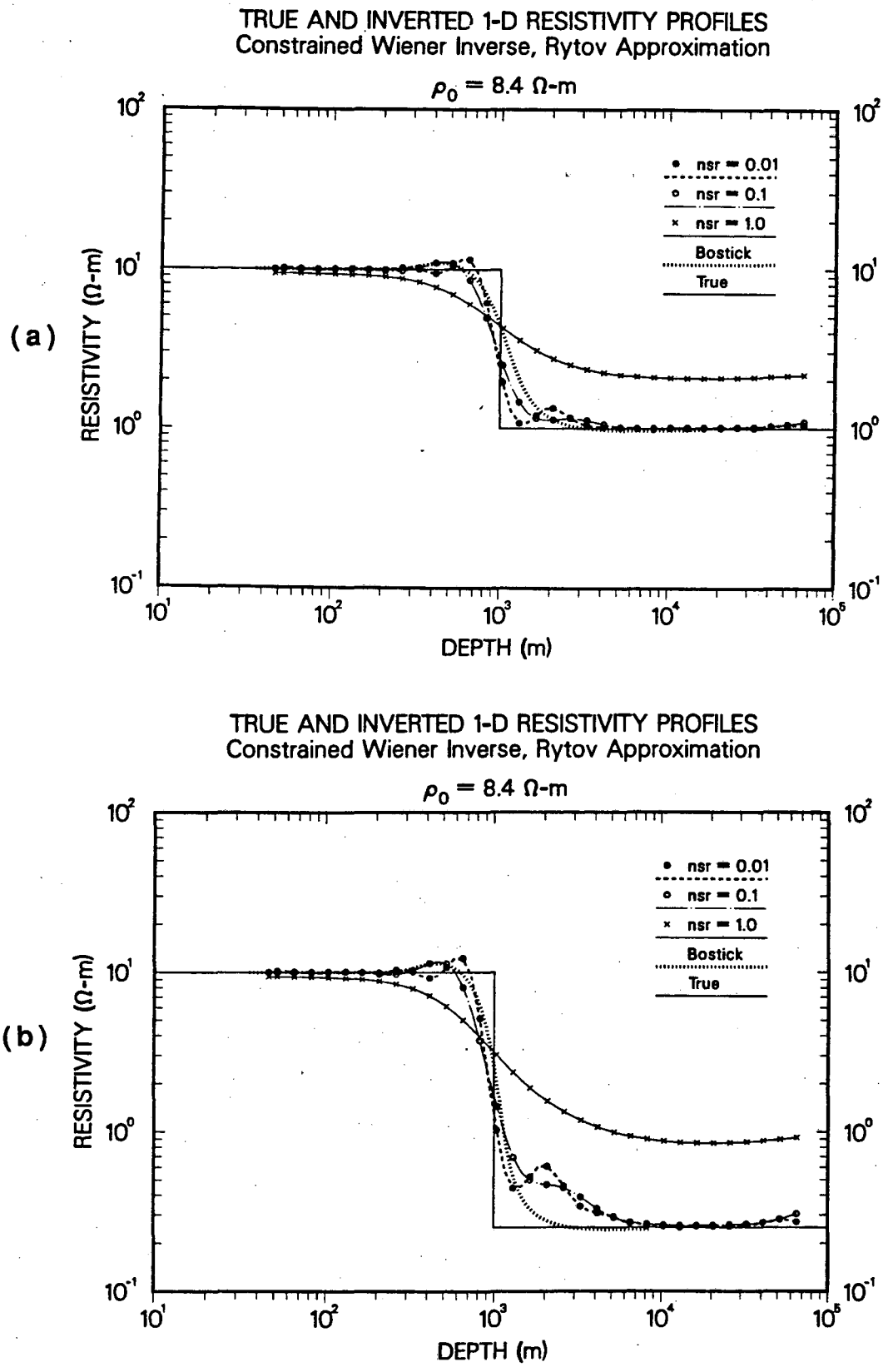

Figure B-2. A study of contrast effects over a conductive step: Rytov inversion.

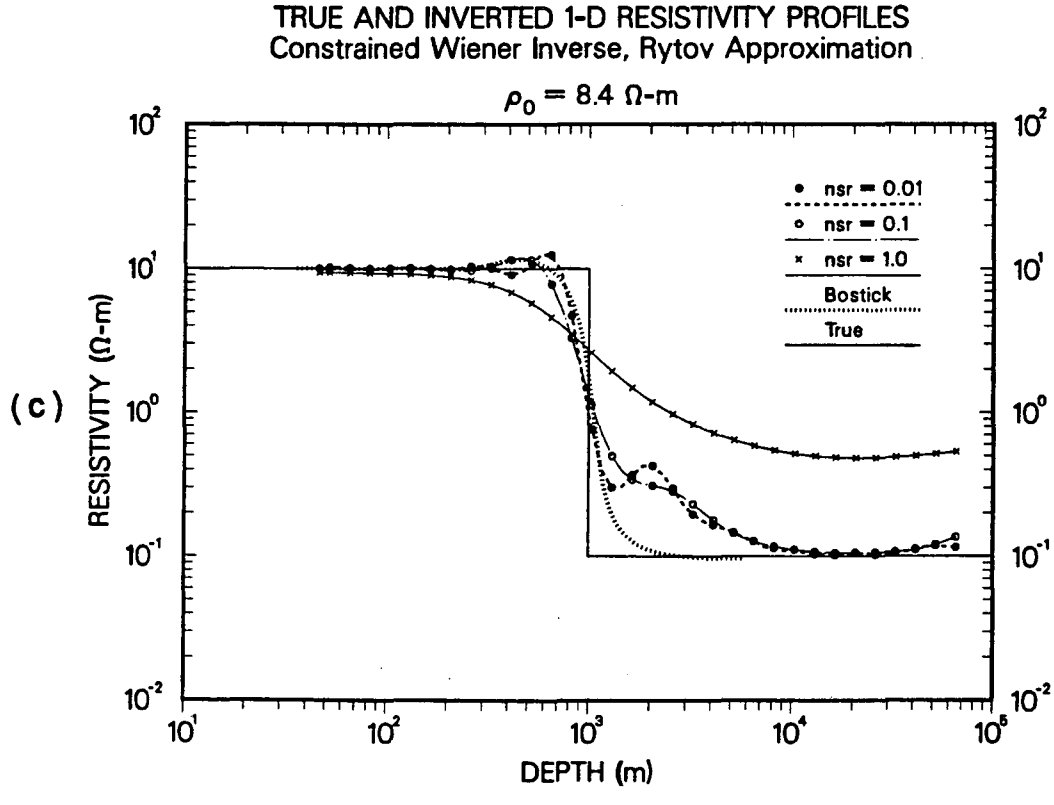

Figure B-2 (continued). A study of contrast effects over a conductive step: Rytov inversion.

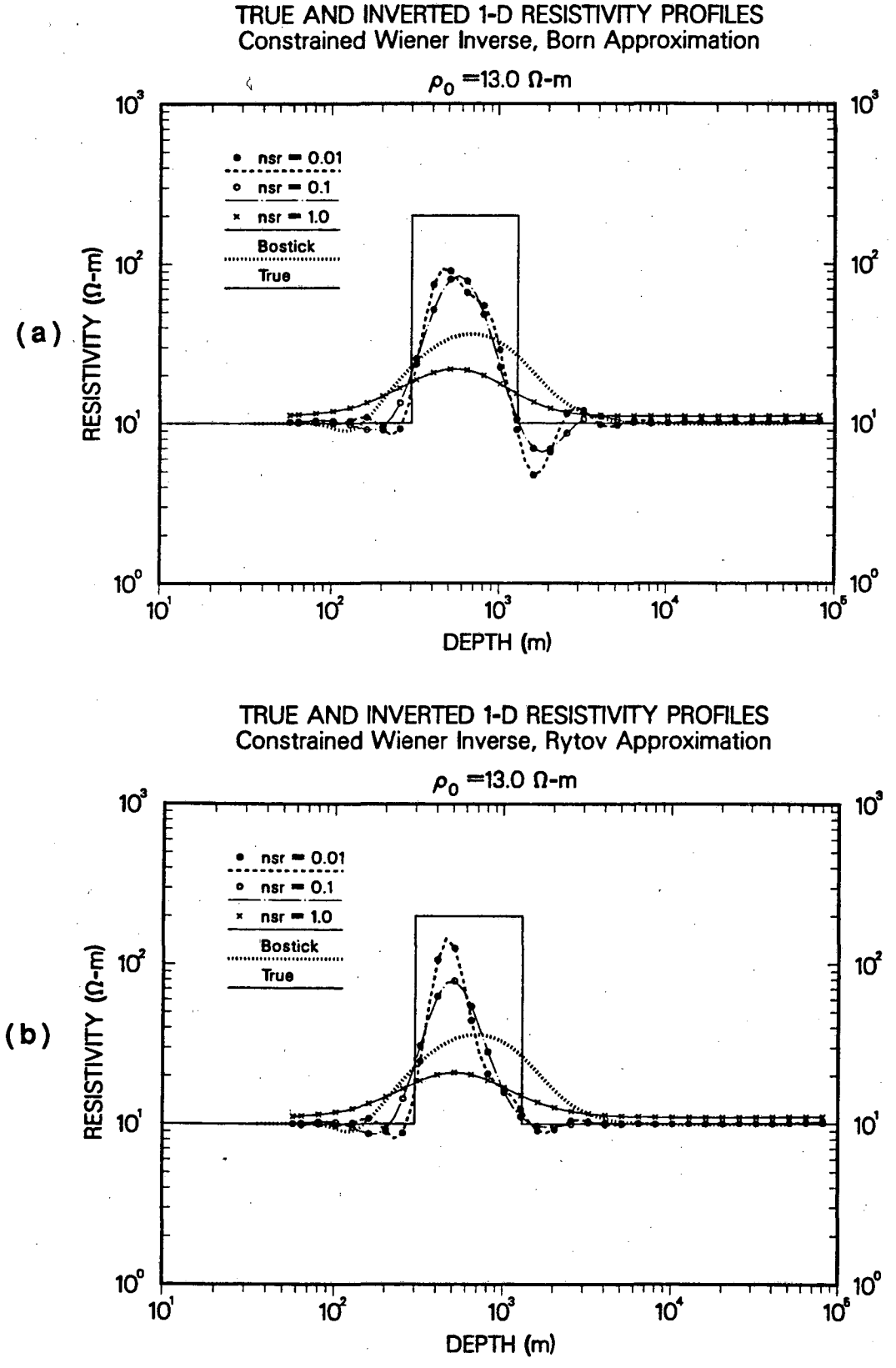

Figure B-3. A resistive anomaly: (a) Born inversion, (b) Rytov inversion, and (c) Rytov inversion with a lower-bound model range constraint.

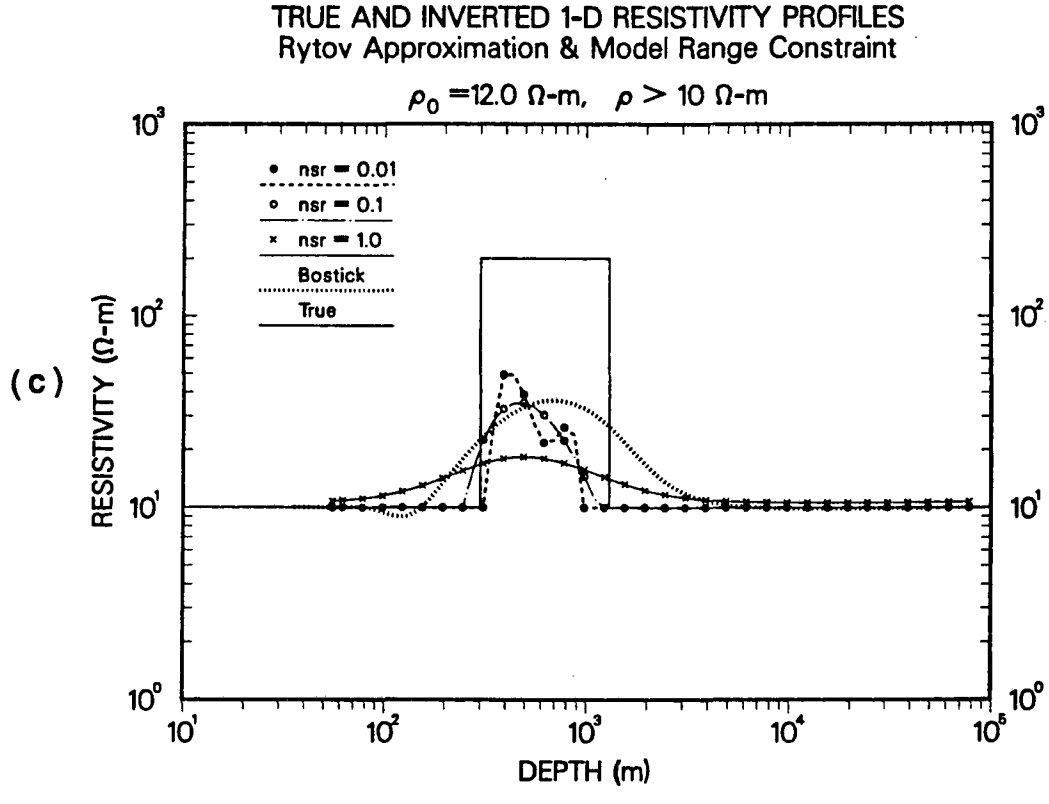

Figure B-3 (continued). A resistive anomaly: (a) Born inversion, (b) Rytov inversion, and (c) Rytov inversion with a lower-bound model range constraint.

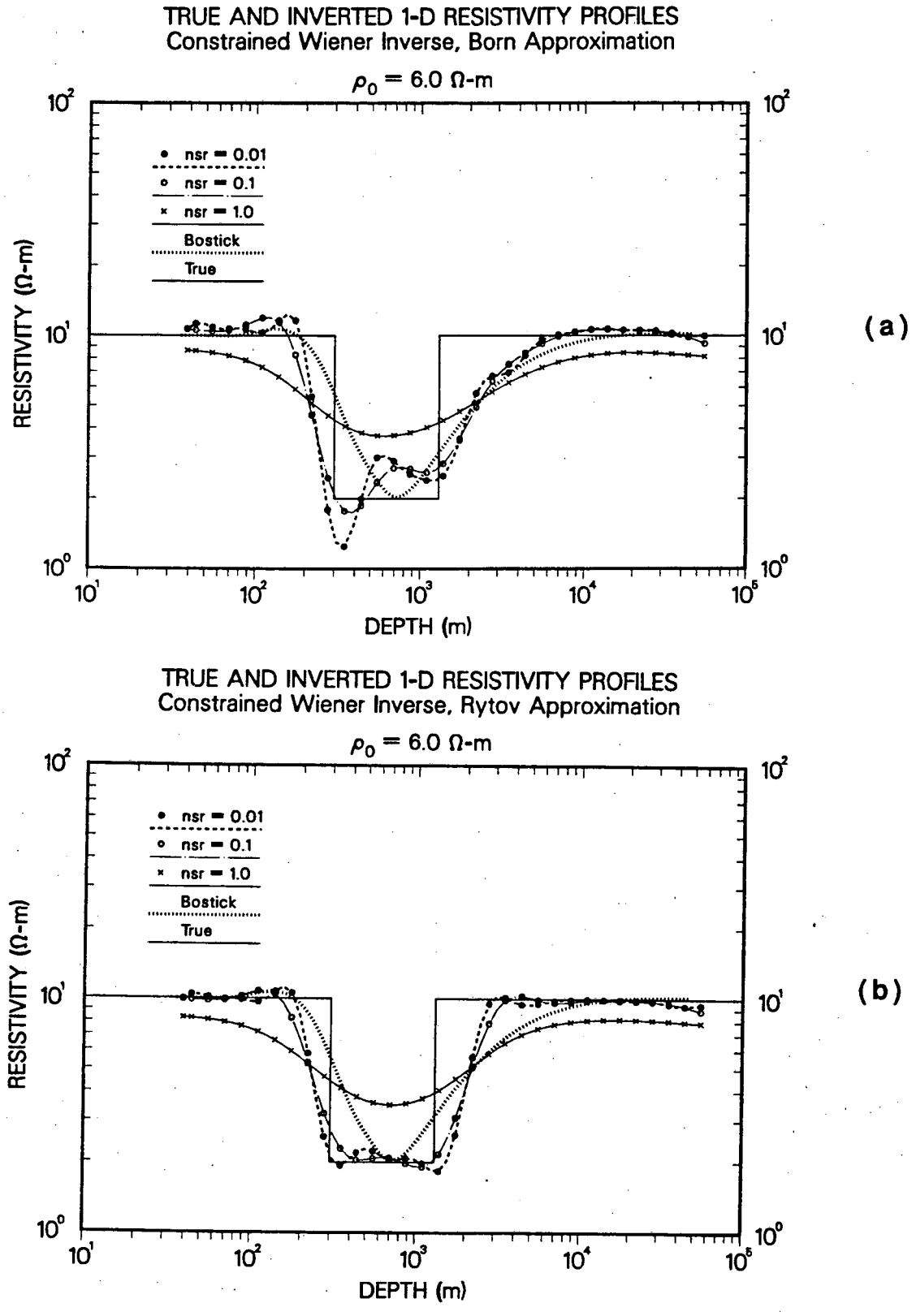

Figure B-4. A conductive anomaly: (a) Born inversion, (b) Rytov inversion, and (c) Rytov inversion with an upper-bound model range constraint.

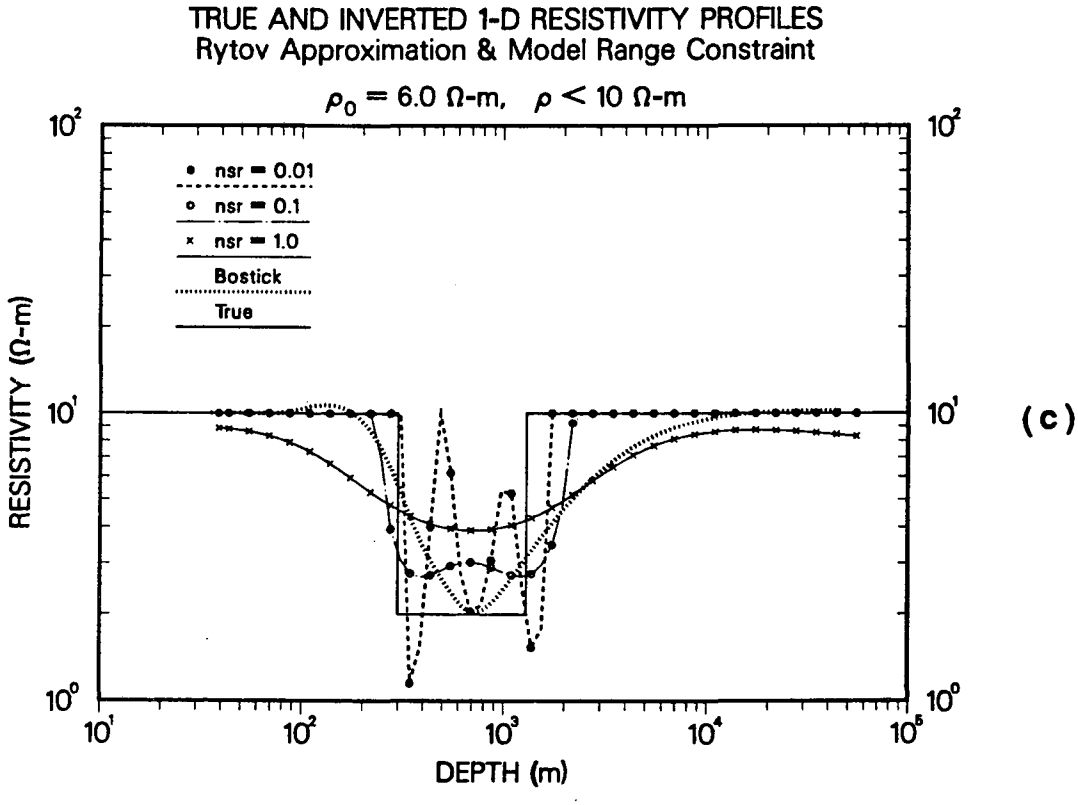

Figure B-4 (continued). A conductive anomaly: (a) Born inversion, (b) Rytov inversion, and (c) Rytov inversion with an upper-bound model range constraint.

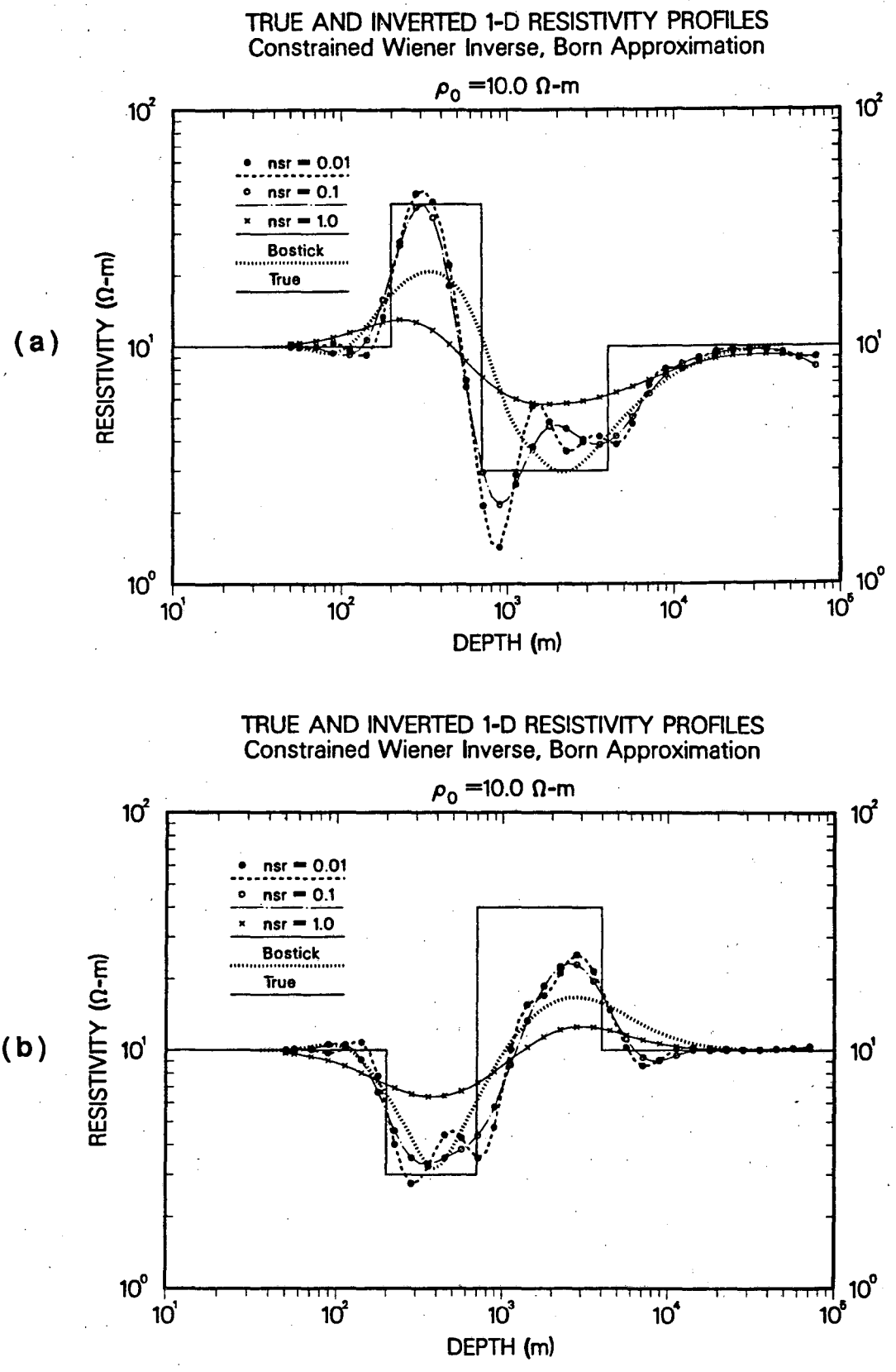

Figure B-5. Resistive and conductive anomalies combined: Born inversion.

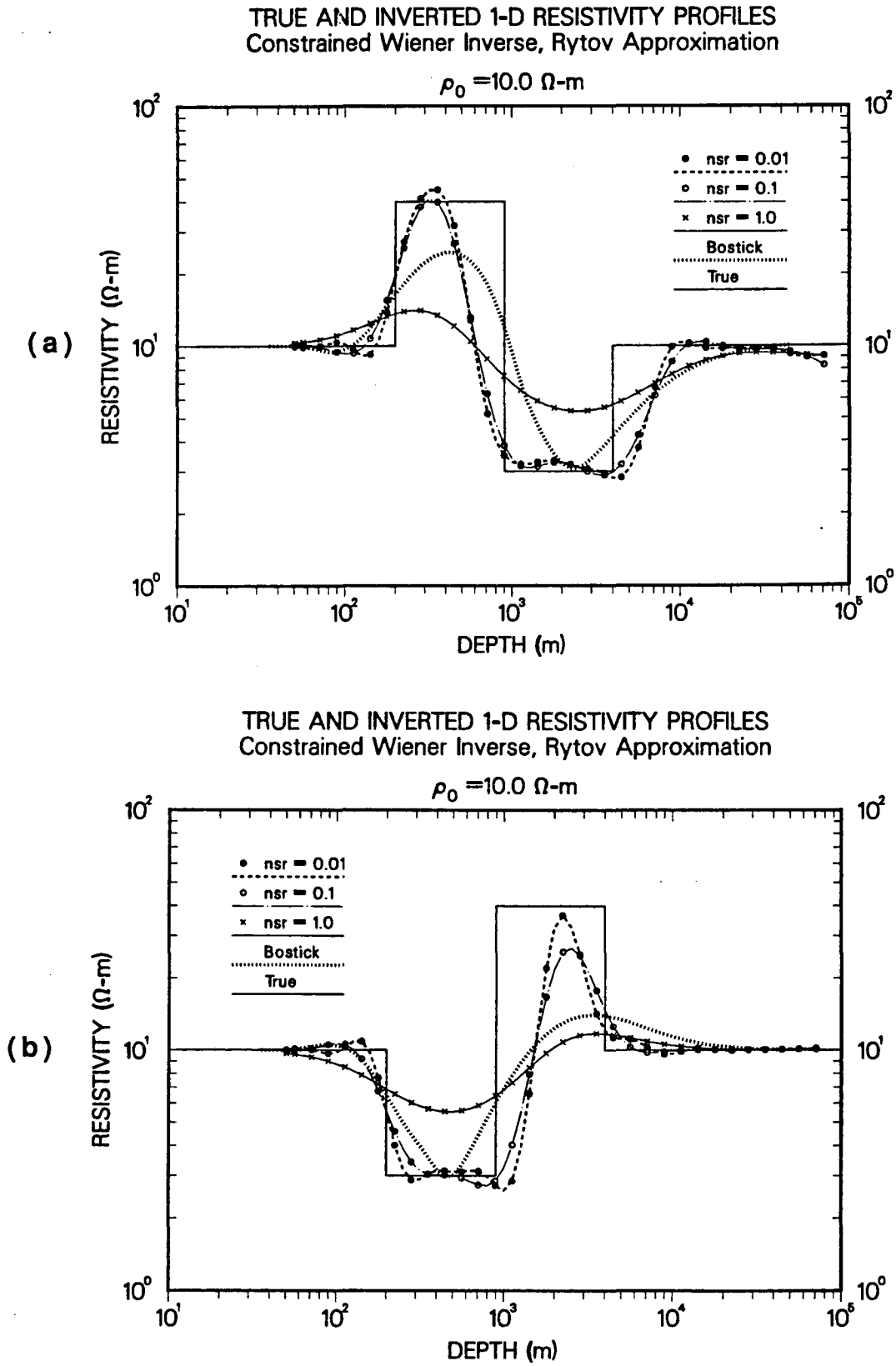

Figure B-6. Resistive and conductive anomalies combined: Rytov inversion.

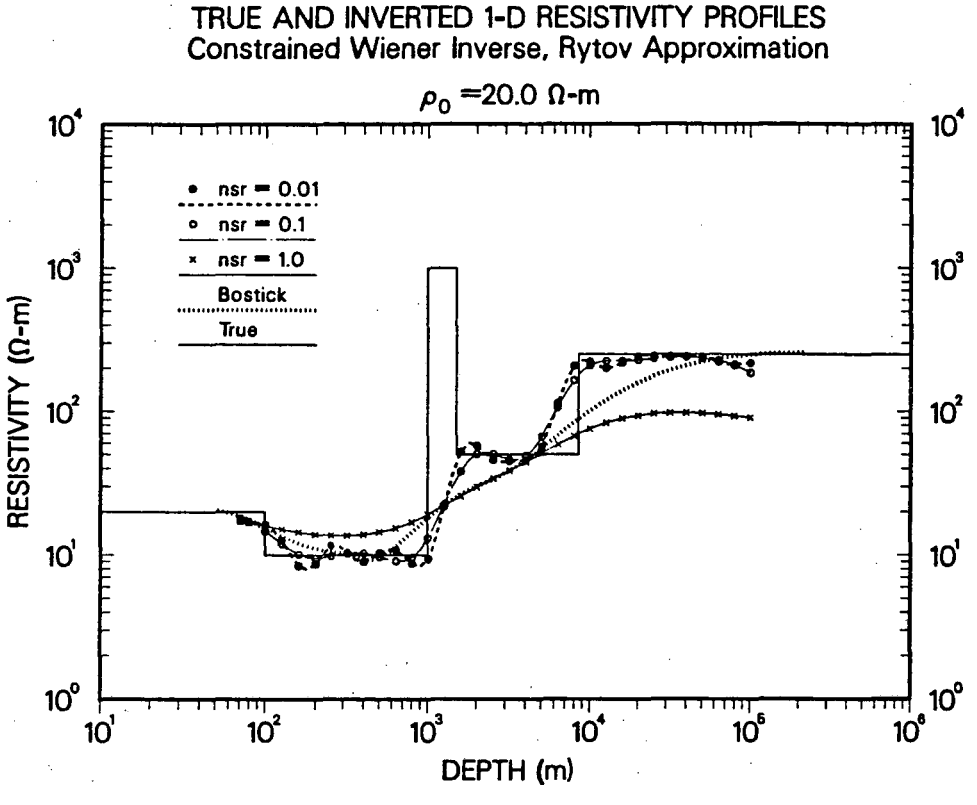

Figure B-7. Smith and Booker's (1988) model example and Rytov inversion.

APPENDIX C

LATERAL LINEAR DEPENDENCE AMONG THE SURFACE 2-D TE FIELDS

C.1 Introduction

The purpose of this appendix is to demonstrate that the linear dependence among all three surface TE fields embodied in the Born approximation is applicable to any 2-D resistivity distribution within the earth. To this end, wavenumber solutions for the surface electric and magnetic fields are derived directly from Maxwell's equations. It is shown that these expressions exhibit the claimed linear relationships.

C.2 Maxwell's equations and linear dependence

Assuming a right-hand Cartesian coordinate frame in which the x axis is normal to strike and the z axis is positioned on the surface and points downward (Figure 4-1), the governing Maxwell's equations for the TE mode are

$$\frac{\partial E_y(x,z,\omega)}{\partial x} = -i\omega\mu\, H_z(x,z,\omega), \tag{C.1}$$

$$\frac{\partial E_y(x,z,\omega)}{\partial z} = i\omega\mu\, H_x(x,z,\omega), \text{ and} \tag{C.2}$$

$$\frac{\partial H_x(x,z,\omega)}{\partial z} - \frac{\partial H_z(x,z,\omega)}{\partial x} = \sigma(x,z)\, E_y(x,z,\omega), \tag{C.3}$$

where the usual $e^{i\omega t}$ time dependency is assumed and $\sigma=1/\rho$. Dividing equation (C.1) through by $E_0(\omega)$ and $H_0(\omega)$, the surface electric and magnetic fields associated with a homogeneous half-space of resistivity ρ_0, respectively, and subsequently transforming the field ratios into the wavenumber domain yields

$$\tilde{H}_z(k,\omega) = -Z_0(\omega)\frac{2\pi k}{\omega\mu}\,\tilde{E}_y(k,\omega), \tag{C.4}$$

where

$$\tilde{H}_z(k,0,\omega) = \mathcal{F}\{\frac{H_z(x,0,\omega)}{H_0(\omega)}\},$$

$$\tilde{E}_y(k,0,\omega) = \mathcal{F}\{\frac{E_y(x,0,\omega)}{E_0(\omega)}\},$$

$Z_0(\omega)$ is the surface wave impedance of the homogeneous half-space, given by

$$Z_0(\omega) = -\frac{E_0(\omega)}{H_0(\omega)} = -\sqrt{i\omega\mu\rho_0} \qquad (C.5)$$

(equation 2.12), and k is the linear wavenumber in the x direction. The definition of the spatial Fourier transform with respect to x, identified with the operator $\mathcal{F}$, is as described in section 4.3. Substitution of equation (C.5) into (C.4) and further algebraic simplification leads to the expression

$$\tilde{H}_z(k,\omega) = i\sqrt{-1}\,\gamma\,\tilde{E}_y(k,\omega), \qquad (C.6)$$

where the variable γ is defined in equation (4.19).

To obtain a similar wavenumber-domain expression between the surface magnetic field components H_x and H_y, consider the solution of equation (C.3) in the air, where $\sigma(x,z)=0$ and the dispersion relation is given by

$$(2\pi k)^2 + \zeta^2 = 0, \qquad (C.7)$$

where ζ is the complementary wavenumber that determines the Laplacian fall-off of the fields away from the surface into the the air. Dividing equation (C.3) through by $H_0(\omega)$ and specializing the exponential solution for $H_z(x,z,\omega)$ on the surface, yields the wavenumber-domain expression

$$-\zeta\,\tilde{H}_x(k,\omega) = 2\pi k\,\tilde{H}_z(k,\omega), \qquad (C.8)$$

where

$$\tilde{H}_x(k,\omega) = \mathcal{F}\{\frac{H_x(x,\omega)}{H_0(\omega)}\}.$$

Substitution of the explicit value for ζ derived from equation (C.7) into equation (C.8) leads to

$$\tilde{H}_z(k,\omega) = iU(\gamma)\,\tilde{H}_x(k,\omega), \qquad (C.9)$$

where $U(\gamma)$ is the sign function defined by equation (4.37). This last expression is equivalent to the space-domain Hilbert transform relations

$$H_x(x,0,\omega) = \frac{1}{\pi}\int_{-\infty}^{+\infty} \frac{H_z(x_0,0,\omega)}{x_0 - x}\, dx_0 \text{ , and}$$

$$H_z(x,0,\omega) = \frac{1}{\pi}\int_{-\infty}^{+\infty} \frac{H_x(x_0,0,\omega)}{x_0 - x}\, dx_0$$

(Bracewell, 1965), which indicate that the surface solutions for both H_x and H_z are spatial analytic components of each other.

Hence, the developments above demonstrate that the spatial linear dependence among the TE field components found with the Born approximation equations is extensive to all situations. In practice, this linear dependency should be taken into account, for instance, when devising procedures to concomitantly invert a combination of two or three of the components into a cross-section of subsurface resistivity. Even though the addition of data makes the inverse problem more overdetermined, the linear dependency exhibited by some of the data may bias performance parameters such as the goodness of fit.

In a different context, because the electric field component is related to the magnetic field components by the single-pole high-pass wavenumber filter $1/\gamma$, the estimation of magnetic field data from electric field data across strike is a very unstable operation even with continuously sampled data. On the other hand, even though the estimation of electric field data from magnetic field data requires a stable low-pass wavenumber filtering operation, this process will not yield the DC wavenumber harmonic because as demonstrated in section 2.6, the magnetic field data are insensitive to such harmonic.

LAWRENCE BERKELEY LABORATORY
UNIVERSITY OF CALIFORNIA
INFORMATION RESOURCES DEPARTMENT
BERKELEY, CALIFORNIA 94720